A resistivity-depth model of the central Azraq basin area, Jordan: 2D forward and inverse modeling of time domain electromagnetic data

Inaugural-Dissertation

zur
Erlangung des Doktorgrades
der Mathematisch-Naturwissenschaftlichen Fakultät
der Universität zu Köln

vorgelegt von
Pritam Yogeshwar
aus Poona, Indien

Köln 2014

Gutachter: Prof. Dr. B. Tezkan
Prof. Dr. A. Junge

Tag der mündlichen Prüfung: 30. Juni 2014

Abstract

The focus of this thesis is the geophysical exploration of the central part of the Azraq basin in the northeastern desert of Jordan. In addition to common 1D inversion techniques, further 2D forward modeling strategies and a rarely used 2D inverse modeling scheme are applied to transient electromagnetic data.
The Azraq area is of potential interest for palaeoclimatical and archaeological research in the frame of the interdisciplinary Collaborative Research Centre 806, entitled *Our Way to Europe* (CRC 806). The project investigates the history of modern human, particularly population movements in the past 190,000 years before present. The center of the Azraq Basin is covered by a 10×10 km^2 mudflat consisting thick sedimentary deposits. To provide the basis for probable future drilling projects within the CRC 806, a 7 km and a 5 km long transects were investigated in the mudflat area. An extensive survey was conducted consisting of 150 recorded central loop transient electromagnetic (TEM) sounding locations. The electrical resistivity tomography (ERT) was applied as a complementary method to validate the TEM results.
Common 1D inversion techniques are applied to interpret the TEM field data and to investigate the uncertainty of the inverse models. The results are patched together to quasi 2D resistivity-depth sections. The derived quasi 2D sections are consistent and provide a detailed image of the subsurface electrical resistivity distribution down to approximately 100 m depth. The results identify a resistive buried basalt layer in the periphery of the mudflat and a resistivity increase inside the high conductive mudflat sediments, which obviously corresponds to the layer below. The subsurface models are in excellent agreement with lithological borehole data and the geological information. Moreover, a transition zone from moderate to very low resistivities is observed, which is of interest for the groundwater management in Azraq.
To verify the derived 1D inverse models, a detailed 2D modeling study is performed. Although the subsurface resistivity structure varies significantly along both investigated transects, the study demonstrates that a 1D inversion is sufficient to interpret the TEM data. Due to reduced data quality at late transient times for a few sounding locations, the deep resistivity contrast inside the mudflat is not well resolved in those zones. Further systematical 2D forward modeling shows that the resistivity increase is in general required to fit the TEM field data.
The 2D forward modeling approach is based on the prior selection of a model and, therefore, does not provide an independent validation of the subsurface resistivity distribution. For this reason, a rarely applied 2D TEM inversion scheme is used to interpret the field data. The obtained 2D inverse models reveal a remarkable agreement with the quasi resistivity-depth sections, which are derived from the 1D results. Moreover, the unsatisfactory resolved deep resistivity contrast below the mudflat is reconstructed by using a-priori information, which is integrated into the parameterization of the model. Accordingly, the 2D inversion provides a strong independent validation of the subsurface resistivity distribution.

Zusammenfassung

Der Schwerpunkt dieser Arbeit ist der geophysikalischen Exploration des zentralen Bereichs des Azraq Beckens in der nordöstlichen Wüste Jordaniens gewidmet. Zur Interpretation von Transient-Elektromagnetik Daten, werden gebräuchliche eindimensionale (1D) Inversionstechniken, zweidimensionale (2D) Modellierungsstrategien, sowie ein bisher selten angewandtes zweidimensionales Inversionsverfahren eingesetzt.
Das Gebiet um Azraq ist von potentiellem Interesse für paläoklimatische und archäologische Forschungsvorhaben des interdisziplinären Sonderforschungsbereichs 806 mit dem Titel *Our Way to Europe* (SFB 806). Das Projekt erforscht die Geschichte des modernen Menschen und insbesondere Migrationsbewegungen im Zeitraum der letzten 190.000 Jahre. Im Zentrum des Azraq Beckens haben sich mächtige Sedimente abgelagert und bilden eine ca. 10×10 km^2 große "Mudflat" (auch Playa genannt). Zum Zwecke der Vorerkundung und um eine Basis für eventuelle zukünftige Bohrungen im Rahmen des SFB 806 zu schaffen, wurden umfangreiche geophysikalische Messungen durchgeführt. Insgesamt wurden dabei 150 Transient-Elektromagnetik (TEM) Stationen vermessen. Zur Validierung der TEM Ergebnisse wurde die Elektrische Widerstands-Tomographie (ERT) als ergänzende Methode angewendet.
Gebräuchliche 1D Inversionstechniken werden dabei zur Interpretation der TEM Felddaten benutzt und die Modell-Unsicherheiten mit äquivalenten Modellen und Parameter-Wichtigkeiten (Importances) abgeschätzt. Weiterhin werden die 1D Modelle zu quasi 2D Sektionen zusammengefügt. Diese abgeleiteten quasi 2D Sektionen sind konsistent und liefern ein sehr detailliertes Bild der elektrischen Leitfähigkeitsverteilung im Untergrund bis ca. 100 m Tiefe. Die Ergebnisse zeigen eine schlecht leitende Basaltschicht im Randbereich der Mudflat und eine Abnahme der Leitfähigkeit innerhalb der Mudflat, die auf die darunterliegende Schicht schließen lässt. Die Untergrundmodelle zeigen eine sehr gute Übereinstimmung mit lithologischen Daten aus Bohrungen sowie mit der geologischen Vorinformation. Darüber hinaus zeigen die Ergebnisse eine laterale Übergangszone von moderaten zu extrem hohen Leitfähigkeiten, die von Interesse für das Grundwasser Management in Azraq ist.
weiterhin wird eine detaillierte 2D Modellierung durchgeführt, um die 1D Ergebnisse zu verifizieren. Diese Studie demonstriert, dass die 1D Interpretation der TEM Daten ausreichend ist, obwohl die laterale Leitfähigkeit des Untergrunds stark variiert. Einige Stationen zeigen eine verminderte Datenqualität zu späten Zeiten im Transienten. Dies führt zu einer geringeren Auflösung der Schicht unterhalb der Mudflat-Sedimente. Systematische Modellierungen zeigen jedoch, dass dieser Kontrast im Allgemeinen benötigt wird, um die Felddaten zu erklären.
Die 2D Modellierung basiert auf der vorherigen Auswahl eines Modells und stellt daher keine unabhängige Validierung der Leitfähigkeitsverteilung im Untergrund dar. Aus diesem Grund, wird ein bisher nicht gebräuchlicher 2D TEM Inversionsalgorithmus zur Interpretation der Felddaten angewendet. Die inversen 2D Modelle zeigen eine bemerkenswerte Übereinstimmung mit den quasi 2D Sektionen. Darüber hinaus rekonstruiert die 2D Inversion den Kontrast der elektrischen Leitfähigkeit innerhalb der Mudflat durch eine geeignete Parametrisierung und Integration von Vorinformation in das Modell. Demzufolge liefert die 2D Inversion eine überzeugende Validierung der Leitfähigkeitsverteilung im zentralen Bereich des Azraq Beckens.

Contents

List of Figures

List of Tables

CHAPTER 1

Introduction

The focus of this thesis is the geophysical exploration of the central part of the Azraq basin in the northeastern desert of Jordan. In addition to common 1D inversion techniques, further 2D forward modeling strategies and a rarely used 2D inverse modeling scheme are applied to transient electromagnetic data.
The Azraq area is of potential interest for palaeoclimatical and archaeological research in the frame of the interdisciplinary Collaborative Research Centre 806, entitled *Our Way to Europe* (CRC 806). The CRC 806 investigates the history of modern human, particularly population movements in the past 190,000 years before present. It is designed to capture the complex nature of dispersal of modern man from Africa to Western Eurasia and particularly to Europe [CRC-806, 2012]. The project investigates various sites in the source areas, along corridors and in target areas of population movements. The Jordan rift valley in the Eastern Mediterranean served as one possible corridor of dispersal of modern man [CRC-806, 2012]. A key issue addressed by the CRC 806, is the reconstruction of the palaeoclimatical conditions in the research areas and in the concerned time range. Very promising archives for a paleoclimatical reconstruction are sedimentary deposits accumulated in dry lakes. The area around the (former) oasis Qa' Al Azraq has been a major spot for prehistoric settlements and was subject to long-term archaeological research [Stanley Price & Garrard, 1975; Copeland, 1988; Byrd, 1988]. It is a unique wetland with pools and marshes located in a large arid environment. In the basin center, a 10×10 km^2 mudflat developed consisting thick sedimentary deposits.
The geophysical investigation presented in this thesis provides the basis for probable future drilling projects within the CRC 806. Information about the subsurface are important to avoid elaborate and costly abortive drilling. The main objective is to investigate the subsurface electrical resistivity structure and particularly to identify the thickness of sedimentary deposits in the central Azraq basin area. The early work of El-Kaysi & Talat [1996] and El-Waheidi et al. [1992] provided information about the thickness of the mudflat deposits, but complete and densely investigated transects using modern geophysical equipment are not available.

To achieve the objective within the CRC 806, a 7 km and a 5 km long transects were investigated from the periphery to the center of the mudflat depression. An extensive survey was conducted consisting of 150 recorded central loop transient electromagnetic

(TEM) soundings. Additionally, the electrical resistivity tomography (ERT) was applied as a complementary method to validate the TEM results.
The TEM mehod is often used for the investigation of shallow sedimentary basins and valley structures [Jørgensen et al., 2003; Danielsen et al., 2003; Steuer et al., 2009]. Moreover, Electromagnetic methods, particularly TEM, are widely used for groundwater studies and aquifer characterization, for example contamination and salinization problems [Fitterman & Stewart, 1986; Goldman & Neubauer, 1994; Tezkan, 1999; Yogeshwar et al., 2012; Papen et al., 2013]. Fundamental overviews of the TEM method are given in [Nabighian & Macnae, 1991; Spies & Frischknecht, 1991] and in several comprehensive reviews related to near surface applications of electromagnetic techniques [Goldman & Neubauer, 1994; Tezkan, 1999; Pellerin, 2002; Auken et al., 2006; Everett, 2011].

In the first part of the thesis, electrical resistivity-depth models are derived along both transects. Common 1D TEM data inversion algorithms are applied and the uncertainties of the models are discussed in detail on the basis of equivalent modeling and parameter importances. The 1D inverse models are patched together to quasi 2D resistivity-depth sections. Furthermore, these sections are put in context with the available geological information and correlated with lithological borehole data.
As stated by Goldman et al. [1994], the conventional 1D interpretation of TEM data by 1D layered earth models has proved feasibility in numerous case studies. Therefore, TEM data is often interpreted by 1D inversion or quasi 2D/3D schemes. A quasi 2D laterally constraint inversion (LCI) was presented by Auken & Christensen [2004], where 1D sounding models are linked together along a profile line. Viezzoli et al. [2008] extended the LCI to a quasi 3D inversion, which is called spatially constraint inversion (SCI). However, there are cases where distortion effects have to be considered and the field data can neither be explained by 1D models nor by quasi 2D/3D schemes [Newman et al., 1987; Goldman et al., 1994]. Although no clear distortion effects are visible in the TEM sounding data recorded in Azraq, the subsurface resistivity varies significantly along both investigated transects. For this reason, it is questionable if a 1D interpretation is adequate. Therefore, the second part of this thesis concentrates on the 2D forward and inverse modeling of the TEM sounding data. An elaborate 2D modeling study is performed to validate the subsurface resistivity structure, which is derived from prior 1D inversion results. The 2D TEM forward modeling utilizes the time domain finite difference algorithm *SLDMem3t* [Druskin & Knizhnermann, 1988, 1994, 1999]. It has been successfully applied to numerous forward modeling studies in 2D/3D involving time domain electromagnetic methods for various source configurations [Hördt, 1992; Hördt et al., 1992, 2000; Hördt & Müller, 2000; Goldman et al., 2011; Sudha et al., 2011; Rödder & Tezkan, 2013].
Forward modeling approaches are always based on a prior selection of a model. Particularly, in 2D/3D a full and random parameter study involves far too many calculations, which is not feasible. As a result, the 2D modeling results are to some extent biased and do not provide an independent validation of the electrical resistivity-depth structure. To carry out an independent validation, a large number of TEM soundings are inverted using the 2D iterative Gauss-Newton inversion algorithm *SINV*, which utilizes the *SLDMem3t* as forward solver [Scholl et al., 2004; Martin, 2009]. Earlier, Commer [2003] applied *SINV* to mountainous long offset transient electromagnetic (LOTEM)

data from Mount Merapi, Indonesia. He used a Marquardt-type restricted 3D inversion with only a few model parameters. Scholl et al. [2004] and Martin [2009] applied the 2D inversion algorithm to LOTEM data from the Araba fault, Jordan. The derived 2D models were in good agreement with the magnetotelluric result presented by Ritter et al. [2003]. Koch et al. [2004] presented a 2D inversion of central loop TEM data using an early version of *SINV*. Recently, Martin [2009] extended *SINV* to a large scale 3D inversion scheme and successfully applied it to synthetic in-loop TEM data generated from a 3D buried conductor model. Nevertheless, *SINV* was not yet routinely utilized for the 2D inversion of TEM data. Therefore, the capabilities of the algorithm are presented in detail and studied on the basis of synthetic models. Finally, *SINV* is applied to the TEM field data to validate the resistivity-depth structure derived from the 1D inverse models.
The multi-dimensional inversion of time domain electromagnetic data is not state of the art, yet. It is still a computational expensive task and the availability of large scale algorithms is limited. Over the past ten years 3D time domain inversion schemes were presented by few authors, e.g. Haber et al. [2007]; Commer & Newman [2008]; Oldenburg et al. [2013]. Recent reviews on 2D/3D numerical forward and inverse modeling for time and frequency domain electromagnetic methods were given by Newman & Commer [2005]; Avdeev [2005]; Börner [2010].

Due to the groundwater problematic in Azraq, an additional motivation evolved during this thesis. The Azraq area is of enormous economical importance to Jordan. Approximately one third of the freshwater supply for Jordan's capital city of Amman is provided from the Azraq [Ibrahim, 1996]. The extensive groundwater exploitation has led to a severe decline in the groundwater table. In the central part of the area the groundwater is hyper-saline. To ensure the freshwater supply, groundwater research has been (and still is) an ongoing and relevant issue over the past 30 years. Several authors used geophysical techniques to investigate the saline groundwater zone [El-Waheidi et al., 1992; El-Kaysi & Talat, 1996; El-Naqa, 2010; Abu Rajab & El-naqa, 2013]. The geophysical investigations can support the ongoing groundwater management in the area because information about the extent of the saline water body can be derived from the results presented in this thesis.

1.1 This thesis

An introduction to the theoretical and conceptual background of the central loop transient electromagnetic (TEM) method is given in chapter 2. The basic theory of geophysical data inversion, which is indispensable in most geophysical interpretation approaches, will be introduced in chapter 3.
The survey area in the central part of the Azraq basin, Jordan and the geological background is briefly introduced in chapter 4. The objectives of the geophysical investigations are formulated according to the regional geology and the scope of the CRC 806. Moreover, the survey design and the processing of TEM field data is discussed. The results obtained by conventional 1D inversion are presented as quasi 2D resistivity-depth sections and the reliability of the derived models is discussed in detail. At the end of chapter 4, the geological information is integrated into the quasi

resistivity-depth sections.
In chapter 5, the theory to the 3D time domain finite difference forward solver *SLDMem3t* is explained. Important aspects of the numerical solver are discussed and an extended analysis on the calculation grid is presented. The grid design is particularly important to obtain a stable and accurate solution for the 2D forward with *SLDMem3t* and the inverse modeling with *SINV*. Moreover, a large number of soundings are interpreted by means of 2D forward modeling and a systematic modeling study is performed to validate the subsurface resistivity structure along both transects.
The Gauss-Newton 2D inversion scheme *SINV* is presented in chapter 6. To investigate the capabilities of the algorithm, it is studied on the basis of two synthetic 2D models. Finally, the subsurface resistivity-depth structure in the Azraq area is independently validated by applying the 2D inversion to the TEM field data.
Chapter 7 briefly summarizes the results of this thesis. Conclusions are drawn and an outlook for future work is given.

1.2 Preliminary notes

The survey was split into two parts. A 50×50 m^2 transmitter loop (Tx-50) was used during the first survey in 2011, whereas a 100×100 m^2 transmitter (Tx-100) was utilized in 2012. Since a lot of work was done during these two surveys, this chronology is also reflected in the presentation of the results. Sounding locations recorded with the Tx-50 setup are labeled for example A27, whereas the Tx-100 soundings are marked with an asterisk, e.g. A*80.
Vectors are presented in lower case, bold-italic characters. An exception are the vector fields $\boldsymbol{E}$, $\boldsymbol{D}$, $\boldsymbol{H}$ and $\boldsymbol{B}$, which are displayed similar to matrices in upper case, bold-italic characters. The time derivative of the magnetic field ($\partial_t \dot{\boldsymbol{B}}$) is termed as induced voltage (U_{ind}) or simply voltage (U). Moreover, the displayed TEM data are normalized to transmitter current I and receiver moment A_{Rx}. They are given in the unit V/Am^2. The electrical resistivity ρ is simply termed as resistivity.

CHAPTER 2

The transient electromagnetic method

Electromagnetic (EM) geophysical induction methods are used to gain information of the earths subsurface structure. They are based on the phenomenon of interaction of time varying electromagnetic source fields with the physical properties of the earth. The methods are divided into frequency and time domain electromagnetic methods. The application of EM methods, using artificial sources, ranges from very shallow exploration, e.g. archeological artifacts and unexplored ordnance detection at a few meter depths, down to several kilometers for hydrocarbon exploration in the oil/gas industry and mineral exploration. Over the past decades EM methods are widely used for environmental and engineering purposes, such as waste site exploration and groundwater studies at depths down to a few hundred meters. Several comprehensive reviews related to near surface applications of electromagnetic techniques in the time and frequency domain were published, e.g Goldman & Neubauer [1994]; Tezkan [1999]; Pellerin [2002]; Auken et al. [2006]; Everett [2011]. The central or in-loop transient electromagnetic (TEM) method operates in the time domain. A transient earth response is measured at distinct time gates after switching off a primary source field in the transmitter. The electrical resistivity distribution mainly determines the diffusion process of the transient EM fields into the ground.
The theoretical basics, which are required to understand the interaction between conductive media and EM-fields, are introduced in this chapter. Specific attention is paid to the description of the TEM method and its characteristic features. These descriptions follow the fundamental work of Ward & Hohmann [1991], Nabighian & Macnae [1991] and Spies & Frischknecht [1991]. The electrical resistivity tomography (ERT) method was applied supplementary to TEM. Therefore, the theory to the ERT method is not presented, but can be found in Knödel et al. [2005] or Telford et al. [1990]. The principles of classical Electrodynamics are found in the standard work of Jackson [1975]. Table 2.1 summarizes the basic variables and quantities used in this chapter.

2.1 Electrical conduction mechanism

EM geophysical induction methods involve the measurement of electric current flow in the conductive earth. Therefore, the electrical resistivity ($\rho = 1/\sigma$) of the ground is crucial. For near surface materials it varies from 0.1 to 10,000 Ωm [Auken et al., 2006].

Table 2.1: *Basic variables and constants used in electrodynamics. Vectors are presented as bold characters. They are given in the International System of Units (SI).*

Meaning	Symbol	SI Unit
electric field intensity	$\boldsymbol{E}$	$\frac{\mathrm{V}}{\mathrm{m}}$
electric displacement field (flux density)	$\boldsymbol{D}$	$\frac{\mathrm{As}}{\mathrm{m^2}}$
magnetic field (flux density)	$\boldsymbol{B}$	$\mathrm{T} = \frac{\mathrm{Vs}}{\mathrm{m^2}}$
magnetic field intensity	$\boldsymbol{H}$	$\frac{\mathrm{A}}{\mathrm{m}}$
current density	$\boldsymbol{j}$	$\frac{\mathrm{A}}{\mathrm{m^2}}$
electric charge density	q	$\frac{\mathrm{As}}{\mathrm{m^3}}$
electrical permittivity	$\varepsilon = \varepsilon_0 \varepsilon_r$	$\frac{\mathrm{As}}{\mathrm{Vm}}$
electrical permittivity of free space	$\varepsilon_0 = 8.845 \cdot 10^{-12}$	$\frac{\mathrm{As}}{\mathrm{Vm}}$
relative dielectric permittivity	ε_r	non-dimensional
magnetic permeability	$\mu = \mu_0 \mu_r$	$\frac{\mathrm{Vs}}{\mathrm{Am}}$
permeability of free space	$\mu_0 = 4\pi \cdot 10^{-7}$	$\frac{\mathrm{Vs}}{\mathrm{Am}}$
relative permeability	μ_r	non-dimensional
electrical conductivity	σ	$\frac{\mathrm{S}}{\mathrm{m}} = \frac{\mathrm{A}}{\mathrm{Vm}}$
electrical resistivity	ρ	$\Omega\mathrm{m} = \frac{\mathrm{Vm}}{\mathrm{A}}$
angular frequency	$\omega = 2\pi f$	$\frac{1}{\mathrm{s}}$
frequency	f	$\frac{1}{\mathrm{s}}$

Electric current $\boldsymbol{j}$ propagates prevalently in three ways in the earth [Telford et al., 1990; Knödel et al., 2005]:
The **electronic conduction** prevails if a material exhibits free electrons. In most cases the electronic conduction of the rock matrix is negligible. Exceptions are found for rocks that contain high conductive minerals.
Often rocks are porous and the pores may be filled with fluids containing free ions, leading to **electrolytic conduction**. The resistivity varies with the mobility and concentration of the dissolved ions [Telford et al., 1990]. These ions can originate for example from dissolved salts or contaminents. Hence, the rocks become electrolytic conductors, where the current propagates by ionic conduction. The well known empirical formula of Archie [1942] relates the bulk/effective resistivity with the resistivity of the pore fluid. The classical formula applies for clean and particularly clay-free (partly) saturated rocks.
The interaction between ions in the pore fluid and negative surface charges of the rock matrix causes an electric double layer at the interface. The concentration of mobile ions increases towards the double layer. The net result is an increased surface conductivity, which is referred to as **double layer conduction** [Ward, 1990a]. Clay minerals exhibit this property to a high degree, because they have a high ion exchange capacity. Therefore, very low resistivity values may occur for wet clay. However, if the pore fluid is high conductive the electrolytic conduction prevails [Ward, 1990a].
In case of EM geophysical induction methods at low frequencies and moderate resis-

tivities the **dielectric conduction** is negligible compared to the other conduction mechanisms. Therefore, the relative electric permittivity ε_r is not considered. Another material property is the relative magnetic permeability μ_r. For most earth materials μ_r is around one.
Table 2.2 summarizes the resistivity of some earth materials. Of particular interest is basalt, sandstone/limestone, clay and sand because these materials are common in the study area. The clay and water content are key parameters. Fresh to brackish and saline groundwater occurs at shallow depths and significantly determines the subsurface resistivity.

Table 2.2: *Typical resistivity ranges of some earth materials which occur in the survey area, Azraq. Values taken from Ward [1990a] and Palacky [1991].*

material	resistivity range ρ in Ωm		
clay	≈1 (wet)	—	100 (dry clay)
shale	≈5	—	30
sandstone	≈40	—	10^3
limestone	≈ 10^3	—	10^5
gravel and sand	≈500	—	10^4
basalt	≈10	—	10^5
salt water	≈0.3	—	1
fresh water	≈2	—	100

2.2 Maxwell's equations

The interaction of electromagnetic fields and matter is based on the four Maxwell's equations and the constitutive relations. Maxwell's equations form a system of coupled first order linear differential equations. In differential and integral form they read as follows:

$$\nabla \cdot \boldsymbol{D} = q \qquad \int_S \boldsymbol{D} \cdot d\boldsymbol{S} = \int_V q \, dV \tag{2.1a}$$

$$\nabla \cdot \boldsymbol{B} = 0 \qquad \int_S \boldsymbol{B} \cdot d\boldsymbol{S} = 0 \tag{2.1b}$$

$$\nabla \times \boldsymbol{H} = \frac{\partial \boldsymbol{D}}{\partial t} + \boldsymbol{j} \qquad \oint_l \boldsymbol{H} \cdot d\boldsymbol{l} = \int_S \left(\boldsymbol{j} + \frac{\partial \boldsymbol{D}}{\partial t} \right) \cdot d\boldsymbol{S} \tag{2.1c}$$

$$\nabla \times \boldsymbol{E} = -\frac{\partial \boldsymbol{B}}{\partial t} \qquad \oint_l \boldsymbol{E} \cdot d\boldsymbol{l} = -\int_S \frac{\partial \boldsymbol{B}}{\partial t} \cdot d\boldsymbol{S} \tag{2.1d}$$

The basic quantities and units are summarized in table 2.1. The integral form of Maxwell's equations are derived from the differential form using Gauss' and Stokes theorem [Jackson, 1975]. **Gauss law** in Eg. (2.1a) states that the charge density q are the sources of the electric (displacement) field $\boldsymbol{D}$. On the contrary, the magnetic flux density $\boldsymbol{B}$ is source free, which follows from **Gauss law for magnetic fields** in equation (2.1b). **Amperè's law** is given in equation (2.1c) and may be illustrated by a line carrying the current density $\boldsymbol{j}$, which causes a circulating magnetic field $\boldsymbol{H}$. Likewise, a time varying electrical (displacement) field $\boldsymbol{D}$ supports a circulating magnetic field.

The first type of current flow $\boldsymbol{j}$ is often called ohmic or galvanic, while the second type of current is called displacement current $\partial_t \boldsymbol{D}$. According to **Faraday's law of induction** in equation (2.1d), a time varying magnetic field $\boldsymbol{B}$ causes a circulating electric field $\boldsymbol{E}$ of opposite sign.
The last two Maxwell's equations (2.1c) and (2.1d) are of particular importance and characterize the EM field behavior well for geophysical induction methods. However, these equations do not have any obvious relationship to matter as such, e.g. the earth physical properties [Keller, 1987]. But, the equations may be coupled with matter via the constitutive relations

$$\boldsymbol{B} = \mu \boldsymbol{H} \qquad \text{and} \qquad \boldsymbol{D} = \varepsilon \boldsymbol{E} \tag{2.2}$$

and Ohm's law for isotropic media

$$\boldsymbol{j} = \sigma \boldsymbol{E}. \tag{2.3}$$

Where σ is the electrical conductivity of the medium. Ohm's law relates the current density $\boldsymbol{j}$ to the electric field intensity $\boldsymbol{E}$ and is the most important constitutive equation in terms of geophysical induction methods. In general σ, μ and ε are tensors, depending on space, time or frequency, temperature and pressure. For isotropic media they reduce to scalar quantities. Moreover, for most earth materials the magnetic permeability μ equals the vacuum permeability μ_0.

2.2.1 Telegraph and Helmholtz equation

Outside of any external sources and in regions of homogeneous conductivity no free charges exist and the electrical field intensity $\boldsymbol{E}$ is source free, hence $\nabla \cdot \boldsymbol{E} = 0$. Likewise, the current density is source free in homogeneous regions and $\nabla \cdot \boldsymbol{j} = 0$. By taking the curl of Faraday's law (2.1d) and substituting $\nabla \times \boldsymbol{B}$ with Amperè's law (2.1c) a decoupled second order differential equation is obtained for $\boldsymbol{E}$. An identical equation is derived for $\boldsymbol{H}$ in the same manner [Ward & Hohmann, 1991]. They are referred to as wave or telegraph equations[1]:

$$\Delta \boldsymbol{\mathcal{F}} - \mu\sigma \frac{\partial}{\partial t} \boldsymbol{\mathcal{F}} - \mu\varepsilon \frac{\partial^2}{\partial t^2} \boldsymbol{\mathcal{F}} = 0 \qquad \boldsymbol{\mathcal{F}} \in \{\boldsymbol{E}, \boldsymbol{H}\}. \tag{2.4}$$

The wave equation may be transformed into the frequency domain by a Fourier transformation with respect to time ($\partial_t \rightarrow i\omega$):

$$\Delta \boldsymbol{\mathcal{F}} - \underbrace{i\omega\mu\sigma \boldsymbol{\mathcal{F}}}_{\text{conduction}} + \underbrace{\mu\varepsilon\omega^2 \boldsymbol{\mathcal{F}}}_{\text{displacement}} = 0 \qquad \boldsymbol{\mathcal{F}} \in \{\boldsymbol{E}, \boldsymbol{H}\}. \tag{2.5}$$

This equation is known as the Helmholtz equation with the wavenumber k, which implies the physical properties of the media: $k^2 = \mu\varepsilon\omega^2 - i\mu\sigma\omega$.

[1] The vector identity $\nabla \times \nabla \times \boldsymbol{\mathcal{F}} = \nabla\nabla \cdot \boldsymbol{\mathcal{F}} - \Delta \boldsymbol{\mathcal{F}}$ is used

2.2.2 Quasi static approximation

For most earth material conductivities and operating frequencies (sampling rates) of systems used for geophysical induction methods the conduction currents ($\sigma \boldsymbol{E}$) are much larger than the displacement currents ($\partial_t \boldsymbol{D}$). Therefore, it is $\mu\varepsilon\omega^2 \ll \mu\sigma\omega$ in equation (2.5). Thus, in the quasi static approximation the Telegraph equation (2.4) and Helmholtz equation (2.5) reduce to:

$$\Delta \boldsymbol{\mathcal{F}} - \mu\sigma\partial_t \boldsymbol{\mathcal{F}} = 0 \tag{2.6a}$$

$$\Delta \boldsymbol{\mathcal{F}} - i\omega\mu\sigma \boldsymbol{\mathcal{F}} = 0 \qquad \boldsymbol{\mathcal{F}} \in \{\boldsymbol{E}, \boldsymbol{H}\}. \tag{2.6b}$$

These are referred to as the time and frequency domain diffusion equations. In the quasi static approximation the wavenumber is:

$$k = \sqrt{-i\mu\sigma\omega} = (1-i)\sqrt{\frac{\mu\sigma\omega}{2}}. \tag{2.7}$$

In very resistive environments (e.g. over crystalline bedrock) and high operating frequencies (sampling rates) the approximation is not valid. Radiomagnetotelluric systems operate up to 1 MHz and do not necessarily obey the diffusion equation in very high resistive environments [Persson & Pedersen, 2002; Kalscheuer et al., 2008]. Then, electrical displacement currents occurring as polarization effects in matter have to be considered. Ground penetrating radar is an exception, where the wave nature is part of the technique and the full wave equation needs to be solved.

Plane wave solution for a uniform conductor
One basic solution of equation (2.6a) is a positive downward decaying EM field with a harmonic time dependence $e^{i\omega t}$ in a uniform conductor with conductivity σ [Ward & Hohmann, 1991]:

$$\begin{aligned} \boldsymbol{\mathcal{F}}(z,t) &= \boldsymbol{\mathcal{F}}_0^+ e^{i\omega t} e^{-ikz} \\ &= \boldsymbol{\mathcal{F}}_0^+ e^{i\omega t} e^{-i\sqrt{\frac{\mu\sigma\omega}{2}}z} e^{-\sqrt{\frac{\mu\sigma\omega}{2}}z} \qquad \boldsymbol{\mathcal{F}} \in \{\boldsymbol{E}, \boldsymbol{H}\}. \end{aligned} \tag{2.8}$$

$\boldsymbol{\mathcal{F}}_0^+$ is the initial amplitude of the EM field and the wavenumber k is given in equation (2.7). The initial amplitude $\boldsymbol{\mathcal{F}}_0^+$ is damped with depth z. In conducting media, the EM wave reduces its amplitude by a factor $1/e$ at a depth

$$\delta_{FD} = \sqrt{\frac{2}{\mu\sigma\omega}}. \tag{2.9}$$

This is referred to as the frequency domain skin depth.

Step excitation solution for a uniform conductor
Following Ward & Hohmann [1991], the basic solution of the time domain diffusion equation (2.6b), which gives useful insights into the transient behavior of EM fields in media, is for an impulse EM field at time $t = 0$ in the plane $z = 0$:

$$\left\{ \begin{array}{c} \boldsymbol{E}(z,t) \\ \boldsymbol{H}(z,t) \end{array} \right\} = \left\{ \begin{array}{c} \boldsymbol{E}_0^+ \\ \boldsymbol{H}_0^+ \end{array} \right\} \frac{\sqrt{\mu\sigma}z}{2\pi^{\frac{1}{2}} t^{\frac{3}{2}}} e^{-\frac{\mu\sigma z^2}{4t}}. \tag{2.10}$$

The depth $z_{max} := \delta_{TD}$ at which the EM fields obtain their maximum for a fixed time $t > 0$ is calculated by taking the derivative with respect to z and equating to zero:

$$\delta_{TD} = \sqrt{\frac{2t}{\mu\sigma}}. \tag{2.11}$$

This is referred to as the diffusion depth for time domain soundings. The skin depth is proportional to $\sqrt{1/\omega}$, whereas the diffusion depth is proportional to $\sqrt{t}$. By forming the time derivative of δ_{TD} the propagation velocity v of the EM-field maximum is obtained:

$$v = \partial_t \delta_{TD} = \frac{1}{\sqrt{2\mu\sigma t}}. \tag{2.12}$$

For a fixed time t the diffusion depth is decreased in a good conductor compared to a poor conductor. Likewise, the diffusion velocity is reduced.

2.3 Central loop transient electromagnetics

There are many configurations used to carry out time domain electromagnetic (TDEM) measurements. A very common setup for deeper exploration is that of a prolonged grounded bipole transmitter, where components of the electrical and magnetic fields are recorded at a certain distance broadside or inline of the transmitter. This is often referred to as the long offset transient electromagnetic method (LOTEM). For shallow investigations it is very popular to use a loop source instead of a grounded wire. A magnetometer, an induction coil or a wire loop can be used as receivers for recording the vertical component of the magnetic field (or its time derivative). If one is particularly interested in multi-dimensional subsurface structures, a three component receiver may be used. If the receiver is placed in the center of the transmitter loop it is referred to as central loop or in-loop, if placed outside it is called separate loop. Soundings carried out with a loop source are referred to as SHOTEM (short offset transient electromagnetic method) or simply TEM. In contrast to LOTEM the closed transmitter-loop is ungrounded and acts as an inductive source. A constant current flows in the loop and is interrupted instantly at time t_0 (step function excitation). Due to the abrupt change of the primary magnetic field, eddy currents are induced in the conductive ground. The induced current system preserves the collapsing primary field and will counter act the current switch-off. Directly after switch-off at t_0^+ the current is confined to the vicinity of the transmitter loop and is an exact mirror-image of the current in the transmitter loop before switch-off. Due to Ohmic loss, the induced surface currents dissipate into the conductive ground with progressing time [Nabighian & Macnae, 1991]. Fig. 2.1(a) illustrates the downward and outward diffusion of the current system for three times after current switch-off in the transmitter. Nabighian [1979] described this concept as “smoke rings blown by the transmitter”. For a uniform or layered halfspace the induced current system will flow in horizontal planes. Hence no vertical component of the electric field $\boldsymbol{E}$ or current density $\boldsymbol{j}$ exists. This is a direct consequence of the resistivity contrast and EM boundary conditions at the air-earth interface, which applies for any inductive source hosted at

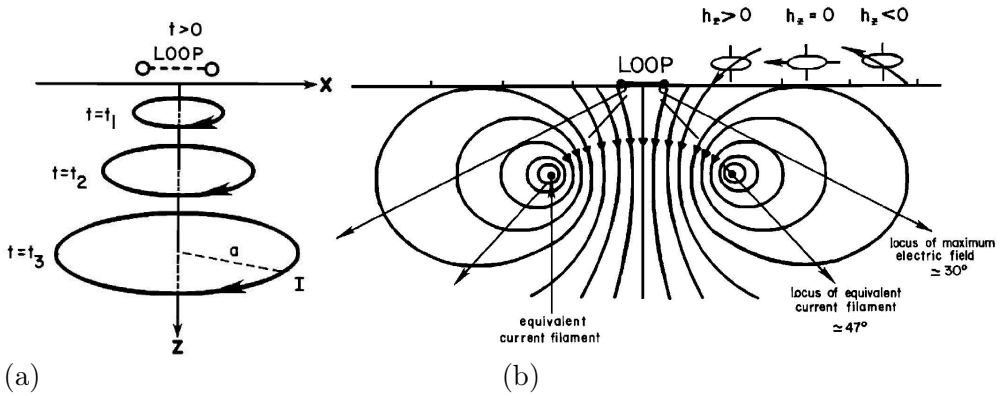

(a) (b)

Figure 2.1: *(a) System of equivalent current filaments over a conductive earth at three times after current switch-off in a transmitter loop. (b) Magnetic field lines and equivalent current filament for one particular time after current switch-off. Both figures are after Nabighian & Macnae [1991].*

the surface [Nabighian & Macnae, 1991]. Such a pure horizontal electric field is referred to as TE-mode (tangential electric) and is of pure toroidal shape. The magnetic field sketched in Fig. 2.1(b) is induced by the equivalent current filament and pure poloidal. Nabighian [1979] showed that for a uniform halfspace the equivalent current filament diffuses downwards at an angle of approximately 47°. It has twice the velocity v of the actual current system (cf. equation (2.12)), which diffuses at a smaller angle of 30°.

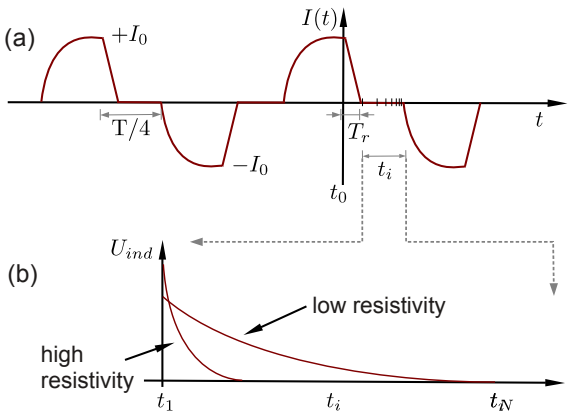

Figure 2.2: *(a) Transmitter current waveform $I(t)$ for a 50% duty cycle. (b) Induced voltage in a receiver loop over a low and high resistive subsurface. T_r is the ramp-time and t_i the distinct acquisition times. Modified from Asten [1987].*

In Fig. 2.2(a) a typical transmitter current waveform $I(t)$ with a 50% duty cycle is illustrated. The direct current is either positive $+I_0$ or negative $-I_0$ before switch-off at t_0. One cycle period T implies two current switch-off and two switch-on pulses. As illustrated, the switch-on is technically not realized that fast as the switch-off and thus often not evaluated. Fig. 2.2(b) displays two possible transients, recorded after current switch-off at distinct time gates t_i in a receiver located in the center of the transmitter. In a high resistive environment, the decay is much steeper than in a low resistive environment. If an induction coil or a wire loop receiver is used instead of a magnetometer, the measured quantity is the induced voltage U_{ind}(t):

$$U_{ind} = -\partial_t \int_{A_{rx}} \boldsymbol{B}\boldsymbol{n} dA_{rx}. \tag{2.13}$$

A_{rx} is the receiver area and $\boldsymbol{n}$ is the surface normal. Before current switch-off the magnetic flux through A_{rx} is constant and the voltage response U_{ind} is zero. Measurements of the magnetic field are referred to as step response and the measurements of its time derivative (or voltage) are called impulse response. In addition to the induced surface

current counteracting the current switch-off, the transmitter system and loop act as own inductive circuit. As a consequence the current switch-off is not instant at t_0. The finite switch-off time is called ramp time T_r and has to be considered at the stage of field data processing (or inversion). Its treatment is explained in section 4.5.1.

Goldman & Neubauer [1994] summarized the main advantages of the TEM method:

- Relatively large investigation depths are achieved with relatively small transmitter loop sizes. Additionally, no galvanic ground coupling is required, which leads to a comparably fast deployment/setup of a TEM sounding station.
- The response is measured in absence of the primary field. Thus, the investigation depth depends on the transmitter moment (transmitter size and current) and acquisition time.
- Very sensitive to conductive targets.
- The current system is focused under the transmitter, which leads to a superior depth-to-lateral investigation ratio. Therefore, TEM measurements can be interpreted better by 1D layered earth models than other configurations, e.g. LOTEM [Spies & Frischknecht, 1991].

2.3.1 Solution for a uniform conducting halfspace

Analytical transient solutions, due to a step excitation, exist for the special case of a uniform conducting halfspace and simplified sources. Assume a large horizontal loop with radius a and current I located at $z = 0$. In the far zone the response of a large circular loop is to a good approximation similar to that of a vertical magnetic dipole (VMD) with moment $m = I\pi a^2$. According to Ward & Hohmann [1991], the vertical component of the magnetic field $\dot{H}_z$ at the center of the loop is given by:

$$\dot{H}_z = \frac{-I}{\sigma\mu_0 a^3}\left[3erf(\Theta a) - \frac{2}{\sqrt{\pi}}\Theta a(3 + 2\Theta^2 a^2)e^{(\Theta^2 a^2)}\right], \tag{2.14}$$

where $\Theta = \frac{1}{\sqrt{2}\delta_{TD}} = \sqrt{\frac{\mu\sigma}{4t}}$. The Gauss' error function is defined as

$$erf(x) = \frac{2}{\sqrt{\pi}}\int_0^x e^{-\tau^2} d\tau. \tag{2.15}$$

For a rectangular transmitter-loop with area A_{rx} an equivalent radius $\tilde{a} = \sqrt{A/\pi}$ may be used. Several other approximations for various transmitter-receiver configurations are found in Spies & Frischknecht [1991]. For theoretical derivations it is referred to Ward & Hohmann [1991] or Keller [1987].

Early and late time approximations

There are two common approximations, which reduce equation (2.14) to simple relations between $\dot{H}_z$ and the subsurface resistivity $\rho = 1/\sigma$. If the transmitter radius a is much larger than the diffusion depth δ_{TD}, it is referred to as far zone sounding. Then the induction number $\beta = a/\delta_{TD}$ is larger than $\sqrt{10}$ [Spies, 1989]. This is usually the

case for early times after current switch-off. For $t \to 0$ (and $\Theta \to \infty$) the Gauss' error function approaches unity and $e^{-\Theta^2 a^2}$ vanishes. Equation (2.14) simplifies to

$$\dot{H}_{z,et} = -\frac{3I}{\sigma a^3}, \tag{2.16}$$

where $\dot{H}_{z,et}$ is proportional to the uniform halfspace resistivity $\rho = 1/\sigma$. The second approximation to equation (2.14) is that for late time stages $t \to \infty$ (and $\Theta \to 0$) the error-function vanishes and $e^{-\Theta^2 a^2}$ approaches unity:

$$\dot{H}_{z,lt} = -\frac{Ia^2}{20\sqrt{\pi}}(\mu\sigma)^{\frac{3}{2}} t^{-\frac{5}{2}} \tag{2.17}$$

At late times the transient decays proportional to $t^{-\frac{5}{2}}$ and $\sigma^{\frac{3}{2}}$. This approximation is valid for near zone soundings, where the induction number is less than one: $\beta = \frac{a}{\delta_{TD}} < 1$ [Spies & Frischknecht, 1991].

Apparent resistivity

The resistivity of a homogenous halfspace, which produces the observed data for each discrete time point separately is defined as the apparent resistivity ρ_a. Equation (2.16) may be rearranged to solve for ρ, which is then referred to as early time apparent resistivity:

$$\rho_{a,et} = -\frac{a^3}{3I}\dot{H}_{z,et}. \tag{2.18}$$

Likewise, a late time apparent resistivity $\rho_{a,lt}$ is obtained by rearranging equation (2.17):

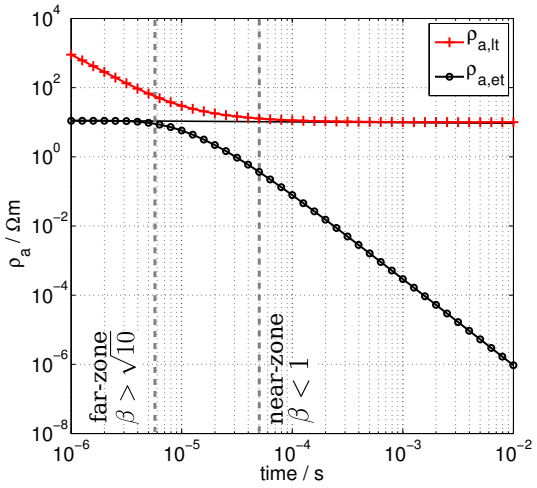

Figure 2.3: *Early $\rho_{a,et}$ and late time approximations $\rho_{a,lt}$ for a uniform halfspace with 10 Ωm. The gray dotted lines mark the near and far zone boundaries.*

$$\rho_{a,lt} = -\left[\frac{Ia^3}{20\sqrt{\pi}}\right]^{\frac{2}{3}} t^{-\frac{2}{3}} \mu \dot{H}_{z,et}^{-\frac{2}{3}}. \tag{2.19}$$

Outside the near and far zone ranges, the apparent resistivity does not reflect the true earth resistivity at all [Spies & Frischknecht, 1991]. However, both transformations are useful as they provide an initial feeling for the resistivity structure and generate a first guess for automatic inversion schemes [Raiche, 1983]. Particularly the late time approximation $\rho_{a,lt}$ is useful, because it reduces the large dynamic range of the TEM transient. To illustrate that, $\rho_{a,et}$ and $\rho_{a,lt}$ are plotted in Fig. 2.3 for a 10 Ωm uniform halfspace. Whilst $\rho_{a,et}$ varies over seven decades of magnitude, $\rho_{a,lt}$ only varies over three decades. Up to 5 μs the far zone assumption is valid and $\rho_{a,et}$ complies with the 10 Ωm halfspace resistivity. The same applies for $\rho_{a,lt}$ in the near zone for times larger than 50 μs, where $\rho_{a,lt}$ approaches the true halfspace resistivity. For intermediate times both approximations

differ significantly from the true resistivity. Any assumptions based on these approximations should be drawn carefully to avoid miss-interpretation. On the one hand there is the well known over- and undershoot phenomenon, which may lead to a false interpretation [Raiche, 1983; Goldman et al., 1994]. On the other hand, the apparent resistivity is dual-valued and the criteria for evaluation is upon the interpreter. Another problem is that $\rho_{a,lt}$ does not reflect the resolution capability of the utilized TEM receiver system, because $\rho_{a,lt}$ is not the measured quantity. Likewise, the noise measurements cannot be transformed. For further details it is referred to Spies & Eggers [1986], who briefly summarized the use and miss-use of apparent resistivity in electromagnetic methods.

In this thesis, often the induced voltage is presented because it is the measured quantity and used as input for the applied inversion schemes. Since the geophysical target in the survey area is a resistor at depth occurring at late times, $\rho_{a,lt}$ is utilized in addition to visualize the TEM data. Furthermore, it is used to derive a-priori information for the 2D inversion scheme presented in chapter 6.

2.3.2 Solution for a 1D layered halfspace

The conventional 1D interpretation of central loop TEM data by a 1D layered subsurface has proved feasible in many field applications [Goldman et al., 1994]. As stated earlier, the method has a superior depth-to-lateral investigation ratio and is more easily interpreted in one dimension than other TDEM configurations, e.g. LOTEM [Spies & Frischknecht, 1991]. The derivations for a 1D layered halfspace are quite elaborate and briefly discussed in Ward & Hohmann [1991] on the basis of Schelkunoff vector potentials. Weidelt [1986] formulated the theory on the basis of two scalar Debye potentials. The induced voltage $U_{z,ind}$ obtained in a receiver loop with area A_{rx} generated by a horizontal electric dipole (HED) sourced at $z = 0$ and dipole moment $D_0 = Idl$ is given by

$$U_{z,ind}(t,r) = \frac{1}{2\pi}\int_{-\infty}^{\infty} \mu A_{rx} e^{i\omega t} \frac{D_0 \sin\phi}{4\pi} \int_0^{\infty} \frac{B_E(k) - k}{B_E(k) + k} k J_1(kr) dk d\omega. \tag{2.20}$$

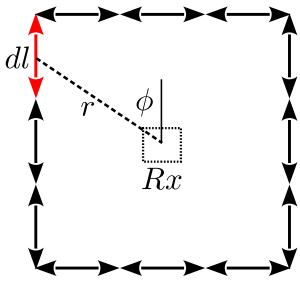

Figure 2.4: *Elementary dipoles forming a transmitter.*

$B_E(k)$ is the reciprocal impedance obtained at the surface, k is the wavenumber and J_1 is the first order first kind Bessel function. The receiver loop is located at a distance r and angle ϕ from the dipole (cf. Fig. 2.4). The solution for a rectangular transmitter loop is obtained by superposition of the response of several elementary dipoles with moment $m = Idl$. In order to achieve an accurate approximate solution, the length of the elementary dipoles dl is determined by the induction number (i.e transmitter-receiver separation/loop size and diffusion depth). In the near zone more dipoles are required than for far zone soundings. Equation (2.20) is solved only for one dipole and all other solutions are calculated by a coordinate transformation [Rätz, 2000]. Alternatively, the transmitter loop may also be constructed by superposition of the solutions calculated for elementary vertical magnetic dipoles [Weidelt, 1986]. The first approach is implemented in the applied inversion-algorithm *EMUPLUS*, which

is used for the 1D inversions of the TEM field data. Equation (2.20) cannot be solved analytical, since it involves the calculation of a Bessel integral of the form

$$g(r) = \int_0^\infty f(k) J_\nu(kr) dk, \qquad \nu = 1. \tag{2.21}$$

Due to the oscillating nature of the Bessel function $J_1(kr)$ for large arguments kr, the numerical evaluation is difficult and requires very small integration steps [Weidelt, 1986]. If $f(k)$ is sufficiently smooth, the evaluation can be accelerated by using a fast Hankel transformation. The logarithmic transformation

$$x := ln(r/r_0) \Leftrightarrow r = r_0 e^x \qquad \text{and} \qquad y := -ln(kr) \Leftrightarrow k = \frac{1}{r} e^{-y}$$

are introduced, where r_0 is a reference length. The substitution of the transformation pair into equation (2.21) yields

$$\underbrace{r g(r_0 e^x)}_{:=G(x)} = -\int_{-\infty}^{\infty} \underbrace{f(\frac{1}{r} e^{-y})}_{:=F(y)} \underbrace{J_1(\frac{r_0}{r} e^{x-y}) \frac{r_0}{r} e^{x-y}}_{:=\tilde{H}(x-y)} dy, \tag{2.22}$$

which is a convolution integral. However, $\tilde{H}(x-y)$ is still a strong oscillating function, but it may be replaced by a low-pass filtered version. The numerical evaluation of equation (2.22) is done by using appropriate filter coefficients for $H(x-y)$. Filter coefficients with ten coefficients per decade are given in Weidelt [1986]. Further explanations to the fast Hankel transformation and the solutions for different dipole sources, as well as for other field components than H_z, are given in Weidelt [1986], Martin [2009] or Petry [1987].

2.3.3 Depth of investigation

The TDEM diffusion depth δ_{TD} is often used to determine the depth at which a layer is detectable for a fixed time point and overburden conductivity. But, the diffusion depth is in practice not the same as the exploration depth. A common estimate for the exploration depth or depth of investigation (doi) for central loop TEM soundings in the near zone (late times) was suggested by Spies [1989]:

$$\delta_{doi} \approx 0.55 \left(\frac{I A_{Tx} \bar{\rho}}{\eta_\nu} \right)^{\frac{1}{5}}, \tag{2.23}$$

where A_{Tx} is the size of the transmitter loop and η_ν is the voltage noise level. A typical η_ν-value for TEM soundings is 0.5 nV/m^2. Moreover, the doi depends on the average resistivity $\bar{\rho}$ of the overburden with $z \leq \delta_{doi}$:

$$\bar{\rho} = \frac{1}{\delta_{doi}} \int_{z=0}^{\delta_{doi}} \rho(z) dz. \tag{2.24}$$

Equation (2.23) may be used prior to a field campaign, to estimate suitable configuration parameters such as transmitter size and current. The δ_{doi}-value may also be

estimated from final 1D inversion models and plotted as a lower depth bound, which is done in this thesis. Then η_ν corresponds to the induced voltage value of the last recorded time point at each sounding. A drawback is that the *doi* is easily over-estimated. For example if a poor resolved deep layer exhibits large resistivities, $\bar{\rho}$ becomes large as well. Therefore, the δ_{doi}-value is considered as a rough and additional estimate. In accordance to an example discussed by Spies [1989] and to avoid overestimation only 70% of δ_{doi} is considered as the exploration depth in this thesis. Likewise to the maximum *doi*, a minimum *doi* is defined by the earliest acquisition time. For depths less than the minimum diffusion depth $\delta_{TD}(t_{min})$ only the bulk resistivity is resolved.
Particularly, for frequency domain soundings Spies [1989] suggested $1.5 \cdot \delta_{FD}$ as a reasonable estimate of the *doi*, where δ_{FD} is the skin depth in equation (2.9). This value is used to derive an approximate exploration depth from the 2D TEM inversion in chapter 6. Moreover, the skin depth δ_{FD} is used as a measure to define extremal bounds for model and grid parameterizations (cf. Hördt [1992]; Martin [2009]).

2.3.4 2D conductivity structures

If loop source TDEM measurements are conducted over essentially multidimensional structures, significant inaccuracies may ocur, when 1D interpretation schemes are applied [Newman et al., 1987; Goldman et al., 1994]. For the previously discussed 1D conductivity distributions the induced currents flow in subsurface horizontal planes and the electric field is pure toroidal. Since the EM fields migrate faster in the resistor and are decelerated in a conductor, lateral subsurface variations cause the EM field to become distorted. The symmetry with respect to the transmitter is lost. Hence, both toroidal and poloidal electric fields are generated.
To illustrate the diffusion process in two dimensions, contour lines of the induced electric field $\boldsymbol{E}$ are displayed in Fig. 2.5 at four times after current switch-off in a 50×50 m^2 transmitter loop. The oberservation plane is a xz-slice at $y = 0$ m in the center of the transmitter. The model is 2D with a vertical boundary at $x = 25\ m$. Left of the boundary the model has three horizontal layers ($\rho_{1-3} = 13$, 4.5, 80 Ωm) and to the right it is homogeneous with $\rho = 0.3$ Ωm. The transmitter is placed on the edge of the vertical boundary.
Similar to the "smoke ring" concept of Nabighian [1979], the maximum of the electric field diffuses down- and outwards from the transmitter. Until $t = 10^{-4}\ s$ the maximum of $\boldsymbol{E}$ follows roughly the red dashed line with 30 degree slope. At later times, the maximum of $\boldsymbol{E}$ prevalently migrates outwards and resides in the good conductive layer before it penetrates the resistor at depth. Right of the fault, the diffusion velocity is significantly decelerated and the maximum of $\boldsymbol{E}$ migrates slower. As a consequence, the whole current system is distorted and not anymore in an horizontal plane.
As illustrated previously in Fig. 2.1(b) the resulting magnetic field is pure poloidal in the 1D case and symmetrical with respect to the transmitter. Thus only a vertical magnetic field component H_z exists in the center. In case of the 2D distorted current system in Fig. 2.5, both components H_z and H_x are generated at the center of the transmitter. Spies & Frischknecht [1991] suggested that the ratio of H_x to H_z may be

used to analyze, whether the subsurface is horizontally layered in the vicinity of the sounding. The ratio is referred to as the TEM tipper:

$$T_H(t) = \frac{H_x(t)}{H_z(t)} \qquad \text{or} \qquad T_U(t) = \frac{U_{ind,x}(t)}{U_{ind,z}(t)}. \tag{2.25}$$

The latter relation is used for induced voltage measurements. Over a 1D earth T_U is zero for all times. According to Spies & Frischknecht [1991], the 1D interpretation is valid for tipper values with $T_U < 0.1$. Newman et al. [1987] showed On the basis of a 3D synthetic geothermal model that the horizontal magnetic field component may be utilized to identify the flanks of a buried anomaly. Spies & Frischknecht [1991] utilized the same model, to illustrate the benefit of the TEM tipper. In chapter 5, the TEM tipper is used to investigate 2D effects in a 2D model, which is derived from the field data. A semi-synthetic TEM tipper is calculated because only the vertical voltage response and no horizontal components were measured in the field.

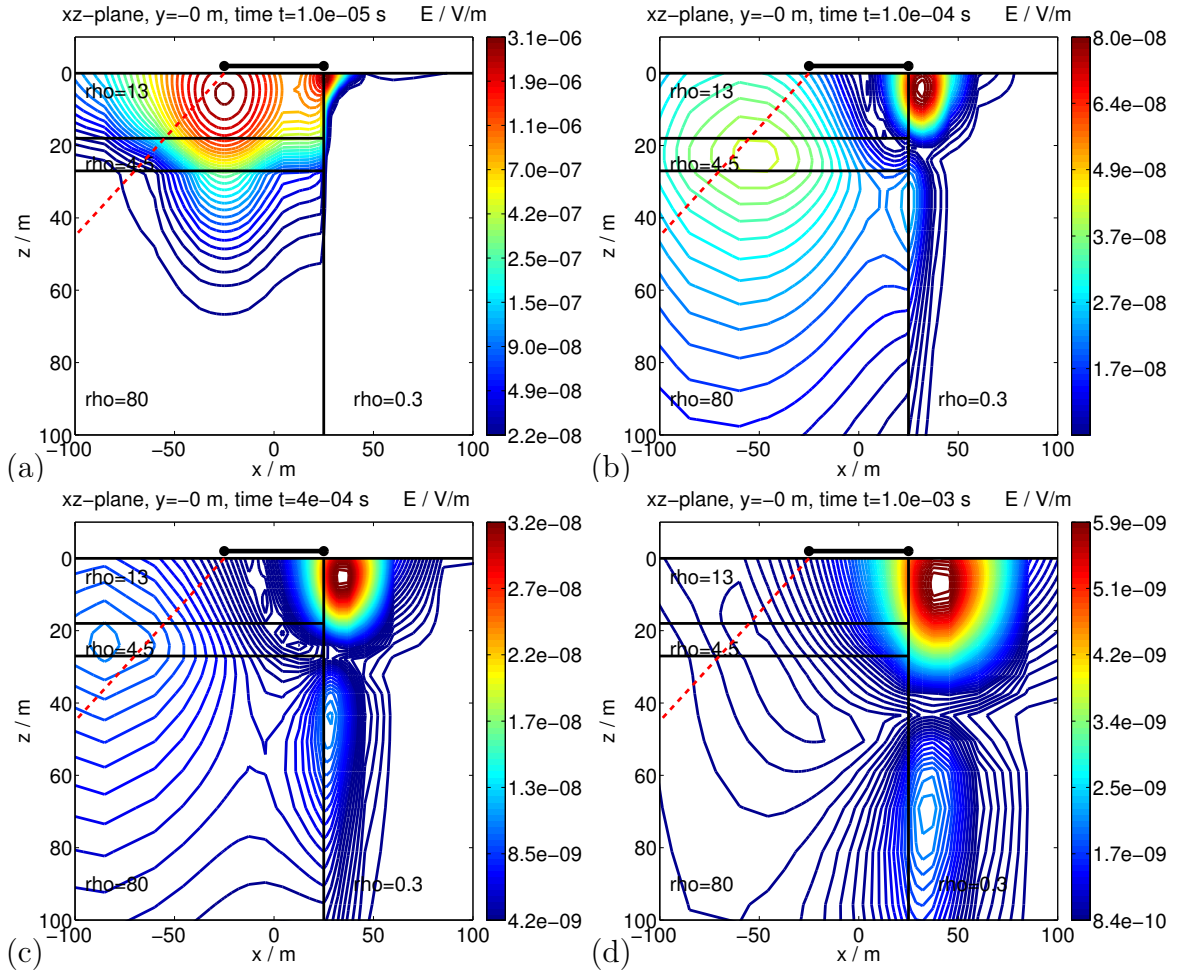

Figure 2.5: *Contour lines of the electric field* $\boldsymbol{E}$ *at four different times after current switch-off in a* 50×50 m^2 *transmitter loop. The plane of view is a* xz*-slice at* $y = 0$ m *through the center of the transmitter. The transmitter is located at* $z = 0$ m *at the edge of a vertical boundary. The model boundaries are denoted by black solid lines. The red dashed line is drawn at an angle of* $30°$ *and marks the diffusion angle of the maximum of the electric field in a homogeneous halfspace.*

The numerical modeling in this thesis is carried out with the TDEM finite difference algorithm *SLDMem3t*, which allows for arbitrary model discretization in three dimensions [Druskin & Knizhnermann, 1988, 1994, 1999]. The algorithm uses a Krylov subspace projection technique and is briefly described in chapter 5. An overview of the state of the art in TDEM numerical modeling in 2D/3D is found for example in the recent reviews given by Börner [2010] and Avdeev [2005]. Integral Equation approaches, which are usually feasible for a limited number of anomalies and thin sheet approximations are not considered in their reviews.

CHAPTER 3

Inversion of geophysical data

Geophysical exploration aims to reconstruct the subsurface structure of the earth from recorded data [Meju, 1994]. The calculation of synthetic data for a model with assigned subsurface properties is called forward problem or forward modeling. It was introduced for the transient electromagnetic method in chapter 2. The automated search for an optimum subsurface distribution of physical properties to explain geophysical data mostly utilizes inverse modeling techniques.

In this chapter two common inversion techniques are presented, which are used for the interpretation of the recorded geophysical field data. These are the Marquardt-Levenberg inversion technique and the Occam technique. The first technique uses a minimum number of model parameters to explain the data, whereas the second technique aims to find a subsurface model with smooth structure. Any obtained model is always a simplification of the reality and geophysical field data usually have observational errors. Therefore, it is particularly important to estimate the model uncertainties. This is done in 1D by using the equivalent modeling technique and model parameter importances [Scholl et al., 2003; Menke, 1984]. In 2D, the sensitivity distribution of the models is used to evaluate the resolution of the results [Martin, 2009].
The 1D inversion of the TEM field data is presented in chapter 4. It is performed with the algorithm *EMUPLUS* Scholl [2001, 2005]. The large scale 2D inversion scheme *SINV* is discussed in chapter 6. It is applied to synthetic data and a large TEM field data set. The current version of *SINV* was basically developed by Scholl et al. [2003] and Martin [2009]. The inversion techniques presented in the following sections are fundamental for both the 1D and the 2D inversion algorithm.

For additional details on the theory of geophysical inversion refer to the books of Menke [1984] and Meju [1994].

3.1 Problem formulation

Assume a geophysical data set $\boldsymbol{d} \in \mathbb{R}^N$ with N discrete data points recorded on the earths surface. The objective is to find a model $\boldsymbol{m} \in \mathbb{R}^M$ with M parameters, such that the calculated model response $\boldsymbol{d'} \in \mathbb{R}^N$ explains the data within their measurement

errors $\delta \boldsymbol{d} \in \mathbb{R}^N$. The calculation of the model response $\boldsymbol{d}'$ of a physical system at discrete observation points is called forward problem:

$$\boldsymbol{d}' = \boldsymbol{F}(\boldsymbol{m}), \tag{3.1}$$

where $\boldsymbol{F} : \mathbb{R}^M \rightarrow \mathbb{R}^N$ is the forward operator, which maps from model to data space. As discussed previously in section 2.3, semi-analytical solutions exist for the central loop transient electromagnetic configuration. They allow to calculate the impulse-response U_{ind} for a 1D layered model, with layer resistivity ρ_i and thickness th_i. For arbitrary 2D/3D resistivity distributions numerical forward algorithms are applied, where the earth is discretized into M cells or voxels, with assigned resistivity ρ_i. In either 1D or 2D/3D case the forward operator depends non-linear on the model parameters and particularly in two dimensions $\boldsymbol{F}(\boldsymbol{m})$ is not a regular function. Hence, a simple inverse formulation $\boldsymbol{m} = \boldsymbol{F}^{-1}\boldsymbol{d}$ to obtain the M model parameters is not possible.

3.1.1 Ill-posed problems

Assume that the forward operator and the model parameters follow a simple linear relationship $\boldsymbol{d} = \boldsymbol{F}\boldsymbol{m}$. The solution to $\boldsymbol{m} = \boldsymbol{F}^{-1}\boldsymbol{d}$ is possible only if the problem is **even-determined** with $N = M$ and their is one exact solution. Then a model can be derived by a direct inversion scheme. If more data/information is available than unknown model parameters the problem is **over-determined** ($N > M$) and usually no exact/unique solution exists. In this case a model is sought, which explains the data best. In contrast to that, an **under-determined** problem with $N < M$ leads to an infinite amount of models, which can explain the data.
Typical geophysical field data is rarely independent. Although practically more data than model parameters may exist ($N > M$) the data information may have a poor structure, such that some parameters are well resolved and others are not at all supported by data. Such **mixed-determined** problems with poor and well resolved model parameters usually occur for geophysical data sets. These problems are referred to as ill-posed and require some type of constraint to stabilize the solution.

3.1.2 Cost-function

As a measure to quantify how well a model explains the data, the squared sum of the residual vector $\boldsymbol{\epsilon} = (\boldsymbol{d} - \boldsymbol{d}')$ can be calculated. However, geophysical data usually exhibits measurement in-accuracies. To take these data errors $\delta \boldsymbol{d}_i$ into account, the error-weighted sum of squared errors is calculated, which conforms to a weighted least square criterion:

$$\begin{aligned}\Phi_d &= \sum_{i=1}^{N} \frac{(d_i - d_i')^2}{\delta d_i^2} \\ &= (\boldsymbol{d} - \boldsymbol{d}')^T \boldsymbol{W}_d^2 (\boldsymbol{d} - \boldsymbol{d}') \\ &= \boldsymbol{\epsilon}^T \boldsymbol{W}_d^2 \boldsymbol{\epsilon}.\end{aligned} \tag{3.2}$$

Where Φ_d is the data cost-function. The quantity e_i is an element of the error-vector $\boldsymbol{\epsilon}$ and is called residual, misfit or prediction error. $\boldsymbol{W}_d^2 = \boldsymbol{W}_d^T \boldsymbol{W}_d$ is the squared weighting matrix with the reciprocal data errors (standard deviations) δd_i on the main diagonal of $\boldsymbol{W}_d$:

$$\boldsymbol{W}_d = \begin{pmatrix} \frac{1}{\delta d_1} & & 0 \\ & \ddots & \\ 0 & & \frac{1}{\delta d_N} \end{pmatrix} \qquad \in \mathbb{R}^{N \times N}. \tag{3.3}$$

3.1.3 χ and *RMS*

For a Gaussian process, the least square estimator is known to be optimal. Hence a measure of data fit is

$$\chi = \sqrt{\frac{\Phi_d}{N}} = \sqrt{\frac{1}{N} \sum_{i=1}^{N} \frac{(d_i - d_i')^2}{\delta d_i^2}}, \tag{3.4}$$

where $\chi = 1$ corresponds to an optimal fit within the data-error. Values less than one correspond to over-fitted data, whereas $\chi > 1$ is not sufficiently fitted. Often χ is termed similar to the root mean square (RMS). Throughout this thesis, the term χ is used for equation (3.4) and RMS is used for the relative root mean square:

$$RMS = \sqrt{\frac{1}{N} \sum_{i=1}^{N} \frac{(d_i - d_i')^2}{d_i^2}} \times 100 \qquad [\ \% \ ]. \tag{3.5}$$

The individual data errors are practically neglected in this formulation. It should be noted that the ℓ^2-norm naturally occurs as measure for Gaussian distributed data errors. But, ℓ^2-norm measures of the data fit are more prone to outliers, than ℓ^1 norm measures [Menke, 1984]. Therefore, both χ and RMS can be miss-leading as a quantitative measure of data fit, if large outliers are present.

3.2 Trial & error forward modeling

By performing several forward calculations $\boldsymbol{d}' = \boldsymbol{F}(\boldsymbol{m})$ for various different models and using χ or RMS to estimate the data fit, a manual type of inversion is achieved. The so-called Hedgehog method yields a systematic sampling of the parameter space within a pre-defined range, whereas the Monte-Carlo method samples the parameter space in a random manner. In an optimal case, a best-fit model is found that minimizes the cost-function Φ_d in equation (3.2). Since the shape of the cost-function may be such that it contains broad and elongated global minima or even several (local) minima, in general no unique best-fit model exists. Therefore, particularly the Monte Carlo inversion is interesting, to obtain a complete set of models that have similar costs. These models are referred to as equivalent. The procedure used in this thesis to obtain the equivalent models is described in section 3.4.3. Both type of trial & error approaches are very

time consuming and can be biased by the subjective choice of the parameter space. However, for a full 2D/3D interpretation of TDEM field data it is not un-common to do it by means of forward modeling. That is due to the limited availability of large scale 2D/3D inversion codes with usually massive computational requirements. In chapter 5, the manual approach is used in the form of a 2D modeling study to interpret a large amount of data by one 2D model. Especially, the quality of the final 2D best-fit model is investigated by variation of selected model structures and analyzing the effect on the data fit.

3.3 Unconstrained least square formulation

Over-determined problems, where too much data/information is present to possess an exact solution, are usually solved by the least-square technique. It aims to find a set of model-parameters, which minimizes the cost-function Φ_d in equation (3.2). Although the method was originally formulated for over-determined problems, the same approach can be adopted to under- or mixed-determined problems, as they occur for geophysical applications. Usually this is done by imposing additional constraints to the solution.

3.3.1 Least square solution of linear problems

If the forward operator $\boldsymbol{F}(\boldsymbol{m})$ depends linear on the model parameters, it is $\boldsymbol{d}'=\boldsymbol{F}\boldsymbol{m}$ and $\boldsymbol{F}$ is a $N \times M$ coefficient-matrix. The cost-function Φ_d in equation (3.2) reads:

$$\Phi_d(\boldsymbol{m}) = (\boldsymbol{d} - \boldsymbol{F}\boldsymbol{m})^T \boldsymbol{W}_d^2 (\boldsymbol{d} - \boldsymbol{F}\boldsymbol{m}). \tag{3.6}$$

To find the minimum of the cost-function, the derivative of $\Phi_d(\boldsymbol{m})$ is calculated with respect to the model parameters $\boldsymbol{m}$ and equated to zero: $\frac{\partial \Phi_d(\boldsymbol{m})}{\partial \boldsymbol{m}} \stackrel{!}{=} 0$. Solving for $\boldsymbol{m}$ leads to the least square solution [Menke, 1984]:

$$\boldsymbol{m} = \underbrace{\left(\boldsymbol{F}^T \boldsymbol{W}_d^2 \boldsymbol{F}\right)^{-1} \boldsymbol{F}^T \boldsymbol{W}_d^T}_{:=\boldsymbol{F}^*} \boldsymbol{W}_d \boldsymbol{d}, \tag{3.7}$$

with the generalized inverse $\boldsymbol{F}^*$. It is implicitly assumed that one best approximate solution $\boldsymbol{m}$ exists, which minimizes the cost function or sum of prediction errors $\Phi_d(\boldsymbol{m})$. If a problem is purely under-determined ($N < M$) the number of solutions that give zero prediction error $\Phi_d = 0$ is greater than one. Hence, the matrix $\boldsymbol{F}^T \boldsymbol{W}_d^2 \boldsymbol{F}$ becomes singular and the least square solution of equation (3.7) will fail. The same applies for mixed determined problems, where practically enough information is available, but the data kernel has a poor structure and some model parameters are not at all supported by the data [Menke, 1984]. Hence, $\boldsymbol{F}^T \boldsymbol{W}_d^2 \boldsymbol{F}$ needs to have full rank (with the determinant $det(\boldsymbol{F}^T \boldsymbol{W}_d^2 \boldsymbol{F})$ unequal to zero) to solve equation (3.7).

3.3.2 Least square solution of non-linear problems

For geophysical electromagnetic induction methods the forward response $\boldsymbol{F}(\boldsymbol{m})$ depends non-linear on $\boldsymbol{m}$ [Meju, 1994]. For comparison see the 1D TEM forward problem in section 2.3.2. Hence, the cost-function in equation (3.2) reads:

$$\Phi_d(\boldsymbol{m}) = (\boldsymbol{d} - \boldsymbol{F}(\boldsymbol{m}))^T \boldsymbol{W}_d^2 (\boldsymbol{d} - \boldsymbol{F}(\boldsymbol{m})). \tag{3.8}$$

However, assume that the response $\boldsymbol{F}(\boldsymbol{m})$ behaves in a linear manner for small model parameter perturbations. To find a suitable set of model parameters $\boldsymbol{m}$, similar to the least square solution in equation (3.7), the forward operator is linearized by a first order Taylor expansion about a given model $\boldsymbol{m}_k$ and higher order terms are neglected:

$$\boldsymbol{F}(\boldsymbol{m})\Big|_{\boldsymbol{m}_k} \approx \boldsymbol{F}(\boldsymbol{m}_k) + \frac{\partial \boldsymbol{F}}{\partial \boldsymbol{m}}\Big|_{\boldsymbol{m}_k} \underbrace{(\boldsymbol{m} - \boldsymbol{m}_k)}_{=\Delta \boldsymbol{m}_k} = \boldsymbol{F}(\boldsymbol{m}_k) + \boldsymbol{J}\Big|_{\boldsymbol{m}_k} \Delta \boldsymbol{m}_k \tag{3.9}$$

Where $J_{ij} = \frac{\partial F_i(\boldsymbol{m}_k)}{\partial m_j}$ is the $N \times M$ Jacobi- or sensitivity matrix. Its entries contain the partial derivatives of the model response with respect to the model parameters and is discussed further below. Replacing $\boldsymbol{F}(\boldsymbol{m})$ in equation (3.8) with the linearized forward operator yields:

$$\Phi_d(\Delta \boldsymbol{m}_k) = (\underbrace{\boldsymbol{d} - \boldsymbol{F}(\boldsymbol{m}_k)}_{:=\boldsymbol{y}} - \boldsymbol{J}\Delta \boldsymbol{m}_k)^T \boldsymbol{W}_d^2 (\underbrace{\boldsymbol{d} - \boldsymbol{F}(\boldsymbol{m}_k)}_{:=\boldsymbol{y}} - \boldsymbol{J}\Delta \boldsymbol{m}_k) \tag{3.10}$$

$$= (\boldsymbol{y} - \boldsymbol{J}\Delta \boldsymbol{m}_k)^T \boldsymbol{W}_d^2 (\boldsymbol{y} - \boldsymbol{J}\Delta \boldsymbol{m}_k) \tag{3.11}$$

In analogy to equation (3.6), Φ_d is now minimized with respect to the model parameter update $\Delta \boldsymbol{m}_k$ and equated to zero. This results in a least square solution for the model update $\Delta \boldsymbol{m}_k$:

$$\Delta \boldsymbol{m}_k = \left(\boldsymbol{J}^T \boldsymbol{W}_d^2 \boldsymbol{J}\right)^{-1} \boldsymbol{J}^T \boldsymbol{W}_d^2 \boldsymbol{y} \tag{3.12}$$

Sensitivity matrix

The least square formulation of non-linear problems requires the calculation of the Jacobian- or sensitivity matrix $\boldsymbol{J}$ to obtain the model update $\Delta \boldsymbol{m}_k$. This can be very time consuming for a large number of model parameters M. If a perturbation approach is used, a number of M forward calculations are required. However, $\boldsymbol{J}$ is of particular interest, because it contains information how sensitive a model parameter is to a perturbation:

$$\boldsymbol{J} = \begin{pmatrix} \frac{\partial F_1(\boldsymbol{m})}{\partial m_1} & \cdots & \frac{\partial F_1(\boldsymbol{m})}{\partial m_M} \\ \vdots & \ddots & \vdots \\ \frac{\partial F_N(\boldsymbol{m})}{\partial m_1} & \cdots & \frac{\partial F_N(\boldsymbol{m})}{\partial m_M} \end{pmatrix} \quad \in \mathbb{R}^{N \times M}. \tag{3.13}$$

As stated earlier, geophysical problems are often mixed determined with poor and well resolved model parameters. For poor resolved model parameters the entries of the Jacobian matrix will become close to zero or even zero. This causes the singularity

problem and an ill-conditioned Jacobian matrix. The matrix product $\boldsymbol{J}^T\boldsymbol{W}_d^2\boldsymbol{J}$ is even more ill-conditioned and leads to either no solution or an unstable solution for $\Delta\boldsymbol{m}_k$.

Iterative Gauss-Newton procedure
Due to the linearization of the forward operator $\boldsymbol{F}(\boldsymbol{m}_k)$, equation (3.12) provides a model update step $\Delta\boldsymbol{m}_k$ such that

$$\boldsymbol{m}_{k+1} = \boldsymbol{m}_k + \Delta\boldsymbol{m}_k \tag{3.14}$$

reduces the cost function and $\Phi_d(\boldsymbol{m}_{k+1}) < \Phi_d(\boldsymbol{m}_k)$. Assume an initial model $\boldsymbol{m}_0$ and an iterative throughout application of the minimization procedure. It is truncated in the k-th iteration, if $\boldsymbol{m}_k$ provides an acceptable data-fit or no further model parameter update $\Delta\boldsymbol{m}_k$ is found. This minimization technique is called iterative Gauss Newton (GN) scheme. The main drawback of the GN technique is that it requires a suitable initial model $\boldsymbol{m}_0$, i.e. a "good first guess". Another problem is that the matrix $\boldsymbol{J}^T\boldsymbol{W}_d^2\boldsymbol{J}$ may become singular or close to singular, which causes the solution of equation (3.12) to fail or "overshoot the linear range" due to solution instability [Meju, 1994].

Steepest descent
The steepest descent is a simple gradient method, where the model update $\Delta\boldsymbol{m}_k$ is searched in the direction of the negative gradient of the cost-function Φ_d in equation (3.8) [Meju, 1994]:

$$\Delta\boldsymbol{m}_k = -\gamma\frac{\partial\Phi_d}{\partial\boldsymbol{m}_k}, \tag{3.15}$$

where the minus sign occurs because of the negative gradient search direction. The derivative of the cost-function Φ_d with respect to the model parameters is:

$$\begin{aligned}\frac{\partial\Phi_d}{\partial\boldsymbol{m}_k} &= -2\left[\frac{\partial\boldsymbol{F}(\boldsymbol{m}_k)}{\partial\boldsymbol{m}_k}\right]^T\boldsymbol{W}_d^2(\boldsymbol{d}-\boldsymbol{F}(\boldsymbol{m}_k)) \\ &= -2\boldsymbol{J}^T\boldsymbol{W}_d^2(\boldsymbol{d}-\boldsymbol{F}(\boldsymbol{m}_k))\end{aligned} \tag{3.16}$$

The model update is found by substituting the above expression into equation (3.15):

$$\Delta\boldsymbol{m}_k = -2\gamma\boldsymbol{J}^T\boldsymbol{W}_d^2(\boldsymbol{d}-\boldsymbol{F}(\boldsymbol{m}_k)). \tag{3.17}$$

Where γ is a constant and determines the stepsize of the model correction. In praxis γ is often determined by a line search such that $\Phi_d(\boldsymbol{m}_k + \Delta\boldsymbol{m}_k)$ is minimized in each k-th iteration. An overview of line-search techniques to find the minimum of a function is given in [Martin, 2009]. The main advantage of the steepest descent method is that it does not require the calculation of the inverse of a (probably) ill-conditioned matrix. Moreover, it has a good initial convergence characteristic. But, in contrast to the GN method, the convergence is bad when the minimum is approached [Meju, 1994]. Often (non-linear) conjugate gradient techniques are used for solving large scale optimization problems, as they have a better convergence characteristic than simple gradient methods [Rodi & Mackie, 2001; Commer & Newman, 2008].

3.4 Marquardt-Levenberg inversion

To avoid overshoots or unbounded solution growth of the model parameter update $\Delta \boldsymbol{m}_k$ when $\boldsymbol{J}^T \boldsymbol{W}_d^2 \boldsymbol{J}$ is ill-conditioned, Levenberg [1944] suggested a damped/constraint least square approach by adding positive weights to the diagonal of $\boldsymbol{J}^T \boldsymbol{W}_d^2 \boldsymbol{J}$. Marquardt [1963] adopted this approach to develop non-linear least square algorithms, which are very common for geophysical data inversion [Meju, 1994]. The Marquardt-Levenberg inversion implemented in the algorithm *EMUPLUS* is usually performed for a minimum amount of layers, particularly with $N > M$. Instead of minimizing only the cost function of the data Φ_d, the length of the model update $\Delta \boldsymbol{m}_k$ is minimized, too. The total cost function reads:

$$\begin{aligned} \Phi &= \Phi_d + \beta^2 \Phi_m \\ &= \boldsymbol{\epsilon}^T \boldsymbol{W}_d^2 \boldsymbol{\epsilon} + \beta^2 (\Delta \boldsymbol{m}_k^T \Delta \boldsymbol{m}_k). \end{aligned} \tag{3.18}$$

Where Φ_m is the model cost-function. The β is a Lagrange multiplier and weights between data closeness Φ_d and step-size of the model update Φ_m. Such type of constraint to the model update is denoted as local regularization. By taking the derivative of Φ with respect to $\Delta \boldsymbol{m}_k$ and equating to zero, the damped least square solution is obtained [Meju, 1994]:

$$\Delta \boldsymbol{m}_k = \underbrace{\left(\boldsymbol{J}^T \boldsymbol{W}_d^2 \boldsymbol{J} + \beta^2 \boldsymbol{I}\right)^{-1} \boldsymbol{J}^T \boldsymbol{W}_d^T}_{:=\boldsymbol{G}^*} \underbrace{\boldsymbol{W}_d (\boldsymbol{d} - \boldsymbol{F}(\boldsymbol{m}_k))}_{:=\boldsymbol{y}_w}. \tag{3.19}$$

Where $\boldsymbol{I} \in \mathbb{N}^{M \times M}$ is the identity matrix and $\boldsymbol{G}^*$ is the generalized Marquardt inverse. The damped least square technique is also called ridge regression. By adding β to the main diagonal of $\boldsymbol{J}^T \boldsymbol{W}_d^2 \boldsymbol{J}$, it is an effective way of handling singularities. For a very small β, equation (3.19) is similar to the unconstrained least square solution in equation (3.12) and the Marquardt-Levenberg scheme becomes the unconstrained iterative GN scheme. For large β the term $\boldsymbol{J}^T \boldsymbol{W}_d^2 \boldsymbol{J}$ is negligible and the solution for $\Delta \boldsymbol{m}_k$ is similar to that of the steepest descent method in equation (3.17), except for a constant factor. For the above reasons, the Marquardt-Levenberg method is an effective hybrid technique, which combines the GN and the steepest descent methods. when the model is far from the correct solution, steepest descent dominates, while GN dominates when the minimum is approached [Meju, 1994].

3.4.1 Singular value decomposition

The singular value decomposition (SVD) is very popular within geophysical data analysis to calculate the inverse of a matrix. The SVD technique is found for example in Menke [1984]. The SVD states that any matrix $\boldsymbol{G} \in \mathbb{R}^{N \times M}$ may be factorized into a product of three others:

$$\boldsymbol{G} = \boldsymbol{U} \boldsymbol{\Lambda} \boldsymbol{V}^T, \tag{3.20}$$

with the following matrices:

- The matrix $\boldsymbol{U} \in \mathbb{R}^{N\times N}$ spans the data space and contains the N eigenvectors $\boldsymbol{u}_i$ of $\boldsymbol{G}\boldsymbol{G}^T$. Similarly, $\boldsymbol{V} \in \mathbb{R}^{M\times M}$ spans the model space and contains the M eigenvectors $\boldsymbol{v}_i$ of $\boldsymbol{G}^T\boldsymbol{G}$.

- Together the matrices $\boldsymbol{G}^T\boldsymbol{G}$ and $\boldsymbol{G}\boldsymbol{G}^T$ have at least $p = \text{rank}(\boldsymbol{G}) \leq min(M, N)$ non-zero positive eigenvalues λ_i^*. The matrix $\boldsymbol{\Lambda} \in \mathbb{R}^{N\times M}$ is of diagonal form and contains the eigenvalues of $\boldsymbol{G}$, which are called singular values $\lambda_i = \sqrt{\lambda_i^*}$. The singular values are arranged in order of decreasing size along the diagonal of $\boldsymbol{\Lambda}$: $\lambda_1 \geq \lambda_2 \geq \ldots \lambda_p > 0$ and $\lambda_{p+1} = \lambda_{p+2} = \cdots = \lambda_k = 0$. Depending on the problem, k is either M or N.

Both, $\boldsymbol{U}$ and $\boldsymbol{V}$, are orthonormal matrices, so that $\boldsymbol{U}\boldsymbol{U}^T = \boldsymbol{U}^T\boldsymbol{U} = \boldsymbol{I}_N$ and $\boldsymbol{V}\boldsymbol{V}^T = \boldsymbol{V}^T\boldsymbol{V} = \boldsymbol{I}_M$ are identity matrices. Moreover, the relations $\boldsymbol{U}^T = \boldsymbol{U}^{-1}$ and $\boldsymbol{V}^T = \boldsymbol{V}^{-1}$ are valid.
With the SVD and the above definitions the inverse of a matrix is obtained by the factorization $\boldsymbol{G}^{-1} = \boldsymbol{V}\boldsymbol{\Lambda}^{-1}\boldsymbol{U}^T$.

SVD of the generalized Marquardt inverse $\boldsymbol{G}^*$

To solve the normal equation (3.19) the generalized Marquardt inverse $\boldsymbol{G}^*$ can be expressed in terms of SVD, where:

$$\boldsymbol{G}^* = (\boldsymbol{J}_w^T\boldsymbol{J}_w + \beta^2\boldsymbol{I})^{-1}\boldsymbol{J}_w^T. \tag{3.21}$$

Without loss of generality, it is used that $\boldsymbol{J}_w = \boldsymbol{W}_d\boldsymbol{J}$ and $\boldsymbol{y}_w = \boldsymbol{W}_d\boldsymbol{y}$. Factorizing $\boldsymbol{J}_w^T\boldsymbol{J}_w$ yields:

$$\boldsymbol{J}_w^T\boldsymbol{J}_w = \boldsymbol{V}\boldsymbol{\Lambda}^2\boldsymbol{V}^T \quad \text{and} \quad (\boldsymbol{J}_w^T\boldsymbol{J}_w)^{-1} = \boldsymbol{V}\boldsymbol{\Lambda}^{-2}\boldsymbol{V}^T. \tag{3.22}$$

Where $\boldsymbol{\Lambda}^2 = \boldsymbol{\Lambda}^T\boldsymbol{\Lambda}$ is used. The first expression in equation (3.22) is substituted into equation (3.21) and rearranged [Lines & Treitel, 1984]:

$$\begin{aligned}\boldsymbol{G}^* &= (\boldsymbol{V}\boldsymbol{\Lambda}^2\boldsymbol{V}^T + \beta^2\boldsymbol{I})^{-1}\boldsymbol{J}_w^T \qquad \text{with: } \boldsymbol{J}_w^T = \boldsymbol{V}\boldsymbol{\Lambda}^T\boldsymbol{U}^T \\ &= \boldsymbol{V}(\boldsymbol{\Lambda}^2 + \beta^2\boldsymbol{I})^{-1}\boldsymbol{\Lambda}^T\boldsymbol{U}^T.\end{aligned} \tag{3.23}$$

With the above expression for $\boldsymbol{G}^*$ and using $\boldsymbol{I} = \boldsymbol{\Lambda}^{-1}\boldsymbol{\Lambda}$ the model update $\Delta\boldsymbol{m}_k$ reads:

$$\begin{aligned}\Delta\boldsymbol{m}_k &= \boldsymbol{G}^*\boldsymbol{y}_w \\ &= \boldsymbol{V}\underbrace{(\boldsymbol{\Lambda}^2 + \beta^2\boldsymbol{I})^{-1}\boldsymbol{\Lambda}^T\boldsymbol{\Lambda}}_{:=\boldsymbol{Q}}\boldsymbol{\Lambda}^{-1}\boldsymbol{U}^T\boldsymbol{y}_w \\ &= \boldsymbol{V}\boldsymbol{Q}\boldsymbol{\Lambda}^{-1}\boldsymbol{U}^T\boldsymbol{y}_w.\end{aligned} \tag{3.24}$$

Where $\boldsymbol{Q} \in \mathbb{R}^{M\times M}$ is a diagonal damping matrix with the entries:

$$Q_{ii} = \begin{cases} \frac{\lambda_i^2}{\lambda_i^2+\beta^2} & \lambda_i > 0 \\ 0 & \lambda_i = 0 \end{cases} \tag{3.25}$$

To gain insights into the relevance of the model parameters, equation (3.24) is rearranged:

$$\underbrace{\boldsymbol{\Lambda}\boldsymbol{Q}^{-1}}_{\propto\lambda_i}\underbrace{\boldsymbol{V}^T\Delta\boldsymbol{m}_k}_{:=\Delta\tilde{\boldsymbol{m}}_k} = \boldsymbol{U}^T\underbrace{\left[\boldsymbol{W}_d(\boldsymbol{d}-\boldsymbol{F}(\boldsymbol{m}_k))\right]}_{=\boldsymbol{y}_w}. \tag{3.26}$$

Where $\Delta\tilde{\boldsymbol{m}}_k = \boldsymbol{V}^T\Delta\boldsymbol{m}_k \in \mathbb{R}^M$ is the transformed/rotated model parameter update vector. Its components are linear combinations of the components of $\Delta\boldsymbol{m}_k$. Hence the model parameters are not resolved separately, but moreover their combinations are resolved. An independently resolved parameter will be only translated and not rotated according to $\Delta\tilde{m}_{k,i} = V_{ii}\Delta m_{k,i}$. The entries of the $\boldsymbol{V}$-matrix can be used to analyze how independently parameters are resolved and which parameter combinations are resolved. In general large singular values λ_i correspond to important model parameters. Since the first term in equation (3.26) is proportional to λ_i, a large singular value contributes significantly to the data update $\boldsymbol{y}_w$ and to the response $\boldsymbol{F}(\boldsymbol{m}_k)$. The same applies to the Jacobian matrix $\boldsymbol{J}$. The smaller a singular-values, the less is the contribution of a component of $\Delta\tilde{\boldsymbol{m}}_k$ to the data update $\boldsymbol{y}_w$. Parameters corresponding to $\lambda_i = 0$ are transformed into the null-space and have zero entries in the Jacobian matrix. Hence they have no effect at all in an inversion.

The Marquardt damping parameter
Small singular values cause the solution of equation (3.24) to become unstable and lead to oscillating models, which can be counter-acted by a suitable damping β. The choice of β defines a singular value threshold. For $\lambda_i \gg \beta$ the solution of equation (3.24) is again the undamped least square solution with $\Lambda_{ii}^{-1} = 1/\lambda_i$ and β has practically no effect. If λ_i is close to zero in equation (3.25) a positive β will avoid the singularity problem. A singular value with $\lambda_i = \beta$ will be damped by a factor $Q_{ii} = 0.5$. As suggested by Jupp & Vozoff [1975], the damping matrix $\boldsymbol{Q}$ may be normalized to the maximum singular value λ_{max} by substituting λ_i with $\hat{\lambda}_i = \lambda_i/\lambda_{max}$ and β with $\hat{\beta} = \beta/\lambda_{max}$. In the 1D inversion algorithm *EMUPLUS* used in this thesis, a default 1% normalized singular value threshold is defined. Therefore, a singular values which is a factor 0.01 smaller than λ_{max} will be damped by a factor 0.5.

3.4.2 Model resolution and parameter importance

As stated earlier the resolution of the model parameters can be estimated from the $\boldsymbol{V}$-matrix. The model parameter resolution matrix $\boldsymbol{R}_{imp} \in \mathbb{R}^{M\times M}$ maps between the estimated $\boldsymbol{m}_{est}$ and the "true parameters" $\boldsymbol{m}_{true}$. It can be derived in terms of SVD from equation (3.7) for the un-damped linear least square problem [Menke, 1984]:

$$\begin{aligned}
\boldsymbol{m}_{est} &= (\boldsymbol{F}_w^T\boldsymbol{F}_w)^{-1}\boldsymbol{F}_w^T\boldsymbol{d}_w && \text{with: } \boldsymbol{d}_w = \boldsymbol{F}_w\boldsymbol{m}_{true}\\
&= \boldsymbol{F}_w^*\boldsymbol{F}_w\boldsymbol{m}_{true} && \text{with: } \boldsymbol{F}^* = \boldsymbol{V}\boldsymbol{\Lambda}^{-1}\boldsymbol{U}^T\\
&= \underbrace{\boldsymbol{V}\boldsymbol{V}^T}_{\boldsymbol{R}_{imp}}\boldsymbol{m}_{true}.
\end{aligned} \tag{3.27}$$

Where $\boldsymbol{F}_w^* = (\boldsymbol{F}_w^T\boldsymbol{F}_w)^{-1}\boldsymbol{F}_w^T$ is the generalized inverse of the unconstrained least square problem. If $\boldsymbol{V}$ spans the complete model space and $p \geq M$, the un-damped least square

solution leads to perfectly independently resolved model parameters with $\boldsymbol{R}_{imp} = \boldsymbol{I}$. In analogy to above, the resolution matrix for the damped Marquardt solution is

$$\begin{aligned} \boldsymbol{R}_{imp} &= \boldsymbol{G}^{*}\boldsymbol{J}_{w} \\ &= \boldsymbol{V}\boldsymbol{Q}\boldsymbol{V}^{T}. \end{aligned} \tag{3.28}$$

For mixed- or under-determined problems, the damped resolution matrix differs from the identity matrix and the estimated model parameters are not independently resolved. Moreover, they are linear combinations of the true model parameters. The importance of each parameter is given by

$$imp_i := R_{ii} \qquad \text{with: } 0 < imp_i < 1. \tag{3.29}$$

The closer imp_i is to one, the better a model parameter is resolved. It should be noted that the resolution matrix is derived from an SVD of the linearized Jacobian and thus does not reflect the parameter resolution of the full non-linear problem [Menke, 1984].

Model error bounds: Geophysical data are generally contaminated with noise and have measurement errors. It is possible to calculate how these data errors are mapped into model parameter errors. The error bounds can be derived by calculating the model covariance matrix [Menke, 1984]:

$$\delta\Delta\boldsymbol{m}_k = \boldsymbol{G}^{*}\boldsymbol{W}_d^{-2}\boldsymbol{G}^{*T}. \tag{3.30}$$

Where $\boldsymbol{G}^{*}$ is the generalized Marquardt inverse. Data with large uncertainties will cause large model variances. The same applies for poor resolved parameters corresponding to small singular values. Similar to the importances, the model error-bounds do not describe the true resolution of the non-linear problem [Menke, 1984]. Therefore, the model variances for the 1D inversion results presented in chapter 4 are estimated from the equivalent models, which are described in the following.

3.4.3 Equivalent models

In an optimal case a best-fit model is found that minimizes the cost-function Φ_d in equation (3.2). Since the shape of the cost-function is usually such that it contains broad and elongated or even several minima, no unique best fit model exists. Particularly if data errors are considered, several models may fit the data similarly within the error-bars. Moreover, poor or non resolved parameters are not supported by data and generally lead to large equivalence. Often only parameter combinations are resolved, which can be analyzed from the entries of the $\boldsymbol{V}$-matrix. In the presence of thin layers with thickness th, two equivalence types occur for the in-loop TEM induction method. Empirically it was found that [Spies & Frischknecht, 1991]:

$$\begin{aligned} \sqrt{th}/\rho = const \quad & \text{for a thin conductive layer,} \\ th^2\rho = const \quad & \text{for a thin resistive layer.} \end{aligned} \tag{3.31}$$

Theoretically the equivalence principle can be derived from the thin sheet solution for an inductive source as discussed in Nabighian & Macnae [1991]. The TDEM response

for a thin sheet depends on the conductivity-thickness product and not separately on the parameters (S-equivalence). A very effective way of estimating the quality of a model is to generate equivalent models by a Monte Carlo approach. Scholl [2005] implemented this approach in the 1D inversion scheme *EMUPLUS*. Each model parameter of a preliminarily best-fit model is perturbed randomly by a pre-defined percentage value and if the data-fit is within a pre-defined acceptable range, the model is stored as equivalent. Otherwise, a separate Marquardt inversion is performed and the procedure is repeated. Although the equivalent models still rely on the initial model, they provide an estimate of the non-linear model parameters variances. Hence, this approach has an advantage, compared to the model parameter importances and error-bounds discussed above, which rely solely on the linearized Jacobian matrix $\boldsymbol{J}$ of the final model [Scholl, 2005].

3.5 Occam inversion

Another very common regularization approach is to impose a global constraint on the model $\boldsymbol{m}_k$ itself. Assume a 1D structure consisting of M layers with pre-defined thickness and M assigned free resistivity values ρ_i. Constable et al. [1987] suggested the Occam inversion for geophysical applications, where in addition to the data cost function Φ_d the structure of a model is minimized by constraining the roughness, i.e. the resistivity difference between adjacent layers. Such roughness measures have been introduced to data inversion by Tikhonov & Arsenin [1977]. Constable et al. [1987] defined two different formulations for the roughness:

$$R_1 = \int \left(\frac{\partial \rho(z)}{\partial z} \right)^2 dz \qquad \text{and} \qquad R_2 = \int \left(\frac{\partial^2 \rho(z)}{\partial z^2} \right)^2 dz. \tag{3.32}$$

Where R_1 is called the first order roughness, since it corresponds to the first derivative of $\rho(z)$ with respect to the depth. Minimization of R_1 is achieved, if the gradient of $\rho(z)$ becomes small. Likewise, R_2 defines a second order roughness and is minimal, if $\rho(z)$ exhibits least curvature. Since $\rho(z)$ is not continuous, but consists of M discrete values ρ_i, the roughness definitions are:

$$R_1 = \sum_{i=2}^{M} (\rho_i - \rho_{i-1})^2 \qquad \text{and} \qquad R_2 = \sum_{i=2}^{M-1} (\rho_{i+1} - 2\rho_i + \rho_{i-1})^2 . \tag{3.33}$$

Both, R_1 and R_2, can be written in a matrix-vector notation $\boldsymbol{R}_1\boldsymbol{m}$ and $\boldsymbol{R}_2\boldsymbol{m}$, respectively. Then the model vector $\boldsymbol{m}$ contains the M resistivity values and $\boldsymbol{R}_1$, $\boldsymbol{R}_2 \in \mathbb{Z}^{M\times M}$ are roughness matrices:

$$\boldsymbol{R}_1 = \begin{pmatrix} 0 & 0 & 0 & \dots & 0 \\ -1 & 1 & 0 & \ddots & \vdots \\ 0 & \ddots & \ddots & \ddots & 0 \\ \vdots & \ddots & -1 & 1 & 0 \\ 0 & \dots & 0 & -1 & 1 \end{pmatrix} \qquad \text{and} \qquad \boldsymbol{R}_2 = \boldsymbol{R}_1^T \boldsymbol{R}_1. \tag{3.34}$$

With the above definitions, the total cost function for the Occam technique reads:

$$\begin{aligned}\Phi &= \Phi_d + \lambda\Phi_m \\ &= \boldsymbol{\epsilon}^T \boldsymbol{W}_d^2 \boldsymbol{\epsilon} + \lambda(\boldsymbol{m}^T \boldsymbol{R}_{1,2}^T \boldsymbol{R}_{1,2} \boldsymbol{m})\end{aligned} \tag{3.35}$$

Where Φ_m is the model cost-function of the first or second order model parameter differences. By substituting $\boldsymbol{\epsilon} = (\boldsymbol{d} - \boldsymbol{F}(\boldsymbol{m}))$ in equation (3.35) with the linearized forward operator given in equation (3.9), taking the derivative with respect to $\Delta\boldsymbol{m}_k$ and equating to zero, the normal equation is derived:

$$\Delta\boldsymbol{m}_k = (\boldsymbol{J}^T \boldsymbol{W}_d^2 \boldsymbol{J} + \lambda \boldsymbol{R}_{1,2}^T \boldsymbol{R}_{1,2})^{-1} [\boldsymbol{J}^T \boldsymbol{W}_d^2 (\underbrace{\boldsymbol{d} - \boldsymbol{F}(\boldsymbol{m}_k)}_{=\boldsymbol{y}}) - \lambda \boldsymbol{R}_{1,2}^T \boldsymbol{R}_{1,2} \boldsymbol{m}_k]. \tag{3.36}$$

Note that in equation (3.35) $\boldsymbol{m}$ has to be substituted with $\boldsymbol{m}_k + \Delta\boldsymbol{m}_k$, to yield a smooth model (update) in each iteration.
On the contrary to the Marquardt inversion with a minimum of layers, the Occam inversion is performed with 20 to 100 layers and a predefined fixed thickness. To solve the normal equation (3.36), it is factorized by a Cholesky decomposition. This is faster and more stable than calculating the inverse of a large ill-conditioned matrix.

The regularization parameter
The regularization parameter λ weights between data closeness Φ_d and model roughness Φ_m. In order to balance the total costs Φ, a large λ will lead to smooth models and an increased data misfit Φ_d. In extreme cases, the inversion is solely driven by the constraint and not by the data. On the contrary, for a small λ the roughness is less constraint and resistivity jumps can occur. For $\lambda \to 0$, the undamped least square solution in equation (3.7) is obtained, which can lead to geological un-plausible and over-structured models with huge parameter contrasts. Therefore, the choice of a suitable regularization parameter is crucial. In general, the Occam inversion is performed with a large initial λ and decreased successively throughout the iterations. In each iteration the appropriate λ is selected according to the discrepancy principle, i.e. the smoothest model with the best fit Φ_d is obtained by a line search [Constable et al., 1987]. A very popular approach is the L-curve criterion suggested by [Hansen & O'Leary, 1993], where the optimum λ is a compromise between data-fit Φ_d and model-roughness Φ_m. A comparison of different techniques for the automatic determination of the regularization parameter λ is found in Farquharson & Oldenburg [2004].

Model resolution and depth of investigation
The roughness criterion R_1 and R_2 are particularly useful to investigate which parts of a model are driven by the regularization parameter during the inversion and are not supported by the data. In those zones, the inverse solutions for R_1 and R_2 usually diverge. Since a R_1 roughness constraint seeks to minimize the gradient, the resulting model usually exhibits constant resistivity at depth. On the contrary, an R_2 constraint model will exhibit constant resistivity change (curvature) at depth. In this way, the application of both criterion can be used to derive a minimum and maximum depth of investigation, which is based on the mathematical inversion procedure. It is a good validation of the *doi* discussed in section 2.3.3, which is based on the physical behavior of the EM fields. Both are used for estimating the *doi* in chapter 4.

CHAPTER 4

Field survey in Azraq, Jordan

A key issue addressed by the Collaborative Research Centre 806 (CRC 806) is the reconstruction of the paleoclimate in the late Quaternary. Very promising archives for a paleoclimatical reconstruction are sediment successions accumulated in dry lakes [CRC-806, 2012]. The Azraq basin in Jordan is a potential target area for research within the CRC 806. The central part of the basin is occupied by a large 10×10 km^2 mudflat consisting of thick sedimentary deposits. Moreover, the area is of tremendous importance to Jordan due to large groundwater resources. To ensure the freshwater supply, groundwater research has been (and still is) an ongoing and relevant issue over the past 30 years [El-Kaysi & Talat, 1996; El-Waheidi et al., 1992; El-Naqa et al., 2007; Abu Rajab & El-naqa, 2013; Kaudse, 2014].
In order to identify suitable drilling locations for paleoclimatical research within the CRC 806, a 7 km and a 5 km long transect were investigated from the edges across the center of the mudflat. A large number of 150 soundings were recorded using the central loop transient electromagnetic (TEM) method and the electrical resistivity tomography (ERT) as a complementary method. The main objective is to investigate the subsurface electrical resistivity structure and particularly to identify the thickness of sedimentary deposits in the Azraq area. Due to the groundwater problematic in Azraq, an additional motivation evolved during this thesis. The geophysical investigations can support the ongoing groundwater management in the area.
The first part of this chapter gives a brief introduction of the survey area in the center of the Azraq basin. Four geological formations were the target for the geophysical investigation and are discussed in the following. Moreover, the hydro-geological background is described because fresh to saline groundwater occurs at shallow depth, which is crucial for the electrical conductivity described in section 2.1. The scope of the survey is formulated with respect to the geology and with respect to the objective of the CRC 806 in section 4.3. Furthermore, the survey setup, the utilized TEM equipment and particularly the data processing are described.
In the second part of this chapter, the TEM field data and resistivity-depth models which are derived from 1D inversion are briefly discussed. Conventional Marquardt and Occam inversion techniques are used. To estimate the quality of the results, both transects are analyzed in detail by model equivalence and parameter importances. The models are correlated and in good agreement with lithological borehole data available in the survey are [Ala'li, 1993; El-Waheidi et al., 1992]. Both resistivity-depth sections

are summarized in the end of this chapter and available geological information is integrated.

The 1D inversion results obtained after the first field survey in Jordan are partly published in Yogeshwar et al. [2013].

4.1 The Azraq basin

There are two large sedimentary basins in Jordan, the El' Jafr in the south of Jordan and the Azraq-Sirhan basin in the northeastern desert of the Jordan plateau. The Azraq basin is the northern extension of the Sirhan basin. The basin structure extends towards Syria in the north and towards Saudi Arabia in the south. It is bounded by two major faults, the Sirhan and the Fuluq fault (cf. Fig. 4.1). The Azraq sub-basin is oriented from northwest to southeast and covers an area of approximately 30×50 km^2 [Ibrahim, 1996]. The basin structure forms a large depression, with a surface catchment area of roughly 13,000 km^2. It is the drainage system of several wadis. The central part of the basin is occupied by the Qa Al Azraq oasis and is situated approximately 500 m above mean sea level. It forms a 10×10 km^2 large mudflat, often also called mud-pan, playa or sabkha. The area has an extremely arid climate with long, hot summers and mild winters [Abu Rajab & El-naqa, 2013] and a low annual precipitation of around 66 mm in Azraq town [Kaudse, 2014].
Due to mineral deposits and groundwater resources, the Azraq area is of enormous economical importance to Jordan. It is also an prospective area for oil exploration. The Hamzeh oil field south of Azraq produces an average of 40 barrel per day [Natural Resources Authority, 2006]. However, the main investigated resource is groundwater. Approximately one third of the freshwater supply for Jordan's capital city of Amman is provided from the Azraq basin [Ibrahim, 1996]. In 1982 the Amman Water and Sewage Authority (AWSA) drilled the "AWSA well field" and over the past 30 years the aquifers are heavily exploited for freshwater. About $15 - 20$ million cubic meter of drinking water is pumped to Amman per year, which is about one third of the total consumption. The major income of the majority of the population is livestock, but an increasing number of farmers are shifting to agriculture [Meshan, 2011]. These local farmers use around 45 million cubic meter water per year [Abu Rajab & El-naqa, 2013]. During the last 20 years the water table level has declined by about 17 m [Meshan, 2011]. Two large springs, Shishan and Druze, originally fed Azraq oasis. Both springs dried out in in the early nineties, because the AWSA well field intercepts the groundwater flow towards them [Ibrahim, 1996]. Today only a small wetland reserve, which consist of pools and marshes, exists and is artificially protected. The preserved wetland was established by the "Royal Society for the Conservation of Nature" (RSCN) and covers only 5% of the oasis [Kaudse, 2014; Meshan, 2011]. Approximately 25 km^2 of the original wet-land has already dried up. However, the Azraq oasis still exhibits the only permanent water body within a 46,000 km^2 large desert and is an important resting place for migratory birds [Ibrahim, 1996]. To preserve the unique ecosystem, restoration projects were established by several national and international institutions, for example the "International Union for Conservation of Nature" (IUCN) [Meshan, 2011].

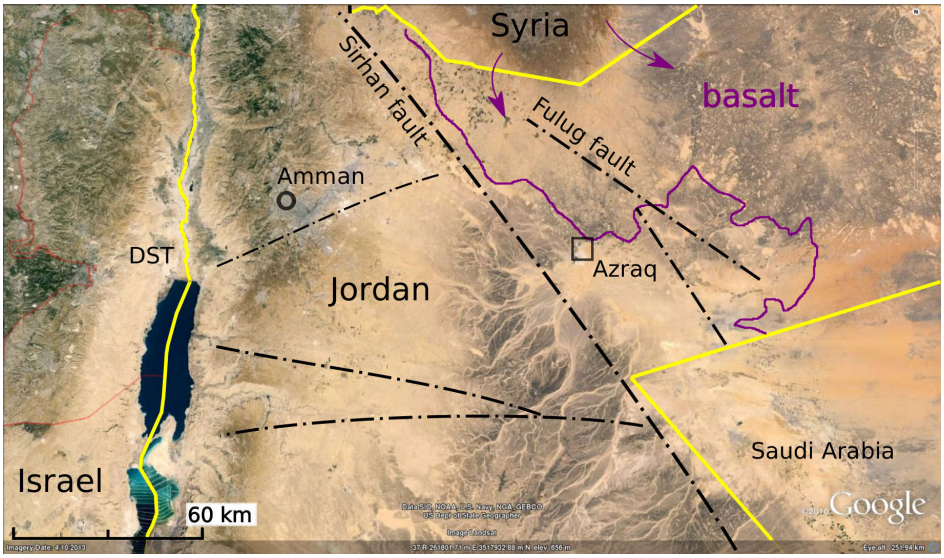

Figure 4.1: *Overview map of northern Jordan with national frontiers marked as yellow solid lines. The major faults and those bounding the Azraq-Sirhan basin are re-drawn from Kaudse [2014] as dashed lines. The Dead Sea Transform fault (DST) approximately coincides with the eastern frontier. The western boarder of the basalt sheet in Jordan is redrawn from Natural Resources Authority [2006] and marked purple. (Background ©2014 Google, Image Landsat, ©2014 ORION-ME)*

Since water is a basic human need, the area around the Qa' Al Azraq oasis was a major spot for prehistoric settlements. The area has been the focus for long term archaeological research in the seventies and eighties [Stanley Price & Garrard, 1975; Copeland, 1988; Byrd, 1988], but also for current archaeological investigations (e.g. Jones & Richter [2011]). The former shorelines of the Qa' Al Azraq mudflat are littered with stone artifacts. The oldest findings can be dated back to the Lower Paleolithic, i.e. more than 300,000 BP [Stanley Price & Garrard, 1975]. Moreover, wetlands provide promising archives for paleoclimatical research, particularly in arid regions. Recently Ahmad [2010] derived paleoclimatical information by dating bulk organic matter from the Azraq area. Jones & Richter [2011] provided a sedimentary record from a spring site close to the boundary of Azraq oasis.

4.2 Geological background

The east Jordan Limestone plateau extends from the rim of the Wadi-Araba Jordan Graben beyond the eastern borders of Jordan [Bender, 1974]. The plateau is covered by extensive basalt lava fields in the north/northeast. They extend from Jebel ed Drouze in Syria southwards across Northeast-Jordan towards Saudi Arabia. The basalt sheet occupies a total area of roughly 40,000 km^2 and around 10,000 km^2 only in Jordan (cf. Fig. 4.1). It belongs to the North Arabian Volcanic Province [Bender, 1974; Ibrahim, 1996]. The thickness reaches more than 1500 m around Jebel ed Drouze and decreases towards the south [Abu Rajab & El-naqa, 2013]. The Azraq-Sirhan basin is a northwest-southeast trending rift basin and its evolution is related to the geodynamic evolution of the Red Sea. The basin structure is more than 300 km long and is truncated at the

Wadi-Araba/Dead Sea transform fault. The Sirhan and Fuluq faults delimit the basin structure in the south and the north, respectively. However, the 30×50 km^2 Azraq sub-basin is intersected by numerous minor faults and lineaments. The 10×10 km^2 large Qa Al Azraq mudflat in the central part of the depression is bounded by faults from all sides. The Al Bayda fault represents the northern boundary and the Qaisiyeh fault represents the western boundary. Both fault locations are marked on the geological map in Fig. 4.2(a). They were subjects of the geophysical field survey discussed in this thesis.

Except for the volcanic tuff and basalt, the Azraq area consists of sedimentary rocks and clay rich Quaternary sediments. Ibrahim [1996] briefly described the geological formations, which occur in the central part of the Azraq basin. Four formations were subject to the field survey and are marked with the corresponding abbreviations on the geological map displayed in Fig. 4.2(a).

The **Abed Olivine Phyric Basalt (AOB)** originates from the earliest volcanism in the area. Its age is expected to be late Miocene ($\approx$5 Ma). The AOB comprises of massive flow units up to 10 m thick and with a total thickness of up to 100 m [Ibrahim, 1996]. It is most abundant and forms irregular shaped boulders at the surface (cf. Fig. 4.3(a)). It outcrops to the northern part of the area and is covered by quaternary sediments towards the mudflat center. Freshwater is extracted from the basaltic aquifer at shallow depths in the northern part of the area. According to Ibrahim [1996], the basalt flow is interrupted at the Al Bayda fault, which bounds the mudflat at the northern edge. As a result of this fault some silt dunes (STD) are raised up to 6 m.

The **Umm Rijam Chert Limestone Formation (URC)** outcrops in the northeast and southwest. It is displayed on the geological map in Fig. 4.2(a) in the lower left corner. The formation consists mostly of chert, chalk and limestone. The formation evolved in the Eocene ($\approx$ 40 Ma). Its maximum exposed thickness is 135 m, but some boreholes showed a thickness up to 310 m. In the northern part of the mudflat, the URC forms the base structure. In the southern part, the URC is covered by a sandstone formation, called Qirma Calcerous Sandstone (QCS). The URC formation is also referred to as the B4 shallow aquifer formation and intensively exploited for groundwater [El-Waheidi et al., 1992]. In appendix A.3, a generalized composite lithological section after Ibrahim [1996] is shown, which corresponds to the geological map and cross-section in Fig. 4.2(a,b).

The **Azraq Quaternary Formation (AQ)** consists of clay, sandy clay intermixed with various evaporates and fragments of gravel, chert, limestone and basalt. It sometimes contains hard layers cemented by gypsum as shown in Fig. 4.3(d). The surface is a present erosion and deposition surface, partly covered by alluvial sediments. At sounding A42, the AQ formation is covered by the Dasha Silt Dunes (STD), which are seen in Fig. 4.3(b). In general the AQ formation is heterogeneous and has a wide variation in lithology [Ibrahim, 1996]. According to Ibrahim [1996], the AQ formation was deposited during upper Miocene to upper Pleistocene. The age of the formation spans a large time range between $\approx 0.02 - 5$ Ma.

The **Alluvial Mudflat (ALM)** in the basin center consists of soft, silty hyper saline clays intermixed with various evaporates. According to the geological map and cross-section in Fig. 4.2(a,b), these Holocene sediments cover the mudflat and occur in several smaller depressions, too. Beneath the ALM, the quaternary sediments of the AQ formation are present, which consist mostly of silty clay in this zone. Sometimes thick

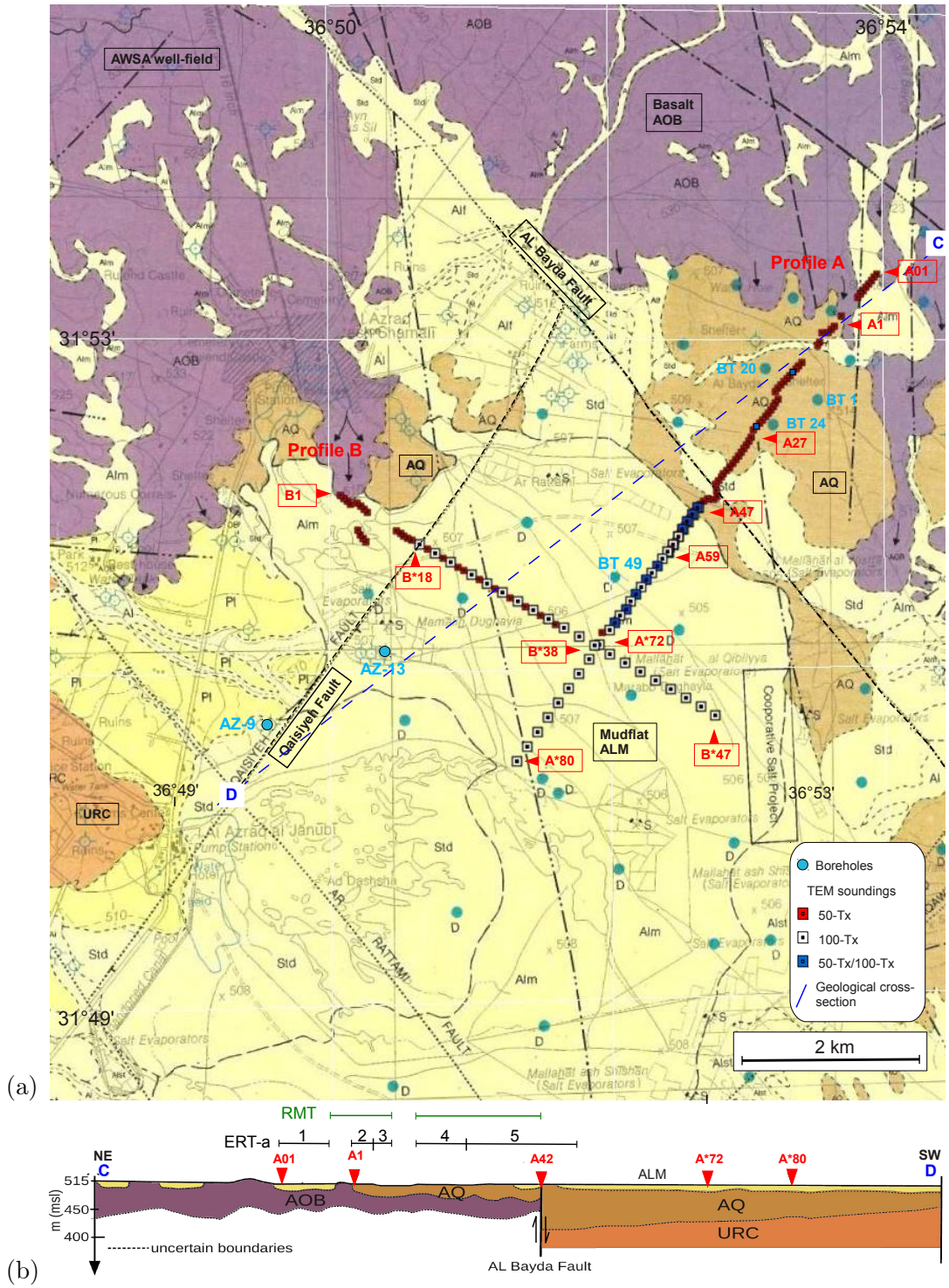

Figure 4.2: *(a) Geological map of the survey area (AQ: Azraq Quaternary Formation, AOB: Abed Olivine Phyric Basalt, URC: Umm Rijam Chert Limestone Formation, ALM: Alluvial Mudflat). Tx-50 TEM soundings are marked red, Tx-100 white. If both were recorded at the same location, it is marked by a blue square. Boreholes are denoted as blue circles (e.g. BT-1 & AZ-9). (b) Geological cross-section for $\overline{CD}$ indicated by a dashed line (both (a,b) modified after Ibrahim [1996]). Locations of the ERT (ERT-1 to ERT-5) and RMT profiles investigated along profile A are marked black and green, respectively. TEM stations are marked as red triangles. Further explanation is given in the text.*

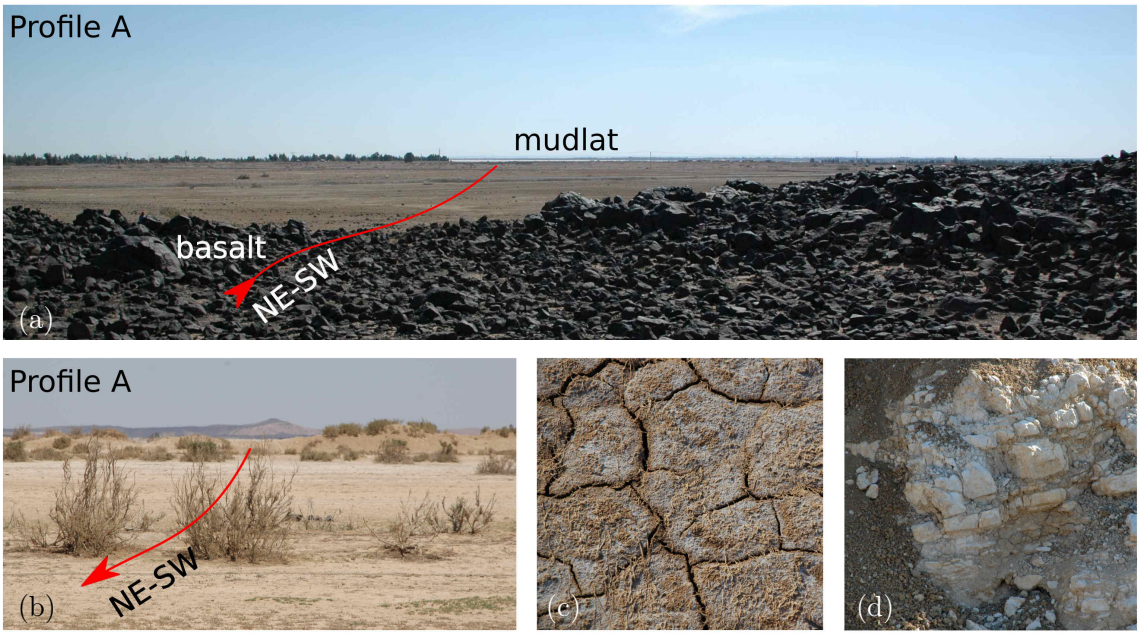

Figure 4.3: *(a) View from the basalt outcrop in north of profile A towards the mudflat in the southwest. (b) Opposite view from the boundary of the mudflat towards the Dasha silt dunes (STD) and towards the basalt outcrop. (c) Magnification of the mudflat surface covered with a thin salt crust. (d) cemented material at a depth of* $0.5 - 1$ *m exposed on the AQ formation along profile A.*

layers of diatomites and in some parts also consolidated layers of gypsum are present. The groundwater is very shallow (<6 m) and hyper-saline. Due to high evaporation, the surface is often covered by a salt crust (Fig. 4.3(c)). The depth down to the URC formation below the mudflat sediments is selectively known by boreholes, which were drilled during a bentonite project [Ala'li, 1993]. Moreover, El-Kaysi & Talat [1996] investigated the central part using Schlumberger vertical electric soundings (VES). According to them the mudflat sediments have a thickness ranging between $40 - 120$ m in the central part with increasing depth towards the southeast. The mudflat is bounded by the Qaisiyeh fault in the northwest (cf. Fig. 4.2(a)) where the URC base is expected to be lowered by 70 m.
The cross-section shown in Fig. 4.2(b) after Ibrahim [1996] shows the depth of the geological boundaries. They are inferred from the outcrops of the formations, as well as from selective lithological borehole data and from the VES results by El-Kaysi & Talat [1996]. However, the depth to the boundaries are marked as dotted lines because they are only selectively and not precisely known.

Hydro-geological situation

Three aquifer systems were defined in the Azraq basin: the upper or shallow aquifer system (B4), the middle aquifer system and the deep aquifer system [Ibrahim, 1996; El-Naqa, 2010]. Due to to the high lithological variability, the ground water occurrence in the upper aquifer system is complex. The depth to the groundwater table ranges between 250 m in the northern lava fields and less than 5 m in the Qa Al' Azraq mudflat. Although the precipitation is low, the mudflat can be flooded during the rainy season. In Fig. 4.4(a), the groundwater level (GWL) below the surface is shown for several well

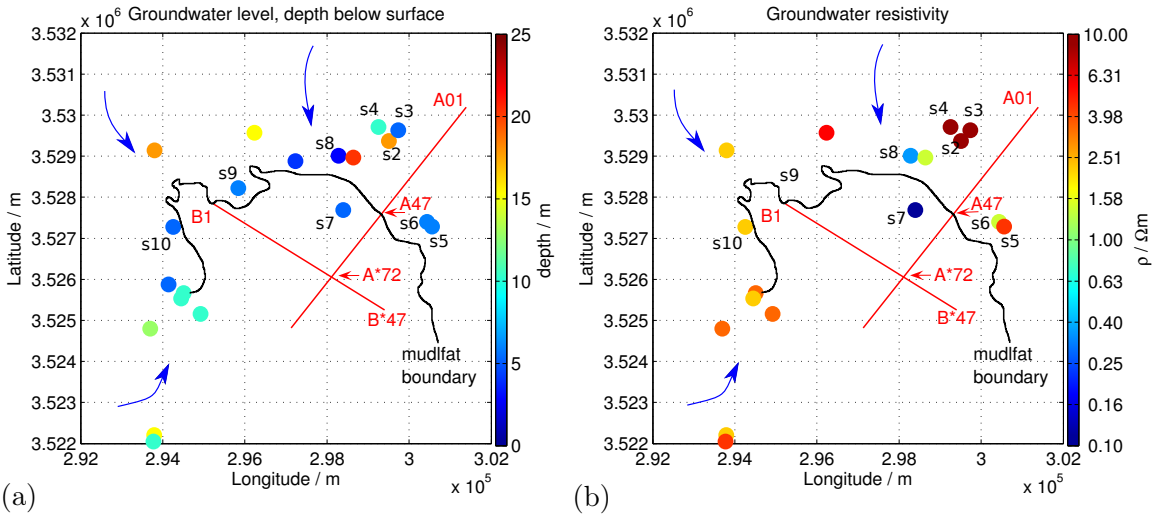

(a) (b)

Figure 4.4: *(a) Depth of groundwater level below surface. (b) Electrical resistivity of the groundwater samples. Selected well samples are labeled S2–S10 and summarized in table 4.1. S7 is located in a salt mine. All sample values are taken from El-Naqa [2010]. The blue arrows indicate roughly the flow direction of surface water. The profiles are plotted as red lines and the approximate northern edge of the mudflat is denoted by a black line.*

Table 4.1: *Groundwater level below the surface and above the mean sea level with the corresponding electrical resistivity of the Groundwater samples. The locations of the well samples (S2–S10) are displayed in Fig. 4.4(a,b). S7 is located in a salt mine. All sample values are taken from El-Naqa [2010].*

well samp	S2	S3	S4	S5	S6	S7	S8	S9	S10
GWL / m	18	5	10	6	6	5	4	6	5
GWL / msl	491	511	502	504	502	501	504	501	504
GW-ρ / Ωm	8.7	9.7	10.8	4.8	1.4	0.06	0.32	–	2.2

samples discussed by El-Naqa [2010]. The corresponding electrical resistivities of the samples are displayed in (b). A few sample values (S2–S10) are given explicitly in table 4.1. On the AQ formation close to the northern part of profile A, the groundwater is extracted for agricultural purposes mostly from depths inbetween 5 to 20 m (samples S2–S4). The depth to the water table is variable and, for example, sample S3 indicates a GWL of only 5 m below the surface. Towards the boundary and inside the mudflat the GWL generally decreases to approximately $4 - 6$ m (samples S5–S10). The basalt layer beneath the AQ formation is known as a good aquifer [El-Waheidi et al., 1992]. Due to high evaporation, the groundwater is hyper-saline inside the alluvial mudflat with an electrical resistivity less than 2 Ωm [Ibrahim, 1996]. Recent well samples indicate an electrical resistivity of 0.32 Ωm on the northern edge of the mudflat. Inside the mudflat extremely low values ($\approx$ 0.06 Ωm) were reported by [El-Naqa, 2010]. On the AQ formation they are mostly around 10 Ωm. However, the salinity of groundwater sometimes differs strong for very closely located wells. This was also reported by [Kaudse, 2014].

The subsurface water content and salinity are key parameters for the electrical conduction described in section 2.1. Therefore, these parameters have to be considered within

an interpretation of electrical resistivity-depth sections derived from geophysical data. As stated earlier, lithological data is available from several boreholes obtained during an bentonite drilling project [Ala'li, 1993]. The locations of the boreholes are marked as blue circles in Fig. 4.2(a). The obtained geoelectrical models are compared and calibrated with the lithological data from borehole BT-1 and BT-49 in section 4.7.1. Both are marked blue and labeled on the map.

The study area has a gentle slope from northwest and northeast towards the center of the basin. The topography is marginal at the edges of the mudflat. However, the mudflat itself is flat.

4.3 Objectives of the geophysical survey

As described in the introduction, a main objective of the CRC 806 is the reconstruction of the paleoclimate during the late Pleistocene in the Eastern Mediterranean [CRC-806, 2012]. Very promising archives for paleoclimatical reconstruction are sediment successions accumulated in dry (clay) lakes. Particularly wetlands are important climate archives in arid regions [Jones & Richter, 2011]. In order to support drilling projects in the area within the CRC 806, the geological boundaries denoted as dashed lines in Fig. 4.2(b) are investigated. This leads to the following main objectives for the geophysical investigations:

1. **Depth of the basalt layer at the mudflat boundaries.**
   Northwest and northeast of the alluvial mudflat, the buried basalt (AOB) serves as an hindrance for any drilling and its depth is the main target of the geophysical survey. That zone was investigated with TEM and additionally with ERT to validate the TEM results.
   The former shorelines in the northeast of the mudflat were spots for prehistoric settlements and are of archaeological interest for the CRC 806. The RMT method is applied to derive electrical resistivity models for the shallow subsurface structure in that particular zone. The results are presented in the Bachelors thesis of Mudler [2013].

2. **Thickness of the sediments deposited in the basin center, the Qa Al Azraq mudflat.**
   A complete and undisturbed sedimentary succession is in general preferred as a climate archive. Therefore, the thickness of the deposited mudflat sediments are of particular interest for research within the CRC 806. The geophysical objective is to resolve the depth to the expected chert limestone formation (URC) below the mudflat sediments. However, the deep sediments of the AQ formation are most likely out of the research time frame of the CRC 806 (< 0.19 Ma BP) and of minor interest. Therefore, a probable layering inside the mudflat is discussed in section 4.8.
   It should be noted that, the early work of El-Kaysi & Talat [1996] and El-Waheidi et al. [1992] already provided information about the thickness of the mudflat deposits, but complete and densely investigated transects using modern geophysical equipment are not available.

The upper aquifer in the central part of the Azraq basin is extensively exploited for agricultural purposes by local farmers and freshwater supply for Amman. The extreme groundwater discharge has lead to a drastic decline of the ground water table over the past 30 years. Due to the water extraction, the saline water body below the mudflat can move towards the fresh water aquifers. El-Kaysi & Talat [1996] and El-Waheidi et al. [1992] studied the condition of the shallow aquifer system and the interface of the fresh- to saline water zone by utilizing Schlumberger vertical electric soundings (VES). Abu Rajab & El-naqa [2013] used the TEM and VES methods to delineate the fresh and saline groundwater interface in the basin. To estimate the volume of the saline water body they applied a spatially constraint inversion (SCI) of the TEM field data [Viezzoli et al., 2008]. Furthermore, the geoelectrical models were correlated with hydrochemical analysis obtained from well samples. However, the soundings conducted by El-Naqa et al. [2007] did not penetrate the base of the mudflat. According to El-Naqa et al. [2007], the severe drawdown of the water table in the Azraq well-field might have caused a reverse in the hydraulic gradient. Furthermore, they stated that signs of salinization have already occurred. Several recent publications show that groundwater research in the Azraq area is of topical interest [El-Naqa et al., 2007; El-Naqa, 2010; Abu Rajab & El-naqa, 2013; Kaudse, 2014]. Due to the groundwater problematic in Azraq, an additional motivation evolved during this thesis. The geophysical investigations can provide information about

1. the lateral extent of the saline water zone
2. the depth of the saline water zone inside the mudflat.

Our results may be integrated into the current groundwater research, like for example groundwater models. Moreover, general information such as the lateral extent of the basalt towards the mudflat and the position/extent of the Al Bayda fault zone might be of interest. According to the geological map, both coincide roughly at sounding A42.

4.4 Survey layout

In order to tackle the objectives stated above, two field surveys were performed in March 2011 and October 2012. Predominantly, the scope of the first survey was to investigate the extent and depth of the basalt. Furthermore, the transition zones from the AQ formation to the mudflat sediments were investigated crossing the Al Bayda and Qaisiyeh faults. The second survey was conducted particularly to resolve the thickness of the mudflat sediments in contrast to the chert limestone basement (URC) below.
Two transects were investigated from the edge across the expected center of the mudflat (cf. Fig. 4.2(a)). Profile A is oriented from northeast to southwest with a total length of 6870 m and Profile B from northwest to southeast with a length of 4900 m. The profiles cross each other at sounding A*72 and B*38. Profile A and the terrain is illustrated by photographs in Fig. 4.3.
The TEM measurements were carried out utilizing a Zonge system, which is the NT-20 transmitter and the GDP-32II receiver unit [Zonge, 2002]. The Zonge system provides two acquisition modes depending on the required exploration depth. The NanoTEM-mode (NT) with relatively short acquisition times corresponds to shallow exploration

Table 4.2: *Parameters of both TEM Profiles. The sounding locations are displayed in Fig. 4.2(a).*

	length	orientation	from/to	# soundings	# Tx-50	# Tx-100
Profile A	6870	NE to SW	A01 - A*80	103	74	29
Profile B	4900	NW to SE	B1 - B*47	47	27	20

Table 4.3: *Parameters of the ERT profiles investigated on Profile A. Their locations are displayed in Fig. 4.2(c).*

ERT profile	ert-a1	ert-a2	ert-a3	ert-a4	ert-a5
length (m)	400	200	150	600	1700
El. sep. (m)	2.5	2.5	2.5	5	5

depth, whereas the ZeroTEM-mode (ZT) allows for long acquisition times and and a larger exploration depth. In order to protect the system against dust, sand and direct sunlight and to accelerate the data acquisition, it was installed in a Zarges box, which was mounted on a cart (cf. Fig. A.2).
A total of 103 soundings were recorded along profile A and 47 along profile B. Their locations are displayed in Fig. 4.2(a) as colored squares. A 50×50 m^2 transmitter and a 10×10 m^2 receiver loop (Tx-50-setup) were used in 2011. These soundings are marked as red and blue squares on the geological map. Data acquisition was performed in both modes, NT and ZT. In order to resolve the mudflat base, a 100×100 m^2 transmitter and the TEM-3 induction coil receiver (Tx-100-setup) were used during the second survey in 2012. The transmitter moment is increased by a factor of four compared to the Tx-50 setup. The TEM-3 coil has an effective receiver area of 10^4 m^2 with a ferrite core and an own pre-amplifier, which significantly improved the late time signal quality. Since it exhibits a quite long antenna delay of 15 μs, it is only suitable for ZT measurements [Zonge, 2002]. Although other configurations using a 200×200 m^2 Tx-loop with either a 50×50 m^2 receiver-loop or the TEM-3 coil were tested, the Tx-100 configuration was most appropriate regarding both, signal strength and survey speed. The Tx-100 sounding locations are marked as white and blue squares in Fig. 4.2(a). The 12 blue squares along profile A denote that the soundings were measured using both, Tx-50 and Tx-100 configurations.
The inter-station distance was 50 m for the majority of soundings. On the mudflat only the URC base below the clay sediments is of particular interest. Thus the inter-station distance was increased to 100 and partly 200 m. The parameters of both profiles are given in table 4.2. All sounding locations are summarized in table A.2 and table A.1.
Besides TEM, additional ERT measurements were performed on Profile A for verification of the TEM measurements. They are separated into five shorter profiles, named ert-a1 to ert-a5, and are displayed in Fig. 4.2(b). Their configuration parameters are summarized in table 4.3. The measurements were performed using the ABEM SAS 4000 multi-electrode system [ABEM, 2010]. A Wenner configuration was chosen since it has a very good signal to noise ratio and good layer resolution capabilities [Ward, 1990b]. Due to roads crossing the survey area, the length of the Wenner array was selected depending on the available space. Three long profiles (ert-a1, ert-a4 and ert-a5) were performed with a roll-along configuration. ERT measurements were not possible on the high conductive mudflat because the signal was strongly noise affected. A probable

reason is that in very good conductors (e.g. salt water) the current is short-circuited and the measured potential difference is very small, even for large potential-electrode separations and low currents. The investigated ERT profiles are summarized in more detail in table A.3.

To get a rough impression of the terrain in the survey area, it is illustrated by a few photographs in Fig. 4.3 and in appendix A.2.

4.5 Processing of the TEM field data

The processing of TEM field data obtained with the Zonge system is described in the following sections. A few issues are particularly important. These are:

- Deconvolution of the transmitter ramp-function [Hanstein, 1992; Lange, 2003] and editing/merging NT and ZT-mode data to one transient [Helwig et al., 2003].
- Lower input voltage limit of the GDP-32II system [Gaidetzka et al., 2001] and the effect of interchanging the receiver polarity [Mollidor, 2008].
- Error estimates for TEM field data and systematic errors considered by the calibration factor [Strack, 1992; Hördt & Scholl, 2004].

4.5.1 Deconvolution of transmitter ramp-function

A measured TEM response $U'(t)$ can be described as a convolution of the un-affected true earth response $U(t)$ and the transmitter system-response $S(t)$:

$$U'(t) = U(t) * S(t). \tag{4.1}$$

The receiver system-response is not considered for central loop TEM, since it is expected to behave linear in the time-range of data acquisition. Furthermore, $U'(t)$ is recorded in absence of the primary field. For an instant transmitter current switch-off at $t = 0$ the transmitter current function is a step and its time derivative is a δ-pulse (impulse system response). However, due to the self-inductance of the TEM transmitter loop, the current turn-off is not instant. The loop can be described as RLC circuit, consisting of a resistor (R), a inductor (L) and a capacitor (C) [Helwig & Kozhevnikov, 2003]. The fastest turn-off is achieved in the critically damped case, but over the conductive ground a complex interaction between loop and ground is present. According to Lenz' law the induced current system counteracts the current turn-off and a good conductor theoretically increases the current turn-off time (T_r-time). The NT-20 system is designed such that the turn-off ramp is linear in the optimal case [Zonge, 2002]. Only the current turn-off is evaluated because it is achieved faster than the turn-on from a technical point of view. The ramp-time T_r depends primarily on the current and the total cable resistance (depending on loop size, turns and cable diameter). For the applied field configuration, the ramp time for the Tx-50 setup is 3.5 μs in NT and 49 - 56 μs in ZT-mode [Zonge, 2002]. For the larger Tx-100-setup T_r is 105 μs in ZT-mode. The relation between a linear current turn-off function and the induced voltage was

described by Fitterman & Anderson [1987]. The current function $I(t)$ for a current I_0, turned off at $t = 0$ s, is given through

$$I(t) = I_0(1 - \frac{t}{T_r}), \qquad 0 < t < T_r. \tag{4.2}$$

The measured induced voltage $U'(t)$ corresponds to the time derivative of the magnetic field (impulse response). Accordingly, the time derivative of the transmitter current function has to be calculated to obtain the corresponding transmitter system response [Fitterman & Anderson, 1987]:

$$\frac{\partial I(t)}{\partial t} = \frac{-I_0}{T_r}, \qquad 0 < t < T_r, \tag{4.3}$$

where $\partial_t I(t)$ is a boxcar function with width T_r. The measured response $U'(t)$ is obtained by a convolution of $\partial_t I'(t) = -1/T_r$ with the unaffected earth response $U(t)$, where $I'(t)$ is normalized to the current I_0:

$$\begin{aligned} U'(t) &= \int_{-\infty}^{t} \frac{\partial I'(t')}{\partial t'} U(t - t')dt' \\ &= -\frac{1}{T_r} \int_{0}^{T_r} U(t - t')dt.' \end{aligned} \tag{4.4}$$

In order to consider the effect of the non-zero turn-off time, the conventional approach is to apply a joint inversion of both, the NT and ZT data sets and consider the turn-off function when the synthetic response $U(t)$ is computed [Fitterman & Anderson, 1987; Raiche, 1984]. As Fitterman & Anderson [1987] suggested, the predicted data is convolved with the ramp-function at each inversion step according to equation (4.4). This approach is used for the soundings on the mudflat, where only ZT-mode was used. When data was recorded in both modes, the effect of the linear ramp is removed from the NT and ZT soundings by applying a parameterized deconvolution of the measured signal and the current turn-off function [Hanstein, 1992; Lange, 2003]. This is done using the *EADEC*-algorithm by Lange [2003]. Subsequently, the NT and ZT data are merged together to one long transient [Lange, 2003; Helwig et al., 2003].
In Fig. 4.5(a), the measured induced voltages at sounding A41 are compared for both modes with the deconvolved data. The ramp-function only influences the early time data points in the particular mode and the amplitude is weaker for a finite turn-off time. According to Spies & Frischknecht [1991], the effect of the finite ramp is negligible for acquisition times t greater than $30 \cdot T_r$. Therefore, the ZT data plotted in Fig. 4.5(a) are affected roughly until $t = 1.5$ ms. Despite the deconvolution, the ZT transient is below the merged long transient. Hence, the ramp must be somewhat longer than actually measured. For the sake of verification, the Marquardt inversion model obtained from the joint inversion of the NT and ZT-mode data is compared with the inversion model of the deconvolved and merged data. As shown in Fig. 4.5(b), both approaches achieve comparable inversion results with marginal differences and slightly different data fit.

Combining NT & ZT-mode transients and data editing
Sometimes a shift between NT and ZT data is present, which might be caused by an inaccurate transmitter current reading or slightly different calibration of both modes.

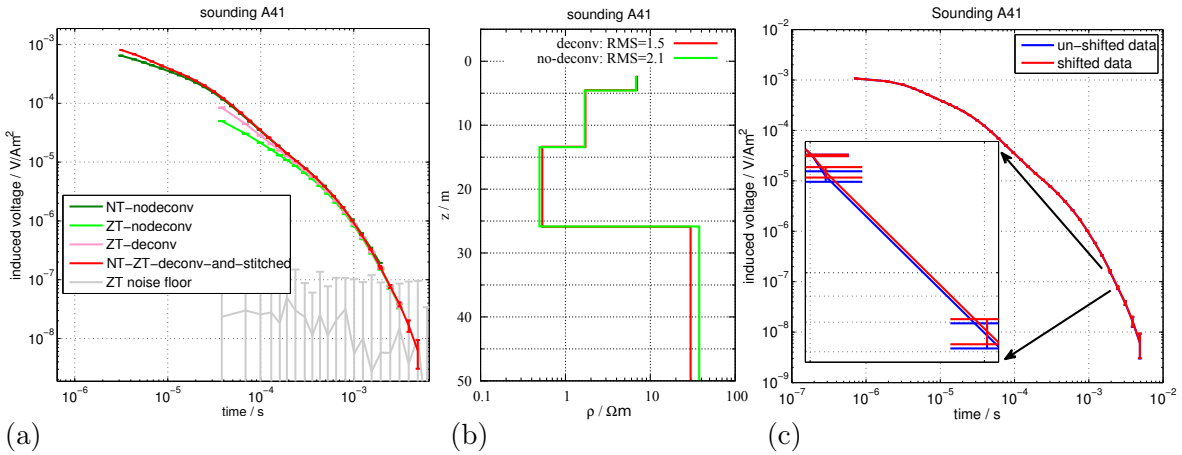

(a) (b) (c)

Figure 4.5: *(a) Comparison of non-deconvolved NT and ZT data (dark/light green), with deconvolved ZT data (pink) and the deconvolved stitched NT/ZT data (red) for sounding A41. The ZT noise floor is indicated in gray. (b) Comparison of the joint inversion model for NT and ZT data (green) with the single inversion model of the deconvolved and stitched transient (red). (c) NT and ZT data joined to one long transient for shifted (red) and un-shifted ZT data (blue).*

This is overcome by shifting the ZT transient to the level of the NT response and removing the overlapping data. The merged transient should be smooth between adjacent data points. The merged NT and ZT data are displayed in Fig. 4.5(c) for zero shift and for an optimal shift by a factor of 1.019, which produces the smoothest transition. In a logarithmic scaled plot, the difference is only visible in large magnification.

Quite often oscillations are observed in the NT-mode early time records, which originate from an undesired oscillation of the current function due to insufficient damping [Helwig & Kozhevnikov, 2003]. Such data points have to be removed from the transients. At late times the data is in general considered until the noise level prevails. For the ZT a noise record is displayed in Fig. 4.5(b). The noise level was quite high for sounding A41 with $\eta_{noi} \approx 10^{-8}$ V/Am^2.

4.5.2 Effect of receiver polarity

Often undesired effects occur in the late time stage of a recorded transients, which might lead to false interpretations. Therefore, the accuracy of the GDP-32II at the lower input voltage limit is of particular interest. The system allows for a maximum input voltage of 5 V and the inbuilt analogue-digital-converter (ADC) has an effective resolution of 13 Bit [Zonge, 2002]. Hence, the smallest resolvable measured signal is:

$$U_{min} = \frac{5\ V}{2^{13} \cdot g \cdot G}\,. \tag{4.5}$$

G is the amplification/gain specified in the instrument settings and the factor $g = 10$ is a fixed system gain used only in NT-mode. Gaidetzka et al. [2001] showed that in NT-mode the late time signal can be amplified and improved by choosing a maximum gain of $G = 2^4 = 16$, instead of using automatic gain mode. Nevertheless the signal might be disturbed. In Fig. 4.6(a), two transients with Gain $G = 1$ and $G = 16$ are displayed,

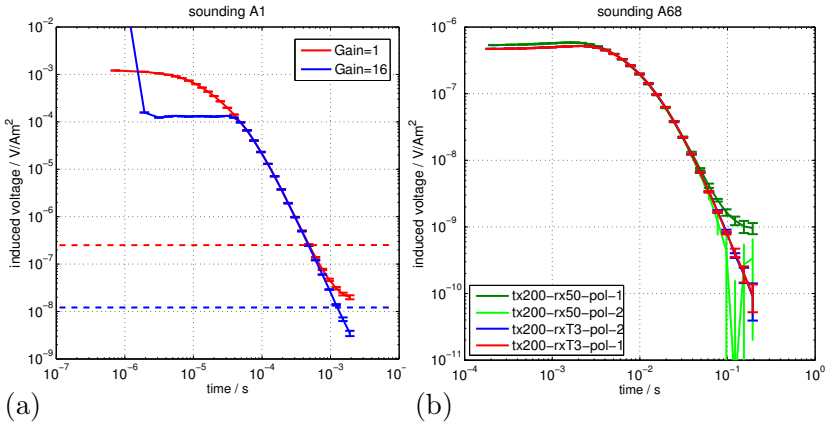

(a) (b)

Figure 4.6: *(a) Transients measured at sounding A1 in NT-mode with a* 50×50 m^2 *transmitter and a* 10×10 m^2 *receiver loop for a minimum gain (G=1, red) and a maximum gain (G=16, blue). The lower input voltage limit* U_{min} *is plotted as dashed lines. (b) Transients for a* 200×200 m^2 *transmitter recorded once with a* 50×50 m^2 *receiver loop (light/dark green) and once with the TEM-3 induction coil (red/blue) for both receiver polarities pol-1/pol-2.*

which were recorded at location A1. The recorded amplified transient is saturated at early times, because the 5 V input limit is exceeded. However, at late stages it seems to be improved compared to the un-amplified transient, which shows an unrealistic voltage increase for the last 4 data points. Obviously this unrealistic response occurs when the recorded voltage drops below the minimum voltage U_{min}, which is marked as a dashed red line in Fig. 4.6(a). Since the error-bars are small and the data quality seems good, this may lead to the false conclusion of a resistivity decrease with depth.
In order to define the reliable time range of a recorded transient, an additional data set is recorded with interchanged receiver polarity at the GDP-32II system [Mollidor, 2008]. From a theoretical point of view, the measured signal should be exactly identical except for the sign. Although Zonge [2002] recommends only the measurement of positive voltages (pol-1), it is safest to measure both polarities. The transients for both polarities (pol-1 and pol-2) are displayed in Fig. 4.6(b) as light and dark green curves for a 200×200 m^2 transmitter loop and a 50×50 m^2 receiver loop at sounding A68 on the mudflat[2]. In contrast to the pol-1 data, the pol-2 measurement results in an unrealistic voltage decrease at late stages with a sign reversal. Therefore, pol-2 data can be significantly misinterpreted as 2D/3D or even induced polarization effects, if the data is not cut-off at late stages. A deviation of 5% between the pol-1 and pol-2 data is used as a cut-off criteria. For this example, the last 6 data points do not meet the criterion and are removed.
In ZT-mode the Gain is set internally/automatically and the late stage data cannot be improved by the system amplification. By using the TEM-3 coil instead of a single turn wire-loop receiver, the polarity effect in the data recorded on the mudflat could be minimized. In Fig. 4.6(b), both polarity data is displayed in red and blue for the configuration using the TEM-3 coil. The late stage data coincides well and no systematic deviation is visible. Although the effective receiver area is only increased by a factor of four compared to the 50×50 m^2 receiver loop data, the late stage data is improved by more than one decade of magnitude using the TEM-3 induction coil.

[2]This configuration was used only in a testing phase and afterwards a 100×100 m^2 transmitter loop with the TEM-3 coil was found best suitable considering signal strength and survey speed

4.5.3 Error estimates for the TEM data

The GDP-32II allows different cycle frequencies or repetition rates f_c. One cycle contains two current turn-off steps, one from positive current I_0^+ to zero and one from I_0^- to zero. The utilized cycle frequency defines the off-time of the transmitter and the last recorded time-point t_{max} (cf. Fig. 2.2, section 2.3). A maximum amount of $c = 2048$ cycles can be recorded, which are internally stacked [Zonge, 2002]. By stacking the transients the signal to noise ratio S/N is reduced according to:

$$\frac{S}{N} = \sqrt{n}\frac{S_0}{N_0}. \tag{4.6}$$

Where S_0/N_0 is the signal/noise ratio of one single record and n is the number of stacks. Internally the GDP-32II system calculates the mean of all cycles and stores the record/transient as a separate block. Since the instrument does not provide a stacking error from the stacked cycles, between $20 - 40$ separate blocks with 1024 cycles each and a high cycle frequency of $f_c = 32\ Hz$ ($t_{max} = 6.07$ ms) were recorded in the field. In order to obtain longer transients, f_c was decreased to 1 Hz ($t_{max} = 193.5$ ms) on the mudflat. For the sake of survey speed, 40 blocks with 64 cycles each were found to be sufficient regarding the signal quality.
To get an impression of the distribution of all data points, a histogram is displayed in Fig. 4.7(a) for all Tx-50 sounding data. The corresponding QQ-plot is shown in Fig. 4.7(b). It should be noted that the data is by no means Gaussian distributed.

Stacking error

From the recorded blocks the mean induced voltage and the stacking error is calculated. This is done by a robust stacking of the blocks, where only 50% of all blocks are used at each sounding [Koch, 2003]. A histogram of the absolute stacking error is shown in Fig. 4.7(c) for all Tx-50 sounding data of the complete survey. The corresponding QQ-plot of the data errors is displayed in Fig. 4.7(d). Except for the largest and smallest errors they follow approximately a normal distribution. If un-correlated data errors are assumed, the least square estimator described in chapter 3 is known to be optimal (Gauss Markov theorem). In Fig. 4.7(e), the obtained percentage stacking error is plotted versus the acquisition time. The stacking error is often around 0.1% or even less, particularly for early times. These small measurement errors are unrealistic because they only reflect the instrument error and not the geological uncertainty (e.g. non 1D environment, anisotropy etc; cf. [Spies & Frischknecht, 1991]). Therefore, they are not suitable for an error-weighted inversion scheme. The cost function and the resulting χ-value will exhibit large values and the obtained models will be simply over-interpreted regarding reliability. Moreover, neighboring sounding locations would be treated different in the inversion and have significantly different data fits. In order not to underestimate the percentage error, a value of 1.6% is defined as the minimum relative error for all data points using the Tx-50 and Tx-100 setups, i.e. smaller errors are set to that value. In Fig. 4.7(f), the absolute data errors δd_{obs} are plotted against the measured data d_{obs}. The red line is calculated according to

$$\delta d = \delta_{d,\%} \cdot d_{obs} + \eta_{noi},$$

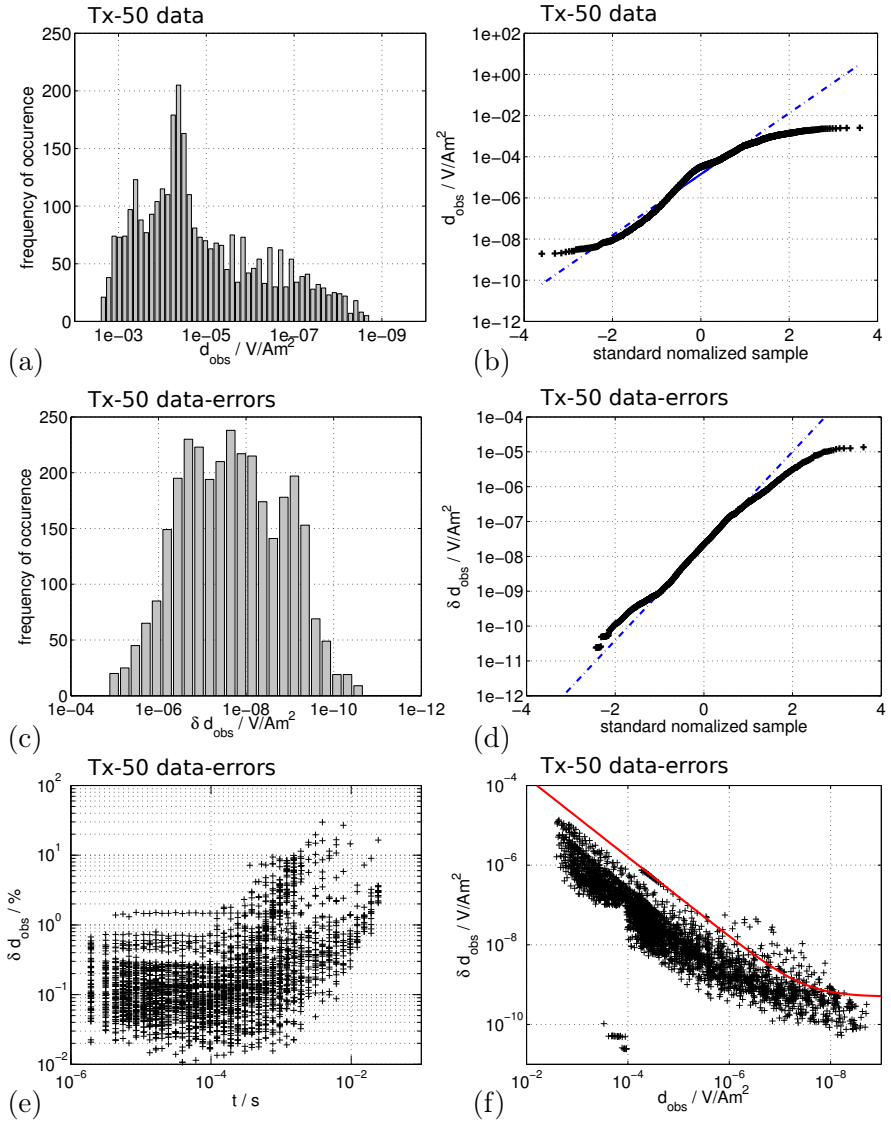

Figure 4.7: *Distribution of all Tx-50 sounding data and stacking errors. (a) Histogram of all data points and (b) corresponding QQ-plot. (c) Histogram of all stacking errors δd_{obs} and (d) corresponding QQ-plot. (e) Percentage stacking errors plotted vs. the acquisition time t. (f) Absolute stacking error plotted against the observed data.*

where $\delta_{d,\%} = 0.016$ is the assumed percentage error and $\eta_{noi} = 5 \cdot 10^{-10}$ V/Am^2 is a typical noise floor. For high voltages the obtained absolute stacking errors tend to be very small and are mostly distributed beneath the red line. The noise level η_{noi} prevails for small voltages. The red line is roughly an upper envelope of the data error up to around $d_{obs} \approx 10^{-5}$ V/Am^2. Therefore, a minimum relative error of 1.6% seems to be a reasonable estimate. With the above estimate the total measurement errors used for the inversion range between 1.6% for the earliest acquisition times and roughly 20% for the very latest times. This is a suitable range for an error weighted inversion. Nevertheless, it should be noted that determining a realistic error estimate for TEM sounding data is a difficult task.

For comparison the distribution of the Tx-100 sounding data and their corresponding stacking errors are presented in a similar manner as above in Fig. A.3 in the appendix.

In order to validate the TEM results, ERT measurements were performed on Profile A. The ERT data is edited visually for data outliers. Data points with high instrument stacking errors are removed from the apparent resistivity pseudosections. The ERT measurement errors are estimated according to Gaussian error statistics taking the instrument stacking error, the voltage error, the geological noise and the geometrical error into account [Günther, 2004]. The estimated ERT measurement errors generally range between 2 and 4%. The ERT data sections are displayed in Fig. A.19.

Calibration factor
The calibration factor (CF) is widely used in LOTEM surveys, where a grounded bipole source is used. Near surface inhomogeneities close to the transmitter electrodes or electrode coupling problems may cause a constant shift on the response [Hördt & Scholl, 2004; Strack, 1992]. However, inductive loop sources do not possess a constant shift such as galvanic grounded sources do. For TEM an additional error occurs, if the system is not well calibrated and/or the transmitter/receiver setup is not accurately installed. For example calibration factor values, of $CF = 0.9 - 1.01$ are easily justified by a 1 m^2 inaccuracy of a 10×10 m^2 receiver loop. Usually the size of both, transmitter and receiver, are not exact and the receiver loop might be also slightly displaced within the transmitter loop. An inexact current reading from the instrument also causes a constant shift of the data. In order to take these systematic errors or constant shift effects into account the calibration factor CF is included as a free parameter into the inversion process, which acts as an multiplier to the predicted data. For the field data CF ranges mostly between $CF = 0.98$ and 1.02.

4.6 The TEM field data

Different approaches are used to visualize the TEM field data recorded along both profiles, A and B. Often the induced voltage is displayed because the inversion, either 1D or 2D, is performed using U_{ind}. Hence, the data fit is calculated according to U_{ind} (for χ and RMS calculation see section 3.1.3). Another reason is that U_{ind} is the measured physical quantity and reflects the data quality best in terms of signal to noise ratio and resolvable signal magnitude. However, U_{ind} varies over several decades of magnitude and is, therefore, difficult to visualize. The common transformation to late time apparent resistivity $\rho_{a,lt}$ reduces the dynamic range and gives a first idea of the subsurface structure [Raiche, 1983]. The approximation does not reflect the subsurface for early times and has to be interpreted carefully. However, since a resistor is expected at depth in the survey area, the visualization using $\rho_{a,lt}$ is particularly useful. By calculating the first order time derivative of $\rho_{a,lt}$ a resistivity increase at late times is visualized by a positive value of

$$\partial_{\tilde{t}} \tilde{\rho}_{a,lt}(t) = \frac{t}{\rho} \partial_t \rho_{a,lt}(t). \tag{4.7}$$

It has to be noted, that the factor t/ρ occurs because the derivative is calculated with respect to the logarithmically transformed values $\tilde{\rho}_{a,lt} = \log_{10}(\rho_{a,lt})$ and $\tilde{t} = \log_{10}(t)$. In contrast to the late time transformation, the early time transformation $\rho_{a,et}$ does not reduce the dynamic range of the transient. Moreover it is valid only for the earliest

times, which often does not correspond to the subsurface depth of interest. Nevertheless, $\rho_{a,et}$ is useful to get an idea of the shallow subsurface resistivity and to derive a-priori information. The transition from early to late time behavior takes place over a wide time-range. In general, it is difficult to define validity limits for the approximations [Spies & Frischknecht, 1991]. The limits can be estimated from the induction number β for an assumed subsurface resistivity. In the transition both approximations do not reflect the true earth resistivities at all. For the $\rho_{a,et}/\rho_{a,lt}$ equations and further discussion regarding both approximations refer to section 2.3.1.

4.6.1 Profile A, northern part: Tx-50 sounding data

A total of 74 soundings were recorded along profile A using the 50×50 m^2 transmitter loop and the single turn 10×10 m^2 receiver loop (Tx-50 setup). Three selected soundings are displayed in Fig. 4.8 as induced voltage U_{ind} as well as $\rho_{a,lt}$ and $\rho_{a,et}$. The soundings A06 and A27, obtained on the AQ formation in the northern part of profile A, indicate an apparent resistivity increase starting at approximately $t = 10^{-4}$ s. Those parts of the transients are highlighted by a blue box in Fig. 4.8. The $\rho_{a,lt}$ increase is supported by around one decade of time. Sounding A06 is located 150 m away from the basalt outcrops (see the geological map in Fig. 4.2(a)). It shows an even more significant and earlier occurrence of the $\rho_{a,lt}$ increase than sounding A27. For sounding A59 on the mudflat the signal strength is increased at late times and the transients are recorded up to $t = 2 \cdot 10^{-2}$ s. The transients are around one decade longer than those obtained on the AQ formation. A resistivity increase below the mudflat sediments, as it is suggested by the geological cross-section in Fig. 4.2(b), is not supported by the $\rho_{a,lt}$ behavior at late times. Moreover, $\rho_{a,lt}$ tends towards $0.2 - 0.3$ Ωm halfspace resistivity.
The $\rho_{a,lt}$ data is plotted in Fig. 4.9(a) as a colorcoded pseudosection and gives an impression of the data variation along the profile. First of all, a characteristic change in the data occurs around sounding A37. At sounding A42, which is the expected position of the Al Bayda fault, the $\rho_{a,lt}$ values are significantly decreased below 1 Ωm at late times. Furthermore, due to the increased signal strength, the recorded time range is longer. The data is laterally continuous and no obvious outliers are present. In particular, the data in the transition zone is smooth.
In order to visualize the resistor at depth in the data, the first order time derivative is calculated from the $\rho_{a,lt}$ data with equation (4.7) and is plotted as a colorcoded section in Fig. 4.9(b). Up to sounding A37, data in the last decade of time of each sounding exhibit a positive slope of the $\rho_{a,lt}$ values. The point of inflection is smooth and consistent along the profile and appears at around $t = 10^{-4}$ s. From A37 onwards, the point of inflection shifts to later times and the increase of $\rho_{a,lt}$ is supported only by a few data points. It disappears almost completely southwest of sounding A53.

4.6.2 Profile A, southern part: Tx-100 sounding data

In the second survey profile A was re-investigated from sounding A47 onwards. The larger 100×100 m^2 transmitter loop with the TEM-3 induction coil receiver (Tx-100 setup) was used in order to resolve the resistor below the mudflat sediments. The data obtained for soundings A*47, A*59 and A*80 are displayed in Fig. 4.10. Note that data

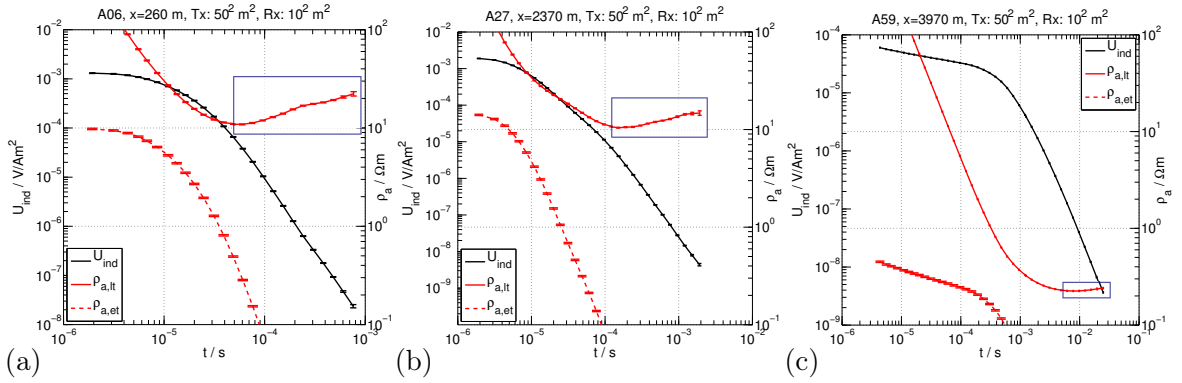

Figure 4.8: *Field data obtained along profile A with the Tx-50 setup for soundings (a) A06, (b) A27 and (c) A59. U_{ind} is drawn in black, $\rho_{a,lt}$ and $\rho_{a,et}$ are marked both red. The $\rho_{a,lt}$ increase is hemmed blue.*

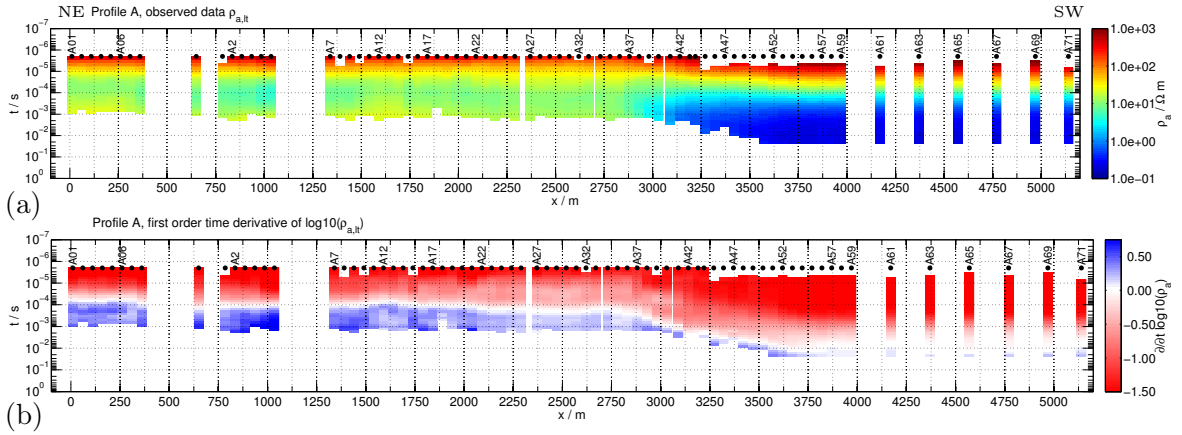

Figure 4.9: *Field data obtained along profile A with the Tx-50 setup. (a) The $\rho_{a,lt}$ values are plotted for each sounding along the profile. (b) First order time derivative of $\rho_{a,lt}$ for each sounding. A positive value of $\partial_t \rho_{a,lt}$ is colorcoded in blue. The Al Bayda fault is expected around sounding A42. The Tx-50 sounding locations are marked as black circles.*

recorded with Tx-100 setup are marked with an asterisk, e.g. A*47. The increase of the $\rho_{a,lt}$ values at late times is significant for all three soundings. The comparison of sounding A*59 in Fig. 4.10(b) with the Tx-50 sounding A59 in Fig. 4.8(c) illustrates the benefit of the larger Tx-100 setup. A clear $\rho_{a,lt}$ increase is visible at late times. In Fig. 4.11(a), the $\rho_{a,lt}$ data is presented as a colorcoded section. The transition between soundings recorded with the larger and the smaller setup is discontinuous, due to the different transmitter size and transmitter delay times. Furthermore, the transients begin at times slightly later than $t = 10^{-4}$ s, because only ZT-mode data were recorded.

However, the first order time derivative of $\rho_{a,lt}$ in Fig. 4.11(b) illustrates the benefit of the larger setup. The point of inflection to a positive slope of $\rho_{a,lt}$ is smooth and continuous along the profile. Between 5 and 10 late time data points at each sounding support the $\rho_{a,lt}$ increase. Although the $\rho_{a,lt}$ increase is not that significant for a few soundings, the continuity (of the $\rho_{a,lt}$ increase) validates it. Between sounding A*57 and A*62 the point of inflection occurs latest in time, which indicates that the resistor at depth might be located deepest in that zone.

For the sake of completeness, all soundings obtained along profile A with the Tx-50 and Tx-100 setup are presented in appendix A.5.

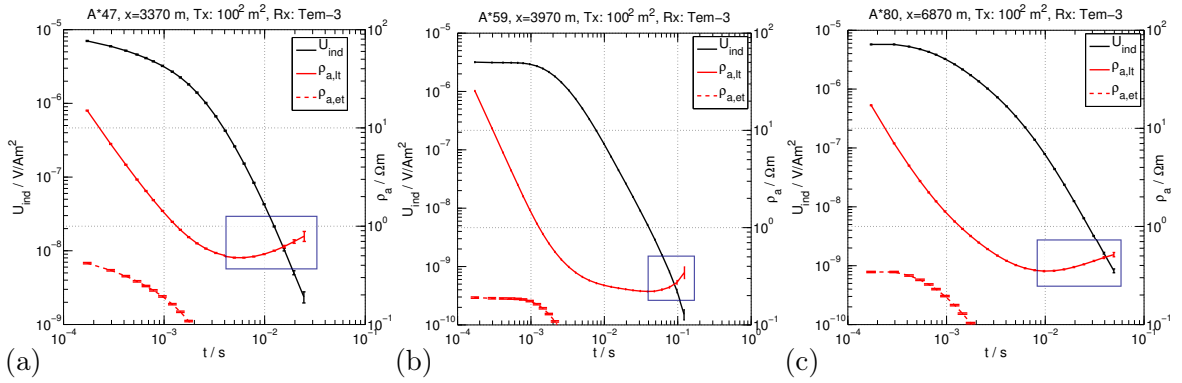

Figure 4.10: *Field data obtained along profile A with the Tx-100 setup for soundings (a) A*47, (b) A*59 and (c) A*80. U_{ind} is drawn in black, $\rho_{a,lt}$ and $\rho_{a,et}$ are marked both red. The $\rho_{a,lt}$ increase is hemmed blue.*

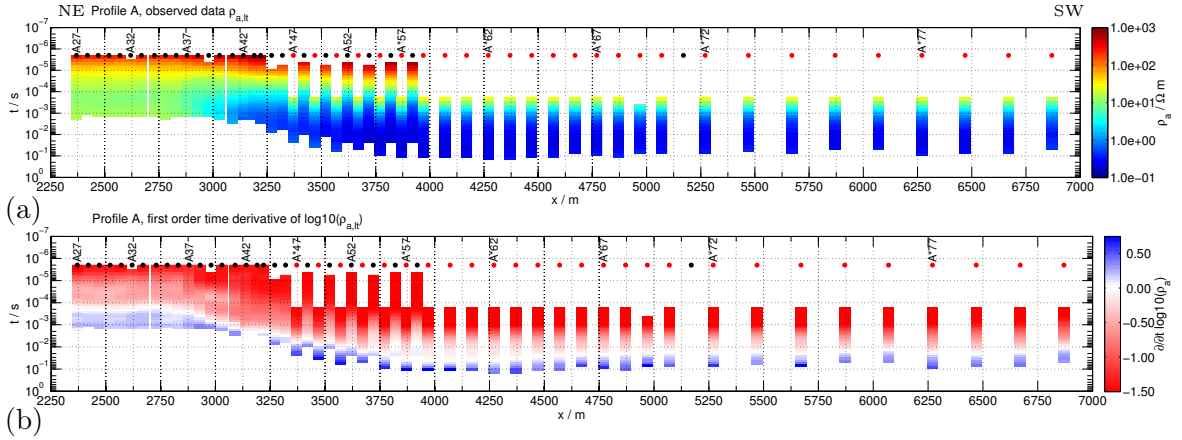

Figure 4.11: *Field data obtained along profile A with the Tx-50 and Tx-100 setup between A27 and A*80. (a) The $\rho_{a,lt}$ values are plotted for each sounding along the profile. (b) First order time derivative of $\rho_{a,lt}$ for each sounding. Positive values of $\partial_t \rho_{a,lt}$ are colorcoded in blue. The Al Bayda fault is expected around sounding A42. The Tx-100 sounding locations are marked as red circles and the Tx-50 are marked black.*

4.6.3 Profile B: Tx-50 and Tx-100 sounding data

A total of 47 soundings were recorded along profile B. The 50×50 m^2 transmitter with the single turn 10×10 m^2 receiver loop (Tx-50 setup) were used for 27 soundings. This profile was also re-investigated during the second survey and 20 additional soundings were recorded using the Tx-100 setup with the TEM-3 receiver coil. With the larger TEM setup the profile was extended up to 5 km length and gaps were filled.
The data recorded at sounding B1, B*31 and B*47 with the Tx-100 setup are presented in Fig. 4.12(a-c). The late time apparent resistivity increase is significant for all three soundings, but strongest for sounding B*31. In Fig. 4.13, all soundings for profile B are presented in a similar manner as for profile A in Fig. 4.11. From the colorcoded $\rho_{a,lt}$ section in Fig. 4.13(a), it can be seen that the transition to the very low subsurface resistivities appears around sounding B9. At that sounding a strong lateral change in the data characteristic is present. According to the geological map in Fig. 4.2(a), the Qaisiyeh fault is expected around sounding B*18. The first order time derivative of

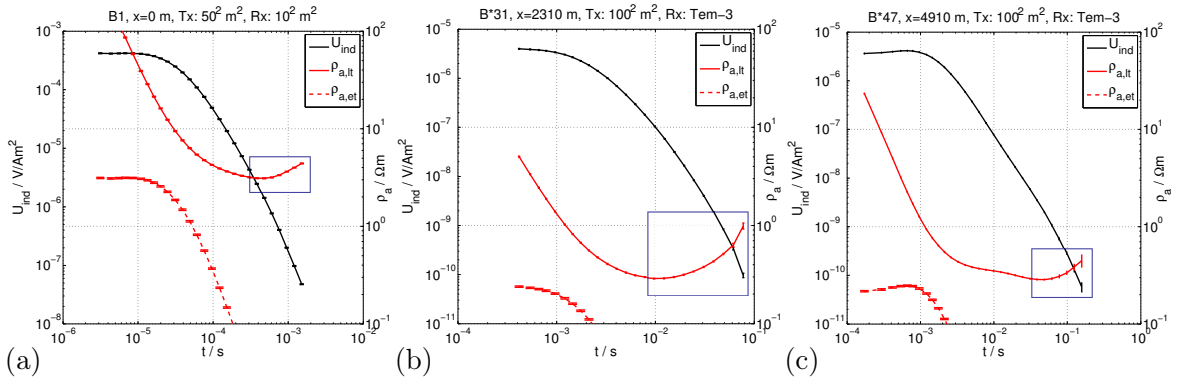

Figure 4.12: *Field data obtained along profile B. (a) B1 was recorded with the Tx-50 setup. For (b) B*31 and (c) B*47 the Tx-100 setup was used. U_{ind} is drawn in black, $\rho_{a,lt}$ and $\rho_{a,et}$ are marked both red. The $\rho_{a,lt}$ increase is hemmed blue.*

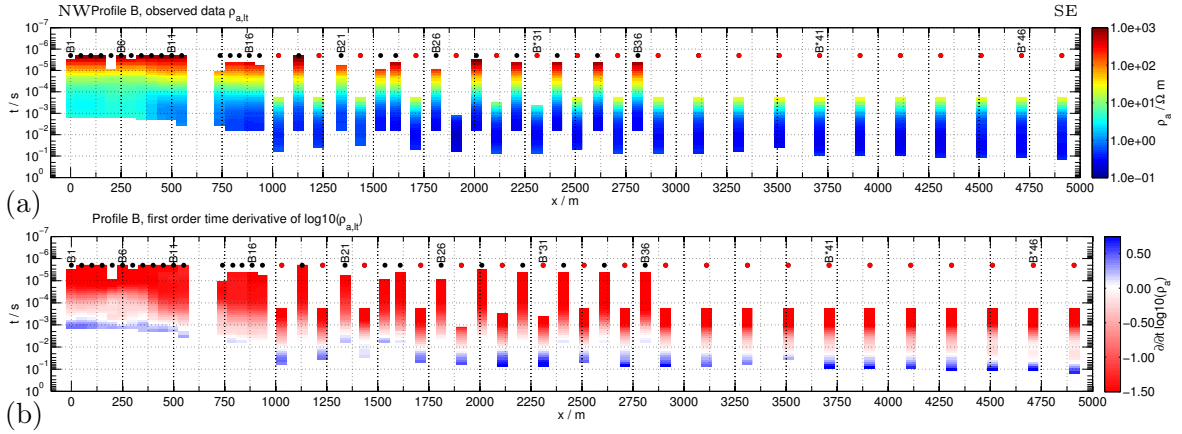

Figure 4.13: *Field data obtained along profile B with the Tx-50 and Tx-100 setup. (a) The $\rho_{a,lt}$ values are plotted for each sounding along the profile. (b) First order time derivative of $\rho_{a,lt}$ for each sounding. Positive values of $\partial_t \rho_{a,lt}$ are colorcoded in blue. The Qaisiyeh fault is expected around sounding B*18. The Tx-100 sounding locations are marked as red circles, whereas the Tx-50 soundings are drawn black.*

$\rho_{a,lt}$ is displayed in Fig. 4.13(b) and visualizes the $\rho_{a,lt}$ increase at late times. Southeast of B12, the soundings recorded only with the Tx-50 setup do not support the apparent resistivity increase and tend towards 0.2 to 0.3 Ωm halfspace resistivity. Considering also the Tx-100 setup, there are two zones, B13–B17 and B21–B24, where the $\rho_{a,lt}$ increase is marginal. For all other soundings (recorded with the Tx-100 setup and marked by red dots in 4.13(b)) the $\rho_{a,lt}$ increase is in general significant. Note that profile A and B cross each other at sounding B*38 and A*72, respectively.
For the sake of completeness, all soundings obtained along profile B are presented in appendix A.6.

4.7 One-dimensional TEM inversion results

The field data for both profiles A and B is interpreted using conventional 1D Marquardt and Occam inversion techniques. Moreover, the quality of the inversion results

is appraised by parameter importances and equivalent modeling. These techniques are briefly discussed in chapter 3.

Due to the two-parted field survey and for comparison with the 2D forward and inverse modeling presented in the forthcoming chapter 5 and chapter 6, the geoelectrical interpretation of profile A is split into two parts. At first, the geoelectrical models obtained on profile A are interpreted for the data recorded with the Tx-50 setup. Subsequently, the Tx-100 soundings are included and the geoelectrical interpretation is done for soundings A27 to A*80, where the focus is to resolve the base below the high conductive mudflat. Profile B is interpreted using both configurations along the profile. Note that in the following illustrations, those soundings which are recorded with the Tx-100 setup are denoted with an asterisk, e.g. A*47 and B*47. Their locations are marked with red dots along each profile line. In general, the quasi 2D resistivity-depth are presented for the Occam R1 and Marquardt inversions. For comparison, the Occam R2 sections are compiled in Fig. A.16.

1D Occam inversion

The 1D Occam inversion is done for a pre-defined number of layers. Here, 30 layers are used with logarithmically equidistant layer thicknesses. The amount of layers is chosen more or less arbitrary, but under-parameterization should be avoided in any case. The upper and lower layer bounds are derived from the skin depth δ_{FD} discussed in section 2.2.2. It is recommended to use approximately $1/3 \cdot \delta_{FD,min}$ as the minimum layer thickness and $3 \cdot \delta_{FD,max}$ as depth of the last layer. In the survey area the resistivity varies from 0.3 Ωm on the mudflat to around 100 Ωm on the basalt formation. For comparability of the inversion models an identical parameterization is used for all soundings. In order to consider the two significantly different subsurface zones along the profiles, $\Delta_{min} = 1$ m and $\Delta_{max} = 300$ m are used as the first layer thickness and last layer depth. These limits are suitable for a sufficient model parameterization.

1D Marquardt inversion

The Marquardt inversion is useful to derive a model with a minimum amount of layers and distinct non-smooth boundaries. The number of initial layers is derived from the Occam models. Three layers are sufficient for most of the soundings along both profiles. However, in the transition zone from moderate to very low resistive subsurface a four layer initial model is used, which significantly improves the data fit. In order to minimize the influence of a-priori information each layer is given the same initial resistivity. Generally, 10 Ωm is selected on the AQ formation and 1 Ωm on the high conductive mudflat for the Tx-50 soundings. The quality/ambiguity of the Marquardt inversion models is estimated from equivalent models and parameter importances. In general, the equivalent models reflect the model uncertainty better than the parameter importances. It is well known, that the Marquardt inversion depends on the starting model [Meju, 1994]. Therefore, the Tx-100 soundings obtained on the mudflat are inverted using approximate starting model resistivities, which are derived from the 1D Occam models. Otherwise, it turned out that the late time data was not fitted satisfactory for some soundings.

4.7.1 Correlation with lithological borehole data

Lithological borehole data are available from a bentonite drilling project in the Azraq area [Ibrahim, 1996; Ala'li, 1993]. The derived 1D electrical models are validated and correlated with the lithological data from two specified boreholes.

AQ/basalt formation: Borehole BT-1
Borehole BT-1 is located in approximately 500 m distance to sounding A14 in the northeastern part of profile A, where the sediments of the AQ formation cover the basalt (cf. Fig. 4.2(a)). Vertical electric sounding (VES) data is extracted at sounding A14 from the 2D ERT pseudosection and used for the 1D inversion. Both, ERT and TEM, 1D models displayed in Fig. 4.14(a,b) are in good agreement within their equivalent models. However, the ERT model shows larger equivalences for both, the resistivity and depth, than the TEM model. Borehole BT-1 is shown in Fig. 4.14(c) and leads to the following correlation with the electrical models:

- The topmost 9 m of BT-1 consists of a clay layer intermixed with evaporates, pieces of limestone, chert, gravel and plant roots. The resistivity for that layer ranges between 10 and 20 Ωm in the corresponding electrical models. The second layer consist mostly of soft clay and exhibits a slightly lower resistivity of approximately $3 - 8$ Ωm. These shallow sediments belong to the AQ formation and are known to be highly variable in their lithology [Ibrahim, 1996]. As discussed in section 2.1, the electrical resistivity depends significantly on the water content. Wet clay can have resistivities around 3 Ωm. The depth to the water table ranges between $5 - 25$ m on the AQ formation and is not known exactly for borehole BT-1. Therefore, the upper 9 m might be dry, whereas the second layer might show a decreased resistivity due to the water content.

- The top of the basalt layer occurs in a depth of 17 m. The resistivity ranges from around 40 to 100 Ωm in the corresponding 1D models. The basalt is known as a good fresh water aquifer and most likely saturated. Therefore, the basalt can have comparably low resistivities. The depth of the basalt is the target of the geophysical investigation in the northern part of profile A and western part of profile B.

For further comparison and validation borehole lithological data for BT-20 and BT-24 are shown in Fig. A.1. The lithology is basically the same as for BT-1, except that BT-24 was obviously not drilled into the basalt. Boreholes AZ-9 and AZ-13 are taken from El-Waheidi et al. [1992] and are displayed in Fig. A.1, too. They are located in the vicinity of profile B towards the northwestern mudflat boundary. Both show the URC chert limestone layer in a depth between 30 and 60 m. All boreholes are marked on the map in Fig. 4.2(a).

Mudflat formation: Borehole BT-49
Lithological data from borehole BT-49 is used to validate the sounding results obtained on the mudflat. It is located in approximately 500 m distance to sounding A65 (Fig. 4.2(a)). BT-49 shows layers of hyper-saline gypsiferous clay, soft clay, silty clay and thick layers of diatomite down to a depth of 70 m [Ala'li, 1993]. According to the derived TEM model, at sounding A65 in Fig. 4.14(e) the resistivity for these layers is

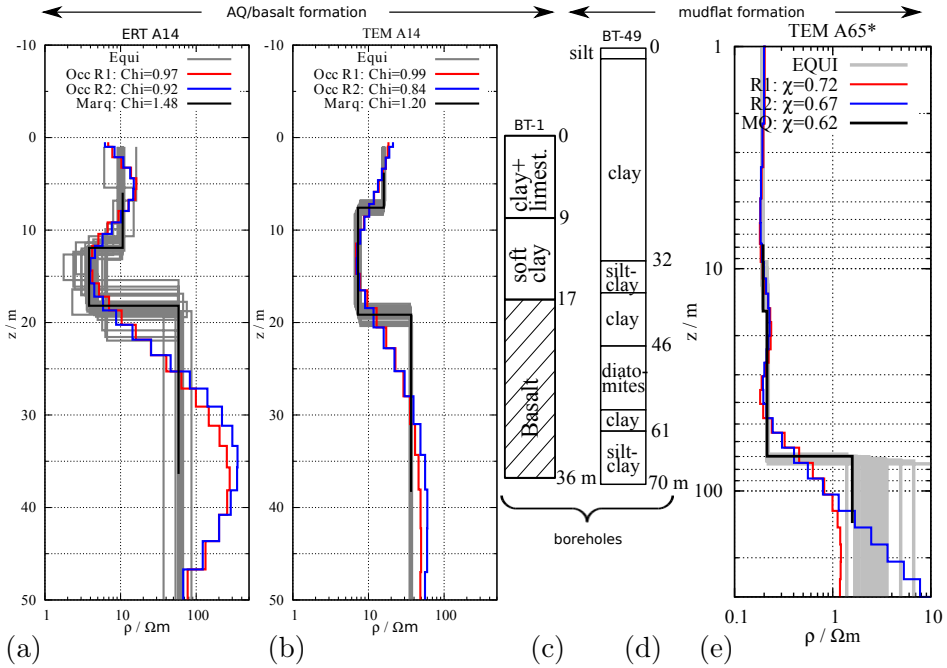

Figure 4.14: *Comparison of 1D electrical models with lithological borehole data. 1D inversion results obtained at sounding location A14 for (a) extracted VES/ERT and (b) TEM data. Lithological data derived from boreholes (c) BT-1 on the AQ/basalt formation and (d) BT-49 on the mudflat. In (e) the 1D TEM inversion result is displayed for sounding A65, which is closest to borehole BT-49. All locations are marked on the geological map in Fig. 4.2(a).*

around 0.3 Ωm. This exceptional low resistivity is caused by hyper-saline groundwater with resistivity less than 0.3 Ωm [El-Naqa, 2010]. The water table on the mudflat is very shallow (often less than 1 m below surface). At a depth of $65 - 70$ m a slight increase of the resistivity to around $1 - 2$ Ωm is observed in the model. The interface matches the drilling depth of the borehole. Most probably the resistivity increase coincides with the base below the mudflat sediments, which is the target to resolve with the soundings recorded on the mudflat. The base is referred to as the URC-formation, which consists of chert and limestone. The outcrops of this formation are present in the northeastern and southwestern part of the area [Ibrahim, 1996].
The correlation with the lithological borehole data demonstrates the overall consistency and reliability of the derived resistivity-depth sections for both transects, which are presented in the following. Moreover it shows, that both applied methods, TEM and ERT, are suitable for the investigation of such geological targets.

4.7.2 Shallow investigations along Profile A, northern part: Tx-50 sounding data

Five selected 1D models, derived from the Tx-50 sounding data along profile A, are displayed in Fig. 4.15. Their locations are marked on the geological map in Fig. 4.2(a). All models have in common that the moderate resistive top surface layer (around $10 - 20$ Ωm) is followed by a mostly thin, less resistive layer and again by a resistor. Sounding A41 exhibits significantly decreased resistivities compared to the other soundings in Fig. 4.15. The models are consistent and in good agreement with the previously

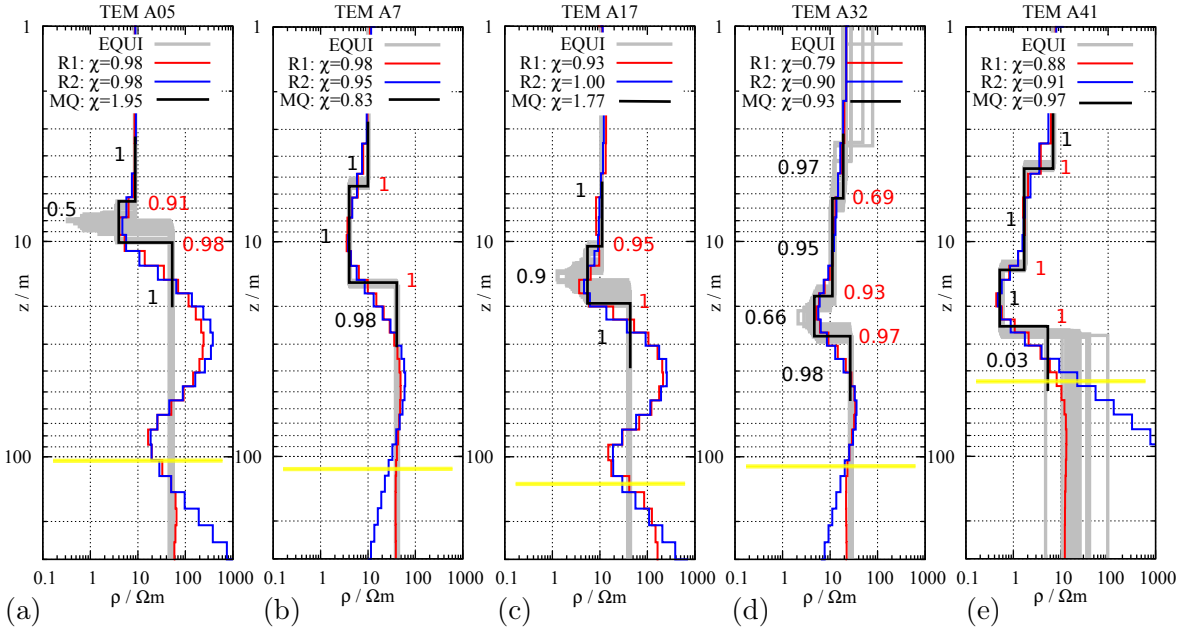

Figure 4.15: *1D inversion results for selected soundings (A05, A7, A17, A32 and A41) obtained along profile A with the Tx-50 setup. Marquardt models (MQ) are denoted in black and the Occam R1 and R2 in red and blue, respectively. The equivalent models (EQUI) are displayed in light gray. The doi after Spies [1989] is marked as a yellow line. The layer depth- and resistivity-importances are displayed in red and black, respectively. The χ value is given in the legend of each model.*

described lithological data, particularly of borehole BT-1 in Fig. 4.14(c). Especially, the top of the basalt layer is evident in all soundings.

2D resistivity-depth section

Subsequently the derived 1D models are stitched together to a quasi 2D resistivity-depth section for all soundings along profile A. The 2D sections for the Marquardt and Occam R1 models are presented in Fig. 4.16(a,b). Both resistivity-depth sections are in good agreement and validate each other. The corresponding data fitting is plotted for each sounding along the profile line in Fig. 4.16(c). The global fitting is almost optimal with $\chi = 1.3$ for all Marquardt models and slightly over fitted with $\chi = 0.92$ for the Occam R1 models. According to the sections displayed in Fig. 4.16(a,b), the subsurface exhibits moderate resistivities for soundings A01–A37. A three layer case is present with a slightly more resistive overburden, followed by a good conductor and a resistor at depth. The first layer exhibits resistivities around 10 Ωm and obviously corresponds to sediments of the AQ formation, which are known to be geologically highly variable [Ibrahim, 1996]. Along the profile the layer occurs to be continuous. The relative thin conductive layer below is also continuous and exhibits resistivities around 5 Ωm. According to the lithological data, this might correspond to a soft (maybe wet) clay layer. Beneath that layer the basalt appears with resistivities mostly around $20 - 100$ Ωm, although the upper bound is naturally not resolved well by the TEM method. Between sounding A05 and A41 the top of the resistive basalt slopes down by roughly 20 m depth, which becomes clearest from the 1D models in Fig. 4.15(a-d). Furthermore, the resistivity of the basalt layer slightly decreases towards the edges of the conductive mudflat sediments, which might be due to increasing salinity of the

groundwater.
The transition zone from moderate to very low resistivities occurs between sounding A37 and A42. This is probably a mixing zone from fresh to brackish water bearing layers to the hyper saline and saturated clay sediments. The resistivity decrease in lateral direction is significant. The hyper saline mudflat sediments have a resistivity around 0.3 Ωm and the water table is shallow. The *doi* is plotted as a black dashed line in Fig. 4.16(a,b) and is around $50 - 60$ m for the Tx-50 setup.
Southwest of sounding A39 the resistive basalt layer seems to continue until sounding A52. According to the geological cross-section in Fig. 4.2(b) the basalt is interrupted at the Al Bayda fault, which is roughly at sounding A42. However, the TEM results suggest that a resistor is present at depths further southwest of A39. This is more obvious when comparing the results of the Tx-50 setup data with the Tx-100 setup data further below in section 4.7.4.

Equivalent models and parameter importances
In order to get an impression of the quality of the 1D stitched Marquardt models, the layer depth and resistivity importances are plotted as a colorcoded section in Fig. 4.16(d). The resistivities and layer depths are mostly resolved well with importance values above 0.8. However, between sounding A39 and A52 the resistivity of the base layer is not resolved. In contrast to that, the depth of the interface is well resolved in this zone. As shown previously in the Tx-50 $\partial_t \rho_{a,lt}$ data-section in Fig. 4.9(b), the resistor is supported only by very few data points in this zone. Furthermore, the equivalent models for sounding A41 (cf. Fig. 4.15(d)) indicate a large equivalence for the last layer with resistivities between 4 and 100 Ωm. Moreover, the Occam R1 and R2 models in Fig. 4.15(d) differ slightly below the interface at a depth of roughly 40 m. The *doi* is marked as a yellow line and is only slightly deeper than the depth of the interface.
The resistivity of the relative thin conductive layer is also not that well resolved in some areas along the profile, e.g. between sounding A27 and A36. The importances range from 0.4 to 0.7. Taking a closer look at the equivalent models in Fig. 4.15(a-d), it is clear that for a thin conductive layer the equivalence increases. In general, it is not possible to resolve the resistivity and the thickness of a thin conductive layer separately. Moreover, the conductance is resolved, which is the product of conductivity and thickness [Nabighian & Macnae, 1991].

Conductor below the basalt
Although the Occam R1 and Marquardt 2D stitched sections match well, some deviations are visible for the deep parts between A01 and A23. According to the 1D Occam models in Fig. 4.15(a-c) the resistivity decreases again at depth. The 2D stitched Occam R1 models in Fig. 4.9(a) show the same behavior for a large number of soundings. This is not supported by the Marquardt models as the resolution below the basalt layer is very poor. Nevertheless, it is possible that below the basalt a good conductor appears again. In order to validate this, sounding A12 and A25 were re-investigated using the Tx-100 setup. A 1D joint inversion is performed for the data-sets, which were recorded using both setups. The derived 1D models show a conductor below the basalt in a depth between $60 - 100$ m. Unfortunately, the data quality of sounding A25 is very poor at late times compared to sounding A12, which exhibits very good data quality. Both derived 1D models, the data and fitting are presented in Fig. A.4. For comparison,

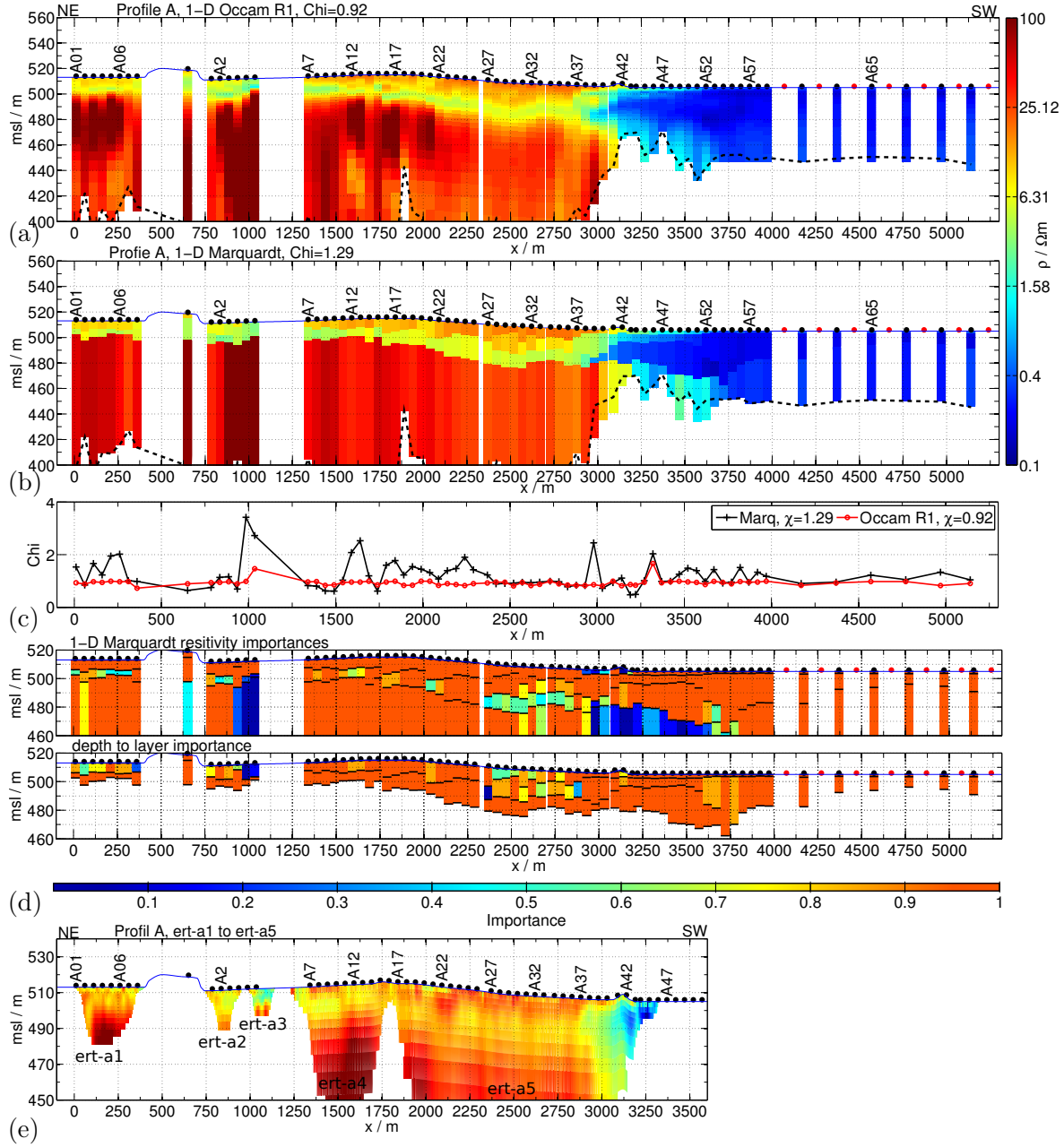

Figure 4.16: *1D inversion results derived solely from the Tx-50 soundings and stitched together as a 2D resistivity-depth section along profile A. (a) Occam R1 models, (b) Marquardt models. (c) Data fitting (χ) for each sounding along the profile. (d) Layer depth and resistivity importances plotted as a colorcoded section. (e) 2D ERT inversion results, where ert-a1 to ert-a5 are patched together. Note that the same color-scale is used for the ERT and TEM sections. The Tx-50 sounding locations are marked as black dots above the model. Locations where Tx-100 setup was used are marked red. The doi is denoted as a dashed line in (a) and (b). The blue line denotes the topography.*

Kaudse [2014] reported a basalt thickness between $40 - 100$ m for the AWSA well field litholog. The AWSA well field is located approximately 7 km northwest of the profile A (cf. Fig. 4.2(a)). However, the structure below the basalt is not further discussed, since it is out of the scope of this thesis.

Short summary: northern part of profile A
From the Tx-50 soundings the objectives stated in section 4.3 are already partly achieved. The overall subsurface resistivity structure is clearly detected. Particularly the depth down to the basalt in the northern part of profile A seems evident. The resistivity of the basalt is around 50 Ωm and slightly decreases towards southwest. This might be due to the increasing groundwater salinity as shown on the map in Fig. 4.4(b). The shallow transition zone from moderate to low subsurface resistivities around the Al Bayda fault is detected. This is expected to be a mixing zone from fresh to brackish and saline groundwater. It occurs between A37 and A42. However, the depth of the base below the mudflat, southwest of A53, is not resolved at all with the Tx-50 setup. Therefore, the mudflat was re-investigated with the Tx-100 setup. The results for profile A are discussed in the following section 4.7.4.
The lateral structure varies significantly in the transition zone between sounding A37 and A42. A 1D interpretation might be an inadequate approach for such lateral subsurface contrasts. Therefore, in section 5.5 a 2D model is derived from the resistivity-depth section to explain the field data between sounding A27 and A59. Furthermore, a 2D modeling study is performed by variation of the basalt layer in the transition zone.

4.7.3 Validation of TEM results by 2D ERT along profile A

As already mentioned previously in section 4.4, ERT data was recorded in the northern part of profile A for verification of the TEM results. The ERT data is inverted in 2D using a second order smoothness constraint inversion algorithm [Günther, 2004]. The regularization parameter is determined automatically in each inversion iteration by the L-curve criterion [Hansen & O'Leary, 1993]. The zones in the models, which are not supported by the data, are masked according to the coverage.
The ERT profiles (ert-a1 to ert-a5) are plotted along Profile A in Fig. 4.16(e). In general, the 1D stitched TEM results match the ERT sections quite well. The basalt stream is well detected for the larger Wenner arrays (ert-a1, ert-a4 and ert-a5). Here, the overlying clay layer is slightly more resistive than in the stitched TEM models in Fig. 4.16(a) and (b). The transition zone is visible at around $x = 3000$ m along the profile line. Therefore, the continuation of the basalt southwest of the Al Bayda fault is unclear from the ERT models. The ERT profiles are fitted with a χ ranging from $2.9 - 3.2$. A quite low resistive shallow subsurface zone is visible for profile ert-a3, which is partly also indicated in the 2D TEM section (cf. Fig. 4.16(a,b)). According to the geological map in Fig. 4.2(a), this zone is partly covered by alluvial sediments. The 2D ERT inversion results are displayed on a larger scale in Fig. A.18 in the appendix. The corresponding ERT field data pseudosections are displayed in Fig. A.19.

4.7.4 Deeper investigations along Profile A, southern part: Tx-100 sounding data

In order to resolve the depth of the mudflat sediments, profile A and B were re-investigated in a second survey using the larger Tx-100 setup. The first order time derivative of $\rho_{a,lt}$ presented in Fig. 4.11(b) visualizes the resistivity increase at depth and the benefit of using that setup. For most soundings on the mudflat, five to ten

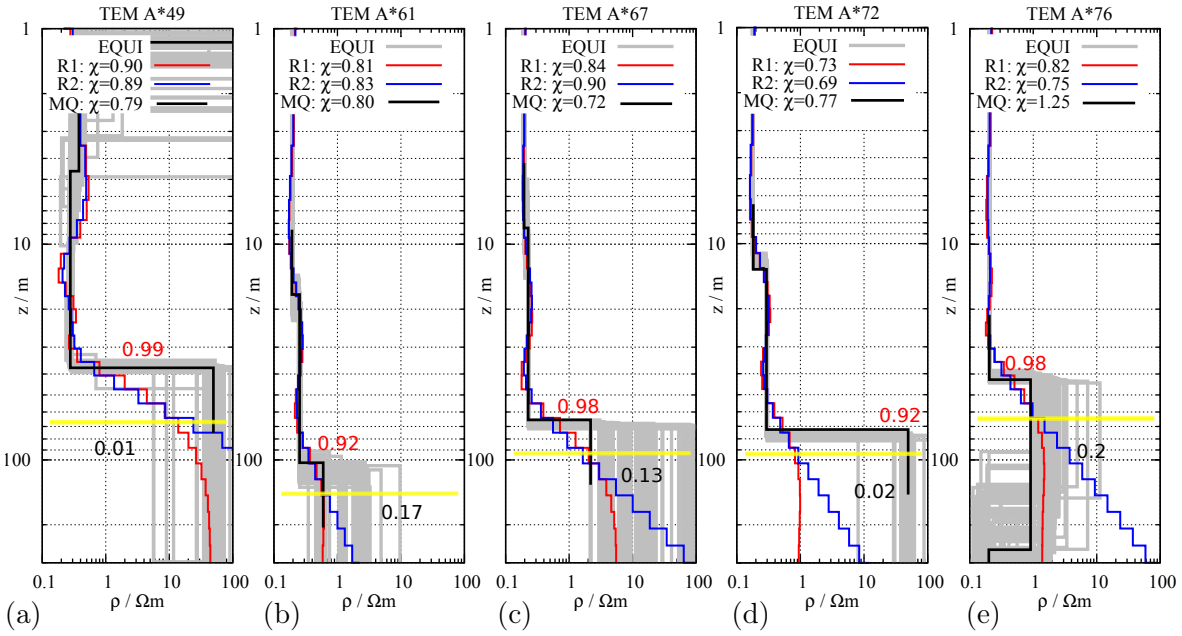

Figure 4.17: *1D inversion results for selected soundings (A*49, A*61, A*67, A*72, A*76) obtained along profile A with the Tx-100 setup. Marquardt models (MQ) are denoted in black. Occam R1 and R2 in red and blue, respectively. The equivalent models (EQUI) are displayed in light gray. The doi after Spies [1989] is marked as a yellow line. The layer depth and resistivity importances are displayed red and black, respectively. The χ value is given in the legend of each model.*

data points show the $\rho_{a,lt}$ increase and indicate a resistor at depth.
1D Marquardt and Occam R1/R2 inversion results are displayed in Fig. 4.17 for five selected soundings recorded with the Tx-100 setup. All five 1D models show a resistive interface at depth. Moreover, they are consistent and in good agreement with lithological borehole data. Particularly A*61–A*76 are comparable to BT-49 (cf. Fig. 4.14(d)). Sounding A*47 is located closest to the northern edge of the mudflat, where the depth of the base layer is around 40 m deep. At sounding A*61 the depth of the interface is increased to roughly 100 m. The depth is again decreased to $z \approx 40\ m$ for sounding A*76 close to the southwestern edge of the mudflat. The *doi* for the models varies roughly between $70 - 130$ m and coincides quite well with the depth, where the Occam R1/R2 models diverge.

2D resistivity-depth sections

The 1D Marquardt and Occam R1 models are stitched together as 2D sections presented in Fig. 4.18(a,b), respectively. The overall structure of the Occam R1 and Marquardt sections is matching well. The continuation of the resistive structure until sounding A56 is evident by including the Tx-100 soundings. Most likely the basalt continues until sounding A*56 and covers the URC formation. Obviously it is not interrupted at the Al Bayda fault, which is expected around sounding A42. Southwest of sounding A56 the resistor slopes downwards quite abrupt. This finding suggests that the Al Bayda fault zone extends over 700 m between A42 and A56, which was not clear from the prior geological information. Between sounding A*57 and A*62 the mudflat reaches its deepest point at around 100 m depth. It slightly slopes upwards to roughly 60 m depth southwest of A*62. According to the geological information the base is

the URC-chert-limestone formation, which outcrops in the northeast and southwest of the area. The upward slope towards southwest is expected to be caused by tectonic lowering of the base at the Al Bayda fault [Ibrahim, 1996]. This is also in agreement with the geological cross-section in Fig. 4.2(b).
In order to avoid misunderstanding, it should be noted that the resistivity of the base layer in the quasi 2D Marquardt section has quite continuous resistivity values around $\rho \approx 20$ Ωm (cf. Fig. 4.18). This is due to the starting models, which were used for the 1D inversion. To obtain a continuous resistivity-depth section, a 1D Marquardt inversion is performed first for sounding A27 located furthest northeast. This derived model is then used as the starting model for the inversion of the data at sounding A28. By successive application, this causes the resistivity of the base layer to become continuous. This approach is only used for the quasi resistivity-depth section and not for the 1D models displayed in Fig. 4.17. Furthermore, it has to be noted that several soundings, particularly on the mudflat, are intentionally overfitted with $\chi \approx 0.5$. The fit of each sounding along the profile is displayed in Fig. 4.18(c). A value of $\chi = 0.5$ is used as threshold to terminate the inversion. This is done because a few soundings exhibit larger errors at late times. Since the late time apparent resistivity increase is continuous and consistent for all Tx-100 soundings, it seems evident even if larger data errors are partly present (see the $\rho_{a,lt}$ data section in Fig. 4.11(b)). Moreover, the $\rho_{a,lt}$ increase is certainly not a instrument bug because always both receiver polarities were measured and in good agreement. For comparison see section 4.5.2. However, to obtain also the models which are not overfitted, a threshold of $\chi \leq 1$ is used for the Marquardt equivalent modeling. Therefore, the equivalent models indeed reflect the model uncertainty with respect to the data errors. For a comparison, all 1D inversion results are given in the appendix. A.7.

Equivalent models and parameter importances
The resistivity of the base is not resolved very well between A40 and A*80. This is evident from the importances displayed in Fig. 4.18(d). According to the equivalent models in Fig. 4.17(a-e) the resistivity of the base layer varies between 1 and 100 Ωm within the equivalent bounds for most of the soundings. The layer interface is usually resolved well according to the importances. However, the importances do not reflect the non-linearity of the inverse problem and might be misleading. For example sounding A*61 (cf. Fig. 4.17(b)), where the base is deepest with around 100 m, exhibits a large equivalence range at the interface, although a value of 0.92 suggests a significant importance. The depth to the interface ranges from approximately $90 - 120$ m with resistivity bounds around $0.4 - 10$ Ωm. Moreover, the *doi* is just below the last layer interface.
This is the case for a few soundings. For a comparison with the other soundings, all 1D inversion results, including the equivalent models, are shown in the appendix. A.7.

Variation of the mudflat base for two soundings
The data and fitting for the above discussed models, A*61 and A*67, are plotted in Fig. 4.19(a,b). Since sounding A*61 exhibits large error-bars at late times, the poor resolution of the last layer is obvious for that sounding. The fitting for the Marquardt model (M1), shown in Fig. 4.17(b), is displayed as a red line. To verify the base, the last layer is removed and the data fit is calculated (M2, blue line). The fit is only slightly decreased ($\chi = 1.2$) compared to the best-fit model M1 ($\chi = 0.8$), where the

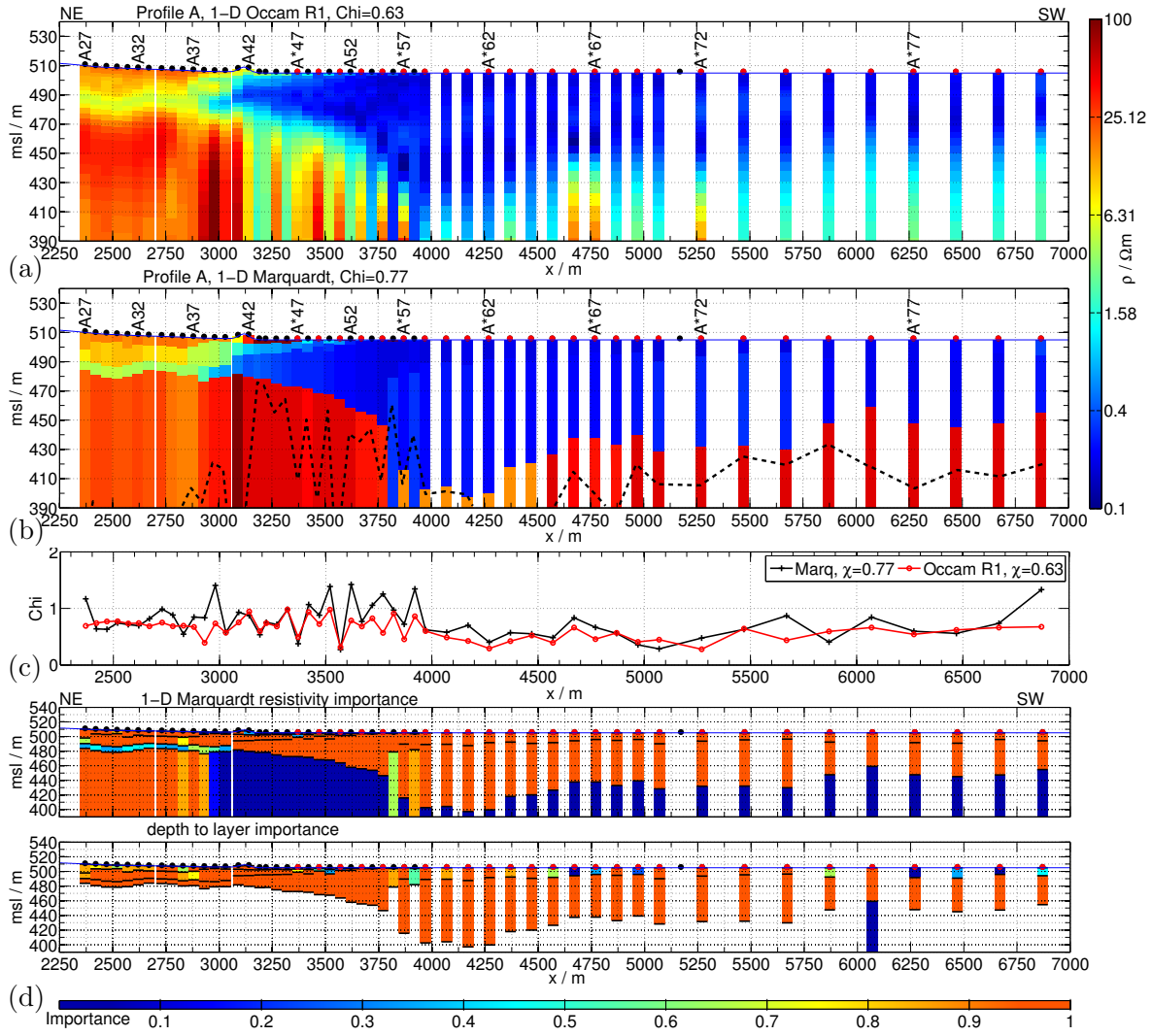

Figure 4.18: *1D inversion results stitched together as a quasi 2D section along profile A. (a) Occam R1 models, (b) Marquardt models. (c) Data fitting (χ) for each sounding along the profile for Occam and Marquardt. (d) Layer depth and resistivity importances plotted as a colorcoded section. The TEM Tx-50 sounding locations are marked as black dots above the model, whereas the Tx-100 locations are drawn red. The doi is denoted as a dashed line in (b).*

base layer is included. If the base layer depth is decreased from $z = 100$ m to 50 m, the fit significantly deteriorates (M3, magenta line). However, the fit remains almost same, if the base resistivity is increased from 0.6 Ωm to 100 Ωm (M4, green line). This shows the poor resolution of the resistivity. In contrast to sounding A*61, the data obtained at sounding A*67 (Fig. 4.19(b)) has quite small errors at late times and shows a strong $\rho_{a,lt}$ increase. The Marquardt model for sounding A*67 in Fig. 4.17(c) is varied in a similar way as done for sounding A*61. In each case (M2 to M4), the fit always significantly deteriorates. Particularly, if the base interface is removed the late time data is not fitted at all with $\chi \approx 5.5$. The effect becomes weaker, if the resistivity is increased from 2.2 Ωm to 100 Ωm. These two examples show that the base below the mudflat is in general evident.

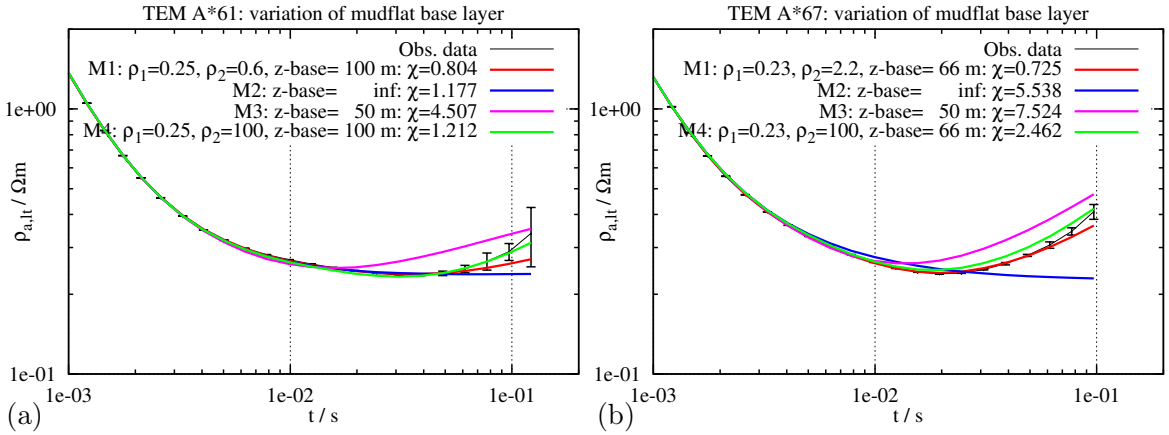

Figure 4.19: *Data (black) and fitting (M1,red) for the 1D Marquardt inversion results at (a) sounding A*61 and (b) sounding A*67. Calculated response for different variations of the base layer: base layer removed (M2,blue); the interface is decreased to $z = 50$ m depth (M3,magenta); base layer resistivity is increased to 100 Ωm (M4, green). The corresponding fit and parameter values are displayed in the legend.*

Short summary: southern part of profile A- mudflat base

Recalling the objectives stated in section 4.3, it can be noted that a resistivity increase is detected below the mudflat, which likely corresponds to the URC formation. The deepest part seems to be located between sounding A*57 and A*62. Since the base of the mudflat is not resolved similarly for all soundings, some uncertainties remain (as shown for sounding A*61). A few soundings exhibit larger errors at late times, which results in a large equivalence of the depth and resistivity of the base layer. In general, the majority of all equivalent models for each sounding show a resistivity increase. Due to the remaining uncertainties, the base of the mudflat is verified by a 2D forward modeling study, including all soundings, in section 5.6.

4.7.5 Shallow and deeper investigations along Profile B: Tx-50 and Tx-100 sounding data

The data obtained along profile B are analyzed in a similar manner as the data obtained along profile A, except that all Tx-50 and Tx-100 soundings are combined. In Fig. 4.20, 1D inversion results are displayed for five selected soundings along the profile. Except for sounding B07, all the other soundings in Fig. 4.20(b-e) are obtained with the Tx-100 setup. All five models indicate a resistive base layer in a depth range from $40 - 90$ m. Between sounding B*29 and B*46 the depth of the interface is increased from 40 m to around 80 m. Sounding B*46 also shows roughly a $20 - 30$ m thick and very low resistive layer above the base layer. Similar to the soundings discussed for profile A, the resistivity of the last layer is mostly not resolved very well. This yields quite low importances and a large resistivity equivalence. Sounding B*20 is an exception, where the resistivity importance of the last layer is larger with 0.64. The *doi* ranges between 70 m and 100 m for those models and coincides well with the depth, where the Occam models differ.

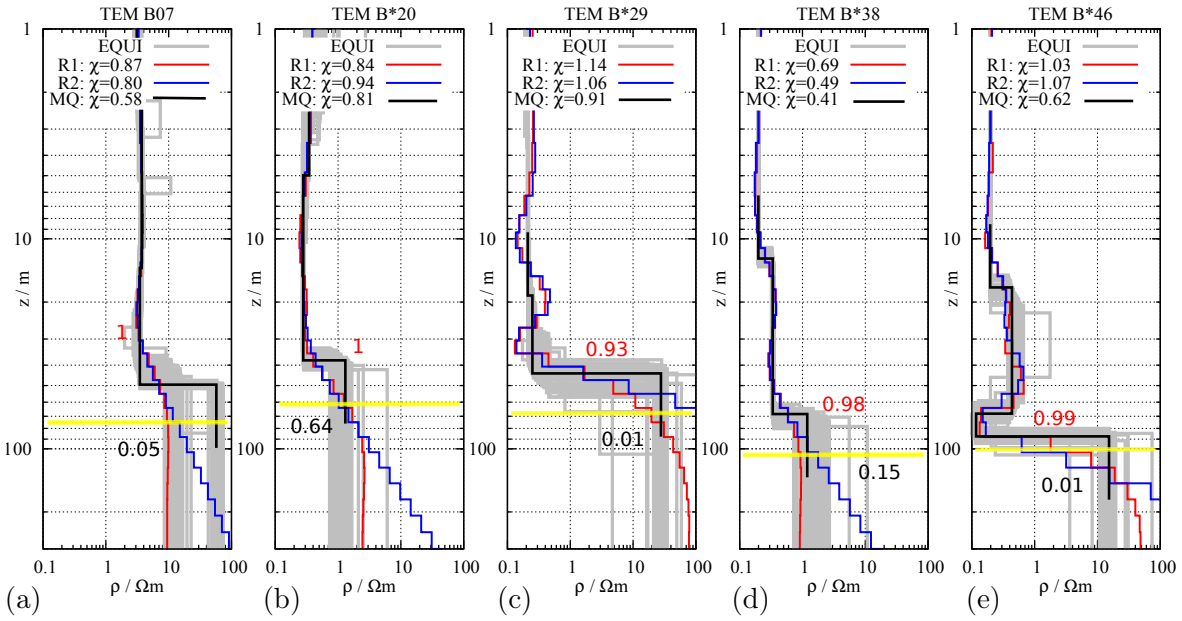

Figure 4.20: *1D inversion results for selected soundings (B07, B*20, B*29, B*38, B*46) obtained along profile B. Except B07 all soundings are obtained with the Tx-100 setup. The Marquardt models (MQ) are denoted in black and the Occam R1 and R2 in red and blue, respectively. The equivalent models (EQUI) are displayed in light gray. The doi after Spies [1989] is marked as a yellow line. The layer depth and resistivity importances are displayed in red and black, respectively. The χ value is given in the legend of each model.*

2D resistivity-depth sections

The quasi 2D stitched sections are displayed in Fig. 4.21(a,b). The Occam R1 and Marquardt sections match well. Note that sounding B08–B12 are shifted approximately 300 m towards the south of the profile (see the map in Fig. 4.2(a)). Therefore, the electrical subsurface structure can differ in that zone.

A resistive structure is present at depth in the northwestern part along profile B (see Fig. 4.21(a,b)). This obviously corresponds to the basalt layer, since the northern part of profile B is in direct vicinity to the basalt outcrops. However, according to the corresponding importances displayed in Fig. 4.21(d), the resistivity is not well resolved in that zone. The same is observed for sounding B07 in Fig. 4.20(a), where the resistivity varies from 10 to 100 Ωm within the equivalent bounds.

The transition zone to the high conductive mudflat clay sediments is present southeast of B10, resulting in a strong lateral resistivity decrease already at shallow depth. Between sounding B10 and B26 an interface is indicated by a slight resistivity increase in a depth range from roughly 20 to 40 m. However, in that zone only four soundings are recorded with the Tx-100 setup and only three of them (B*18, B*20 and B*25) indicate a significant increase of $\rho_{a,lt}$ at late times. Sounding B21 and B23, recorded with the Tx-50 setup indicate only a small $\rho_{a,lt}$ increase. For comparison, see the time derivative of $\rho_{a,lt}$, which is displayed in Fig. 4.13(b). For this reason, the interpretation of the shallow interface beneath sounding B21–B24 is uncertain. Most likely, it does not correspond to the base of the mudflat. However, the resistivity of the last layer is better resolved in that zone, than in other zones. The importances, displayed in Fig. 4.21(d), are larger than 0.5. The equivalent models calculated for sounding B*20 are shown in Fig. 4.20(b). They indicate resistivity bounds between 1 and 7 Ωm in that zone.

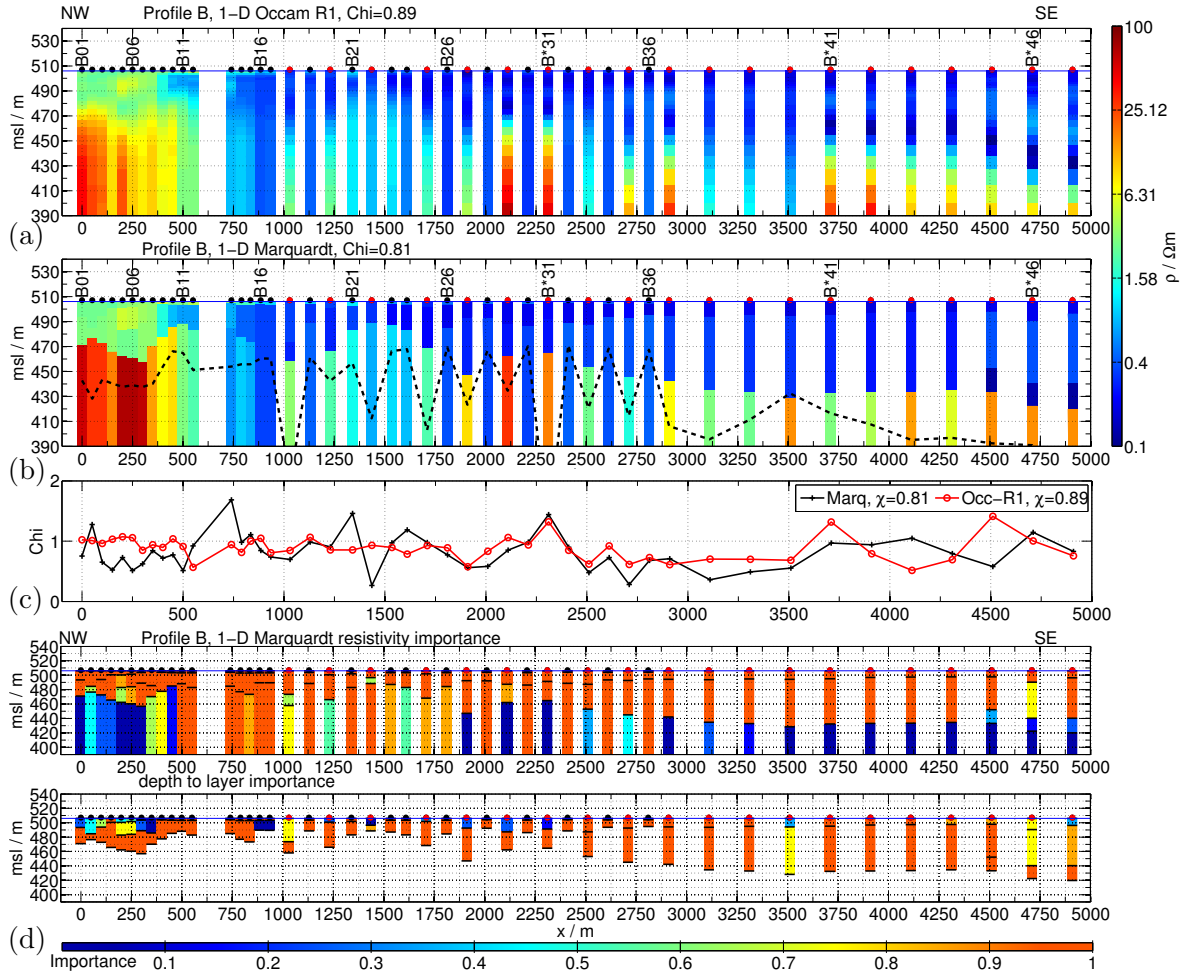

Figure 4.21: *1D inversion results stitched together as a quasi 2D section along profile B. (a) Occam R1 models, (b) Marquardt models. (c) Data fitting (χ) for each sounding along the profile for Occam and Marquardt. (d) Layer depth and resistivity importances plotted as a colorcoded section. The TEM Tx-50 sounding locations are marked as black dots above the model, whereas the Tx-100 locations are drawn red. The doi is denoted as a dashed line in (b).*

Between B*27 and B*47 the subsurface structure is less ambiguous. The depth of the base layer slopes downwards to approximately 80 m depth. The resistivity increase is evident for most of the soundings recorded with the Tx-100 setup. An exception are the soundings B*39 and B*40, where $\rho_{a,lt}$ shows only a slight increase. For comparison see the plot of $\partial_t \rho_{a,lt}$ in Fig. 4.13(b). However, southeast of B*27 the resistivity importances for the Tx-100 soundings are generally below 0.2. The resistivity equivalence of the last layer ranges between 1 and 100 Ωm for sounding B*29, B*38 and B*46, which are displayed in Fig. 4.20(c-e).

Variation of the mudflat base for two soundings

In order to investigate the effect of the last layer on the data fit, the second layer of the best-fit Marquardt models obtained at sounding B*20 and B*38 is extended to infinity. The calculated response is plotted in Fig. 4.22(a,b). Sounding B*20 shows a significant increase of $\rho_{a,lt}$ at late times. If the base layer is removed (M2, blue line), the fit deteriorates to $\chi \approx 5$, compared to the fit of the best-fit Marquardt model (M1, red line). In contrast to that, sounding B*38 does not show such a significant $\rho_{a,lt}$-increase,

due to larger errors at late times. However, the fitting deteriorates to $\chi \approx 1.8$, if the base layer is removed. This demonstrates exemplarily that a more resistive base layer is required to fit the late time data.

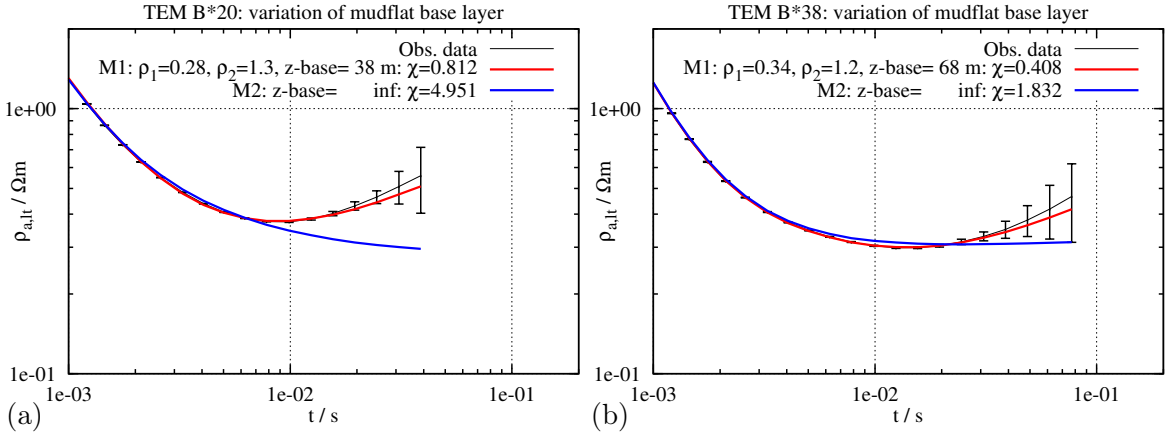

Figure 4.22: *Data (black) and fitting (M1,red) for the 1D Marquardt inversion results at (a) sounding B*20 and (b) sounding B*38. The blue line (M2) shows the calculated forward response, if the base layer is removed. The corresponding fit and parameter values are displayed in the legend.*

Short summary: profile B

The interpretation of profile B is not as obvious as for profile A. Particularly between B21and B24 a very shallow resistivity increase is detected, which is not clearly associated to the URC base. According to the geological map in Fig. 4.2(a) the Qaisiyeh fault is located at sounding B*18. Southeast of the Qaisiyeh fault the base is supposed to be lowered by 70 m [Ibrahim, 1996], which is in contradiction to the very shallow occurrence of the URC formation. Furthermore, from the 2D sections the fault position is not that clear, which is also due to a *doi* of roughly 40 m between B11 and B*18. However, in the northwestern part of profile B the resistivity increase at 30 m depth obviously corresponds to the basalt, which is in the direct vicinity. Southeast of sounding B26 the resistivity increase appears at roughly 30 m depth and slightly dips down towards sounding B*47. Obviously this corresponds to the URC chert limestone formation. Profile A and B cross each other at sounding A*72 and B*38, respectively. Both soundings match well. Due to a limited *doi* on the high conductive mudflat, the resistivity increase is not supported significantly by all Tx-100 soundings. Similar to profile A, a 2D modeling study is presented in section 5.6 to verify the base below the good conductor.

4.8 Integration of geophysical interpretation with the geological information

In order to provide a basis for a geological interpretation, the derived resistivity-depth sections are summarized and the already known geological, hydro-geological and lithological informations are integrated. The forthcoming interpretation does not claim to be complete but can be seen as a basis for further refinements.

The quasi 2D TEM resistivity-depth sections are displayed in Fig. 4.23(b,c) for both profiles. Here, only the sections derived by the 1D Marquardt models are presented. For comparison, a similar graphic is compiled in Fig. A.17 for the Occam sections. Furthermore, the geological cross-section discussed in section 4.2 is plotted in Fig. 4.23(a) for comparison with the resistivity-depth section of profile A. The major and well known geological formations are marked in both resistivity-depth sections and in the geological cross-section with the abbreviations defined in section 4.2. Secondary features, which have been found, are highlighted as well. The following conclusions are drawn from the resistivity-depth sections and the geological informations:

AOB The top of the Abed Olivine Phyric Basalt (AOB) is detected along both profiles in a depth range from approximately 20 to 40 m. The resistivity ranges mostly between 20 and 100 Ωm, although the upper bound is naturally not resolved that well by the TEM method.

AQ The buried basalt is covered along both profiles by sediments belonging to the AQ formation, which are generally clay rich. However, they are highly heterogeneous and may be intermixed with evaporates, sand, pieces of chert, limestone, basalt and gravel. The depth to the water table is variable. According to the well samples in Fig. 4.4(a) it is between 5 and 18 m in the northern part of profile A. It is possible that the shallow conductive zone denoted as S1 corresponds to a rise of the groundwater level. A similar conductivity increase is observed in the ERT models around x= 1100 m in Fig. 4.16(e).

AF Although the geological cross-section suggests that the basalt is interrupted at the Al Bayda fault (AF), it obviously continues towards southwest until $x \approx 4000$ m. That zone is denoted as S2. Here, the top of the resistor (basalt) drops down steeply by almost 50 m. This finding also suggests that the Al Bayda fault zone may extend over 700 m between A42 and A56, which was not clear from the prior geological information.

S3 According to the Occam resistivity-depth section, displayed in Fig. 4.16(a), the basalt seems to be interrupted at a depth of roughly 540 m above mean sea level marked as S3 along profile A. The interface is uncertain and denoted as a dashed line in Fig. 4.23(a). The 1D resistivity-depth models are displayed in Fig. A.4 in the appendix for sounding A12 and A25, which were re-investigated with the Tx-100 setup. Both models indicate that a good conductor appears between $z = 70 - 100$ m depth below the basalt.

QF The Qaisiyeh fault (QF) is expected to be located at $y = 1000$ m along profile B. However, no significant correlation with the electrical models is visible in that zone. Probably the QF is located at $x \approx 500$ m towards northwest and coincides with an interruption of the basalt. However, since the depth resolution of the electrical models is rather poor in that zone, the interpretation is uncertain.

ALM/AQ Thick sediment sequences, which belong to the Alluvial Mudflat formation (ALM) and the Azraq Quaternary formation (AQ), are deposited in the Qa Al Azraq mudflat. The water table is very shallow (less than a few meters below surface) and the groundwater is hyper saline (see section 4.2). These mostly soft-

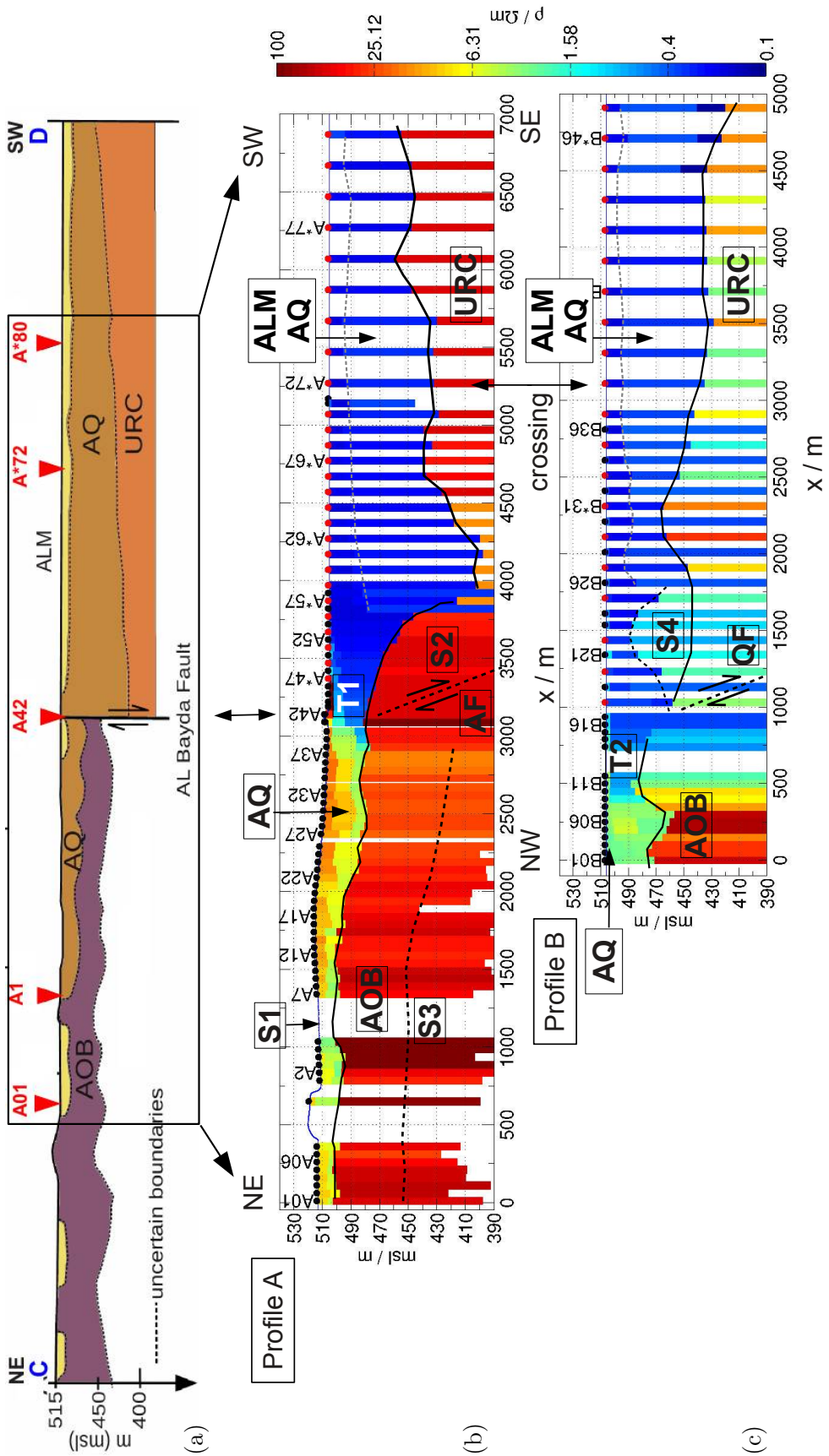

Figure 4.23: *(a) Geological cross-section modified after Ibrahim [1996], which is representative for profile A. Quasi 2D resistivity-depth sections for (b) profile A and (c) profile B derived from the 1D Marquardt models. Their locations are shown on the map in Fig. 4.2. All geological formations and features are labeled in the resistivity-depth sections. Uncertain boundaries are displayed as dashed lines in (b) and (c). Further information is given in the text.*

silty and hyper saline clay sediments show extremely low electrical resistivities around $0.2 - 0.5$ Ωm along both profiles.

T1/T2 The transition zone from fresh over brackish to saline groundwater occurs around T1 and T2 along profile A and B, respectively. Here the electrical resistivity drops significantly in lateral direction.

URC The Umm Rijam Chert Limestone (URC) is expected to be the base below the mudflat sediments. Along profile A, the depth to the URC is around 100 m at $x \approx 4000$ m and then decreases again towards southwest. The top of the base confirms the slope of the URC, which is sketched in the geological cross-section. Along profile B, the depth to the URC is uncertain between sounding B21–B24. Further southeast of B25 the base has a gentle slope and the depth increases to roughly 100 m.

For further comparison, a generalized lithological section and borehole data is compiled in Fig. A.2 and Fig. A.1, respectively. The locations of these boreholes are shown on the geological map in Fig. 4.2(a).

Layering inside mudflat

In some zones the conductive mudflat sediments (ALM/AQ) indicate a layering. The shallow resistivity contrast indicated by a dashed line around **S4** may correspond to such a layering instead of corresponding to the base of the mudflat (URC). However, the interpretation is ambiguous. According to the VES results of El-Waheidi et al. [1992] the upper part of the chert limestone base (URC formation) is less resistive at the northwestern boundary of the mudflat. They suggested that in some parts a mixing zone in the chert-limestone aquifer might cause the resistivity decrease. From this point of view the URC base might be only 10 to 15 m between sounding B21–B24, but saturated/intermixed with brackish to saline groundwater.
Most of the 1D inversion results indicate a slight and shallow interface inside the mudflat, particularly the soundings recorded with the Tx-50 configuration and in NT-mode. This interface is marked in Fig. 4.23(a,b) by a dashed gray line. Maybe the slight resistivity contrast corresponds to an interface of the ALM and AQ formations. It occurs roughly between $z = 10 - 20$ m depth and is deepest around A57 along profile A. Likewise, almost all soundings southeast of B26 indicate such a shallow resistivity contrast. For comparison, a compilation of 1D models obtained along both profiles is given in appendix A.7.

4.9 Conclusions from the 1D inversion results

A 7 km and a 5 km long transect were investigated along profile A and B, respectively. The derived 2D resistivity-depth sections are consistent and in good agreement with the geological information. Furthermore, they were correlated with lithological borehole data, which verifies the reliability of the models and also the used methods. Both profiles were analyzed in detail by model equivalence and parameter importances. The data fitting is generally good.

Four main geological formations were subject to the field survey, namely the basalt (AOB), the Quaternary sediments (AQ), the alluvial mudflat sediments (ALM) and the chert limestone basement (URC). Uncertain depth of geological boundaries were identified along both profiles. Particularly the depth down to the basalt layer is determined along profile A and in the northwestern part of profile B. The resistive basalt layer is obviously not interrupted at the Al Bayda fault and continues approximately 700 m below the mudflat sediments until sounding A56, where a strong decline of the resistor is present. This finding suggests that the Al Bayda fault zone extends over 700 m length and was not clear from the prior geological information. Furthermore, a resistivity increase below the mudflat sediments is detected along both profiles and verified exemplarily by 1D modeling studies, equivalent models and parameter importances. Most likely the resistivity increase corresponds to the URC base. The deepest part along profile A is around 100 m deep. Along profile B, the URC gently dips down towards the southeast and appears at a depth of roughly $90 - 100$ m at the last sounding location. The resistivity of the base layer is generally not resolved well below the high conductive mudflat. Furthermore, some soundings exhibit larger late time measurement errors, which leads to large equivalent bounds for the last layer. In order to support probable drilling projects within the CRC 806, the detection of the depth down to the URC base below the mudflat and the depth to the basalt layer were the main objectives. Although the investigation of the fresh to saline groundwater zone was no primary target, a shallow transition zone from moderate to very low resistivities was determined precisely along the profiles. This is known to be a mixing zone from freshwater bearing layers to the hyper saline clay sediments inside the mudflat. Azraq is heavily exploited for freshwater and the lateral extent and thickness of the saline water body in the basin center is of topical interest for the groundwater management.

At this point, the primary objectives of the geophysical survey are achieved. Although no clear distortion effects are visible in the TEM sounding data, the subsurface resistivity varies significantly along both investigated transects and it is questionable if the 1D interpretation is adequate. Moreover, some soundings using the Tx-100 configuration exhibit larger data errors at late transient times than other soundings. The base of the mudflat is not resolved well for those soundings, although the resistor at depth is generally indicated by an increase of the late time apparent resistivity data for all soundings. To validate the derived quasi 2D resistivity-depth sections, particularly the resistive mudflat base, the field data is interpreted by 2D forward modeling in chapter 5 and by a 2D inversion in chapter 6.

CHAPTER 5

Two-dimensional TEM forward modeling

In chapter 4, the TEM field data was interpreted by 1D layered earth models and the results were stitched together to quasi 2D resistivity-depth sections. These 2D sections are in good agreement with the geological information. According to Goldman et al. [1994], the conventional 1D interpretation of TEM field by a 1D layered earth model has proved to be feasible in many case studies. The TEM method has a superior depth-to-lateral investigation ratio and the current systems are prevalently focused under the transmitter loop [Spies & Frischknecht, 1991]. However, there are cases where the field data cannot be explained by 1D models and data distortion effects have to be considered [Newman et al., 1987; Goldman et al., 1994].

Although no clear distortion effects are visible in the TEM sounding data, the resistivity varies significantly along both investigated profiles and it is questionable, if a 1D interpretation is adequate. Therefore, in this chapter the obtained TEM data is additionally interpreted by means of 2D forward modeling. The objective of the 2D modeling study is to further investigate the validity of the derived quasi 2D resistivity-depth sections. At first a 2D subsurface model is constructed from the 1D models in the transition zone along profile A between sounding A27 and A71. The 1D Occam and Marquardt results derived from the Tx-50 soundings, are used as a basis for the 2D modeling. Different zones of the derived 2D models are varied to study the effect on the synthetic response characteristics and the data fitting. Subsequently, the Tx-100 soundings are included and 2D models are derived for both profiles. This study aims to investigate the more resistive base below the mudflat sediments. A 2D modeling study is performed by variation of the depth and resistivity of the base layer.
The forward modeling is based on the finite difference (FD) algorithm *SLDMem3t* [Druskin & Knizhnermann, 1988, 1994, 1999]. It allows the computation of transient EM fields in time domain in three dimensions and for arbitrary model parameterization. The code is well tested and has been applied to many case- and feasibility studies involving mainly forward modeling, e.g. Hördt et al. [1992], Hördt & Müller [2000], Goldman et al. [2011] and Sudha et al. [2011]. For a successful application of the *SLDMem3t*, aspects of the numerical algorithm have to be considered. Therefore, in the first part of this chapter a brief theoretical introduction to the *SLDMem3t* is given. To calculate the transient data, the construction of a suitable FD grid is required. This is a key issue which is addressed by an extended grid analysis in the subsequent sections.

Furthermore, a convenient approach to validate the grid and to derive numerical modeling errors is suggested. The *SLDMem3t* is also utilized as forward operator $\boldsymbol{F}(\boldsymbol{m})$ in the large scale inversion scheme *SINV* presented in chapter 6.

5.1 The *SLDMem3t* TDEM forward solver

Among the publications by the developers of the *SLDMem3t* [Druskin & Knizhnermann, 1988, 1994, 1999], the theory to the algorithm was briefly described by a few authors, e.g. Hördt et al. [1992]; Weidelt [2000]; Martin [2009]. In this section, I particularly refer to Martin [2009] as he analyzed the *SLDMem3t* performance in more detail. Furthermore, Weidelt [2000] provided a comparative study for numerical modeling of transient EM-fields and briefly explained the theory behind *SLDMem3t*. He concludes, that among the compared numerical modeling techniques, the latter was found to be very efficient. During the last decade a large progress has been made in the field of geo-electromagnetic modeling. For details on numerical modeling refer to the comprehensive reviews by Newman & Commer [2005]; Avdeev [2005]; Börner [2010].

For the theoretical description of the *SLDMem3t*, Maxwell's equations formulated in section 2.2 are required in differential form. Ampère's and Faraday's law in the quasi-static approximation read:

$$\nabla \times \boldsymbol{B} = \mu_0(\sigma \boldsymbol{E} + \boldsymbol{j}^e) \tag{5.1}$$

$$\nabla \times \boldsymbol{E} = -\partial_t \boldsymbol{B} \tag{5.2}$$

The basic induction equation is derived by taking the *curl* of Faraday's law and substitution of $\nabla \times \boldsymbol{B}$ with Ampère's law:

$$\nabla \times \nabla \times \boldsymbol{E} + \mu_0 \sigma \partial_t \boldsymbol{E} = -\mu_0 \partial_t \boldsymbol{j}^e, \tag{5.3}$$

where $\boldsymbol{j}^e$ denotes the external current density before source-field switch-off ($t = 0$). An equivalent equation can be derived for the evolution of $\boldsymbol{B}$ by substitution of $\boldsymbol{E}$ in Maxwell's equations.
In order to solve equation 5.3 in three dimensions, the EM-fields are sampled on a Yee-Lebedev staggered grid [Yee, 1966]. A Yee-cell is shown in Fig. 5.1(a). The $\boldsymbol{E}$-field components are obtained along the edges of each cell and are edge-averaged. Within *SLDMem3t*, the associated $\partial_t \boldsymbol{B}$-field components are obtained on faces by taking the *curl* of $\boldsymbol{E}$. The $\partial_t \boldsymbol{B}$-field components are face averaged. As a consequence, non of the field components are sampled at the same locations.
On the one hand the discretization on a regular grid by a finite difference (FD) approach is numerically easy to implement. On the other hand, complex geometries are difficult to realize, as it is possible on unstructured grids used in finite element (FE) methods.

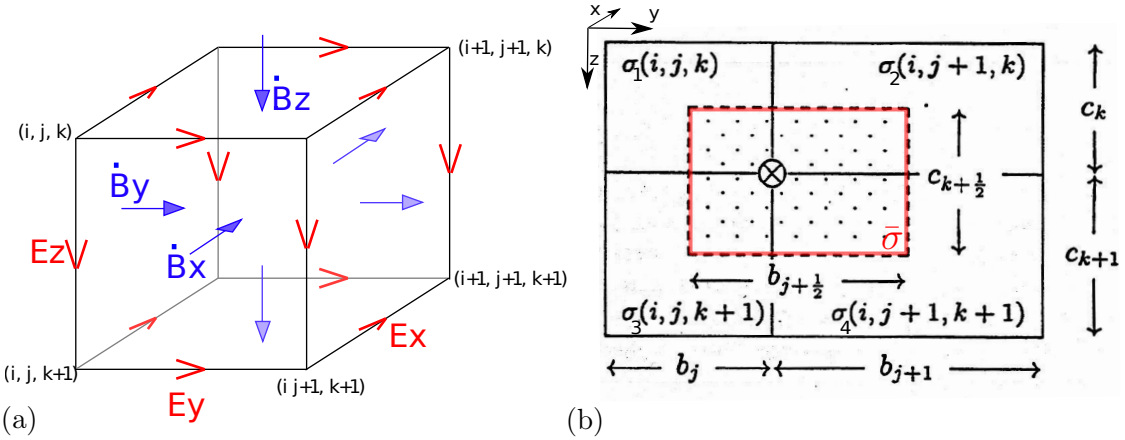

Figure 5.1: *(a) Yee-cell on which the EM-field components are sampled (after Martin [2009]). (b) Geometry for the material averaging scheme. The averaging area $\bar{\sigma}$ is hemmed red and the field component is obtained at $\otimes$ [Weidelt, 2000].*

5.1.1 Material averaging

Usually the conductivity σ_i is assigned directly to each cell within an FD or FE scheme, resulting in as many σ_i as cells used for the discretization. Within *SLDMem3t*, a material averaging scheme is implemented, which is displayed as a 2D simplification in Fig. 5.1(b). The red boxed prism exhibits the arithmetic average $\bar{\sigma}(i, j + 1/2, k + 1/2)$ of the adjacent cells (σ_1 to σ_4). The prism has the size of $a_i \times b_{j+1/2} \times c_{k+1/2}$ and is centered at the location marked as $\otimes$, where the x-component of the electric field $E_x(i, j+1/2, k+1/2)$ is calculated. By throughout application of this scheme, the conductivity discretization becomes independent from the FD grid and arbitrary model discretization are theoretically possible. Since the conductivity distribution is assigned internally to the underlaying Yee-grid, in practice *SLDMem3t* is subject to the same restrictions regarding model complexity as common FD schemes.
It should be noted that it is not possible to visualize the effective conductivity distribution for the complete model and all field components, because the prism areas for which each average conductivity $\bar{\sigma}$ is obtained are overlapping. Nevertheless, the effective conductivity for each node (edge or face center) can be displayed separately. An example is shown for the E_x component in section 5.3.5.

5.1.2 Boundary conditions

Except at the earth-air interface, homogeneous Dirichlet conditions are imposed on the boundary $\partial\Omega$ of the modeling domain Ω, i.e. the tangential electric field is zero:

$$\boldsymbol{n} \times \boldsymbol{E} = 0. \tag{5.4}$$

This implies that the electric field is perpendicular on $\partial\Omega$ and the perfect conducting boundary serves as a magnetic insulator, with:

$$\boldsymbol{n} \cdot \boldsymbol{B} = 0, \tag{5.5}$$

where $\boldsymbol{B}$ is parallel on $\partial\Omega$. Such a simple boundary condition may introduce errors if $\partial\Omega$ is not placed several skin depth away from the source $\boldsymbol{j}^e$ [Börner, 2010]. At the earth-air interface ($z = 0$) Dirichlet boundary conditions of the form

$$\boldsymbol{n} \cdot \boldsymbol{E} = 0 \tag{5.6}$$

are imposed, which enforces that current cannot leak into free space. However, a problem arises at the earth-air interface from the FD formulation. It requires that the EM-fields are calculated in free space to obtain the desired fields at the surface $z = 0$. The field components $E_{x,y}$ are obtained at $z = 0$, whereas the corresponding $B_{y,x}$ would be located at $-c1/2$, which is half a grid spacing in free space. Therefore, $B_{y,x}$ at $-c1/2$ are expressed in terms of the electric field:

$$\partial_t B_y(x_0, y_0, -c1/2) = \partial_x E_z(x_0, y_0, -c1/2) - \partial_z E_x(x_0, y_0, -c1/2) \tag{5.7}$$

$$\partial_t B_x(x_0, y_0, -c1/2) = \partial_y E_z(x_0, y_0, -c1/2) - \partial_z E_y(x_0, y_0, -c1/2). \tag{5.8}$$

The left hand side of equation (5.7) and (5.8) are obtained using an exact integral boundary condition, for which only the electric field components E_x/E_y calculated at $z = 0$ are required. For further explanations refer to Weidelt [2000] and Druskin & Knizhnermann [1988, 1994].

5.1.3 Initial conditions

The external current density, i.e. source term, for a step excitation is:

$$\boldsymbol{j}^e(t) = \boldsymbol{j}^e(t) \cdot \Theta(-t), \tag{5.9}$$

where $\Theta(-t)$ denotes the Heavi-side or boxcar function. The initial condition for a current switch-off is derived by substituting the source term into equation (5.1) directly before switch-off t_0^- and after t_0^+:

$$\frac{1}{\cancel{\mu_0\sigma}}\cancel{\nabla \times \boldsymbol{B}(t_0^-)} - \boldsymbol{E}(t_0^-) - \frac{1}{\sigma}\boldsymbol{j}^e(t_0^-) = \frac{1}{\cancel{\mu_0\sigma}}\cancel{\nabla \times \boldsymbol{B}(t_0^+)} - \boldsymbol{E}(t_0^+) - \frac{1}{\sigma}\boldsymbol{j}^e(t_0^+), \tag{5.10}$$

where $\boldsymbol{j}^e(t_0^+)$ is by definition zero, due to the source switch-off. After Weidelt [2000] both induction terms ($\nabla \times \boldsymbol{B}(t_0^+)$ and $\nabla \times \boldsymbol{B}(t_0^-)$) are negligible to a first approximation and the initial condition for the electric field at time $t = 0$ is:

$$\boldsymbol{E}^{s.off}(t_0^+) = \boldsymbol{E}(t_0^-) + \frac{1}{\sigma}\boldsymbol{j}^e(t_0^-), \tag{5.11}$$

where $\boldsymbol{E}^{s.off}(t_0^+) = \boldsymbol{E}(t_0^+)$ is the electric field after and $\boldsymbol{E}(t_0^-)$ directly before current switch-off. $\boldsymbol{E}(t_0^-)$ is the direct current field $\boldsymbol{E}^{DC}$. The second term on the right hand side denotes the source term before switch-off. For a current switch-on at time $t = 0$ the DC-field is zero directly before (t_0^-) and after switching (t_0^+). From equation (5.10) the initial condition for a switch-on is:

$$\boldsymbol{E}^{s.on}(t_0^+) = -\frac{1}{\sigma}\boldsymbol{j}^e(t_0^+), \tag{5.12}$$

where $\boldsymbol{E}^{s.on}(t_0^+) = \boldsymbol{E}(t_0^+)$. The source-term $\frac{1}{\sigma}\boldsymbol{j}^e(t_0^+)$ in equation (5.11) and (5.12) is equivalent for switch-off and switch-on. Hence the relationship is:

$$\boldsymbol{E}^{s.off} = \boldsymbol{E}^{DC} - \boldsymbol{E}^{s.on}. \tag{5.13}$$

A direct current field $\boldsymbol{E}^{DC}$ only exists for galvanic-inductive sources, like a grounded dipole. For a purely inductive source, like a non-grounded wire-loop, $\boldsymbol{E}^{DC}$ is zero and the switch-off field

$$\boldsymbol{E}^{s.off} = \frac{1}{\sigma}\boldsymbol{j}^e(t_0^+) \tag{5.14}$$

is equivalent to the switch-on field, except for a sign ($\boldsymbol{E}^{s.off} = -\boldsymbol{E}^{s.on}$). The fields calculated with the *SLDMem3t* are either for current switch-off or switch-on. As described in section 2.3, usually switch-off is used for inductive sources.

5.1.4 The system matrix

In the FD formulation the $\nabla \times \nabla\times$-operator in the basic equation (5.3) is discretized into the system matrix $\boldsymbol{A}$. The discrete formulation of the finite difference operators working on the node and edge field values are given in Druskin & Knizhnermann [1994]. The discrete analogue of the basic equation (5.3) for a current switch-off reads:

$$\boldsymbol{A}\boldsymbol{f} + \partial_t \boldsymbol{f} = 0 \quad t > 0, \quad \boldsymbol{f}(t_0^+) = \boldsymbol{f}_0. \tag{5.15}$$

Where $\boldsymbol{f} \in \mathbb{R}^N$ is a vector containing all electric field components $\boldsymbol{E}$ sampled on the Yee-grid and $\boldsymbol{f}_0$ denotes the initial condition $\boldsymbol{E}^{s.off}(t_0^+)$ in equation (5.14). The number of non-trivial field components within the domain Ω is:

$$N = (n_x - 1)n_y n_z + n_x(n_y - 1)nz + (n_x - 1)(n_y - 1)nz \approx 3 \cdot n_x n_y n_z. \tag{5.16}$$

The vanishing (and therefore trivial) field components at the perfect conducting boundaries are excluded from $\boldsymbol{f}$. The system matrix $\boldsymbol{A} \in \mathbb{R}^{N\times N}$ connects the electrical field components and since the Yee-scheme is used it has the following attributes:

1. $\boldsymbol{A}$ is symmetric due to the self-adjoint $\nabla \times \nabla\times$-operator. Hence $\boldsymbol{A} = \boldsymbol{A}^T$.

2. $\boldsymbol{A}$ is positive definite, which implies that the eigenvalues are non-negative and the eigenvectors of $\boldsymbol{A}$ are linear independent. Therefore $\boldsymbol{A}$ is diagonalizable.

3. $\boldsymbol{A}$ is high dimensional ($dim(\boldsymbol{A})$ =column-rank = row-rank = N)

4. $\boldsymbol{A}$ is sparse and has at most 13 entries per row (or column). These much elements are needed to calculate one component of the discretized $\nabla \times \nabla\times$-operator on a Yee-grid inside the domain Ω. The field components, which are required to solve equation equation (5.15) e.g. for one edge averaged electric field component e_x are displayed in Fig. 5.2.

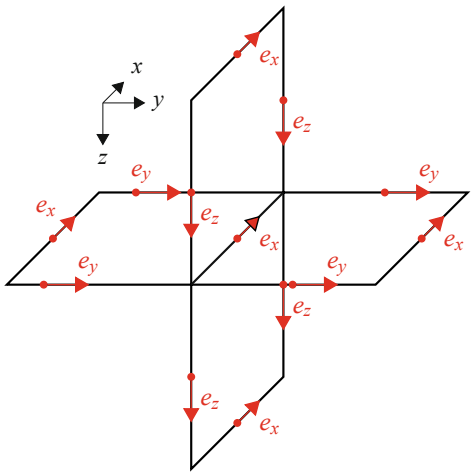

Figure 5.2: *Components of the electric field required for calculation of one element of the* $\nabla \times \nabla \times$*-operator [Börner, 2010].*

Equation (5.15) is an ordinary differential equation with $\boldsymbol{A}$ as a linear coefficient matrix and the exact solution reads:

$$\begin{aligned} \boldsymbol{f}(t) &= \exp(-t\boldsymbol{A})\boldsymbol{f}_0 \\ &= \sum_{m=0}^{\infty} \frac{1}{m!}(-t\boldsymbol{A})^m \boldsymbol{f}_0. \end{aligned} \tag{5.17}$$

The problem is that a direct evaluation of the matrix-exponential as proposed in equation (5.17) is not feasible [Börner, 2010]. Due to the above listed attributes of the system matrix $\boldsymbol{A}$, the following relations are valid [Saad, 2000]:

$$\begin{aligned} \boldsymbol{A} &= \boldsymbol{\phi}\Lambda\boldsymbol{\phi}^{-1} \qquad\qquad \text{with:} \quad \boldsymbol{\phi}^{-1} = \boldsymbol{\phi}^T \\ \exp(\boldsymbol{\phi}\Lambda\boldsymbol{\phi}^T) &= \boldsymbol{\phi}\exp(\Lambda)\boldsymbol{\phi}^T. \end{aligned} \tag{5.18}$$

Where the matrices Λ and $\boldsymbol{\phi}$ contain the eigenvalues λ_n and eigenvectors ϕ_n of the system matrix $\boldsymbol{A}$, respectively. The evaluation of the matrix exponential can be carried out by substitution of equation (5.18) into equation (5.17):

$$\begin{aligned} \boldsymbol{f}(t) &= \boldsymbol{\phi}\exp(-\Lambda t)\boldsymbol{\phi}^T\boldsymbol{f}_0 \\ &= \sum_{n=1}^{N} (\boldsymbol{\phi}_n^T \boldsymbol{f}_o)\boldsymbol{\phi}_n \exp(-\lambda_n t). \end{aligned} \tag{5.19}$$

Again the problem remains, that the direct computation of the eigenvalues and eigenvectors for the high dimensional matrix $\boldsymbol{A}$ is prohibitively expensive [Druskin & Knizhnermann, 1999].

5.1.5 The Lanczos method

The series of matrix products $(\boldsymbol{f}_0, \boldsymbol{A}\boldsymbol{f}_0, \boldsymbol{A}^2\boldsymbol{f}_0, \dots)$ in equation (5.17) motivates another formulation [Börner, 2010]. The solution is obtained in an M-dimensional subspace of

the N-dimensional solution space spanned by $\boldsymbol{A}$ and $\boldsymbol{f}_0$. The subspace $\mathcal{K}_M$ is spanned by the Krylov Vectors:

$$\mathcal{K}_M(\boldsymbol{A}, \boldsymbol{f}_0) := \{\boldsymbol{f}_0, \boldsymbol{A}\boldsymbol{f}_0, \boldsymbol{A}^2\boldsymbol{f}_0, \ldots, \boldsymbol{A}^{M-1}\boldsymbol{f}_0\}. \tag{5.20}$$

The accuracy of the approximate solution of equation (5.17) is dependent on the Krylov subspace dimension M. An orthonormal basis (ONB) $\boldsymbol{V}_M := \{\boldsymbol{v}_i, \ldots, \boldsymbol{v}_M\} \in \mathbb{R}^{N\times M}$ of the Krylov subspace $\mathcal{K}_M$ is obtained by the Lanczos process, which is based on the recurrence relation:

$$\begin{aligned} \boldsymbol{A}\boldsymbol{v}_i =& \boldsymbol{v}_{i-1}\beta_{i-1} + \boldsymbol{v}_i\alpha_i + \boldsymbol{v}_{i+1}\beta_i \\ &\text{with:} \quad \beta_0\boldsymbol{v}_0 = 0, \quad \boldsymbol{v}_1 = \boldsymbol{f}_0/\|\boldsymbol{f}_0\| \\ &\text{and:} \quad \alpha_i = \boldsymbol{v}_i^T\boldsymbol{A}\boldsymbol{v}_i, \quad \beta_i = \|\boldsymbol{A}\boldsymbol{v}_i - \alpha_i\boldsymbol{v}_i - \beta_{i-1}\boldsymbol{v}_{i-1}\|. \end{aligned} \tag{5.21}$$

In each iteration $i \leq M$ of the Lanczos process one ONB-vector $\boldsymbol{v}_i$ is obtained. In matrix-vector notation equation (5.21) reads:

$$\boldsymbol{A}\boldsymbol{V}_M = \boldsymbol{V}_M\boldsymbol{T}_M + R_M, \tag{5.22}$$

where $\boldsymbol{T}_M \in \mathbb{R}^{M\times M}$ is a tridiagonal matrix. In other words, neglecting the remainder R_M, $\boldsymbol{A}$ is compressed by $\boldsymbol{T}_M \approx \boldsymbol{V}_M\boldsymbol{A}_M\boldsymbol{V}_M^T$ and the initial vector $\boldsymbol{f}_0$ is compressed by $\tilde{\boldsymbol{f}}_0 = \boldsymbol{V}_M^T\boldsymbol{f}_0 \in \mathbb{R}^M$ [Börner, 2010]. Substituting $\boldsymbol{A}$, equation (5.15) is reduced to a much simpler M-dimensional tridiagonal problem:

$$\begin{aligned} & \boldsymbol{V}_M\boldsymbol{T}_M\boldsymbol{V}_M^T\boldsymbol{f}(t) + \partial_t\boldsymbol{f}(t) = 0, && \boldsymbol{f}_0(t_0^+) \\ \xrightarrow{\boldsymbol{V}_M^T\cdot} \quad & \underbrace{\boldsymbol{V}_M^T\boldsymbol{V}_M}_{=\boldsymbol{I}}\boldsymbol{T}_M\boldsymbol{V}_M^T\boldsymbol{f}(t) + \partial_t\boldsymbol{V}_M^T\boldsymbol{f}(t) = 0, && \boldsymbol{V}_M^T\boldsymbol{f}_0(t_0^+) \\ \Longrightarrow \quad & \boldsymbol{T}_M\tilde{\boldsymbol{f}}(t) + \partial_t\tilde{\boldsymbol{f}}(t) = 0, && \tilde{\boldsymbol{f}}_0(t_0^+). \end{aligned} \tag{5.23}$$

The solution vector $\tilde{\boldsymbol{f}}(t)$ is obtained in the low-dimensional Krylov subspace $\mathcal{K}_M$ by calculating the eigenvectors $\boldsymbol{s}_M$ and eigenvalues θ_M of $\boldsymbol{T}_M$ and solving equation (5.19) for $\tilde{\boldsymbol{f}}(t)$. Finally the solution is transformed to original N-space by:

$$\boldsymbol{f}(t) = \boldsymbol{V}_M\tilde{\boldsymbol{f}}(t) = \boldsymbol{V}_M\exp(-t\boldsymbol{T}_M)\boldsymbol{V}_M^T\boldsymbol{f}_0. \tag{5.24}$$

The time steps can be chosen arbitrarily, since no discretization in time is necessary and the same matrices $\boldsymbol{V}_M$ and $\boldsymbol{T}_M$ are used for each time step [Börner, 2010]. Time domain electromagnetic (TDEM) solvers which use a time stepping scheme, require sufficiently small time steps to obtain an accurate solution. For large time ranges over several decades, which is usually the case in TDEM, cause time stepping FD-TDEM or FE-TDEM algorithms to be more cost expensive than the *SLDMem3t*.

5.1.6 Computational load, convergence and error sources

Throughout the $MS = M$ iterations of the Lanczos-process within *SLDMem3t*, the solution is obtained in the Krylov subspace $\mathcal{K}_M$. In each iteration it is transformed to the original space only for the last time point t_{max} at a specified control receiver.

Druskin & Knizhnermann [1994] showed that the subspace dimension MS should be at least

$$MS \gg \frac{4}{\Delta_{min}} \sqrt{\frac{t_{max}}{\mu_0 \sigma_{min}}}. \tag{5.25}$$

Where Δ_{min} is the minimum grid spacing used for the FD approximation. For large t_{max} and low conductivity σ_{min} the required dimension MS increases significantly. In general, the maximum required iterations exceed this bound because the orthogonality of the eigenvectors $\boldsymbol{v}_i$ break down. The computational load increases with $\sqrt{t}$ and more iterations MS are required to obtain an accurate late time response. The evolution and convergence of a test solution for each subspace iteration/dimension MS is shown subsequently in section 5.3.6.
The computational load depends on the dimension of the system matrix $\boldsymbol{A}$ and the dimension of the Krylov subspace MS. But, the storage of the components $\boldsymbol{V}_M$ is only required for those nodes where the field is to be computed. Therefore, if all three E-field components are calculated in the complete modeling domain Ω, the total memory/storage is:

$$\text{RAM} \approx MS \times 3 \times n_x \times n_y \times n_z \times 8 \text{ Byte}. \tag{5.26}$$

For the 2D inversion in chapter 6, the memory is calculated according to equation (5.26) since the electric field is computed in the whole spatial domain Ω. For a relatively fine discretization (e.g. $n_x = n_y = n_z = 60$) and large MS (e.g. $MS = 12000$), the storage requirements are immense with around 58 GB. On the contrary, for only one desired field component (for example E_x) the required storage is simply $1 \times MS \times 8$ Byte. To reduce the dependency of the storage requirements with MS, Eiermann & Ernst [2006] proposed a restarted Krylov subspace algorithm, which uses a fixed subspace dimension $M = MS$. They update only the most recent approximation $\boldsymbol{v}_{i=M}$ and discard all basis vectors except the last.
Very often a systematic deviation for early times is observed for *SLDMem3t* calculations. After Weidelt [2000], these deviations originate from an inaccurate initial field computed by the exact integral boundary condition at the earth-air interface. Another source of systematic errors is of course an insufficient discretization of the $\nabla \times \nabla \times$-operator. The error-sources are analyzed in detail in section 5.3.

5.2 Parameterization of the model

Usually FD or FE modeling grids coincide with the forward calculation grid and the complexity of the model geometry is restricted to the grid discretization. The material averaging scheme implemented in *SLDMem3t* allows practically for arbitrary model parameterization, which is independent from the calculation grid. The model is parameterized by defining three dimensional rectangular blocks and assigning the resistivity. The size and location of these blocks may be arbitrary. If 2D structures are modeled, the blocks are extended to infinity along the strike direction. Complex structures are approximated by a large number of blocks, often resulting in several ten thousands. Examples of quite complex models are given by Goldman et al. [2011] for a sub-marine

model and by Commer et al. [2005] for topographic models. For further details on building a model, refer to Druskin & Knizhnermann [2000]. It has to be noted that complex resistivity distributions require a sufficient grid discretization. Otherwise they are averaged out by the material averaging scheme. From that point of view, the model parameterization should be chosen according to the grid of the forward calculation and/or vice versa.

5.3 *SLDMem3t* extended grid analysis

Zhdanov & Varentsov [1997] stated that it is particularly important to control the accuracy of a numerical solution. In order to validate the accuracy of the *SLDMem3t* solution and define criteria for the grid selection, the numerical solution is generally compared with the semi-analytical solution for a 1D model. Martin [2009] performed an elaborate grid analyses for the *SLDMem3t*. The grid is designed by using the automatic grid generator *make_ sldm_ grid*. Guidelines for the grid generation especially for *SLDMem3t* are also found in Hördt et al. [1992]. The crucial point in using *SLDMem3t* is to design an appropriate calculation grid on which the electric field values $\boldsymbol{E}$ (and $\dot{\boldsymbol{B}}$) are calculated and the transient data is obtained. A few aspects are considerably important, to guarantee sufficient forward modeling results:

1. Martin [2009] has analyzed different calculation grids briefly and suggested a logarithmically spaced grid in all three spatial directions, which originates from the transmitter. Further details are given in section 5.3.1.

2. The grid should guarantee an accurate solution for a specified time range and model resistivity distribution. If solutions are calculated for time ranges longer than three decades, a multi-grid approach should be used by splitting the time range (details in section 5.3.2). Otherwise the solution may become inaccurate at late transient times.

3. The possibility of defining arbitrary resistivity distributions, can be misleading. Therefore, the grid should be related to the model, otherwise resistivity structures are averaged out within the material averaging scheme. Model boundaries are considered precisely only if the grid is sufficiently fine around those. A very fine discretized model parameterization and a very coarse spatial grid discretization in a region of interest is meaningless. In order to guarantee sufficient discretization, often a mixed logarithmic-linear grid has to be designed or additional grid lines are included around model boundaries. Further details in section 5.3.5.

4. The computation time and storage/memory-requirements in terms of *RAM* should be reasonable, especially if the *SLDMem3t* is implemented in an inverse modeling scheme using several source fields. For only a few "trial and error" runs or a systematical preliminary study, the computational requirements are rather irrelevant. A very fine discretized grid does not guarantee the most accurate solution, but will increase the computational costs significantly. Refer to section 5.3.3 and section 5.1.6.

5. Depending on the resistivity distribution, the grid should hold for a wide resistivity range. This is particularly important in an iterative inversion scheme. Hördt & Müller [2000] suggested to keep the ratio of resistivity contrasts less than 1/100, which is not guaranteed in an automatic inversion scheme. As shown further below in section 5.3.4, even larger contrasts can be modeled. A drawback is that the resulting transients are often less accurate.

6. The accuracy of the numerical solution should be checked and considered when a quantitative data-fit is estimated. In this thesis, only grids with a maximum numerical or systematical error less than 2% compared with a 1D analytical solution are used. Details are given in section 5.3.7.

If the resistivity varies laterally strong for different zones within the model, it is necessary to design and validate the calculation grid for each zone separately. The quasi 2D resistivity depth sections derived from the field data presented in section 4.7 indicate different major zones: a) the basaltic or AQ formation, which exhibits a resistivity range between $\rho \approx 4 - 100$ Ωm, b) the transition zone with resistivities varying from $\rho \approx 0.3 - 50$ Ωm and c) the mudflat zone with resistivities around $\rho \approx 0.3$ Ωm. Therefore, the grids are designed and validated for each zone considering the above stated criteria.

5.3.1 Spatial grid discretization

As shown in Fig. 5.3, a transmitter is always set up by superposition of several bipoles, which are located on the edges between adjacent grid lines. As a result, it is possible to define tilted transmitters as suggested by Hördt et al. [1992], or even very complex shaped transmitters as a Marine Circular Electric Dipole, which consists of 8 arms distributed around a central electrode [Haroon et al., 2013]. In general the grid is always designed according to the transmitter. For the central loop configuration shown in Fig. 5.3(a,b) the grid lines are distributed symmetrically around the transmitter and $\dot{B}_z$ is obtained in the center between adjacent grid lines. Furthermore, they are distributed logarithmically in Fig. 5.3. The logarithmic distribution of grid lines seems most appropriate, due to the exponential decay of the diffusive EM-fields. The skin depth δ_{FD} introduced in equation (2.9) is derived from the EM wave number k and is therefore the major criteria for the grid design. In explanation, at late times the EM-field exhibits a larger wave number k and a coarse grid is sufficient, whereas at early times k is small. A linear grid discretization is not feasible, because it leads to far more grid lines than actually needed to satisfy the perfect conductor EM boundary conditions at infinite space. To avoid too many grid lines, the grid spreads logarithmically inward, outward and downward from the transmitter (see Fig. 5.3) according to the minimum and maximum skin depth. Hördt et al. [1992] suggested

$$\delta_{FD}^{min*} = \frac{1}{3} \cdot \sqrt{\frac{t_{min}\rho_{min}}{\pi\mu_0}} \qquad \text{and} \qquad \delta_{FD}^{max*} = 3 \cdot \sqrt{\frac{t_{max}\rho_{max}}{\pi\mu_0}} \tag{5.27}$$

as the minimum and maximum grid spacing range, respectively. According to equation (5.27), the grid is always designed (a) for the particular transmitter configuration, (b) the resistivity range of a defined model and (c) the required time range of a solution.

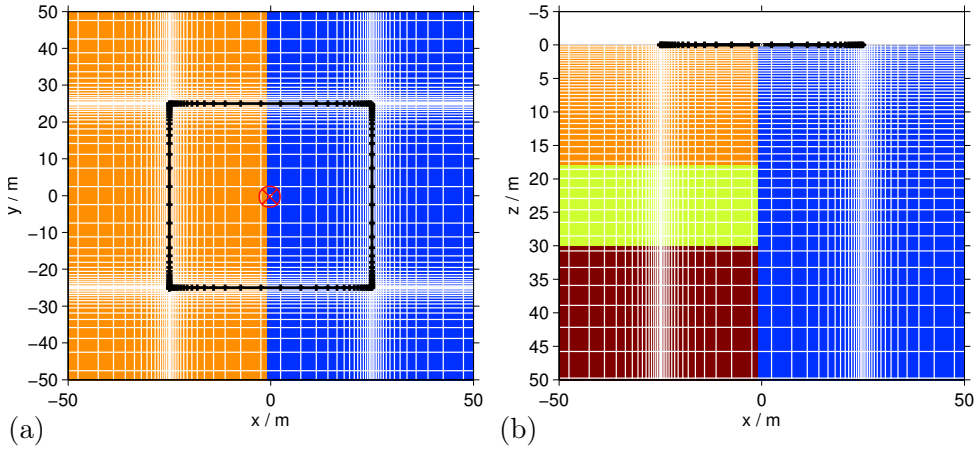

Figure 5.3: *(a) xy-plane view and (b) xz-plane view of the grid and model around the rectangular Tx-50 transmitter. The transmitter is denoted as a black crossed line. The $\dot{B}_z$ (or $U_{ind,z}$) receiver is located at $\otimes$ in (a). The grid is displayed white and the underlaying model is drawn colored-coded in the background.*

Other criteria for spatial grid discretization

Another important criteria is the number of grid lines used. How to determine suitable values for n_x, n_y and n_z is described subsequently in section 5.3.3. Furthermore, additional grid lines may be necessary to either better reflect the model structure or to allow the calculation of certain receiver positions. The latter can also be done by interpolation to a certain position from several other receivers. Since the EM-fields are non-linear in space, it is more accurate to avoid interpolation and include grid-lines at positions, where the solution is required.
Furthermore, the grid lines do not coincide with the model boundaries, neither lateral nor vertical. When checking the grid accuracy against 1D analytical solutions the latter can cause a systematical error. For large deviations additional grid lines have to be incorporated.

5.3.2 Overlapping multi-grids for large time ranges

As stated earlier in section 5.1.6, the MS Krylov subspaces which are required to obtain an accurate solution increase with $\sqrt{t}$. Therefore, Hördt et al. [1992] suggested to use a maximum of three decades for the time range of the grid, because the solution might become unstable/inaccurate at late times. The recorded field data obtained on the conductive mudflat are usually longer than three decades in time. Therefore, a multi-grid approach is used, where two grids are designed with an overlapping time range. The results from both, the early and late time grid, are patched together. The overlapping transients are plotted in Fig. 5.4. The early time grid is designed for a time-range of $t = 10^{-7} - 10^{-4}$ s and the late time grid for $t = 10^{-5} - 10^{-2}$ s. Both grids are designed according to the equation (5.27). Therefore, the late time grid is much coarser than the early time grid. As a consequence, the material averaging scheme leads to different effective resistivity distribution for both grids and systematical shifts between both transients are unavoidable and have to be checked. For the example in Fig. 5.4, the shift is marginal and negligible.

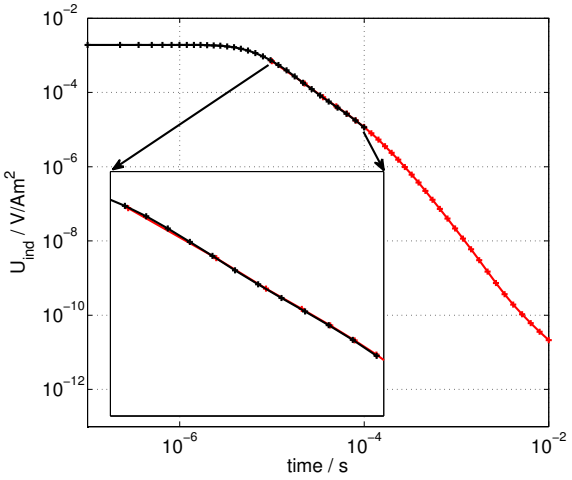

Figure 5.4: *U_{ind} calculated for the early (black) and late time grid (red) with a magnification for the overlapping time range.*

5.3.3 Variation in the number of grid lines

The numerical solution accuracy of the *SLDMem3t* is not necessarily increased by refining the grid. On the one hand a very fine discretized grid will lead to longer calculation times and on the other hand a spacing smaller than δ_{FD}^{min*} will increase the sparsity of the system matrix $\boldsymbol{A}$ and its condition number. Based on the approach of Martin [2009], a simple and effective way to design suitable grids for both, forward and inverse modeling using the *SLDMem3t* algorithm is suggested. Assume a Tx-50 transmitter and a required time range $t = 10^{-6} - 10^{-3}$ s, then an appropriate grid can be found in three steps:

1. At first, a 1D model is selected which roughly represents the resistivity structure for a certain zone along a profile. In accordance to the resistivity-depth sections derived from the field data, a three-layer model with

   $$\rho_{1-3} = (10,\ 5,\ 50)\ \Omega\text{m} \quad \text{and} \quad z_{1-3} = (5,\ 20,\ \infty)\ \text{m}$$

   is used. The model represents roughly the layering on the basalt/AQ formation along profile A.

2. The grid spacing is calculated using equation (5.27) and the number of grid lines are varied laterally and vertically from $n_{x,y,z} = 40$ to 90. In lateral direction the grid is usually designed symmetrically. The *SLDMem3t* solution is calculated for each permutation of $n_{x,y}$ and n_z.

3. For each permutation of $n_{x,y}$ and n_z the *SLDMem3t* solution is compared to the analytical solution via the (un-weighted) Root-Mean-Square (*RMS*), defined in equation 3.5.

The *RMS* values calculated from the *SLDMem3t* and *EMUPLUS* solutions for each permutation of $n_{x,y}$and n_z are shown in the color-coded plot in Fig. 5.5(a). Intuitively, one expects a more accurate solution with an increasing number of grid lines. As mentioned earlier, this is not the case and the solution accuracy is very prone to variations of n_{xy} and surprisingly not to n_z, which was also reported by Martin [2009]. For example, the *RMS* for $n_{xy} = 64$ is worse than for $n_{xy} = 60$ grid lines. From the

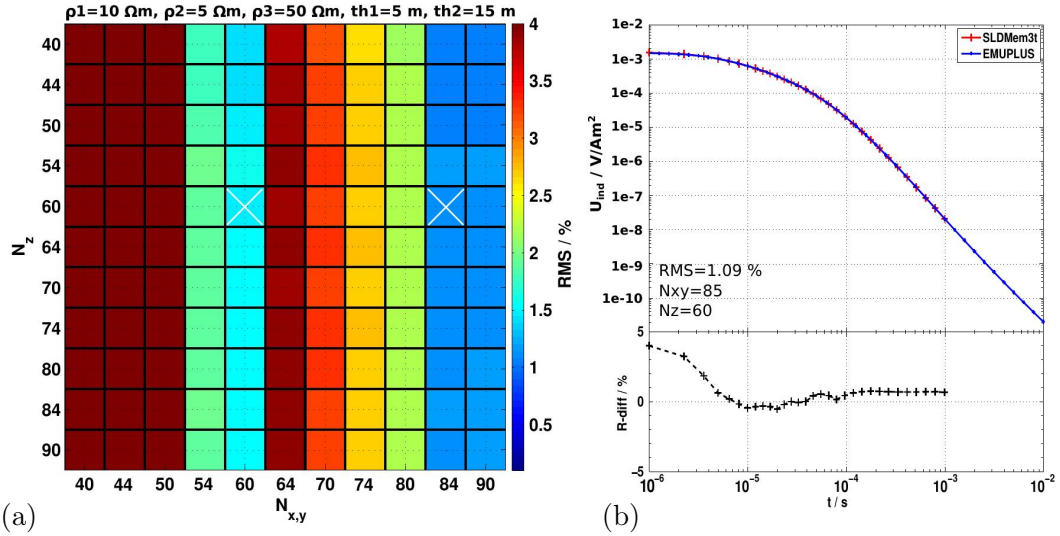

Figure 5.5: *(a) RMS calculated for each permutation of n_{xy} and n_z. (b) Comparison of the SLDMem3t and 1D EMUPLUS solutions for $n_{xy} = 84$ and $n_z = 60$.*

color-coded plot two appropriate grids are selected, which are marked as white crosses in Fig. 5.5(a):

1. The fine discretized grid with $n_{xy} = 84$ and $n_z = 60$ exhibits an *RMS* less than 0.6%. The comparison of both, the *SLDMem3t* and the *EMUPLUS* solution is plotted in Fig. 5.5(b). According to the relative difference displayed below the plot, it is less than 1%, except for the first three time points.
2. The coarse grid with $n_{xy} = 60$ and $n_z = 60$ exhibits an *RMS* less than 1.5% and is useful for preliminary studies, as it requires less computational effort.

Although the solution does obviously not dependent on n_z, the possibility of an under-discretization is avoided by not taking the least number for n_z. The largest value is not selected, due to longer calculation times.

5.3.4 Variation in the resistivity values

Up to know, the best combination of n_{xy} and n_z is determined for a particular three layer 1D model. It is not clear if the solution is sufficiently accurate for a wide resistivity range. To address this problem, the selected grids are checked for a simple two layer model with varying resistivity $\rho_{1,2}$ from 0.1 to 100 Ωm. The thickness of the first layer is kept fix at 15 m. The *RMS* is calculated from the *SLDMem3t* and *EMUPLUS* solutions for all combinations of ρ_1 and ρ_2. Exemplarily the result is shown in the color-coded plot in Fig. 5.6(a) for the fine grid with $n_{x,y} = 84$ and $n_z = 60$. The grid does not provide accurate solutions for overburden resistivities less than 3.2 Ωm, independent from the underlaying resistivity. If the resistivity contrast becomes large ($\rho_1/\rho_2 \geq 100/0.2$) the *RMS* increases to more than 3%. Nevertheless, the selected grid obviously provides accurate solutions for a wide resistivity range with *RMS*-values below 2%, which is hemmed by a black line in Fig. 5.6(a). In Fig. 5.6(b), the numerical and analytical solutions are compared for the combination $\rho_1 = 50$ and $\rho_2 = 1.6$ Ωm. The relative difference is around zero throughout the whole time-range.

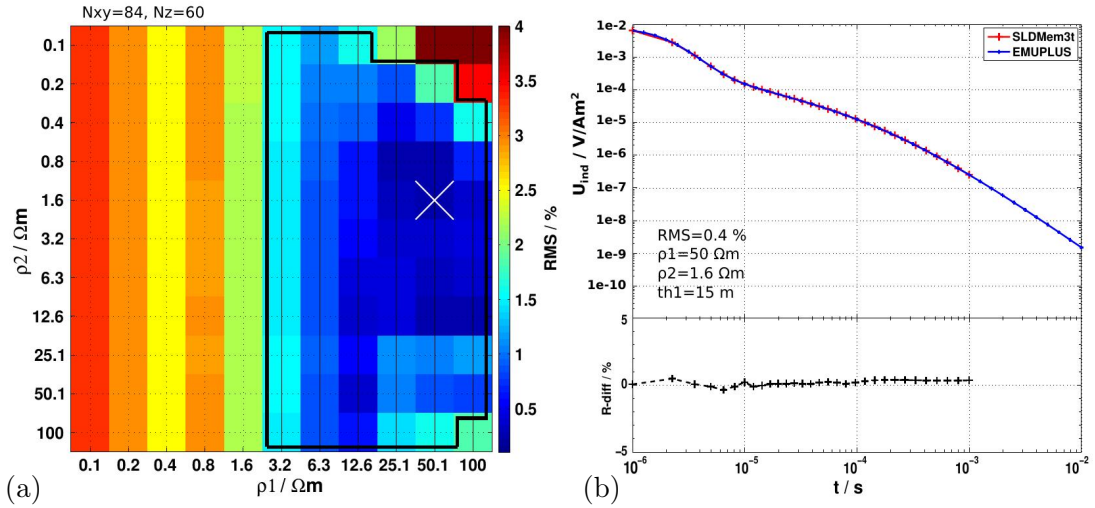

Figure 5.6: *Variation of the resistivity for the fine discretized grid with $n_{x,y} = 84$ and $n_z = 60$. (a) RMS calculated for each permutation of ρ_1 and ρ_2 of a two layer model. The thickness of the first layer is fixed to 15 m. The resistivity combinations, where the RMS is less than 2% is hemmed black. (b) Comparison of the SLDMem3t and EMUPLUS solutions for resistivities $\rho_1 = 50\ \Omega m$ and $\rho_2 = 1.6\ \Omega m$. The combination is indicated by a white cross in (a).*

From the study it is obvious, that except on the high conductive mudflat the fine grid would provide accurate solutions for the quasi 2D resistivity-depth sections presented in section 4.7. For the conductive mudflat zone another grid is designed and verified by the same procedure. The same approach is also applied to both transmitter configurations, either the Tx-50 or the Tx-100 setup.

5.3.5 Lateral grid discretization refinement

The grid is verified in detail by comparing the *SLDMem3t* solution with 1D semi-analytical solutions. Hence it is uncertain, if a grid is sufficiently discretized to image a lateral inhomogeneity. A 2D verification of the solution generally involves the application of other numerical TDEM modeling algorithms. Here, a convenient way is presented to validate qualitatively if the grid is sufficiently discretized in lateral direction with respect to the underlaying model.
The problem of model discretization errors can arise within the *SLDMem3t*, if grid lines are missing at lateral boundaries. Assume a TEM sounding, where certain transmitter/receiver (Tx/Rx) locations are realized by shifting the model with respect to the grid. To illustrate this, a simple fault model is shown in Fig. 5.7(a), where the grid is plotted as white lines. For a Tx/Rx location at $x = -1000$ m left of the fault, the vertical grid lines are very coarse around the fault. Due to the material averaging scheme discussed in section 5.1.1, the resistivity distribution will be different from that which is shown in Fig. 5.7(a). Since there is no vertical grid line around $x = 0$ m, the red hemmed cell for example will exhibit an effective resistivity of $\rho_{eff} = 59\ \Omega$m. This value is used for the calculation of the E_x component. The green hemmed cell shows the area, which is used to calculate the effective resistivity for an E_y component located at the center marked as a green cross. The vertical magnetic field component

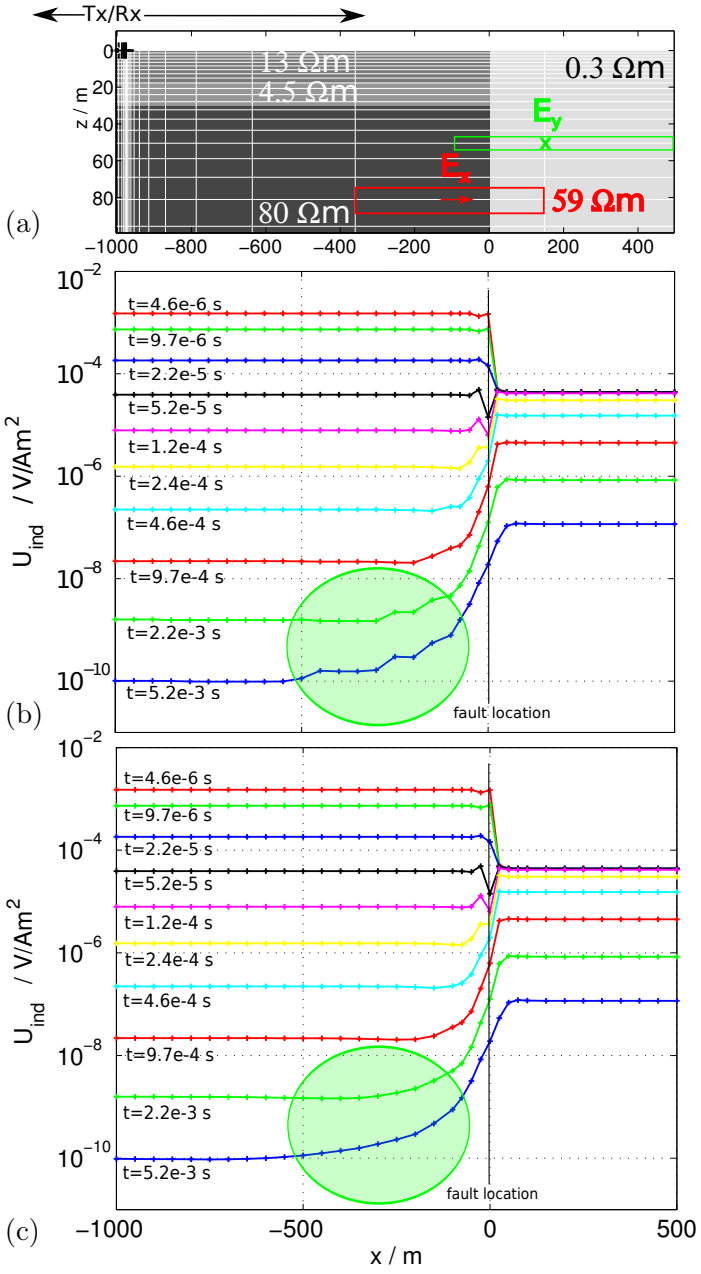

Figure 5.7: *(a) Simple fault model with a vertical fault at 0 m. The Tx/Rx setup is located at $x = -1000$ m and the grid lines are drawn white. No grid line is present directly on the fault. The red boxed cell denotes the effective area and assigned effective resistivity ($\rho_{eff} = 59\ \Omega m$) used for calculating the E_x component at the center marked by a red arrow. The green hemmed area and its effective resistivity is used to calculate E_y at the location denoted by a green cross. (b) U_{ind} calculated for various distance of Tx/Rx away from the fault. The response is plotted against the Tx/Rx location for several times. Here, the original grid without refinement (displayed in (a)) is used for the calculation. In (c), the same response are shown as in (b), except that grid lines are now included around the fault.*

$\dot{B}_z$ (and U_{ind}) is calculated from the electric field $\boldsymbol{E}$ by Faraday's law. In Fig. 5.7(b), the response $U_{ind}(x,t)$ is plotted for different transient time-points and different Tx/Rx fault distances $-1000 \leq x \leq 500$. The response shows a step-like behavior, which depends on the time and the Tx/Rx distance from the fault. In Fig. 5.7(c) the response

$U_{ind}(x,t)$ is calculated similarly, except that now vertical grid lines are included around the fault. Compared to the response without additional grid lines, a smooth response is now obtained.

Although, *SLDMem3t* allows an arbitrary model discretization, internally the implemented material averaging scheme calculates the effective resistivity of each cell (see in section 5.1.1). By calculating the response of a simple fault or quaterspace model for different distances from the fault, it is possible to check, whether the response is smooth with respect to the fault distance. If not, but a accurate solution is required, grid lines may be included at a lateral boundary. Moreover, the example shows that the model and the calculation grid should be in proportion to each other. In explanation, a coarse grid and a very fine model geometry in an area of interest makes little sense, as the structure will be averaged out. This qualitative approach is convenient to check the grid and model discretization for 2D calculations based on the *SLDMem3t*. It can be applied in a similar manner to 3D models.

5.3.6 Convergence control parameters

Besides comparing the *SLDMem3t* solution to a 1D semi-analytical solution, there are three control parameters, which are useful to check the convergence of the solution for each MS step of the Lanczos process. Consider a Tx-50 central loop configuration and the fine discretized grid with $n_{x,y} = 84$ and $n_z = 60$ discussed in section 5.3.3. Moreover, the three layer model with $\rho_{1-3} = (10,\ 5,\ 50)$ Ωm and $z_{1-3} = (5,\ 20,\ \infty)$ m is used. For each iteration $MS = M$. the *SLDMem3t* writes three control parameters, which are called RES, $PROGN$ and EPS:

- RES is a test solution calculated for the last time point at a specified control receiver. For the central loop configuration it is convenient to use a $\dot{B}_z$ control receiver at the surface grid center. RES should converge towards a stable solution. In case the solution is unstable or does not converge, RES will oscillate. If the algorithm is terminated too early, the calculated response deviates from the analytical response, particularly at late times.
- $PROGN$ is the absolute difference between RES of the current and a previous iteration and should be ideally zero.
- EPS is the relative difference between RES of the current and previous iteration:

$$EPS_i = \frac{PROGN_i}{RES_i} = \frac{RES_i - RES_{i-1}}{RES_i} \times 100, \tag{5.28}$$

  where i is the actual iteration. Within the *SLDMem3t* the Lanczos process is terminated if EPS is below a predefined threshold.

In Fig. 5.8(a), RES is plotted versus MS for every hundredth iteration. According to equation (5.25), at least $MS = 1900$ iterations are required (for grid/model specifications: $\Delta_{min} = 0.42$ m, $t_{max} = 10^{-3}$ s, $\rho_{max} = 50$ Ωm). Clearly $MS = 1900$ is much too small. Moreover, between $MS = 5500 - 7000$ the solution converges towards a stable value, which can be seen in the focused plot in Fig. 5.8(b). The *SLDMem3t* solution

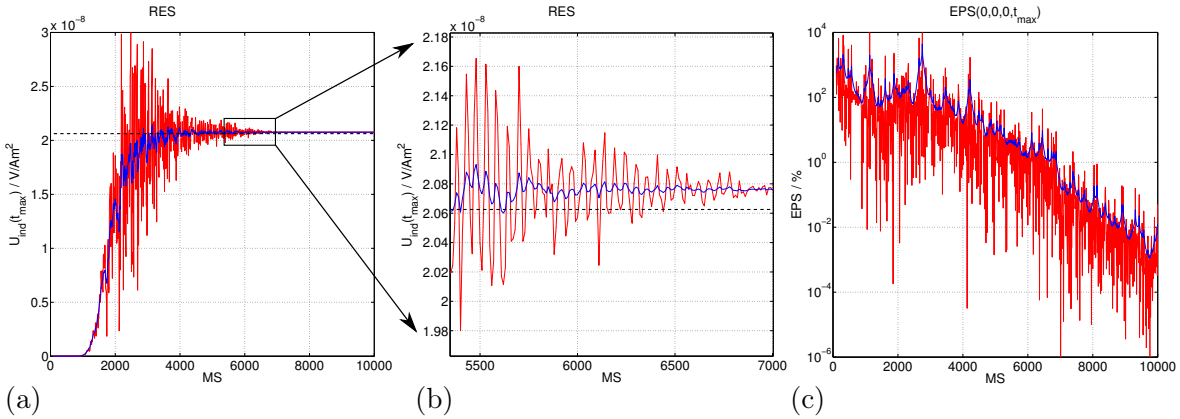

(a) (b) (c)

Figure 5.8: *(a) Evolution of RES (U_{ind}) for every hundredth iteration MS and (b) focused plot for RES. The weighted moving average is marked blue. The analytical solution is plotted as a black dashed line. (c) Evolution of EPS for every hundredth iteration.*

does not converge exactly to the analytical solution (denoted as a black dashed line). A small shift with a relative difference of 0.7% is present, which is obviously systematic. Such a systematic shift/error can be caused by the discrete approximations of the EM-field equations [Zhdanov & Varentsov, 1997]. Nevertheless, a deviation less than 1% is sufficiently accurate. If one is dealing with a transient sign reversal at late times, *RES* will most likely alternate with respect to the sign due to numerical noise (inaccuracy of very small values). In that case, a second grid for late times is recommended as described previously in section 5.3.2.
In Fig. 5.8(c), *EPS* is plotted versus the iteration *MS*. For $MS = 7000$, it is already below 1% according to the moving average. Since *EPS* jumps by several orders of magnitude, the Lanczos process would terminate already for $MS = 4000$, even if a very small threshold $EPS \approx 10^{-4}\%$ is defined. To avoid a too early termination, Martin [2009] suggested to check *EPS* thrice (for the actual and two previous iterations). Alternatively, a very low threshold for *EPS* can be chosen, to avoid early truncation and therefore, accept longer calculation times. During this thesis, a too early truncation was observed a few times, wherefore always $MS = 12000$ iterations are calculated. Nonetheless, the redundant computational effort should be generally considered and estimated, especially prior to the 2D inversion.
The convergence parameters are useful to check the stability and convergence of the solution. Moreover, one can justify the truncation of the Lanczos process at a certain iteration. However, in order to obtain an estimate of the *SLDMem3t* accuracy, a comparison with an analytical solution is necessary.

5.3.7 Numerical modeling errors

The problem addressed in this section is how to quantify *SLDMem3t* modeling errors and moreover, how these errors are considered when determining the data fit posterior to 2D forward and inverse modeling. It is not meaningful to fit field data with a specified *RMS* or χ without considering the modeling errors.
The easiest way to derive a modeling error is to calculate the relative difference between

the numerical and analytical solution of each time point at the stage of the *SLDMem3t* grid check. Consider again the fine discretized grid with $n_{x,y} = 84$ and $n_z = 60$ discussed in section 5.3.3. As shown earlier in Fig. 5.6(a), the black hemmed area marks the resistivity combinations, for which the grid provides solutions with an *RMS* less that 2%.

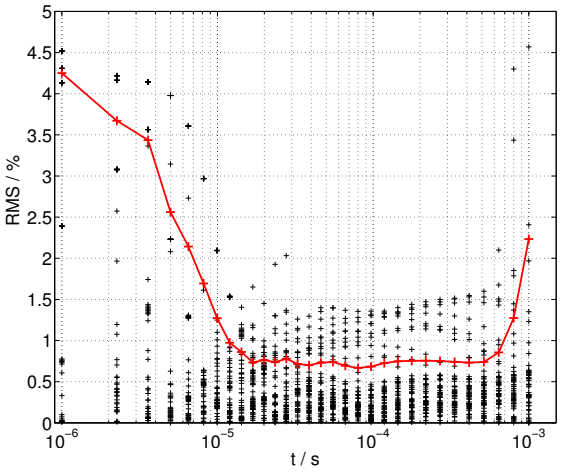

Figure 5.9: *Residuals calculated for each time point and all combinations of ρ_1/ρ_2 within the black hemmed area shown in Fig. 5.6. They are denoted as black crosses. The red line is the mean RMS calculated for each time point.*

To illustrate the modeling errors, the distribution of residuals for each time point and each combination of ρ_1/ρ_2, within the black hemmed area of Fig. 5.6(a), are calculated. The residuals are plotted in Fig. 5.9 as black crosses and are distributed between 0 and 5%. To illustrate the time dependence of the *SLDMem3t* solution, the *RMS* is calculated for each time point, which is denoted as a red line. The *RMS* ranges between 1 and 4% for early times ($t < 10^{-5}$ s). At intermediate times, it drops below 1% and increases again for the last two time points. The time dependency is a well known phenomenon of the *SLDMem3t*, because its computational load increases with $\sqrt{t}$, i.e. the number of required iterations MS depends on t_{max} [Weidelt, 2000]. Moreover, Weidelt [2000] stated that large early time residuals may be caused by an in-appropriate integral boundary condition at the earth-air interface.
The mean *RMS* equals 1.2% and is calculated from all residuals shown in Fig. 5.9. For the sake of simplicity and in order not to underestimate the errors, a percentage *SLDMem3t* error of $\delta d_{i,sld} = 1.5\%$ is used in this thesis. An overall error estimate for each individual data point δd_i^* is derived by using Gaussian error propagation:

$$\delta d_i^* = \sqrt{\delta d_{i,obs}^2 + \delta d_{i,sld}^2}. \tag{5.29}$$

Where $\delta d_{i,obs}$ is the percentage error estimated for the field data as described in section 4.5.3.
Another approach to obtain more meaningful numerical errors $\delta d_{i,sld}$, is to extract 1D models beneath each sounding location from a final 2D model. Then, the error $\delta d_{i,sld}$ can be calculated from the numerical and analytical solution for each extracted 1D model and individual data point. Therefore, this more expensive approach is applied in section 5.5.2 for a final 2D model used for the forward modeling of the field data.

Since the time discretization is arbitrary for the *SLDMem3t* scheme, it is suggested to use the same time supporting points, which are used for the 1D analytical solution and for the field data. Otherwise, the interpolation between logarithmic time points can lead to unwanted interpolation errors.

5.4 2D synthetic modeling for a fault structure

The quasi 2D resistivity-depth sections presented in section 4.7 show a strong lateral resistivity variation from moderate to very low subsurface resistivities. This section aims to illustrate and analyze the effect of such a lateral resistivity variation on central loop TEM data. A simple fault model is generated and synthetic data is calculated for different distances from the fault structure. The model displayed in Fig. 5.10(a) is rather simplified compared to the 1D stitched models along profile A shown in section 4.7.2. Left of the vertical fault a three-layer case is present, with a conductor sandwiched between two resistors, where

$$\rho_{1-3} = (13,\ 4.5,\ 80)\ \Omega\text{m} \quad \text{and} \quad z_{1-3} = (18,\ 10, \infty)\ \text{m}.$$

A high conductive homogeneous half space with 0.3 Ωm is located to the right of the fault. In Fig. 5.10(b), the voltage response $U(x,t)$ is plotted for different distances from the fault and several transient time points. The abrupt lateral subsurface change affects the transient data depending on the time and the Tx/Rx fault distance. The time-range where the 2D distortion of the data has to be considered is hemmed in gray in Fig. 5.10(b). In the following only times with $t \leq 10^{-3}$ s are considered. This is approximately the latest transient time point recorded in the field northeast of the Al Bayda fault at sounding A42. According to the red drawn line with $t = 9.7e-4$ s, U_{ind} for times earlier than $t \leq 10^{-3}$ s are affected maximal up to $x \approx -200$ m

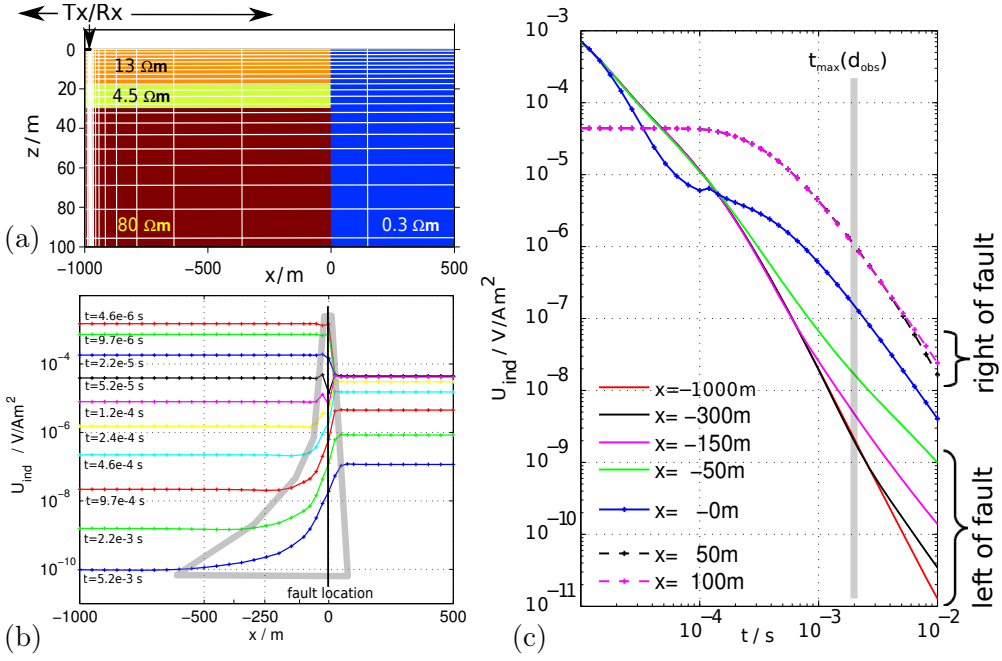

Figure 5.10: *(a) Simplified 2D vertical fault model representing roughly the subsurface structure along profile A in the survey area. The grid is displayed as white lines. Tx/Rx denotes the TEM location, which is shifted between $x = -1000$ and 500 m. (b) Induced voltage $U_{ind}(x,t)$ for distinct time points and plotted along the profile for various Tx/Rx fault distances. The 2D affected data is hemmed by a gray line. (c) Transients (U_{ind}) calculated for different fault distances. The vertical gray line, denotes the last time point of the transients (t_{max}), which were recorded northeast of the Al Bayda fault along profile A in the field. The times and distances are given in the corresponding legends.*

fault-distance to the left of the fault. Right of the fault, the diffusion depth is significantly decreased and the effect on the response U_{ind} is marginal. In Fig. 5.10(c), the voltage response U_{ind} is plotted for different fault distances. The vertical gray line, denotes t_{max} of the transients recorded left of the Al Bayda fault along profile A. For the furthest location at $x = -1000$ m there is no fault effect visible and the transient represents the three-layer background model response. Towards the fault (from the left), the voltage is increased at late times and indicate the conducting zone. Only the early times remain undisturbed. Directly on the fault, at $x = 0$ m, the transient is dominated by the fault effect for all times. Comparing the transients right of the fault at $x = 50$ and 100 m only a slight difference is visible at the latest times.

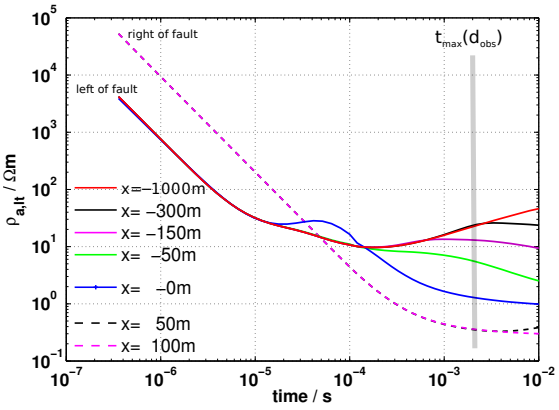

Figure 5.11: *Synthetic TEM $\rho_{a,lt}$ transients for different fault-distances.*

To gain more insights, the induced voltage is transformed to late time apparent resistivities $\rho_{a,lt}$. In Fig. 5.11, the synthetic $\rho_{a,lt}$ data are plotted for the same fault-distances as in Fig. 5.10(c). The characteristic $\rho_{a,lt}$ overshoot around $t = 10^{-5} - 10^{-4}$ s for the sounding located at $x = 0$ m is caused by the strong lateral resistivity change. Newman et al. [1987] discussed a similar effect for data obtained over 3D-structures. Moreover, a strong $\rho_{a,lt}$ decrease occurs at late times for all soundings left of the fault, which indicates a good conductor. The $\rho_{a,lt}$ soundings obtained right of the fault indicate only a slight resistivity increase at late times.

5.4.1 1D inversion of synthetic fault affected data

It is obvious that the 1D inversion, either Occam or Marquardt, of fault affected data as shown in Fig. 5.10(c), may lead to wrong subsurface models and, therefore, to significant miss-interpretation. In Fig. 5.12, the 1D Marquardt inversion models are patched together to a quasi 2D section. An initial 10 Ωm half space model with four layers is used. The resulting quasi 2D stitched section varies significantly from the original model as follows:

- The true 80 Ωm basement shows a slight resistivity decrease towards the fault starting at $x = -900$ m. At $x = -500$ m the decrease becomes significant and would be miss-interpreted. At the same time the *RMS* is increased.

- Between $x = -150$ and 50 m the original model is not reproduced and a good conductor is visible at depth below the resistor. Although not that prominent, right of the fault between $x = 0 - 50$ m, a resistor is placed below the conductor.

In order to avoid a false interpretation, some authors suggest the removal of data points which are affected by 2D and 3D distortion prior to a 1D inversion, e.g. Bedrosian et al. [2013]. In Fig 5.13, the comparison of the 1D inversion results with and without fault-affected data points are shown exemplarily for the sounding located at x =-300 m.

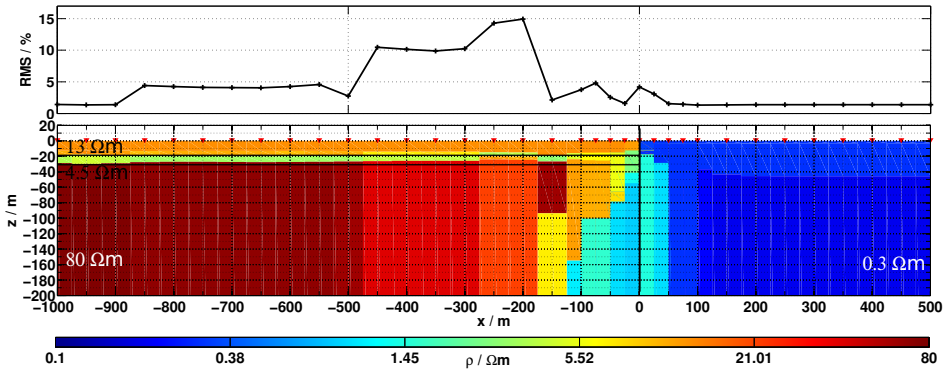

Figure 5.12: *1D stitched Marquardt inversion results derived from synthetic 2D fault affected data. The RMS is plotted above the model for each sounding. The true models is marked by black lines.*

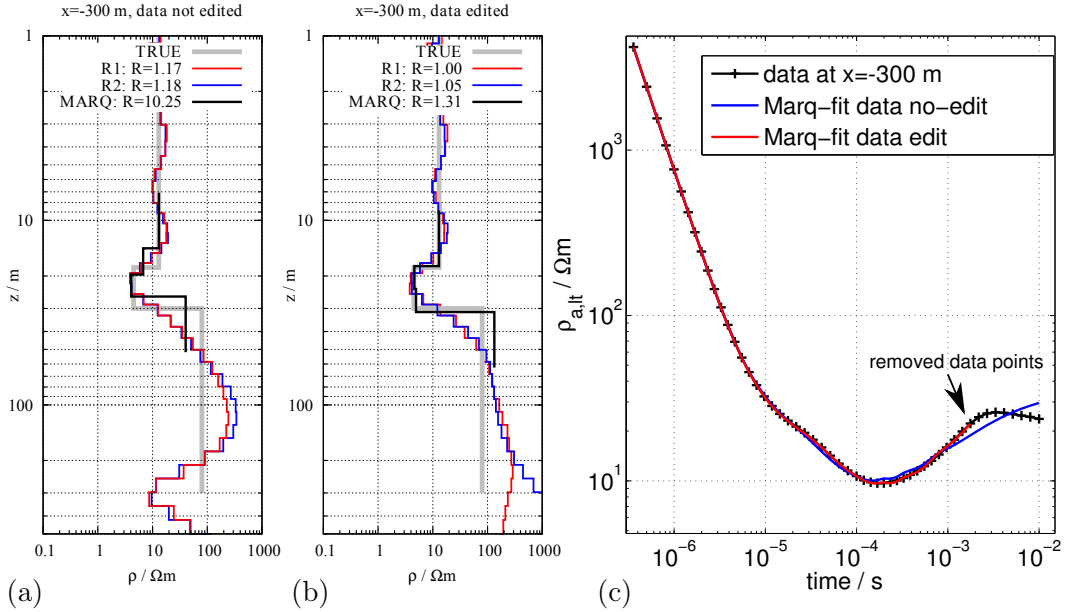

Figure 5.13: *Comparison of 1D inversion results (Marquardt and Occam R1/R2) of synthetic fault affected data at sounding location x =-300 m. Inversion result for (a) the non-edited data and (b) the data points for $t > 2$ ms are removed. The true background model is denoted by a gray line. (c) Synthetic data (black) and Marquardt inversion fitting for non-edited (blue) and edited data (red).*

Concluding from Fig. 5.11, data points for times greater than $t = 2$ ms are assumed to be distorted and are removed. The 1D Marquardt model is derived from the non-edited data in Fig. 5.13(a) and shows a too low resistivity of $\rho \approx 30$ Ωm for the last layer. The late time data with $t > 1$ ms is not fitted at all and the RMS is 10%. If the data points for $t > 1$ ms are removed, the fit is significantly improved and the Marquardt model coincides well with the true three layer background model left of the fault. Since the Occam inversions R1/R2 are done with 30 logarithmic equidistant layers, the edited and non-edited data is fitted well with $RMS \approx 1$. Nevertheless, to fit the non-edited data, a conductor is placed at depth and the models would be definitely miss-interpreted. This is not the case for the edited data and the inversion results match the true model well.

5.4.2 Analysis of 2D distorted data by subtracting a 1D background response

In Fig. 5.14(a), the same fault model is displayed as in Fig. 5.10(a), except that the x- and z-ranges are changed to match profile A between sounding A27 and A71. The inter-station distance is 50 m and the fault is located at sounding A41 (x =3100 m). Bedrosian et al. [2013] suggested to visualize 2D affected data by constructing a 1D background model left and right of a fault. Then, a 1D background model response U_{ind}^{1D} is calculated and subtracted from the 2D affected data. This approach is applied to the 2D response U_{ind}^{2D} of the model shown in Fig. 5.14(a). A three-layer background model response is subtracted from U_{ind} left of the fault. Right of the fault, the 0.3 Ωm homogeneous halfspace response is subtracted. The percentage relative difference

$$\text{R-diff} = \frac{U_{ind}^{2D} - U_{ind}^{1D}}{U_{ind}^{2D}} \times 100 \qquad [\%]$$

is plotted for each time point along the profile in Fig. 5.14(b). The color-coded section visualizes which soundings and corresponding time range differ from the 1D model response. For sounding A41, directly on the fault, the response is affected throughout the whole time range, whereas at station A36 only the last time decade is affected, showing a deviation of more than 10%. Right of the fault the effect is negligible, except for the latest times of sounding A42. The blue and red dotted lines in Fig. 5.14(b) mark the earliest and latest recorded data points in the field, respectively. If this time-range is considered, only three to four soundings (A38-A41) are obviously affected. A drawback is that for "realistic" 2D models, which are derived from field data, the construction of an appropriate 1D background model is difficult. Thus, this approach is mainly interesting for synthetic studies prior to a survey.

5.4.3 Analysis of 2D distorted data by using a TEM-tipper

In section 2.3.4, the TEM-tipper T_U was introduced, which was described by Spies & Frischknecht [1991] to visualize multidimensional subsurface effects. Over a 1D layered earth, the horizontal magnetic fields in the center of a loop transmitter are theoretically zero. Therefore, a few authors used the horizontal magnetic field components to investigate multidimensional structures. For example Newman et al. [1987] described the behavior of the horizontal magnetic field over 3D conductors. Rödder [2010] and Koch et al. [2003] applied a 3-component receiver setup ($\dot{B}_{x,y,z}$) to investigate the Araba fault in south Jordan.
Consider again the fault model presented in Fig. 5.14(a). To investigate the fault affected data, the ratio of the horizontal magnetic field $\dot{B}_x$ (or $U_{ind,x}$) and the vertical magnetic field $\dot{B}_z$ (or $U_{ind,z}$) are calculated. This is referred to as the TEM-tipper. Since the strike is y-oriented, the $\dot{B}_y$ component vanishes. In Fig. 5.15(a) the ratio of $T_U = U_{ind,x}/U_{ind,z}$ is displayed as a colored section along the profile. Ratios less than 0.01 are colored gray and ratios larger than 0.1 are plotted dark red. Spies & Frischknecht [1991] stated that for ratios $T_U < 0.1$ a 1D interpretation of TEM data is generally valid. The similarity of the TEM tipper to the approach suggested by Bedrosian et al. [2013] in Fig. 5.14(b) is remarkable. The same number of soundings

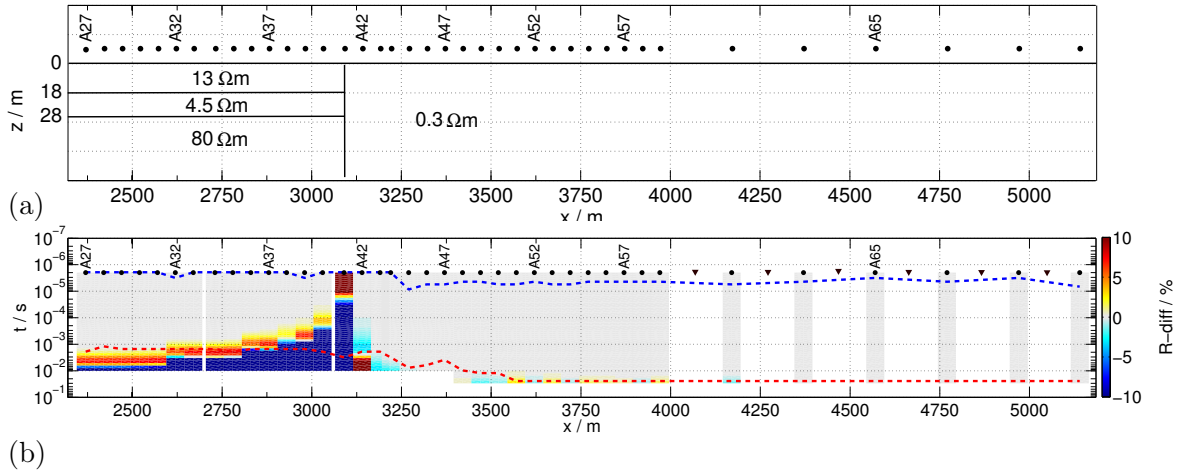

Figure 5.14: *(a) 2D fault model with a three layer case left of the fault and a 0.3 Ωm homogeneous right of the fault. The fault is located at sounding A41. (b) Relative difference calculated from the 2D response and a 1D background model response (left and right of fault). See text for further explanations.*

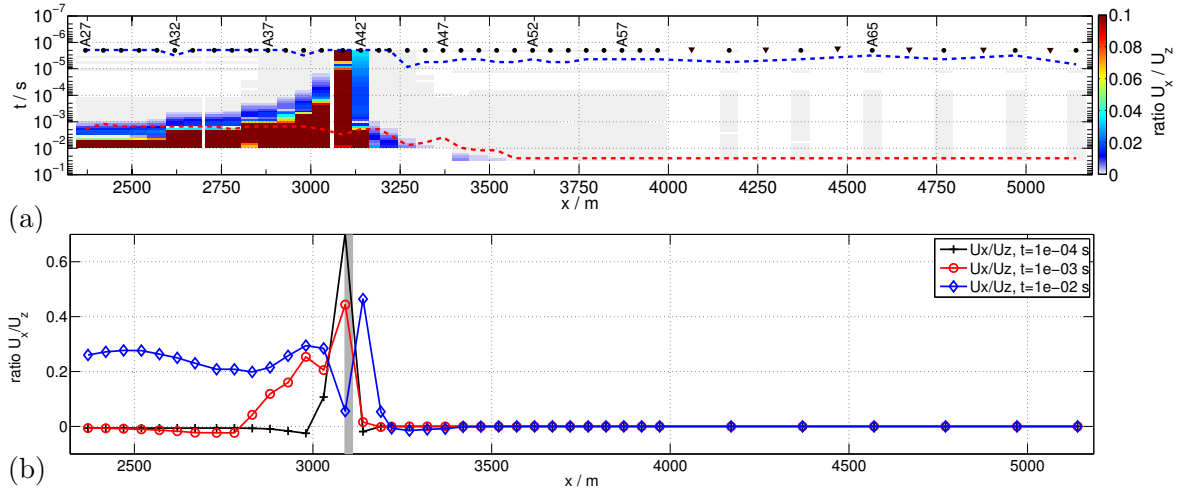

Figure 5.15: *Consider the same model as displayed in Fig. 5.14(a). (a) Tem tipper $T_U = U_x/U_z$ plotted for each time point along the profile. (b) T_U plotted for three distinct time points against the profile*

are 2D affected with Tipper values $T_U > 0.1$. If only data points in the time range between t_{min} (blue dotted line) and t_{max} (red dotted line) are considered, three to four soundings (A38-A41) are affected. In Fig. 5.15(b), the tipper T_U is plotted for three distinct time points. For $t = 10^{-4}$ s the fault location is pin-pointed by a large tipper value $T_U \approx 0.6$. The last recorded time point left of the Al Bayda fault in the field is $t \approx 10^{-3}$ s. The corresponding red drawn line shows that five soundings have Tipper values with $T_U > 0.1$.

Although the TEM tipper was not measured in the field, it can be used at least to some extent to analyze how much 2D effect a derived model would generate. The approach provides similar results compared to that suggested by Bedrosian et al. [2013], but has a significant advantage because no simplified background model is required. For the extreme fault example discussed in Fig. 5.15, maximal three to five soundings (A39-

A41) within the field data time-range cannot be interpreted in 1D, without significant miss-interpretation. To gain information, how much 2D effect the models derived from the field data will generate, the TEM-tipper is calculated subsequently in section 5.5.2 exemplarily for a 2D model.

5.5 2D forward modeling of Tx-50 sounding data: transition zone along profile A

Quasi 2D resistivity-depth sections were derived in section 4.7.2 from the Tx-50 sounding data along profile A. The subsurface structure varies laterally from moderate resistivities on the basalt formation to very low resistivities on the mudflat. Therefore, it is uncertain if a 1D interpretation is adequate, when the structure becomes essentially 2D. To validate the derived quasi resistivity-depth sections, 2D models are derived in the following from the 1D Occam and Marquardt results. The focus is on the transition zone between sounding A27 and A59. The Al Bayda fault is expected around sounding A41.
The 2D forward modeling has two main objectives. The first is to derive a 2D model, which quantitatively explains the field data for a large number of soundings. Three strategies are followed: at first a rather simple model is derived manually; in the second step a model is derived by spatial interpolation from 1D Occam models and from 1D Marquardt models. The second objective is to perform a 2D modeling study and to investigate the subsurface structure in the transition zone, i.e. how well is the lateral extent of the resistive layer supported by the Tx-50 sounding data.

In advance, it should be pointed out that these derived 2D models are biased at least to some extent. They are always constructed from existing 1D models, and not independently reconstructed as it would be the case in a 2D inversion.

5.5.1 2D model derived qualitatively from 1D results

In the first step, a 2D block model is derived visually from the quasi 2D resistivity-depth section along profile A (cf. section 4.7.2). The idea behind, is to start with a rather simple model and to perform systematical studies by perturbation of different zones. The derived 2D model presented in Fig. 5.16 exhibits a global χ of 8.72 (*RMS* = 16.44%), which is a poor fitting. Therefore, the model does not explain the data

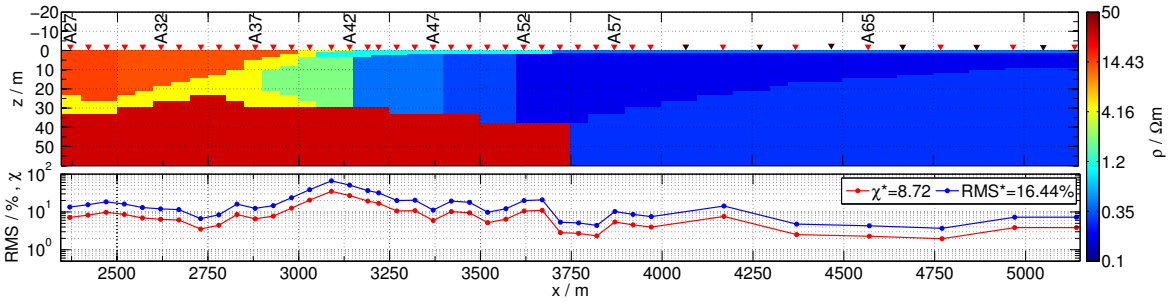

Figure 5.16: *2D model derived visually/manually between soundings A27 and A65 along profile A. The corresponding misfit, χ and RMS, are plotted below the model for each sounding.*

quantitatively well. Especially between sounding A37 and A47, a strong lateral resistivity variation is present and the *RMS* increases up to 100%. Only for the last five soundings, the *RMS* is below 10%. Since the field data is not fitted well, the model is not suitable as a starting point for further systematic forward modeling.
As the manual approach for deriving a 2D model is very time consuming and not feasible

for fitting the field data quantitatively, the idea was dropped. For systematic modeling studies, without trying to fit real field data, this approach is of course feasible.

5.5.2 2D model derived from 1D Occam results

In order to reach a sufficient starting point model for the 2D modeling study, the 1D stitched Occam R1 section is linearly interpolated onto a 2D model grid. The crucial point is, therefore, the discretization of the 2D model grid. The discretization in z-direction matches exactly the layering of the 1D Occam models presented in section 4.7.2. To achieve coarser or finer models the lateral discretization of the 2D model grid is varied between Δ_x =50, 25 and 10 m. The coarsest lateral discretization exhibits one model column beneath each sounding and is, therefore, a one-to-one image of the quasi 2D Occam resistivity-depth section.
In Fig. 5.17(a-c), three derived 2D models are displayed for a lateral discretization Δ_x =50, 25 and 10 m. The coarsest model in Fig. 5.17(a) explains the field data for 39 soundings with a global χ of 1.49. The global *RMS* is double, as neither the field data errors nor the *SLDMem3t* modeling errors are taken into account. In the transition zone between sounding A37 and A52 the misfit slightly increases, but is mostly below $\chi = 5$. At sounding A47, the resistivity increase is not resolved and a 50 m wide gap is visible in the model. For a fine discretization with $\Delta_x = 10$ m the 2D model becomes quite smooth. The global χ is 2.85 and almost double compared to the coarsest model. For comparison, the 1D stitched Occam models presented in section 4.7.2 exhibit a global χ of 0.9.
All three 2D models explain the field data for a total of 39 soundings and are therefore suitable as starting point models for a 2D modeling study. But, from a practical point of view, all three models are too smooth and do not have distinct model boundaries. Therefore, they are not suitable to systematically analyze the variation of different model zones.
In order to reach a model with distinct boundaries, another approach was tried. The resistivities are joined into either $N_\rho = 20$, 10 or 5 logarithmically equidistant resistivity-bands between 0.1 and 50 Ωm. The results are displayed in Fig. A.20(a-c) in the appendix. The model with $N_\rho = 5$ resistivity bands has distinct boundaries, but the fit deteriorates to $\chi \approx 7$. On the contrary, the models with $N_\rho = 20$ and 10 resistivity bands have a good fit, but no distinct model boundaries. Therefore, these models are not useful as starting point models and the idea is not pursued further.

As a conclusion it can be noted that the Occam models are not suitable for the systematic 2D modeling study. Therefore it is done on the basis of the 1D Marquardt models subsequently in section 5.5.3. However, since the best-fit 2D model in Fig. 5.17(a) explains the field data well, it is used for further analyzes in three steps:

- The distribution of data residuals are analyzed to verify if they depend on the subsurface resistivity structure.

- The TEM-tipper is calculated to gain insight, how much 2D effect the best-fit model generates. This approach was also previously applied to a synthetic fault model in section 5.4.3 and is in very good agreement to another approach presented by Bedrosian et al. [2013].

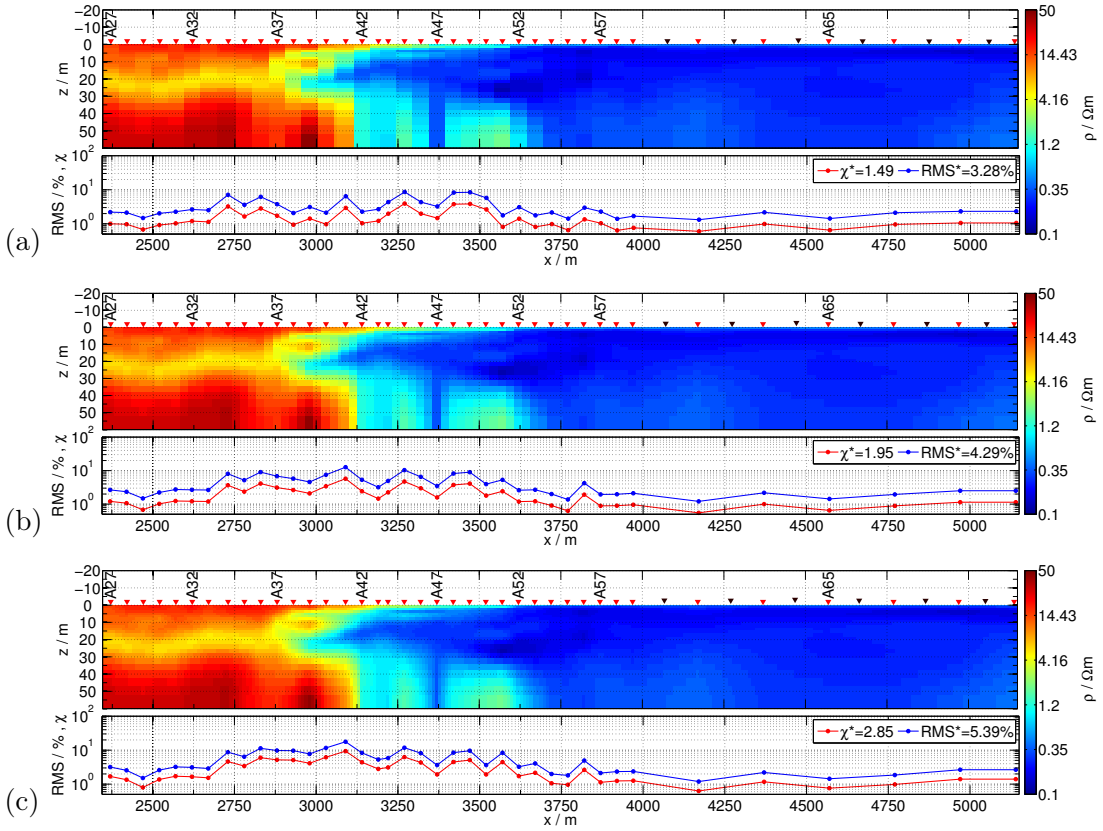

Figure 5.17: *2D models derived by spatial interpolation of 1D Occam results onto a 2D grid for a lateral discretization of (a) $\Delta_x = 50$ m, (b) $\Delta_x = 25$ m and (c) $\Delta_x = 10$ m. The corresponding RMS and χ are displayed below each 2D model.*

- The *SLDMem3t* modeling errors are analyzed by comparing each column of the 2D model separately with the analytical 1D response. This approach is used as a final grid check, to validate the accuracy of the *SLDMem3t*.

Data fit and distribution of residuals

The 2D model for the coarse discretization in Fig. 5.18(a) quantitatively explains the field data best. The global fit $\chi = 1.49$ is not much worse than for the quasi 2D resistivity-depth section derived from the Occam R1 results. In Fig. 5.18(b), the distribution of the data residuals $(d_{obs} - d_{calc})/\delta d^*$ are plotted for each time point along the profile. For comparison, the total error estimate δd^* is discussed in section 5.3.7. The residuals generally range between ± 5 and seem more systematically distributed towards larger values. Especially between sounding A34 and A50 and at late times the residuals increase. Obviously, the larger residuals occur mainly in the transition zone, where the subsurface structure is more two-dimensional. Southwest of sounding A52, on the low resistive mudflat, the data fit is almost optimal with $\chi \approx 1$. Likewise, the residuals are very small northeast of sounding A33. Moreover, the alternation of the residual sign seems systematic, although the deviations are small. A few large outliers are present, which deteriorate the global fit. If 1% of the data (13 data points) with the largest residuals are neglected, the χ improves by 24% from 1.49 to $\chi = 1.14$. This demonstrates that the ℓ^2-norm residual calculation is prone to outliers. The distribution of residuals as a histogram and QQ-plot is shown in Fig. A.21 in the appendix. The QQ-plot indicates a non-normal distribution particularly for the largest residuals. In

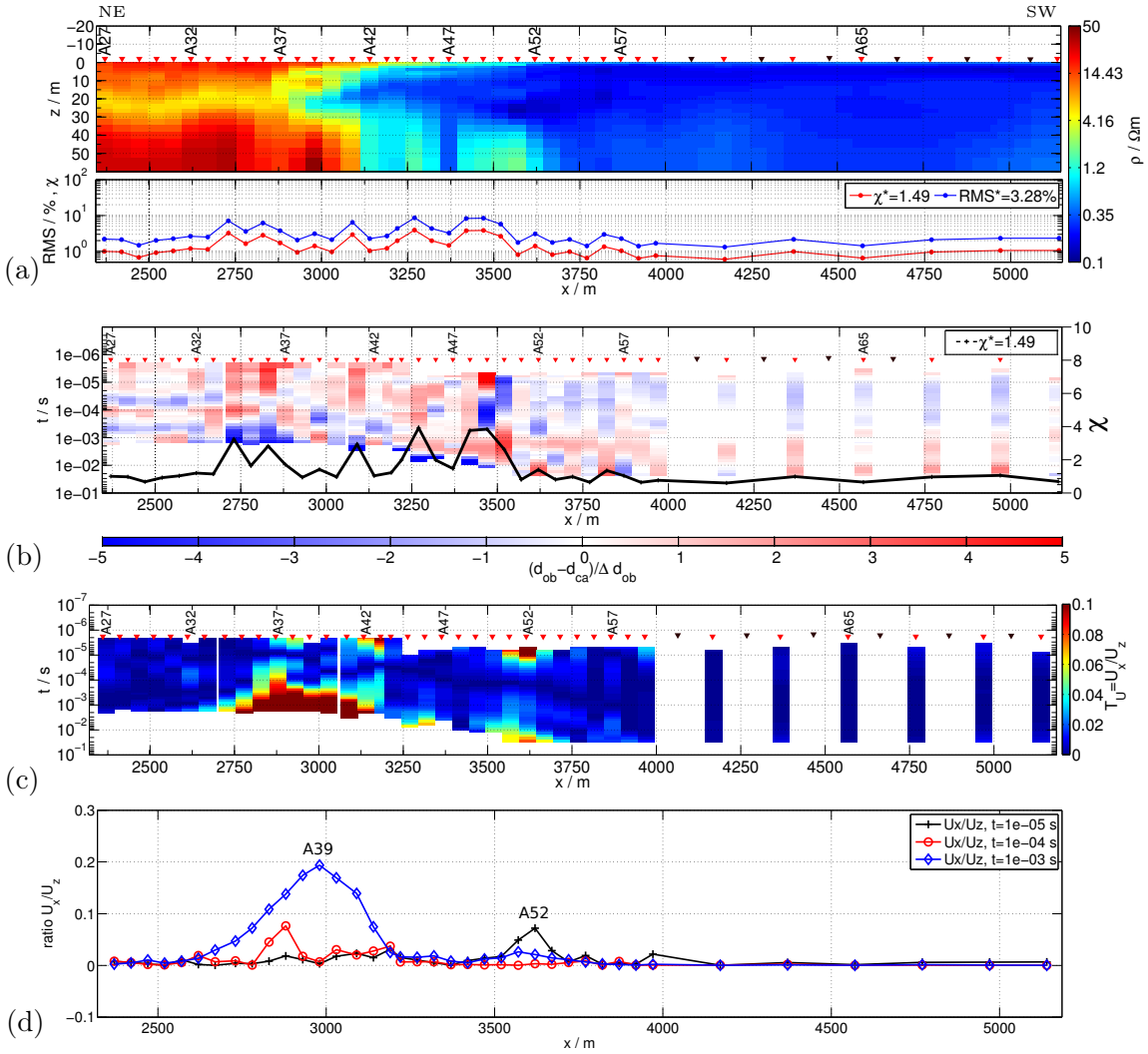

Figure 5.18: *(a) Best-fit 2D model derived from 1D Occam results. (b) Distribution of residuals for each time point and sounding plotted against the profile line. (c) TEM-tipper $T_U = U_x/U_z$ calculated from the field data (U_z) and the synthetic horizontal induced voltage response (U_x). (d) Ratio of U_x/U_z plotted for three distinct time points versus the sounding location.*

Fig. 5.19 the observed and calculated data are shown for three soundings: A27, A41 and A71. The data fit is not that good for sounding A41 in particular for the last decade of time, resulting in a χ of 2.9 and large late time residuals. The other soundings are fitted optimal with $\chi \approx 1$.

Analyzing 2D effects by the TEM tipper

In section 5.4 the 2D effect is analyzed on the basis of a simplified 2D vertical fault model. The TEM-tipper T_U is now used to investigate how much 2D effect the best-fit model in Fig. 5.18(a) would produce. Since the horizontal component of the voltage response U_x was not measured in the field, the TEM-tipper is calculated from a synthetic U_x and from the measured field data $U_{ind,z}$. This semi-synthetic TEM-tipper T_U is displayed in Fig. 5.18(c) as a colorcoded section. Spies & Frischknecht [1991] stated that for values $T_U < 0.1$ the TEM data can be interpreted in 1D. For the best-fit model, T_U is less than 0.1 for almost all soundings and time points, except between

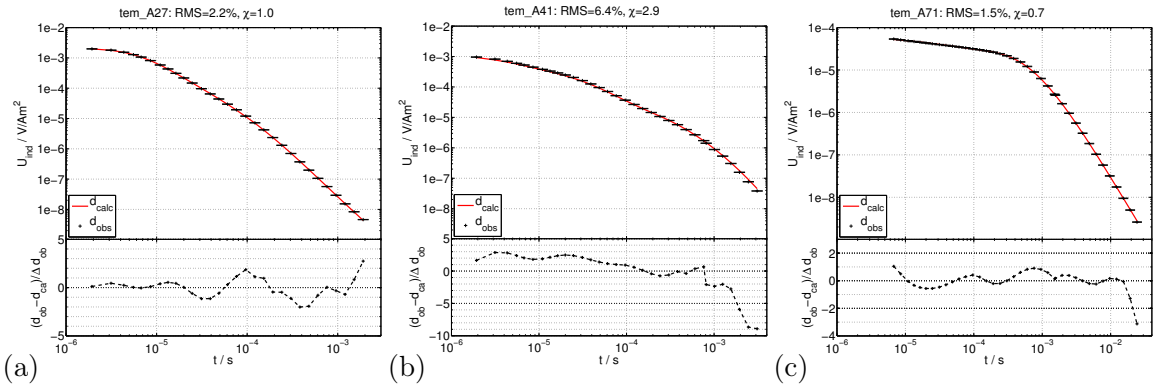

Figure 5.19: *Observed and calculated data for the 2D best fit model for sounding (a) A27, (b) A41 and (c) A71. The residual is displayed below the corresponding plot*

sounding A36 and A41. The lateral resistivity variation is most significant in that zone. Sounding A37 coincides with the shallow inset of the good conductor. Compared to the neighboring soundings, the tipper value is increased already at earlier times for that sounding. According to Fig. 5.18(d), T_U is maximal for the last time point $t = 10^{-3}$ s at sounding A39. Moreover, the larger T_U values coincide partly with the larger late time residuals shown in Fig. 5.18(b). Therefore, it is possible that these larger late time residuals are due to a 2D effect in the TEM data.
The benefit of the semi-synthetic TEM-tipper is limited because the horizontal magnetic voltage response was not measured in the field. However, it is an alternative approach to that suggested by Bedrosian et al. [2013], where a 1D background model response is subtracted from the 2D response (for comparison see section 5.4.2). For future TEM surveys over strong lateral subsurface contrasts, measurements of U_x may provide useful additional information. A drawback is that an accurate $\dot{B}_x$-configuration is difficult to realize in the field. If the receiver is not placed exactly in the center of the transmitter loop, a significant response is measured [Newman et al., 1987]. Therefore, one has to know the exact position for a quantitative interpretation of the horizontal voltage response.

SLDMem3t modeling errors derived from final 2D model

In order to investigate the *SLDMem3t* modeling errors, a 1D grid check is performed for the best fit 2D model in Fig. 5.18(a). At first a 1D model is extracted from the 2D model beneath each sounding location. Then the 1D response is calculated with the *SLDMem3t* and compared to the analytical solution with *EMUPLUS*via the *RMS*. The obtained residuals are plotted for each time point versus the sounding location in Fig. 5.20. It is obvious that the deviations are of systematic nature, although they are maximal around ±3%. Recalling the theory to the *SLDMem3t* in section 5.1, a major accuracy limitation is the FD formulation itself, i.e. the discretization of the $\nabla \times \nabla \times$-operator into the system matrix. Therefore, systematic deviations are plausible. Slightly larger residuals are present for later times between sounding A39 and A46. These are reflected in an *RMS* increase up to around 1.5%. The resistivity decreases at depth in that zone and the accuracy of the designed late time grid slightly deteriorates.
From the grid check presented in section 5.3.7, a constant *SLDMem3t* modeling error δd_{sld} =1.5% is assumed for the sake of simplicity. Now, from the final grid check a global *RMS* of 0.72% is derived. Actually only for two soundings the misfit is around 1.5%.

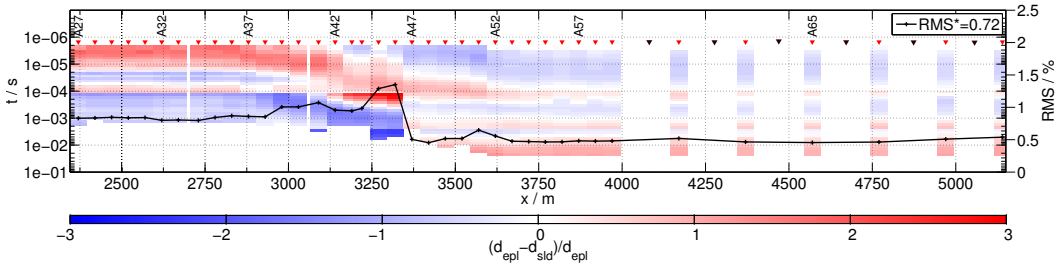

Figure 5.20: *SLDMem3t grid check for the best fit 2D model. A 1D model is extracted beneath each sounding location of the 2D best fit model in Fig. 5.18(a). The residuals are calculated from the 1D numerical and 1D analytical solutions. The black line denotes the RMS calculated for each sounding.*

The designed overlapping grids obviously produces very stable results for all soundings and a wide resistivity range.

5.5.3 2D model derived from 1D Marquardt results

The previously presented 2D model in Fig. 5.18(a) already explains the field data well, but does not exhibit distinct boundaries. Thus, it is not suitable for a systematic 2D modeling study. In order to derive a 2D model which is suitable for a systematic forward modeling study, the quasi 2D Marquardt resistivity-depth section presented in section 4.7.2 is interpolated onto a 2D model grid. The focus is on the transition zone from the moderate resistive basalt formation to the low resistive mudflat along profile A. Particularly, on the low resistive mudflat the EM skin depth is small for the earliest transient time ($\delta_{FD} \approx 0.5$ m). To avoid interpolation errors, the vertical discretization Δ_z of the 2D model is constructed separately from each Marquardt 1D model. As a result, a large amount of grid lines in z-direction are required. With this approach it is possible to image the 1D stitched Marquardt section exactly.
In Fig. 5.21, the 2D model derived from the 1D stitched Marquardt results between sounding A27 and A71 is displayed. The global χ is 1.45 and as good as for the 2D model derived previously from the 1D Occam results. Both models are well comparable, except that the 2D Occam model shows a shallow resistive feature at sounding A39. Although not present in the 2D Marquardt model, the fit does not increase around that sounding and is generally satisfactory along the profile line. Obviously both derived 2D models, the Occam- and Marquardt-type explain the field data well and are more or less equivalent according to the data fit.

The 2D Marquardt model in Fig. 5.21 has distinct layer boundaries and is suitable for the perturbation of selected zones, i.e. a systematic forward modeling study. The basalt layer zone beneath the high conductive mudflat is now varied to investigate if it is redundant or supported by the field data. The lateral extent of the basalt layer is varied between sounding A39 and A52. Furthermore, the resistivity and upper layer boundary is varied.

Lateral extent and resistivity of the basalt layer
In Fig. 5.22, the modified best fit 2D Marquardt model is presented. The lateral continuation of the resistive basalt towards southwest (indicated by a red line) is interrupted

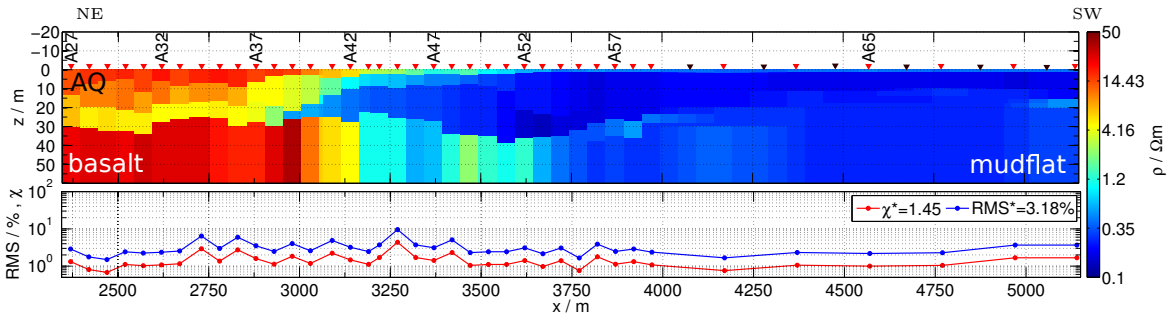

Figure 5.21: *2D model derived from 1D stitched Marquardt results for soundings A27 to A71 along profile A. The corresponding χ and RMS for each sounding location is displayed below the model.*

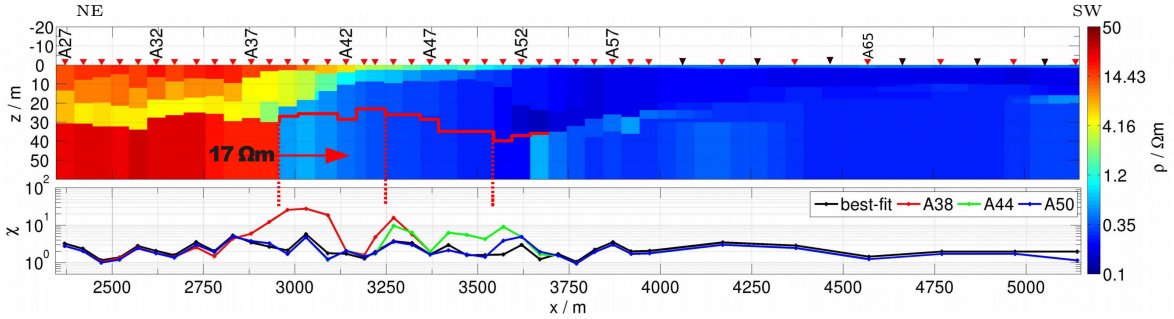

Figure 5.22: *Variation of the resistive basalt layer between sounding A39 and A52. The top of the layer is depicted as a red line and interrupted after sounding A38, A44 and A50. The resistivity is chosen homogeneous with 17 Ωm. The corresponding χ are displayed below the model.*

after sounding A38, A44 and A50. The resistivity is chosen homogeneous with 17 Ωm. The following conclusions are derived:

- If the resistive basement is completely removed, the χ, displayed in Fig. 5.22 as a red line, increases compared to the best fit χ (black line). Although the layer is interrupted after sounding A38, two soundings left of A38 are affected. The χ for those soundings also deteriorates.

- If the layer is continued until sounding A44, the χ marked as a green line in Fig. 5.22 differs everywhere right of that sounding. Left of sounding A44, χ matches the best fit χ.

- If the resistor extends until sounding A50 (blue line), only the three following soundings indicate a slightly increased χ. Everywhere else it matches the best fit χ (black line).

Except for three soundings (A43, A44 and A47), the resistor is generally supported by all other soundings. Therefore, the lateral extent of the resistor below the high conductive mudflat sediments is required to fit the data.
To investigate the upper and lower resistivity bounds of the base layer between sounding A39 and A52, it is varied from $\rho = 0.1$ to 20 Ωm. According to the best-fit 2D Marquardt model in Fig. 5.21, the average resistivity ranges around $\rho \approx 1 - 2$ Ωm. In Fig. 5.23 the field data and the calculated response are displayed for a base layer resistivity of $\rho = 0.1$, 2 and 20 Ωm. If the resistivity is set to 0.1 Ωm the late time data

is not fitted. In contrast to that, the residuals which are plotted below the transients, do not change much if the resistivity is increased from 2 to 20 Ωm. This shows that the upper resistivity limit is not well resolved.

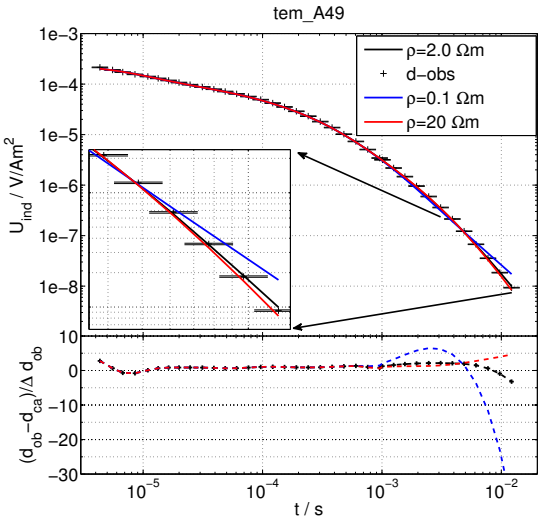

Figure 5.23: *Field data and calculated 2D response for sounding A49. The resistivity of the base layer is varied between sounding A38 and A52 as displayed in the legend. The corresponding residuals are plotted below the transients.*

Variation of the depth to the basalt layer

To further investigate the impact of the base layer on the model response, the depth to the base is slightly varied. The original best fit model is drawn as a white line in Fig. 5.24. At first, the depth to the base layer is minimized as indicated by the red line. Afterwards, the depth is increased to $z \approx 30$ m.

The best-fit χ is displayed as a black line for each sounding in Fig. 5.24. If the depth to the base layer is decreased (green line), χ increases significantly for all soundings between A38 and A52. Likewise, χ increases if the depth to the base layer is increased. Soundings A42, A46 and A47 are exceptions because the transients are slightly shorter. The comparison of the field data and the calculated response for sounding A41 in Fig. 5.25 demonstrates the influence of the layer depth. In both cases, the late time data is not fitted and the residuals are large.

Although the variation of the depth to the resistor is marginal below sounding A39, it has a significant impact on the data fit. For this reason, the inset of the thin good conductor below sounding A39 in roughly 20 m depth is evident. At least for this model, it is not possible to fit the data well without it.

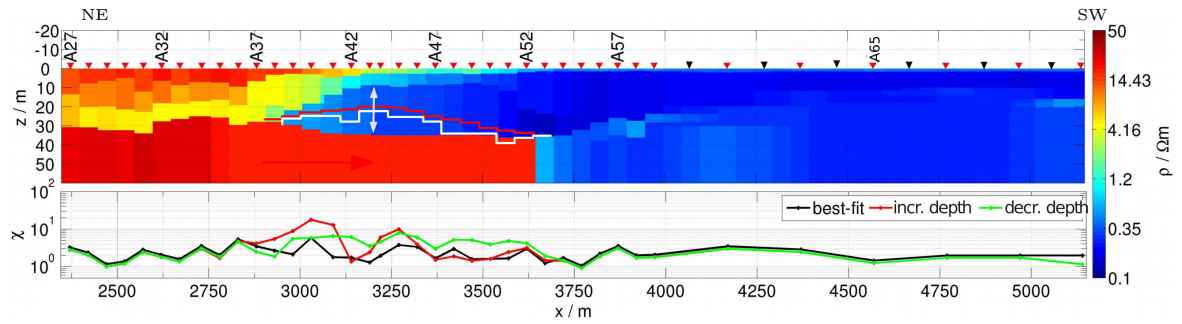

Figure 5.24: *Variation of the depth of the base layer between sounding A39 and A50. The original best-fit model is depicted as a white line. The minimal depth of the layer is indicated by the red line. The corresponding χ for each depth variation is displayed below the model.*

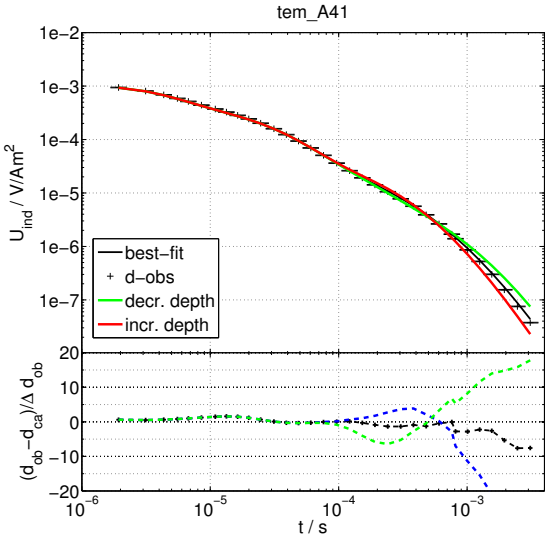

Figure 5.25: *The field data and calculated 2D response are displayed for sounding A41 for a variation of the depth to the basalt layer (as shown in Fig. 5.24). The corresponding residuals are plotted below.*

Discussion of lateral extent of the basalt layer

Recalling the geological map and cross-section presented in Fig. 4.2, the basalt layer is supposed to be interrupted around sounding A41 and to coincide with the Al Bayda fault. Based on the modeling results of the Tx-50 data, it is evident that the resistor is extended at least up to sounding A52. Further southwest of sounding A52, the depth of investigation of the Tx-50 configuration is not sufficient to resolve the base of the mudflat. Conclusively, it can be said that the modeling study validates the resistivity-depth section along profile A, which was derived from 1D models in chapter 4. For comparison refer to the 1D stitched results in Fig. 4.16.

5.6 2D forward modeling of Tx-100 sounding data: deep mudflat base

In the second field survey 47 soundings were obtained with the Tx-100 configuration to investigate the more resistive and deep base below the high conductive mudflat. According to the geological information in section 4.2, the base is a chert limestone formation (URC). The 1D stitched models, presented in section 4.7.4 and section 4.7.5, generally show the resistor at depth along both profiles. But, not all soundings supported the resistivity increase similarly within the data errors and some uncertainties remain. To verify the deep basement structure for all soundings simultaneously along each profile, a 2D forward modeling study is performed.

5.6.1 Validation of the mudflat base along profile A

The 2D best-fit model constructed from the 1D stitched Marquardt models obtained along profile A is displayed in Fig. 5.26(a). The focus is on the zone between sounding A27 and A*80. The 2D modeling is performed at first for the original model, where the base structure is included. Secondly, the base is removed between sounding A42 and A*80. Afterwards the depth to the base and the base resistivity is varied.

Base removed southwest of A42
Compared to the best-fit 2D model in Fig. 5.26(a), the global χ increases from 2.13 to 4.33 if the resistor is removed. The best-fit χ is denoted by a red line and the calculated χ, if the base is removed, is drawn magenta in Fig. 5.26(b). Between sounding A*55–A*61 and A*72–A*74, the removal of the resistive base does not affect the data fitting. This is also obvious from the error weighted residuals for each sounding displayed in Fig. 5.26(c). No larger residuals are visible at late times for the soundings A*57 to A*62 and only slightly larger ones are obtained between A*72 and A*74.
Exemplarily, two soundings (A*55 and A*73) are plotted in Fig. 5.28(a,b). Although χ does not change if the resistor is removed, it is clearly supported by the data obtained at sounding A*55. The same applies to sounding A*73, where the last 3 data points are not fitted if the resistor is removed although χ does not increase. Moreover, for both soundings the residuals plotted below the transients in Fig. 5.28(a,b) increase at late times. In total 19 soundings obtained with the Tx-100 setup support the resistor at depth clearly within the data errors. For the other 8 soundings the errors are larger at late transient times and the resistor is less significant.
Nevertheless, the general trend of the $\rho_{a,lt}$ data is consistent for all soundings. If the data errors are not considered and the *RMS* is calculated instead of χ, all Tx-100 soundings (except A*57 and A*59) indicate a significantly deteriorated data fit. This is obvious from Fig. 5.26(d) and shows that the TEM data in general supports the resistor at depth.

Depth to base
In the next step, the interface is decreased to z =70 m depth between sounding A*57 and A*65. The interface is denoted by a dashed orange line in Fig. 5.26(a). According to the black line in Fig. 5.27(a), χ deteriorates for all soundings between A*57 and A*65. By further decreasing the depth to $z = 55$ m between sounding A*57 and A*74, the fit also deteriorates (blue line). It can be said that the upper/minimum depth to the resistor in the original 2D model is well supported by the data.

Base resistivity
Finally, the base resistivity is varied from $\rho = 0.5$ to 2.5 and to 100 Ωm between sounding A42 and A*80. In Fig. 5.27(b), χ is plotted for the best-fit model response (red line) and the modified 2D model response. For ρ=0.5 Ωm, χ significantly deteriorates between A42 and A*55 (black line). Conclusively, the base resistivity must be larger than 0.5 Ωm in that zone. The same applies to a few soundings southwest of A*62, where χ deteriorates. A base resistivity of ρ=2.5 Ωm and 100 Ωm does not change the global fit much, compared to the best fit of the original model. Therefore, the lower resistivity bound ranges between 0.5 and 2.5 Ωm. The upper bound is at least 100 Ωm, or even more.

5.6.2 Validation of mudflat base along profile B

Profile B is now investigated by a similar 2D modeling study as done for profile A. Since the northernmost part of profile B is already inside the mudflat zone, the base is varied along the complete profile. In Fig. 5.29(a), the 2D model constructed from the 1D Marquardt models is displayed. In comparison to profile A, a resistivity increase occurs partly at shallower depth.

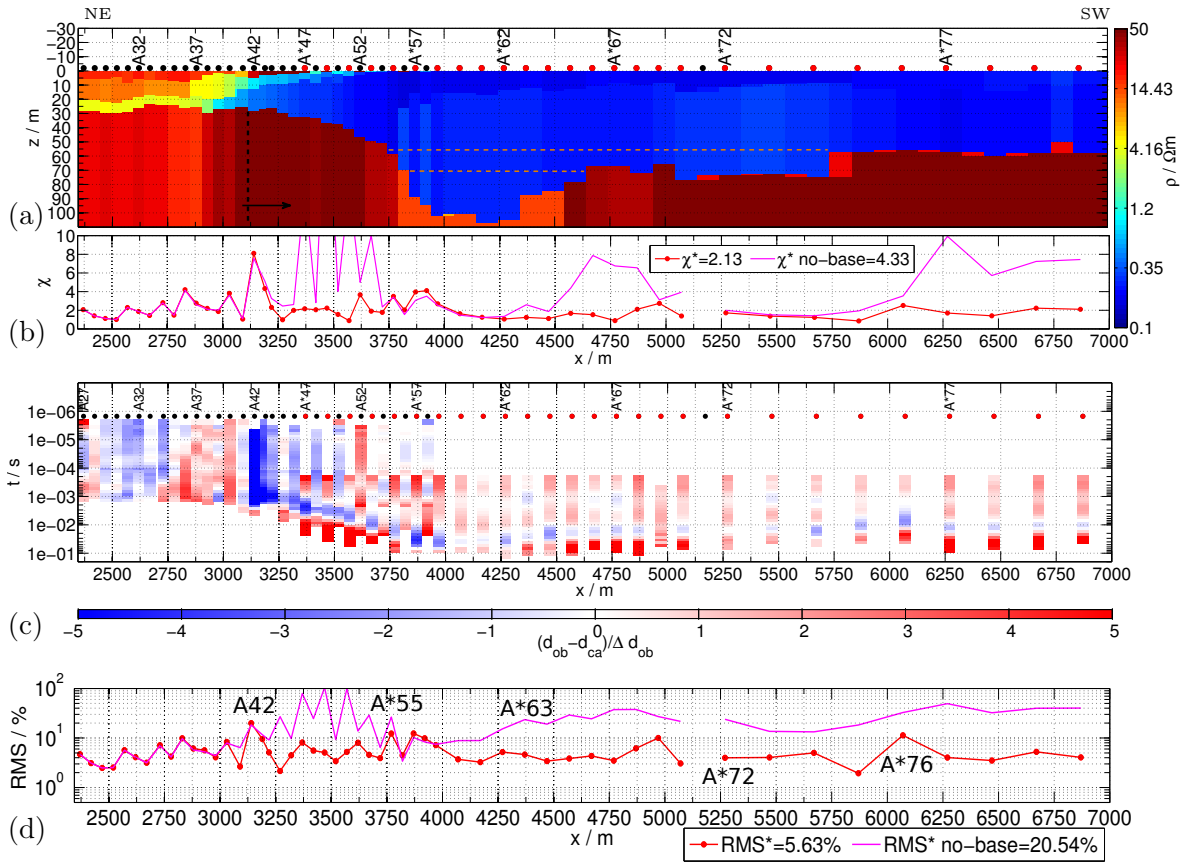

Figure 5.26: *(a) 2D model derived from 1D stitched Marquardt results along profile A. The Tx-100 soundings are included and their locations are marked as red dots above the model. (b) Base removed southwest of A42: below the 2D model, the best-fit χ is plotted for each sounding (red line). If the resistor at depth is removed between A42 and A*80, the magenta plotted χ is obtained at each sounding. (c) residuals calculated from the 2D model response without base structure for each time point and sounding. (d) Same plot as in (b), except that the RMS without error-weighting is shown.*

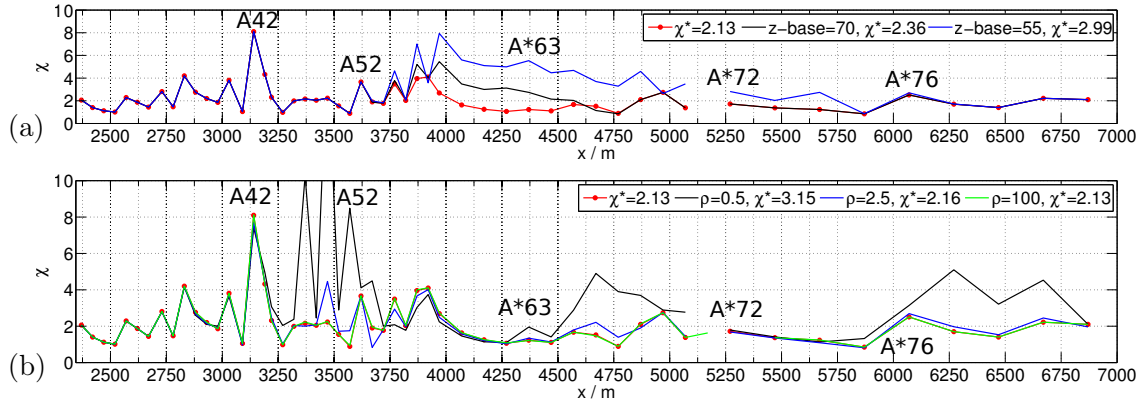

Figure 5.27: *Consider the model in Fig. 5.26. (a) Depth to base (dashed orange lines in the model): χ after increasing the depth to the base to $z = 70$ m between sounding A*57 and A*65 (black line); χ after decreasing the depth to base to $z = 55$ m between sounding A*55 and A*75 (blue line). (b) Base resistivity: calculated χ after a resistivity variation from ρ=0.5, 2.5 to 100 Ωm.*

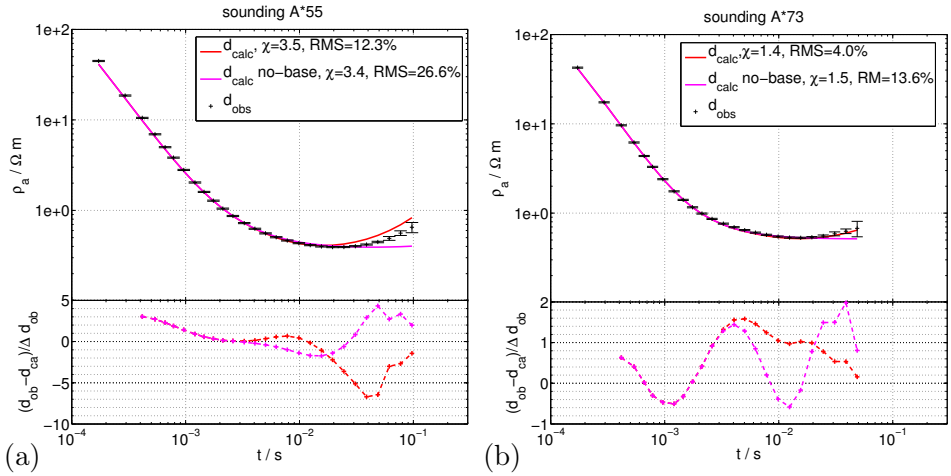

Figure 5.28: *Data and 2D model response for (a) sounding A*55 and (b) sounding A*73. The response without the base is denoted in magenta. The corresponding residuals are plotted below the transients. The χ and RMS values are given in the legend*

Base removed along the complete profile

The original 2D best-fit model has a global fit of $\chi = 2.3$. If the resistor at depth is removed along the complete profile, the global fit deteriorates to $\chi = 5.02$. As indicated by the magenta line in Fig. 5.29(b), the resistor is required to fit the data between B1 and B12. In that zone, only Tx-50 soundings were recorded. Further southeast, between B13 and B17, the fit does not change and the slight resistivity increase is uncertain. In contrast to that, the comparably shallow resistivity increase southeast of B17 is again supported by the data. As a result, χ increases between B17 and B26, if the last layer is removed.
Due to the limited *doi* of the Tx-50 soundings, southeast of B27 only the Tx-100 soundings should be considered. According to the χ, five Tx-100 soundings between B*33 and B*40 do not support the resistor at depth. Likewise, the residuals plotted in Fig. 5.29(c) do not indicate large late time deviations in that zone. Exceptions are sounding B*35 and B*37, which show slightly larger residuals, although χ does not change. Concluding, six of twenty soundings recorded with the Tx-100 setup do not support the basement structure within their data errors. These are B*20, B*27, B*33 and B*38 to B*40.
If the data errors are neglected and the *RMS* is calculated instead of χ, all soundings (except B*20 and B*27) show a significantly deteriorated fit (cf. Fig. 5.29(d)). This is a clear indication that the general trend of the late time data supports the resistivity increase for all soundings.

Exemplarily, the field data and 2D model response is displayed in Fig. 5.30(a,b) for sounding B*18 and B*37. The data for sounding B*18 clearly indicates the late time apparent resistivity increase and is not fitted if the base layer is removed. The same applies to sounding B*37, although χ does not increase much if the resistor is removed. According to the *RMS*-values given in the legend of Fig. 5.30(b), the fit changes from 7% to 21.5%. Moreover, the residuals plotted below the transient increase at late times.

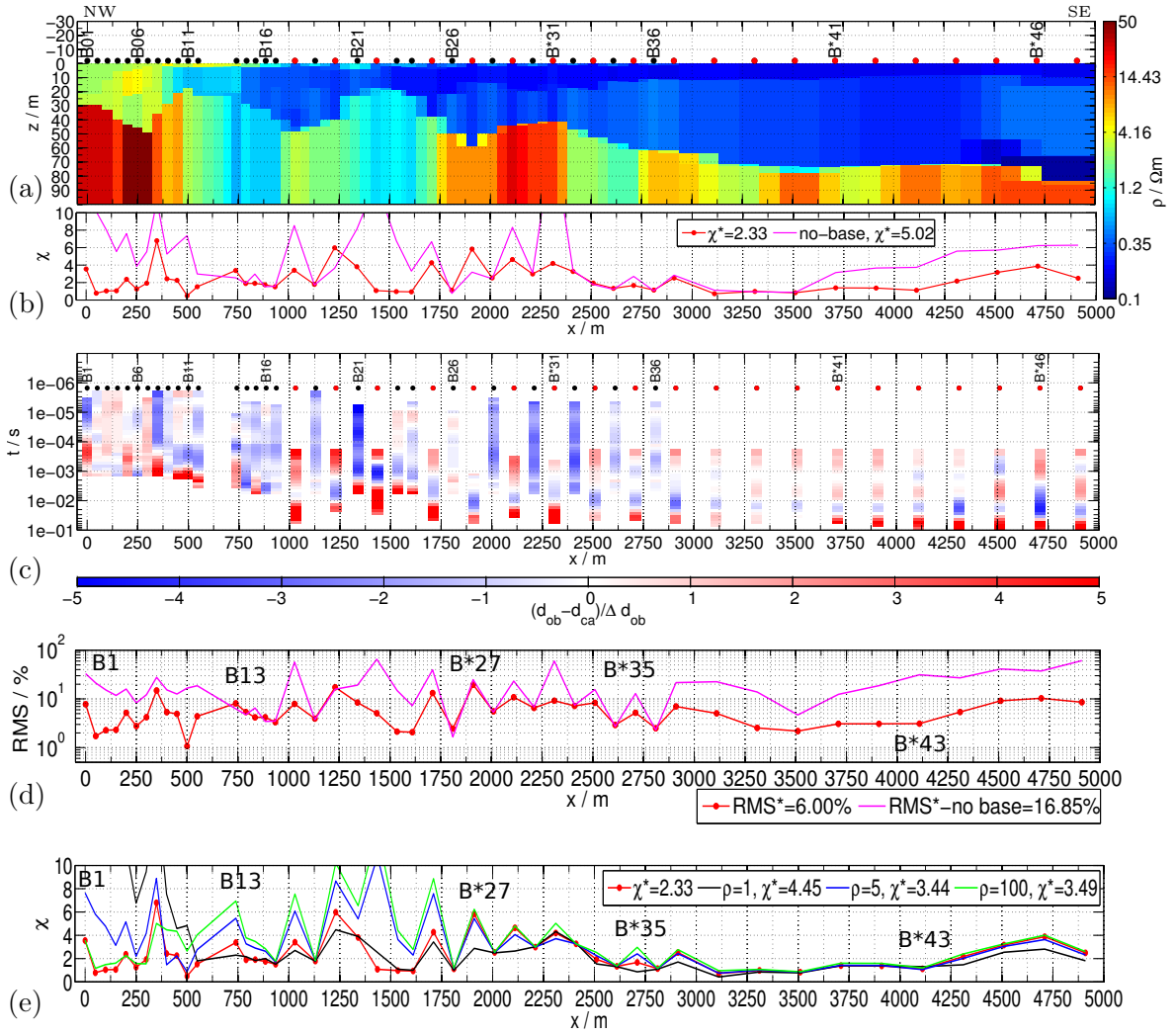

Figure 5.29: *(a) 2D model derived from 1D stitched Marquardt results along profile B. The Tx-100 soundings are included and their locations are marked as red dots above the model. (b) Base layer removed along the complete profile: below the 2D model, the best-fit χ is plotted for each sounding (red line). If the resistor at depth is removed, the magenta plotted χ is obtained at each sounding. (c) Residuals calculated from the 2D model response without base structure for each time point and sounding. (d) Same plot as in (b), except that the RMS is calculated instead of χ. (e) Changing the base resistivity: calculated χ after varying the base resistivity from ρ =1 to 5 and to 100 Ωm.*

Base resistivity

The χ is displayed along the profile line for three different base resistivities in Fig. 5.29(e). It deteriorates significantly northwest of B12, if ρ is decreased below $\rho \leq 5$ Ωm. In contrast to that, it does not change if ρ is set to 100 Ωm (green line). In this zone, the buried basalt is expected and higher resistivities are present at depth. Further southeast, in the zone between B12 and B*47, the fitting is best for ρ=1 Ωm resistivity (black line). For a few soundings the fit is slightly improved compared to the fit of the original model. Between sounding B12 and B26 the fit deteriorates significantly for a base resistivity larger than $\rho \geq 5$ Ωm (blue line). Obviously lower resistivities are present at shallow depths in that zone.
Compared to the fit of the original 2D model (red line), the fit does not change even

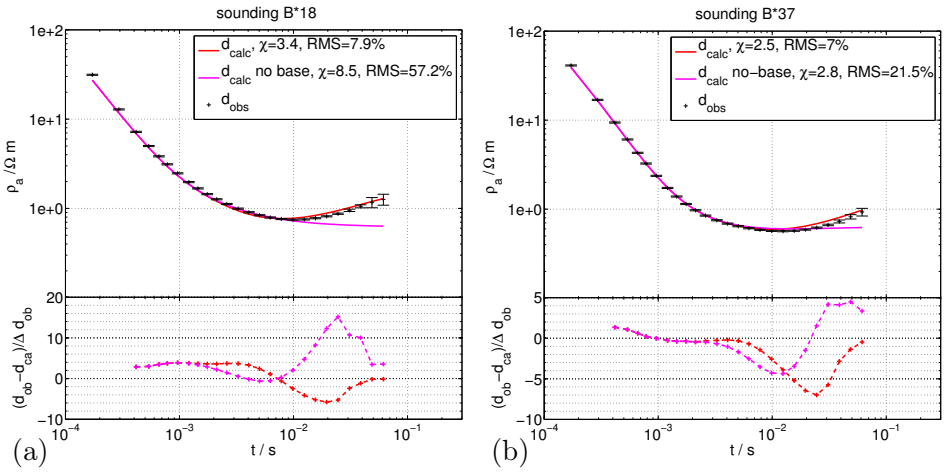

Figure 5.30: *Field data and 2D model response for (a) sounding B*18 and (b) sounding B*37. The model response without the base is denoted in magenta and the best-fit response in red. The corresponding residuals are plotted below the transients. The χ and RMS values are given in the legend.*

for a base resistivity of $\rho = 100$ Ωm southeast of B26 (green line). Therefore, the upper resistivity bound is not resolved and may be even larger than 100 Ωm. According to the deteriorated χ in Fig. 5.29(b), where the base is removed, the lower resistivity bound must be larger than 0.3 Ωm. The reason is that $\rho = 0.3$ Ωm is approximately the resistivity of the overlaying mudflat sediments. Since the fit does not deteriorate much for $\rho = 1$ Ωm, the lower resistivity bound is between $\rho = 0.3$ and 1 Ωm southeast of B26.

5.6.3 Discussion of the base layer below the mudflat

According to the geological information, the chert limestone formation (URC) is present below the mudflat sediments. This expected resistor is validated along both profiles. Although a few soundings do not support the resistor well within the measurement errors, the global χ significantly deteriorates if the resistor is removed. Furthermore, the residuals usually increase at late times. If the data errors are not considered and the *RMS* is calculated instead of χ, nearly all soundings significantly support the resistor along both profiles. This clearly shows that the general trend of the data is similar for all soundings and verifies the resistivity increase below the mudflat.
Moreover, the base is at least as deep as it is in the original best-fit 2D model along profile A. If the depth is decreased, the late time data is not fitted. It should be noted that in general the resistivity is not resolved well for both profiles. The resistivity can increase at least up to $\rho = 100$ Ωm and down to 2.5 Ωm without deteriorating the data fit along profile A. Along profile B, the base resistivity can drop down to $\rho \approx 1$ Ωm. An exception is the buried basalt northwest of sounding B12, where resistivities larger than 5 Ωm are required to fit the data. The upper resistivity bound is at least 100 Ωm for the base layer, except between sounding B13 and B26, where resistivities less than 5 Ωm are obviously present and the interface is very shallow.

5.7 Conclusions from the 2D forward modeling results

Extending the work of Martin [2009], an effective way was presented to obtain a suitable calculation grid for the *SLDMem3t*. The approach was also useful to check the accuracy of the solution for a wide resistivity range and various resistivity contrasts. Furthermore, a qualitative approach was suggested which can be used to analyze if the lateral grid discretization is sufficient to sample the model resistivity distribution and to verify if a grid refinement is required.
At first a synthetic 2D fault model was constructed, which is a simplification of the resistivity structure between sounding A27 and A71 along profile A. The 2D effect on synthetic TEM data was demonstrated on the basis of this model. Further analysis of the synthetic data showed that three to four synthetic soundings up to 200 m fault distance are significantly 2D affected within the acquisition time range of the field data. In the second step, a 2D model was derived from the stitched 1D inversion results between sounding A27 and A71. The 2D model generally explains the field data well and only slightly larger residuals are present, where the lateral resistivity variation is maximal. The global fit of the 2D model is almost optimal with $\chi \approx 1.5$ and comparable to the global fit of the 1D stitched models. Therefore, the 2D modeling results validate the 1D inversion results. As a conclusion it can be noted that the 1D interpretation of the TEM field data is obviously sufficient, although a strong lateral resistivity variation is present. The good interpretability of TEM data by 1D layered earth models is a well known advantage of the method [Spies & Frischknecht, 1991; Goldman et al., 1994].
Moreover, an attempt was made to estimate the 2D effect which the final best-fit model produces. A semi-synthetic TEM-tipper was calculated from horizontal synthetic voltage data (U_x) and the field data (U_z). The TEM-tipper shows that maximal six soundings are 2D affected at late transient times. Certainly, the benefit of this approach is limited because the 2D model was derived from vertical voltage data and the horizontal component of the magnetic field was not measured. For future TEM surveys over strong resistivity contrasts the measurement of the horizontal voltage component may provide useful additional information of the subsurface dimensionality and whether a 1D interpretation is adequate.
To investigate the base below the mudflat, the 2D models along both profiles were further investigated by variation of the deep resistive layer. The 2D modeling demonstrated, that the resistor is generally required to fit the field data. Some soundings exhibit larger errors at late times and do not support the resistor as well as other soundings. If the data errors were not considered in the modeling, all soundings clearly support the resistivity increase at depth. As a consequence the late time data is not fitted and the *RMS* significantly deteriorates. As it is common for the TEM method, the base resistivity is not well resolved. Therefore, it can vary roughly between 2.5 Ωm and 100 Ωm in most zones and along both investigated transects.

A drawback of the 2D modeling is, that it was based on the prior selection of a model. In the case presented here, it was a one-to-one image of the stitched 1D models derived in section 4.7. Therefore, the 2D modeling is not an independent validation of the subsurface resistivity distribution. In order to obtain a less biased and more independent validation of the subsurface, more number of soundings are interpreted using the 2D TEM inversion scheme *SINV*. The results are presented in the following chapter 6.

CHAPTER 6

Two-dimensional TEM inversion

The large scale inversion algorithm *SINV* has been mainly used for the 2D interpretation of LOTEM data generated by a grounded bipole transmitter [Scholl et al., 2004; Martin, 2009]. Commer [2003] originally introduced the algorithm to perform a restricted 3D inversion of LOTEM data with only a few model parameters and termed the code *SINV* (*S*parse *INV*ersion). It was recently extended by Martin [2009] to allow for a full large scale 3D inversion. He successfully applied *SINV* to synthetic data over a buried conductor using either a bipole or a loop transmitter configuration with multiple receivers. Koch et al. [2004] presented a 2D inversion of central loop TEM data using an early version of *SINV*. Nevertheless, the algorithm was not routinely tested for the inversion of central loop TEM data in two dimensions, yet.

To gain insights into the inversion algorithm, its optimization and regularization scheme, *SINV* is applied to two synthetic models in the following. The major focus is the investigation of (a) the influence of the model parameterization on the inversion process; (b) the possibilities of building in a-priori information; (c) the pareto optimization of the regularization parameters. Particularly, the pareto optimization is a key issue of the inversion process.

In the previous chapter 4, quasi 2D resistivity depth-sections were derived along both profiles A and B by patching together 1D results. Since the structure is essentially 2D in the transition zone from the basalt formation to the high conductive mudflat, the question was raised if a 1D interpretation is adequate. Therefore, 2D models were derived from the 1D stitched sections previously in chapter 5. The 2D models generally explain the field data well and the structure along both profiles was verified by a 2D modeling study. In spite of this, the 2D modeling study was based on a-priori information derived from 1D results and, therefore, it is to some extent biased.
To provide an independent validation of the subsurface resistivity structure, the 2D inversion is applied to the field data. The focus is on profile A because it covers the complete transition zone, whereas the northwestern end of profile B is already located on the mudflat (cf. Fig. 4.2). In the first step, a subsurface 2D inverse model is derived from the Tx-50 soundings between A27 and A59 in the transition zone, where the structure is essentially 2D. The obtained results are briefly discussed with respect to the sensitivity/coverage, the choice of an appropriate initial model, the model parameterization, the pareto optimization and the computational requirements of the 2D

inversion. In the second step, the data recorded with the Tx-100 setup are included to independently reconstruct the base below the mudflat by using the 2D inversion. A total number of 53 soundings are inverted between A27 and A80*. The example also presents a convenient and promising approach to incorporate a-priori information into the initial model parameterization.

6.1 The inversion scheme *SINV*

The basic inversion concepts of geophysical field data introduced in chapter 3 are also valid for the two dimensional inverse problem. Thus, similar notations are used in the following.
The inversion algorithm *SINV* allows for the spatial reconstruction of the subsurface resistivity distribution in two and three dimensions. It uses the iterative Gauss-Newton minimization technique, where the full Jacobian matrix is explicitly calculated in each iteration. Therefore, a fast, accurate and stable forward solver is required. In the inversion scheme *SINV* the 3D finite difference time domain solver *SLDMem3t* is implemented, which is presented in detail in chapter 5. Moreover, *SINV* is a hybrid scheme and combines the damped Marquardt, the steepest descent and the roughness constraint Occam techniques. These common techniques for solving the non-linear inverse problem are described in chapter 3. For a 2D resistivity distribution the objective function reads

$$\begin{aligned}\Phi &= \Phi_d + \beta\Phi_{m,1} + \lambda_{x,z}\Phi_{m,2} \\ &= \boldsymbol{\epsilon}^T \boldsymbol{W}_d^2 \boldsymbol{\epsilon} + \beta(\Delta \boldsymbol{m}_k^T \Delta \boldsymbol{m}_k) + [\lambda_x(\boldsymbol{m}^T \boldsymbol{R}_x^T \boldsymbol{R}_x \boldsymbol{m}) + \lambda_z(\boldsymbol{m}^T \boldsymbol{R}_z^T \boldsymbol{R}_z \boldsymbol{m})]. \end{aligned} \tag{6.1}$$

Where $\boldsymbol{W}_d^2 = \boldsymbol{W}_d^T \boldsymbol{W}_d$ is the squared diagonal $N \times N$ weighting matrix, $\boldsymbol{\epsilon} = (\boldsymbol{d} - \boldsymbol{d}')$ is the error-vector, $\Delta \boldsymbol{m}_k$ is the model update in the k-th iteration and $\boldsymbol{R}_x$, $\boldsymbol{R}_z \in \mathbb{R}^{M \times M}$ are two dimensional roughness matrices. Only first order roughness is used for all inversions. The regularization parameters β and $\lambda_{x,z}$ balance the model cost-functions $\Phi_{m,1}$ and $\Phi_{m,2}$, respectively. Since a smooth model $\boldsymbol{m}_{k+1}$ is sought, $\boldsymbol{m}$ is replaced with $\boldsymbol{m} = \boldsymbol{m}_k + \Delta \boldsymbol{m}_k$. Minimization of Φ with respect to $\Delta \boldsymbol{m}_k$ leads to the following normal equation in each k-th iteration:

$$\begin{aligned}\Delta \boldsymbol{m}_k = &(\underbrace{\boldsymbol{J}^T \boldsymbol{W}_d^2 \boldsymbol{J} + \beta \boldsymbol{I} + \lambda_x \boldsymbol{R}_x^T \boldsymbol{R}_x + \lambda_z \boldsymbol{R}_z^T \boldsymbol{R}_z}_{:=\boldsymbol{G}})^{-1} \\ &[\boldsymbol{J}^T \boldsymbol{W}_d^2 (\boldsymbol{d} - \boldsymbol{F}(\boldsymbol{m}_k)) - \lambda_x \boldsymbol{R}_x^T \boldsymbol{R}_x \boldsymbol{m}_k - \lambda_z \boldsymbol{R}_z^T \boldsymbol{R}_z \boldsymbol{m}_k] \end{aligned} \tag{6.2}$$

Where $\boldsymbol{J} \in \mathbb{R}^{N \times M}$ is the Jacobian matrix and $\boldsymbol{I} \in \mathbb{R}^{M \times M}$ is the identity matrix. The updated model parameters are calculated according to

$$\boldsymbol{m}_{k+1} = \boldsymbol{m}_k + \alpha \Delta \boldsymbol{m}_k. \tag{6.3}$$

Where $\alpha \geq 0$ defines the step-length of the model update in the k-th iteration. The inverse of $\boldsymbol{G}$ is not calculated explicitly to solve equation (6.2) for $\Delta \boldsymbol{m}_k$. Moreover, the linear equation (6.2) is solved by a more stable and faster Cholesky decomposition [Martin, 2009]. However, the problem of singularity of G likely causes the Cholesky de-

composition to fail if no sufficient regularization is used [Scholl et al., 2003]. Therefore, a damping factor β and global roughness constraints λ are used to stabilize the linear system. Details on matrix factorizations to solve linear equation equation systems of the form $\boldsymbol{Ax} = \boldsymbol{b}$ are found in [Martin, 2009].

6.1.1 Regularization approach

To solve the non-linear ill-posed inverse problem the regularization parameters β, λ_x and λ_z are introduced. Although α is a step-length and not strictly a regularization parameter, it is determined in the same way as the other parameters. The Occam regularization parameters λ_x and λ_z constrain the horizontal and vertical roughness of the model [Tikhonov & Arsenin, 1977]. The ratio of both parameters may be fixed during the inversion and a global λ_k is introduced. The Marquardt damping parameter β constrains the model update $\Delta\boldsymbol{m}_k$. If β is zero a pure Occam inversion is realized and equation (6.2) is similar to that suggested by De Groot-Hedlin & Constable [1990]. If β is sufficiently large, then $\boldsymbol{J}^T\boldsymbol{W}_d^T\boldsymbol{W}_d\boldsymbol{J}$ becomes negligible compared to the other terms. The inversion will have a gradient type character. Assume λ is zero at the same time, then a pure steepest descent inversion is realized with β acting as the step length:

$$\Delta\boldsymbol{m}_k = \beta\boldsymbol{J}^T\boldsymbol{W}_d^2(\boldsymbol{d} - \boldsymbol{F}(\boldsymbol{m}_k)). \tag{6.4}$$

A large β usually results in small model updates $\Delta\boldsymbol{m}_k$. This is counter-acted by the step-length parameter α according to equation (6.3). Vice versa, probable overshoots of the model update are prevented by choosing smaller values for α.

Pareto optimization

The ensemble of all regularization parameters is quite sophisticated and requires a multi-variate line search in terms of inner optimization for three to four parameters (Pareto optimization). Suppose the ratio of λ_x/λ_z is fixed and the three other regularization parameters $\boldsymbol{\Gamma} = (\alpha,\ \beta,\ \lambda_k)$ are kept free. In the first iteration, β (and λ_k) are successively increased until a solution of equation (6.2) is obtained. In case the model update does not reduce the data cost-function Φ_d the regularization parameters $\boldsymbol{\Gamma}$ are updated by a separate Marquardt inversion [Scholl et al., 2003]. All parameters are perturbed by 10% and a Jacobian matrix $\boldsymbol{J}_\Gamma \in \mathbb{R}^{N\times 3}$ is calculated for the three regularization parameters:

$$\boldsymbol{J}_\Gamma = \frac{\partial\boldsymbol{F}(\boldsymbol{m}(\boldsymbol{\Gamma}))}{\partial\boldsymbol{\Gamma}}. \tag{6.5}$$

Internally this procedure implies that equation (6.2) has to be solved for $\Delta\boldsymbol{m}(\Delta\boldsymbol{\Gamma})$ in order to calculate the Jacobian $\boldsymbol{J}_\Gamma$ of the regularization parameters. If equation (6.2) cannot be solved for $\Delta\boldsymbol{m}$, the damping β is successively increased by a multiplier. If the procedure repeatedly fails, the largest eigenvalue of $\boldsymbol{J}^T\boldsymbol{W}_d^T\boldsymbol{W}_d\boldsymbol{J}$ is selected as β. Subsequently, an update $\Delta\boldsymbol{\Gamma}$ for the regularization parameters is calculated by solving the normal equation

$$\Delta\boldsymbol{\Gamma} = \left(\boldsymbol{J}_\Gamma^T\boldsymbol{W}_d^2\boldsymbol{J}_\Gamma + \mu\boldsymbol{I}\right)^{-1}\boldsymbol{J}_\Gamma^T\boldsymbol{W}_d^2(\boldsymbol{d} - \boldsymbol{F}(\boldsymbol{m}_k)). \tag{6.6}$$

The damping factor μ stabilizes the Marquardt inversion of the regularization parameters. It is successively increased until a solution of equation (6.6) is obtained. The regularization parameters are then stored and the solution of equation (6.2) is calculated. If the data cost-function is not reduced, another inversion of the regularization parameters is performed. Otherwise, the corresponding model and the regularization parameters are stored and updated in the same manner in each iteration.
In case β is fixed to a too small value the inversion may already fail for the first iteration, because the Cholesky decomposition repeatedly fails and no solution of equation (6.2) is obtained. Practically, the λ should increase and stabilize the inversion in such cases. But, a large λ usually implies a smooth model which does not necessarily decrease the misfit. This causes the algorithm to be trapped in the internal optimization. Therefore, β is required for the current inversion scheme *SINV*.
There are different approaches to determine suitable regularization parameters. The discrepancy principle was suggested by Constable et al. [1987], where a line search is done for λ and that value which minimizes the misfit functional ϕ_d is selected. Practically, the similar criterion is used in the inversion scheme *SINV*, although not only a line search is performed [Martin, 2009]. A comparison of different techniques for the automatic determination of the regularization parameter λ is found in Farquharson & Oldenburg [2004].

6.1.2 Sensitivity calculation

The calculation of the Jacobi matrix $\boldsymbol{J}$ is generally the most time consuming task in a large scale inversion [Hördt, 1998]. In order to accelerate the inversion, the sensitivities are calculated using the adjoint Green function (AGF) approach, which was already proposed by McGillivray et al. [1994] for the frequency domain. It was adapted for direct sensitivity calculation in the time domain by Hördt [1998] and Martin [2009].
Due to the reciprocity theorem, the receiver may act as the source and the transmitter as the receiver. According to Hördt [1998], the sensitivities are obtained by a convolution of the electric field in the subsurface due to a transmitter at the surface with the electric field impulse response ($\partial_t \boldsymbol{E}$) due to another transmitter, which replaces the original receiver.
The 3D background response $\boldsymbol{E}^{bg}$ is obtained by a single forward calculation using the *SLDMem3t*. $\boldsymbol{E}^{bg}$ is calculated in a pre-specified region (grid frame) around the original transmitter and not for the complete modeling domain, because the storage requirements of the *SLDMem3t* become very large (cf. section 5.1). At least a maximum skin depth is chosen as spatial extension for that smaller grid frame. Outside the smaller grid frame, the sensitivities are set to zero. To obtain the dyadic Green function, the original receiver acts as the source. For time domain electromagnetic methods, where the excitation is usually a step function, the dyadic Green function is the time derivative of the electric field $\partial_t \boldsymbol{E}$ (adjoint field). The Jacobian matrix $\boldsymbol{J}$ is then obtained by a time domain convolution of the background electric field $\boldsymbol{E}^{bg}$ with the dyadic Green function.
The implementation involves essentially more effort, .e.g. interpolation of background and adjoint fields from the numerical grid to the model and removing singularities close to the transmitter-receiver location. A brief explanation of the numerical calculation of the sensitivities and its implementation into the inversion algorithm *SINV* is found

in Martin [2009] and Martin et al. [2003].
Moreover, Farquharson & Oldenburg [1996] showed that the adjoint fields ($\partial_t \boldsymbol{E}$) may be calculated in 1D without loosing multidimensional information. They are referred to as 3D/1D hybrid approximated sensitivities. For one transmitter and one receiver, the sensitivities are obtained by a single 3D and a single 1D forward calculation, whereas the perturbation approach requires as many forward calculations as model parameters M. For that reason, the AGF approach is accelerated by a factor $M/N_{Rx} = M/1$ compared to the perturbation approach, where N_{Rx} is the number of receivers [Hördt, 1998]. It is therefore suitable for large scale 2D/3D inversions. Martin et al. [2003] and Martin [2009] compared both approaches and concluded that the AGF sensitivities are more accurate than the sensitivities obtained by perturbation. The reason is that the perturbation method is prone to finite difference round-off errors using *SLDMem3t*. Moreover, the AGF sensitivities comply reciprocity and are symmetric with respect to the transmitter and receiver.

For the 2D inversion using *SINV* it is recommended that the sensitivities are in a comparable range of magnitude. If not, deeper zones of a model might not be reconstructed. Therefore, very large sensitivity amplitudes close to Tx-Rx are corrected [Martin et al., 2003; Martin, 2009].

Normalized coverage
The coverage C_j for each of the M model parameters is obtained by summation of each column of the Jacobian matrix:

$$C_j = \frac{1}{C_{max}} \sum_{i=1}^{N} \left| W_{d,ii} J_{ij} \right|, \qquad j = 1, \ldots, M. \tag{6.7}$$

The coverage may be reshaped to $\boldsymbol{C} \in \mathbb{R}^{M_z \times M_x}$, where M_z is the number of rows and M_x is the number of columns. To display the relative effect of model parameters within the inversion, $\boldsymbol{C}$ is often normalized to its maximum C_{max}. Naturally, the sensitivity depends on the model parameterization, i.e. larger cells exhibit larger sensitivity amplitudes. For visualization purpose, $\boldsymbol{C}$ is normalized to the area of each cell. With the normalization different parameterizations become better comparable to each other. Martin [2009] defined values between $1 \geq C_j > 10^{-2}$ as well resolved cells and $10^{-2} \geq C_j > 10^{-4}$ as poorly resolved cells. Smaller values correspond to non-resolved cells.

Depth of investigation
The coverage is an important tool to investigate the resolution of model parameters of an inverse model. To derive an approximate depth of investigation (*doi*), the coverage is correlated with the maximum skin depth δ_{FD}^{max}. For a homogeneous model $1.5 \cdot \delta_{Fd}^{max}$ is a good estimate of the *doi* [Spies, 1989]. The 2D inversion of the TEM data is usually carried out with a starting model, which is either homogeneous for the complete domain or at least column-wise homogeneous below sounding locations. Based on the coverage calculated for the starting model, a threshold C_{doi} is derived by calculating $z_{doi} = 1.5 \cdot \delta_{FD}^{max}$ for one sounding. The value C_{doi} is then derived from the column of $\boldsymbol{C}$ corresponding to the sounding and from the row corresponding to z_{doi}. Below the sounding the model should be approximately homogeneous. For models that differ from

those described above, the method is unsuitable. The derived threshold C_{doi} is plotted as an isoline in the coverage section of all further iterations. In the following graphs it is always denoted as a white line.

6.1.3 Data weighting

The weighted least-square inversion significantly dependens on the error-weights. By changing the error of particular data points, it is possible to weight them and force the inversion process to fit certain data. In Fig. A.22, an example with synthetic data is presented, where the late time data is significantly down-weighted. Thus, the late time data are not fitted and corresponding deeper parts of the model are not reconstructed. To avoid a probable down-weighting of the late time data, a constant data error of $\delta d_{i,tot} = 2.2\%$ is used for the 2D inversion of the field data, where

$$\delta d_{i,tot} = \sqrt{\delta d_i^2 + \delta d_{i,sld}^2}. \tag{6.8}$$

This error implies the minimum relative data error $\delta d_i = 1.6\%$ discussed in section 4.5.3 and the *SLDMem3t* forward modeling error $\delta d_{i,sld} = 1.5\%$ derived in section 5.3.7. Especially for the reconstruction of the resistor below the mudflat, the late time data of the soundings recorded with the Tx-100 setup is important. It contains the information of the deep resistor. As discussed in section 6.1.2, the magnitude of the Jacobian can vary over several decades. This circumstance may already cause an insufficient update for the late times, for which the corresponding entries of the Jacobian matrix are usually small. Hence, additional down-weighting of those elements in the Jacobian matrix that correspond to late times and deep structures is avoided.

6.1.4 Data transformation

TEM data usually vary over several orders of magnitude. To balance the weight of each datum in the inversion process, it is transformed logarithmically. Otherwise, the inversion might be driven by high amplitude data points [Meju, 1994]. It turned out, that a linear data transformation reproduces the same structure, but the inversion takes more iterations to converge.
In cases where data exhibits sign reversals, a logarithmic transformation is not suitable. This is, for example, always the case, where data is recorded with the separate loop TEM configuration and for several LOTEM configurations. Moreover, a horizontal magnetic field recorded for the central loop configuration exhibits a sign-reversal, if multidimensional effects are present. The horizontal magnetic field recorded slightly off the center of the transmitter loop will also exhibit a sign-reversal for a 1D subsurface. To transform such data, Hördt [1992] suggested a scaled area-sinus-Hyperbolicus function. This transformation is also implemented in *SINV*.

6.1.5 *SLDMem3t* grid design

Multi-grids are avoided to significantly reduce the computational costs in the 2D inversion. Moreover, further uncertainties, due to numerical inaccuracy of the solution are

avoided. In explanation, only one grid, which is valid for a time range of three decades, is used for each sounding. Therefore, on the high conductive mudflat the early time data is not considered in the inversion. Since the resistivity varies significantly along profile A, separate grids are designed for the moderate resistive and the conductive zones. The grid is designed and verified as briefly discussed in section 5.3. As also shown in section 5.3.3, the *SLDMem3t* solution is prone to the grid discretization in a somewhat erratic/random manner. Therefore, an adaptive grid, which is adjusted to the resistivity distribution of each inversion step, is avoided. Instead, an elaborate grid check is preferred preliminary to the inversion.

6.1.6 Model parameterization

The implemented forward operator *SLDMem3t* uses a material average scheme and the model parameterization can be chosen more or less arbitrary. Hence, the inversion grid does not have to match the forward modeling grid. For further explanation refer to the modeling section 5.2.

Vertical discretization
A logarithmically equidistant parameterization in z-direction (Δ_z) is often used, since this relates best to the exponential decay of diffusive electromagnetic fields [De Groot-Hedlin & Constable, 1990]. A logarithmic parameterization leads to larger cells at depth and up-weighting of the corresponding sensitivities, due to larger integration areas. This should reduce the condition number of the Jacobian matrix and stabilize the linear normal equation system [Martin, 2009]. Another advantage is that usually the number of model parameters are reduced.
In preliminary studies, it turned out, that a linear discretization shows a smoother sensitivity distribution, which is easier to interpret. Furthermore, a linear spacing with $\Delta_z = 2.5$ m reconstructs the resistivity distribution very well and is used in most of the 2D inversions.
To reconstruct very shallow near surface inhomogeneities, a mixed logarithmic-linear depth parameterization was tested for the 2D inversion of the field data. A synthetic study showed that it is not suitable because the transition from one to another parameterization produced artifacts.

Lateral discretization
In lateral direction the discretization is linear equidistant, because the inter-station distance in the field was usually 50 m. A coarse parameterization is obtained by using only one 50 m wide model column beneath each TEM sounding. The finest discretized parameterization used is $\Delta_x = 5$ m and produces smooth models. A drawback is that in zones where the model is less supported by the data, it sometimes leads to artifacts and scattered features.

Boundary conditions for 2D inverse modeling
A homogeneous background is included and extended to infinity in lateral direction and positive z-direction. At depths greater than the approximate *doi* the model spacing is logarithmically increased downwards. Similarly, it spreads logarithmically outwards towards both sides of the model.

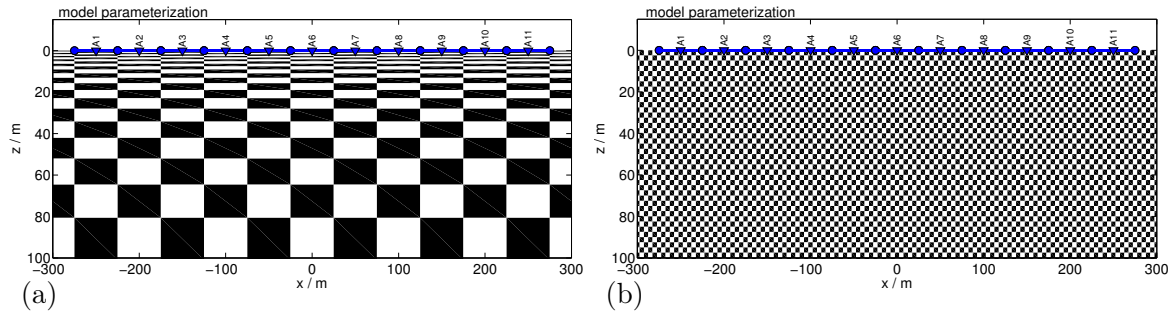

Figure 6.1: *2D model parameterization for (a) a logarithmic equidistant vertical model parameterization (Δ_z) and coarse lateral parameterization with $\Delta_x = 50$ m. (b) Linear equidistant parameterization with $\Delta_x = 5$ m and $\Delta_z = 2.5$ m. Transmitters and receivers are marked as blue circles and triangles, respectively. For both parameterizations, 11 TEM stations are drawn for a Tx-50 setup at the surface.*

An example for a logarithmic vertical and coarse lateral parameterization with $\Delta_x = 50$ m is shown in Fig. 6.1(a). The model consists of $M = 20 \times 24 = 480$ model parameters and 11 TEM stations with a Tx-50 setup drawn at the surface. Exactly one model column is used beneath each transmitter. In Fig. 6.1(b), a fine equidistant model parameterization with $\Delta_x = 5$ m and $\Delta_z = 2.5$ m is displayed. The total number of free parameters is $M = 182 \times 58 = 10556$. Both, logarithmic and linear discretization, are tested for synthetic data in section 6.3.3.

Fixed structures and resistivities

By including fixed 2D blocks, pre-defined structures can be passed to the inversion. Either the resistivity of these blocks are fixed, for example to integrate a-priori information, or the resistivity is inverted. Since these blocks can be chosen quite large compared to the overall cell size, their sensitivity is usually significantly increased. The increased sensitivity naturally forces a strong update for the large blocks. However, a-priori information is necessary to define size and position of the fixed blocks.
Particularly in the case of central loop TEM and large induction numbers, the near surface zones are usually treated as 1D. If the structure is not essentially 2D or 3D, multi-dimensional effects occur at later times. Hence, it is justified to fix top surface layers in the inversion process. The resistivities may be derived from prior 1D inversion results.

6.2 2D inversion of synthetic data: a standard magnetotelluric model

The first example is a standard 2D model, which is often used in magnetotellurics to check the spatial reconstruction capabilities of an inversion algorithm, e.g. Smith & Booker [1991], Siripunvaraporn & Egbert [2000] and Rodi & Mackie [2001]. This model is adapted to demonstrate the capabilities of the 2D inversion algorithm *SINV* for inverting TEM sounding data.
A resistor with $\rho_1 = 100$ Ωm and a conductor with $\rho_1 = 1$ Ωm are embedded in a host with a moderate resistivity of 15 Ωm. Both blocks are 100 m wide and 20 m thick

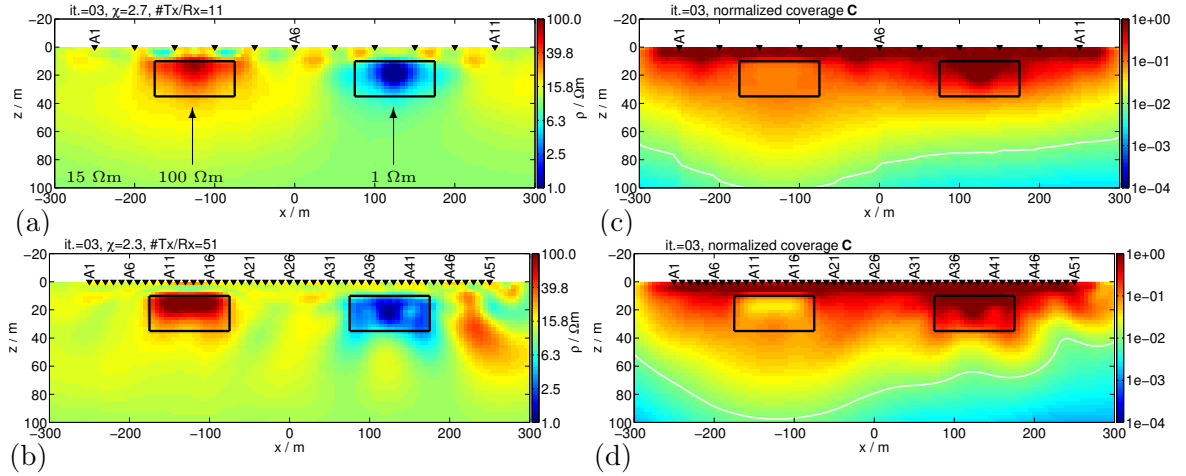

Figure 6.2: *2D inversion of a standard magnetotelluric model. The background resistivity of the true model is 15 Ωm. The block-edges are hemmed black and labeled with their true resistivity values $\rho = 100$ Ωm and 1 Ωm. The models obtained after the third inversion iteration (It 3) are displayed in (a) for a total number of #Tx/Rx=11 soundings with 50 m spacing and in (b) for #Tx/Rx=51 soundings with 10 m spacing. Their locations are marked as black triangles. The corresponding coverage is displayed in (c) and (d). The doi is drawn as a white line. The iteration number and the actual χ are given above the models.*

starting at a depth of 10 m. The positions of these blocks are displayed in Fig. 6.2. Even if this model does not have conceivably realistic applications as such, a good conductor embedded in a resistive host is a typical model in the exploration of mining targets. Whereas a resistive target with sharp boundaries embedded in a good conductive host often occurs in the marine environment, e.g. resistive hydrocarbon or freshwater targets [Zhdanov, 2009]. The model is particularly useful to demonstrate the resolution capabilities of the TEM induction method for resistive and conductive structures.
In Fig. 6.2(a), the obtained 2D model is displayed. The inversion is done for synthetic data of 11 Tx-50 soundings and a 10 Ωm halfspace is used as a starting model. The sounding locations are displayed as black triangles. Both blocks are reconstructed at least to some extent. Since only two soundings are directly above each block, they are reconstructed very blurred and the block edges are not sharply reproduced. If a dense data set with a total of 51 Tx-50 soundings and an inter-station distance of 10 m is passed to the inversion, the edges are much better delineated. Especially the good conductor in Fig. 6.2(b) is well reproduced. The 15 Ωm background resistivity is also reconstructed, except towards the right side of the model a resistive artifact appears.
Both coverages displayed in Fig. 6.2(c,d) are meaningful with respect to their corresponding models. As expected, the sensitivity is increased for the conductive block, compared to that of the resistive one. Moreover, the coverage is more accentuated at the location of the blocks for the case where 51 soundings are used. The *doi* ranges from around 100 m on the left side to roughly 70 m on the right, which are plausible estimates.
In Fig. 6.3, the calculated χ is plotted versus the sounding locations for the initial 10 Ωm halfspace (blue) and both final 2D models, with either 11 or 51 inverted soundings. For the soundings over the resistive block χ ranges from $\chi = 1$ to 2, whereas it deteriorates to $\chi \approx 5$ over the conductor. Due to a lower resistivity contrast between the block and the background, the sounding data over the resistor is fitted better than

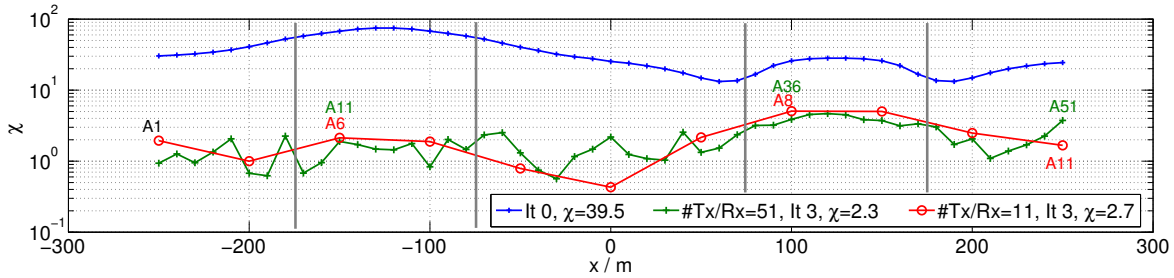

Figure 6.3: *χ plotted vs. the sounding location along the profile line. The blue line corresponds to the χ of the 10 Ωm starting model. The red (#Tx/Rx=11) and green line (#Tx/Rx=51) correspond to the final models displayed in Fig. 6.2(a) and (b), respectively. The global χ is denoted in the legend.*

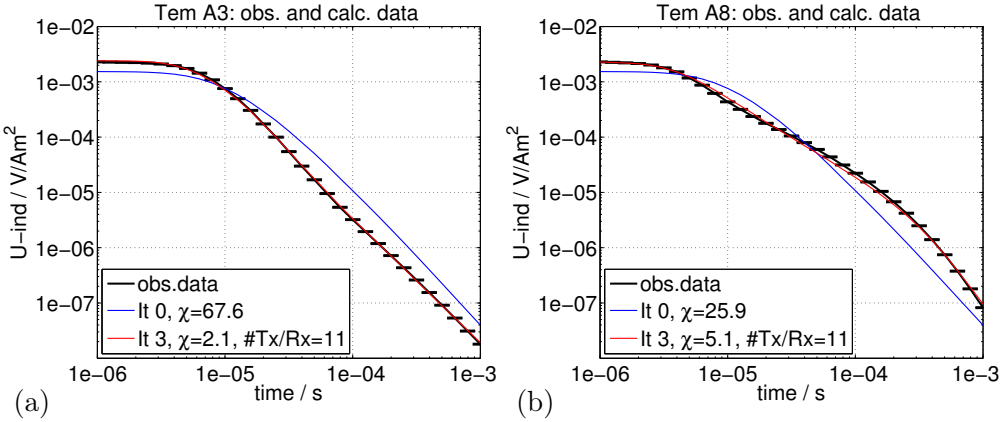

Figure 6.4: *Synthetic data calculated for the true model (ods.data, black) and response of the initial (it 0, blue) and final model (It 3, red) for sounding (a) A3 and (b) A8. The sounding locations are displayed in Fig. 6.2(a).*

over the conductor. The initial global χ is around $\chi \approx 40$ and significantly improves for both final models to $\chi \approx 2.3$ and $\chi \approx 2.7$.
In Fig. 6.4(a,b), the response curves are displayed for soundings A3 and A8 for the model where a total of 11 soundings are used (displayed in Fig. 6.2(a)). The improvement of the fit from the initial 10 Ωm halfspace to the final model response is remarkable for both locations. In comparison to sounding A3, the data for sounding A8 exhibits a strong curvature between $t = 10^{-5}$ and 10^{-4} s. This part of the transient corresponds to the top edge of the conductor and is not fitted optimal. Naturally, it is difficult to reconstruct such high and distinct resistivity contrasts, due to the imposed roughness constraints in the inversion process.

6.2.1 Inversion with a-priori information

In order to demonstrate the capabilities of the inverse process, a-priori information is incorporated. Particularly in the case of a large scale 2D inversion, including a-priori information can reduce the model ambiguity and stabilize the inversion process. Commonly the resistivity of model cells can be fixed in certain regions to integrate for example lithological borehole data or results obtained from other methods. Another possibility is to force the inversion to fit a certain structure by including fixed blocks in the model parameterization. In Fig. 6.5, the initial (It 0) and final 2D model (It 03) are

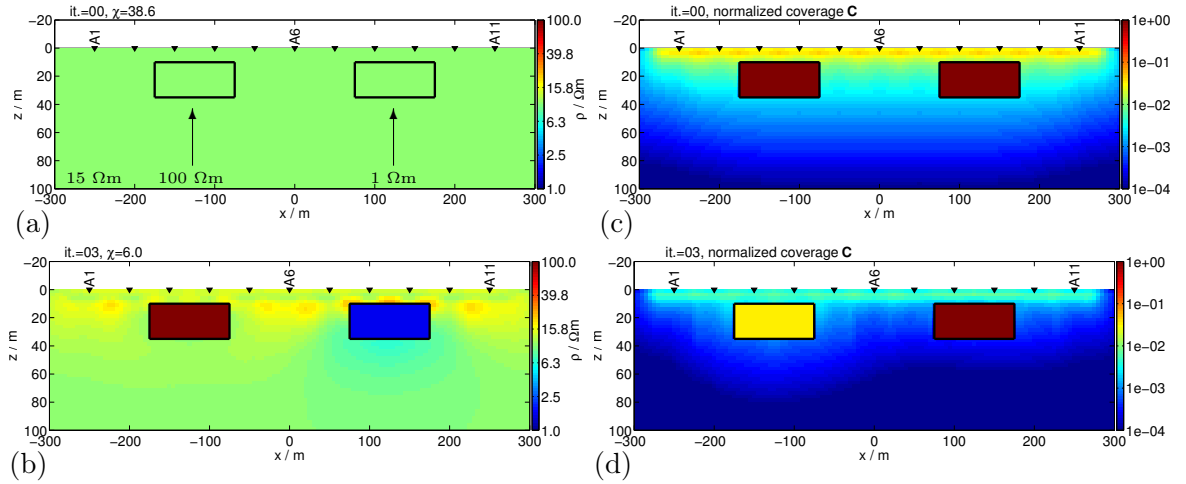

Figure 6.5: *2D inversion result of synthetic data for a buried resistor and conductor embedded in a 15 Ωm halfspace. (a) 10 Ωm starting model (It 0). (b) inversion result after the third iteration (It 3). The corresponding coverages are displayed in (c,d). The block-edges and the resistivity values are given in starting model. The sounding locations are marked as black triangles. The iteration number and the actual χ are displayed above the models.*

displayed with their corresponding coverages. The parameterization is the same as for the previous example (Δ_x=5 m, Δ_z = 2.5 m), except that the shape of the two blocks is already included in the initial model. The sensitivity of the 10 Ωm starting model is extremely increased for both blocks, which results in a large update for both. In the third iteration χ is reduced to $\chi = 6$ and the resistivity of both blocks (1 and 100 Ωm) are exactly reproduced. As expected, the coverage is increased for the good conductor compared to that of the resistor. The overall fit is not as good as for the previously discussed models with the uniform parameterization. Due to the very large coverage magnitude for the two blocks, the surrounding is not updated sufficiently anymore during the inversion process.
The approach of incorporating larger blocks into the model parameterization is applied to the field data obtained with the Tx-100 setup in the forthcoming section 6.6. Since the objective is to reconstruct the base under very high conductive mudflat sediments, this approach is promising because the sensitivities for larger blocks are considerably increased. As a result, the inversion is provides a sufficient update of the deep zones in the model.

6.3 2D inversion of synthetic data: a basin model

The 2D standard model consisted of two sharply bounded blocks embedded in a moderate resistor. A second model is studied to investigate the internal pareto optimization, the sensitivity and the model parameterization. The model, displayed in Fig. 6.6(a), is a shallow basin structure and corresponds more to the real situation in the survey, than the previously discussed block model. It contains of a 10 m thick overburden with a resistivity of 15 Ωm. The host structure has a resistivity of 30 Ωm and the slope of the basin flanks is 18°. Furthermore, the basin is 60 m deep with a resistivity of 5 Ωm, which is less than the surrounding material. The structure may also be interpreted as a

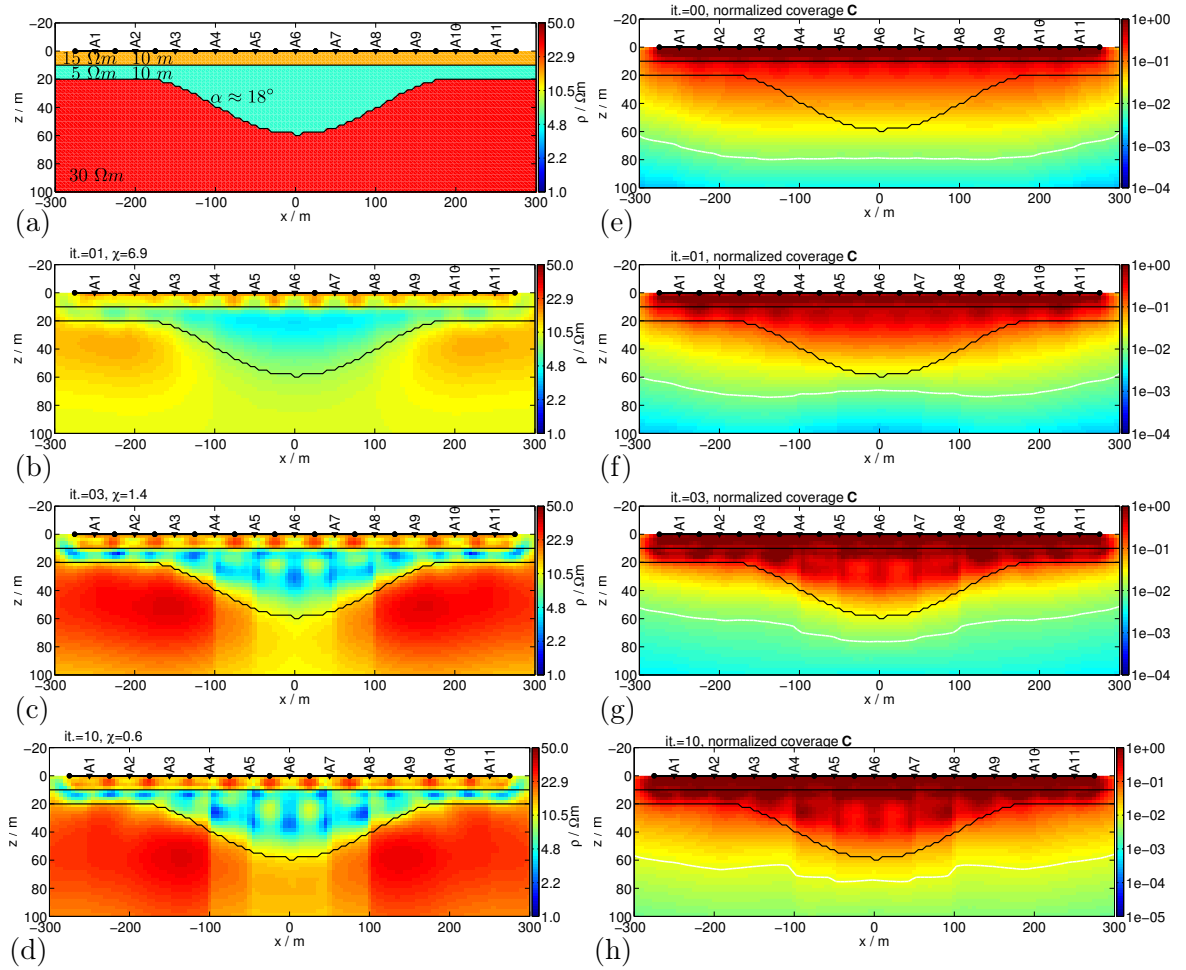

Figure 6.6: *2D inversion of synthetic data for a shallow basin structure. (a) True model. (b-d) Inversion results for iterations 1, 3 and 10. (f-h) Corresponding normalized coverage* $\boldsymbol{C}$*. In (e) the normalized coverage for the 10 Ωm initial model is plotted. The doi is plotted as a solid white line in the coverage sections. The transmitter and receiver locations are denoted as black dots and triangles, respectively. The iteration number and the actual* χ *are displayed above the models.*

buried valley. It is an interesting target and there are several case studies on the investigation of buried valley structures using the TEM method, e.g. Jørgensen et al. [2003], Danielsen et al. [2003] and Steuer et al. [2009]. Particularly, Steuer [2008] showed that a valley structure with 18° slope can produce artifacts, when a common 1D inversion is used for interpretation. Of course, it also depends on the time range of TEM data acquisition.

The inversion is done for 11 Tx-50 soundings with a typical data time range from $t = 10^{-6}$ to 10^{-3} s. Noise is not added to the data and a constant data error of $\delta d_i = 2\%$ is chosen arbitrary. A fine parameterization similar to that shown in Fig. 6.1(b) with $\Delta_x = 5$ m and $\Delta_z = 2.5$ m is used. The initial model is a 10 Ωm halfspace. In Fig. 6.6(b-d), the inversion results for the iterations It=1, 3 and 10 are displayed. The inversion converges fast and generally reproduces the overall structure already in the first iteration. The resistivity of the host structure is well reconstructed after the third iteration with an nearly optimal χ of 1.4. In the tenth iteration the data is over-fitted with $\chi = 0.6$ and the model is over-structured particularly in the valley zone. In Fig. 6.7,

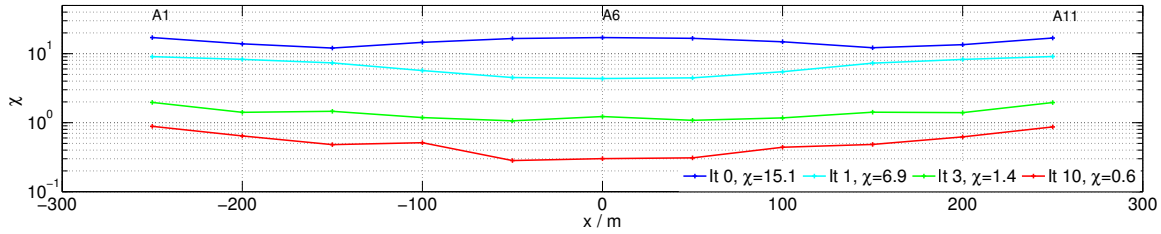

Figure 6.7: *χ plotted at each sounding along the profile line for the starting model and iterations 1, 3 and 10. The global χ is denoted in the legend.*

χ is plotted versus the sounding locations for the initial model and the corresponding iterations. The soundings over the valley structure are fitted slightly better for all three iterations. The data fitting for two selected soundings A2 and A5 are displayed in Fig 6.8(a,b). Both are fitted well and the residuals plotted below are small for the third iteration.

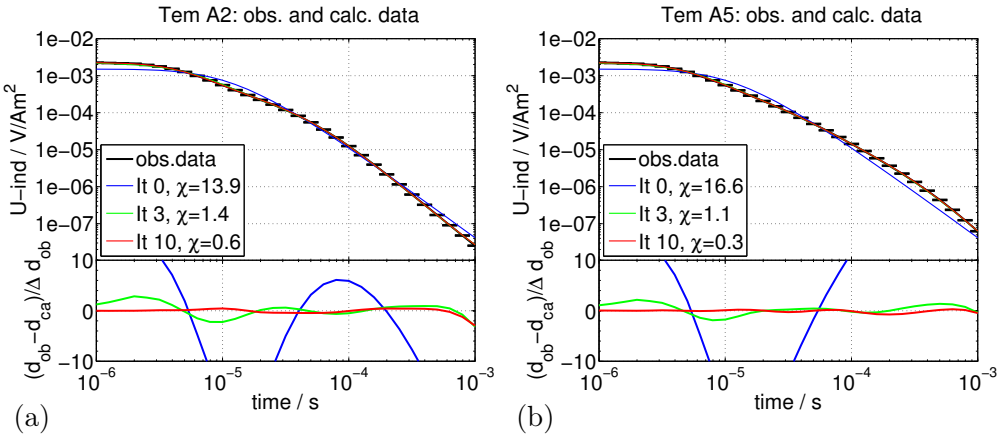

Figure 6.8: *Synthetic data (obs.data) and model response for soundings (a) A2 and (b) A5. The response for the starting model (It 0), the third (It 3) and the tenth iteration (It 10) are plotted. The corresponding residuals are displayed below the transients.*

6.3.1 Sensitivity and depth of investigation

In Fig. 6.6(e-h), the corresponding normalized coverage $\boldsymbol{C}$ is plotted for the homogeneous starting model and the three selected iterations (It 1, 3 and 10). Because the sounding locations are overlapping at the transmitter loop (black dots) the coverage is maximized beneath and forms a lobe type of structure. For the third and tenth iteration an increased coverage is visible for the good conductive basin zone. As expected, the structure of the coverage reflects the model structure and vice versa. Towards both sides of the model the overall magnitude of $\boldsymbol{C}$ slightly decreases at depth. Due to very small Occam regularization parameters, the model becomes quite rough and scattered in the third iteration. Likewise, the coverage exhibits scattered zones in the same manner. If the model becomes too rough the background fields calculated with the *SLDMem3t* may become corrupted. As a consequence the calculated sensitivities may also become corrupted.
The *doi* is derived from the coverage as described in section 6.1.2 and is plotted as a

solid white line in Fig. 6.6(e-h). As expected, for the first iteration the coverage and *doi* estimate is slightly decreased in the middle part of the model, where the less resistive basin structure is present. In the following iterations, the *doi* is maximized in the central part and appears to be under-estimated towards both sides of the model. It should be noted, that the derived *doi* is an approximate estimate.

6.3.2 Pareto optimization of the regularization parameters

In the first three iterations the model is updated significantly and χ is improved from $\chi = 15.1$ to 1.4. The convergence of the damped iterative Gauss-Newton scheme is known to be very good, particularly for the first inversion steps. The following iterations produce only a comparable small misfit decrease. In Fig. 6.9, the χ and all four regularization parameters (α, β, λ_x and λ_z) that control the inversion process are plotted. Both horizontal and vertical Occam regularization parameters (λ_x and λ_z) are small compared to the Marquardt damping β throughout all iterations. Moreover, both are decreased in every iteration which causes the 2D model in Fig. 6.6(b-d) to become more structured. As a result the inversion is stabilized by the Marquardt damping β. Since no further update is yielded after the sixth iteration, the ratio of λ_x to λ_z is significantly changed. However, at that stage the inversion process is dominated by the Marquardt damping β and not by the Occam regularization. In order to avoid over-structured models, it is recommended to select any model before the sixth iteration. Of course the choice depends on the data fit and the desired model roughness. An almost optimal fit with $\chi = 1.4$ is reached in the third iteration. For the current example the parameter α, which controls the step-size of the inversion update, remains around one for all iterations. Hence, it does not influence the stepsize of the model update. The pareto optimization of the regularization parameters is highly non-linear [Scholl, 2004] and the interaction of all four parameters is difficult to control. Moreover, the regularization is dependent on the parameterization of the model.

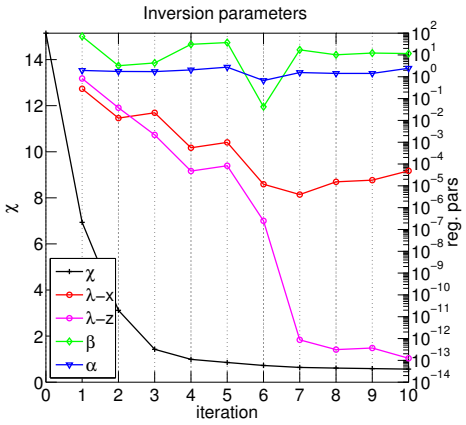

Figure 6.9: *Evolution of the global fit χ and inversion regularization parameters α, β, λ_x and λ_z for each iteration.*

Fixed ratio λ_x/λ_z of the regularization parameters

To gain better control of the regularization parameters, a global λ_k is introduced in the pareto optimization and the ratio of λ_x/λ_z is fixed. The inverse models in Fig. 6.10(a-d) are reconstructed for a fixed ratio $\lambda_x/\lambda_z = 2$. The inversion terminates after the sixth iteration with $\chi = 2.1$. The evolution of χ, λ_k, β and α is displayed in Fig. 6.11, where λ_k and β behave in a similar manner. In the second iteration, both are decreased approximately by a factor of ten, which results in a considerable model update. The corresponding stepsize $|\Delta \boldsymbol{m}_2|$ is largest. As visible in Fig. 6.10(a,b), the overall model structure becomes more pronounced. Although the global λ_k and β are increased again by approximately two decades in the third iteration, no clear change is visible in the subsurface structure and the stepsize is comparably small. For all following iterations,

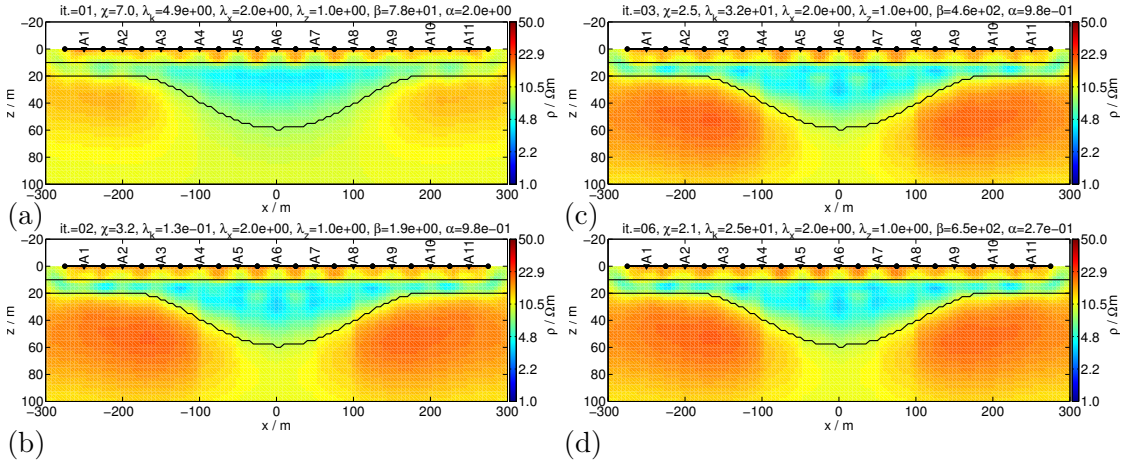

Figure 6.10: *2D inversion results for the basin structure for a fixed ratio λ_x/λ_z=2. The global λ_k, β and α are kept free. (a-d) Iterations 1, 2, 3 and 6. Inversion parameters are plotted above each model.*

λ_k and β do not change that much. Furthermore, the step length α is reduced in the last two iterations, which obviously prevents an overshoot of the model update. Compared to the previously discussed models in Fig. 6.6(b-d), the structure remains relatively smooth throughout all iterations. The optimization with a global λ_k usually causes the inversion to terminate before the model becomes over-structured and scattered, which is a decisive advantage over leaving the ratio free. *SINV* utilizes the discrepancy principle. Therefore, it is not possible to reverse the process and to obtain a smooth model subsequent to a very structured model.

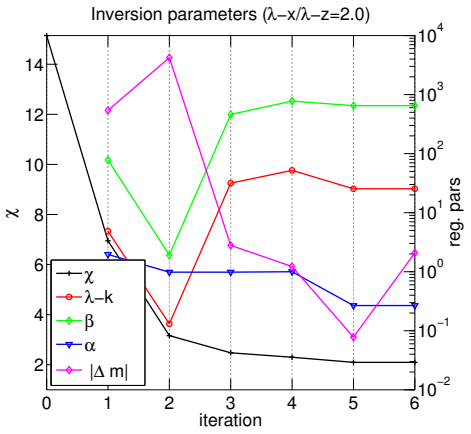

Figure 6.11: *Evolution of the global fit χ and inversion regularization parameters λ_k, β and α for the inverse models displayed in Fig. 6.10. The ratio of $\lambda_x/\lambda_z = 2$ and is fixed. The stepsize $|\Delta \boldsymbol{m}_k|$ is drawn in magenta.*

In order to avoid over-structured models in the early iterations, large starting values for the Occam regularization parameters are in general recommended [Scholl et al., 2003]. Nevertheless, if too large initial values $\lambda_x = 10^3$ and $\lambda_z = 10^3$ are selected, merely one update $\Delta \boldsymbol{m}_k$ is calculated and the algorithm terminates. This is the case in the second example displayed in Fig. 6.12(a), where a very smooth model is reconstructed in the first iteration. Although the global λ_k is not fixed, the internal Marquardt inversion of the regularization parameters does not produce a set of suitable parameters after the first iteration. The global λ_k is not sufficiently reduced to balance the fixed large initial values of λ_x and λ_z. Due to convergence problems, the inversion terminates after one iteration with $\chi = 9.4$. The pareto optimization of the regularization parameters in the second iteration took 90 hours without any improvement.

Conclusions from the regularization

If all parameters are left free, often very coarse/structured models are reconstructed already in early iteration and the process cannot be reversed. This is decisively con-

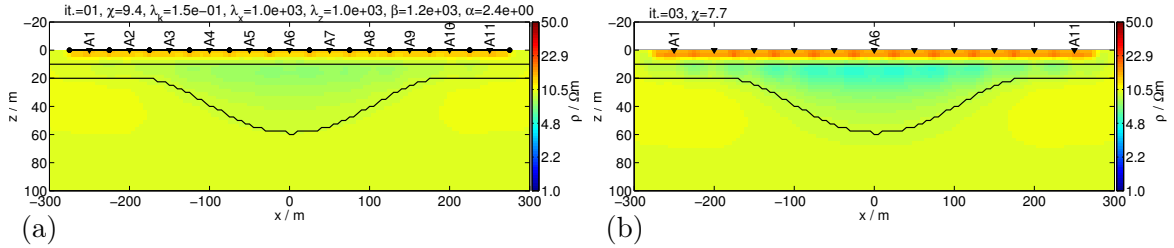

Figure 6.12: *2D inversion results for the basin structure for different regularizations. In (a) the ratio $\lambda_x/\lambda_z = 1$, but the starting values are large with $\lambda_x = \lambda_z = 10^3$. (b) The Marquardt damping β is fixed to $\beta = 10^6$. The global regularization λ_k is kept free in the inversion process for (a) and (b).*

trolled by fixing the ratio of λ_x/λ_z and using a global λ_k. Small ratios $\lambda_x/\lambda_z = 0.5 - 2$ turned out to be best suitable for the results presented in this thesis. By setting the initial parameters λ_x and λ_z to very high values, the inversion is very likely to be terminated without a suitable update. It has to be noted, that it is difficult to separately control the influence of the Occam and Marquardt damping. If the Marquardt damping β is fixed to a very small value, practically a pure Occam type of inversion is possible. Anyhow, tests with synthetic and field data for various $\beta \leq 10^5$ values did not lead to a convergence of the algorithm. On the one hand, the Cholesky decomposition of the normal equation (6.2) fails if both, λ and β are small. On the other hand, if λ is too large, no model update is found which decreases χ. As a result, the inversion algorithm is trapped in the pareto optimization. Only one inversion run with a very large $\beta = 10^6$ did not fail, but the basin structure shown in Fig. 6.12(b) is not well reconstructed. Therefore, at the current development stage of *SINV* the damping β is required and it is not possible to perform a pure Occam-type inversion.

6.3.3 Variation in the model parameterization

By choosing a parameterization with less number of model parameters, the inversion is significantly accelerated due to a faster Cholesky decomposition. Furthermore, models with less number of parameters are less prone to artifacts and scattered features during the inversion. Moreover, larger cells exhibit larger sensitivities and the solution of the linear equation system is more stable. In Fig. 6.13(a,b), the results are displayed for a logarithmic depth and two coarse lateral parameterizations with $\Delta_x = 25$ m and $\Delta_x = 50$ m, respectively. Due to the increased sensitivity of the blocks directly below the transmitters, the finer discretized parameterization leads to scattering for the shallow

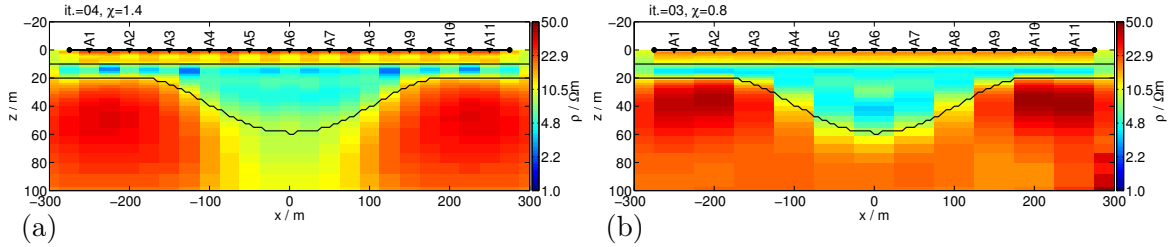

Figure 6.13: *Final 2D models for two different model parameterizations Δ_x. In (a) the medium coarse parameterization with Δ_x =25 m is displayed and the coarsest with $\Delta_x = 50$ m in (b). The depth parameterization Δ_z is logarithmic equidistant.*

zone towards both sides, i.e. alternating resistivities for the upper 20 m. In the central part of the model, the structure is smoother than for the very fine parameterized models presented previously in Fig. 6.6(c,d). By choosing exactly one 50 m wide model column beneath each transmitter, the model does not show any artifacts or scattered features for the shallow zone. On the one hand, the flanks of the valley are only reproduced relatively coarse and step-like. On the other hand, such a coarse parameterization produces stable results and explains the synthetic data well.

6.4 Inversion of Tx-50 sounding data: coarse parameterization

The subsurface structure is essentially two dimensional along profile A. In the previous chapters, the TEM field data was interpreted using conventional 1D inverse modeling and 2D forward modeling. Particularly, the 2D forward modeling results discussed in chapter 5 are based on the quasi 2D resistivity-depth sections, which are derived from prior 1D results. Therefore, these 2D results do not provide an independent validation of the subsurface structure. To derive an independent 2D model and validate the resistivity-depth sections, the 2D inversion algorithm *SINV* is applied to the TEM field data. A total number of 33 Tx-50 soundings between A27 and A59 are simultaneously inverted in the first step. In this particular zone the transition from the moderate resistive basalt formation towards the high conductive mudflat sediments is present. For comparison see the quasi 2D resistivity-depth sections in section 4.7.2.

6.4.1 Inversion using a homogeneous starting model

To minimize the influence of a-priori information, a homogeneous halfspace starting model is used in the first step. Between the basalt formation ($\rho \approx 10 - 30$ Ωm) and the conductive mudflat ($\rho \approx 0.3 - 1.0$ Ωm) a large resistivity contrast with a factor of around 100 is present. Therefore, the inversion is performed twice for different starting model resistivities $\rho_{m0,1} = 5$ Ωm and $\rho_{m0,2} = 1$ Ωm, respectively. To accelerate the inversion, a logarithmic depth parameterization and a coarse lateral parameterization is used with one model column beneath each sounding, hence Δ_x =50 m. In Fig. 6.14(a,b), the inversion results are displayed for the 5 Ωm and 1 Ωm initial models.
The inversion performed with the 5 Ωm starting model reconstructs the overall subsurface structure well. The comparability to the 1D stitched Occam results presented in section 4.7.2 is remarkable. Between A27 and A40 the thin conductive layer embedded between the resistors is smooth and continuous. Furthermore, the shallow thin resistive feature below sounding A39 is reproduced, which is also visible in the 1D stitched Occam models along profile A.
In Fig. 6.14(c), the calculated χ is plotted versus the sounding location for the initial (red dotted line) and the final model (red crossed line). Northeast of sounding A40 the data is fitted very well with a χ ranging from $\chi \approx 2$ to 5. The χ decreases in that zone from around $\chi \approx 100$ to values mostly below $\chi \approx 5$. Due to the unsuitable starting model for the zone southwest of A40, the fit is only slightly improved there and χ ranges from $\chi \approx 2$ to 100. Accordingly, the global fit is poor with $\chi \approx 33$.

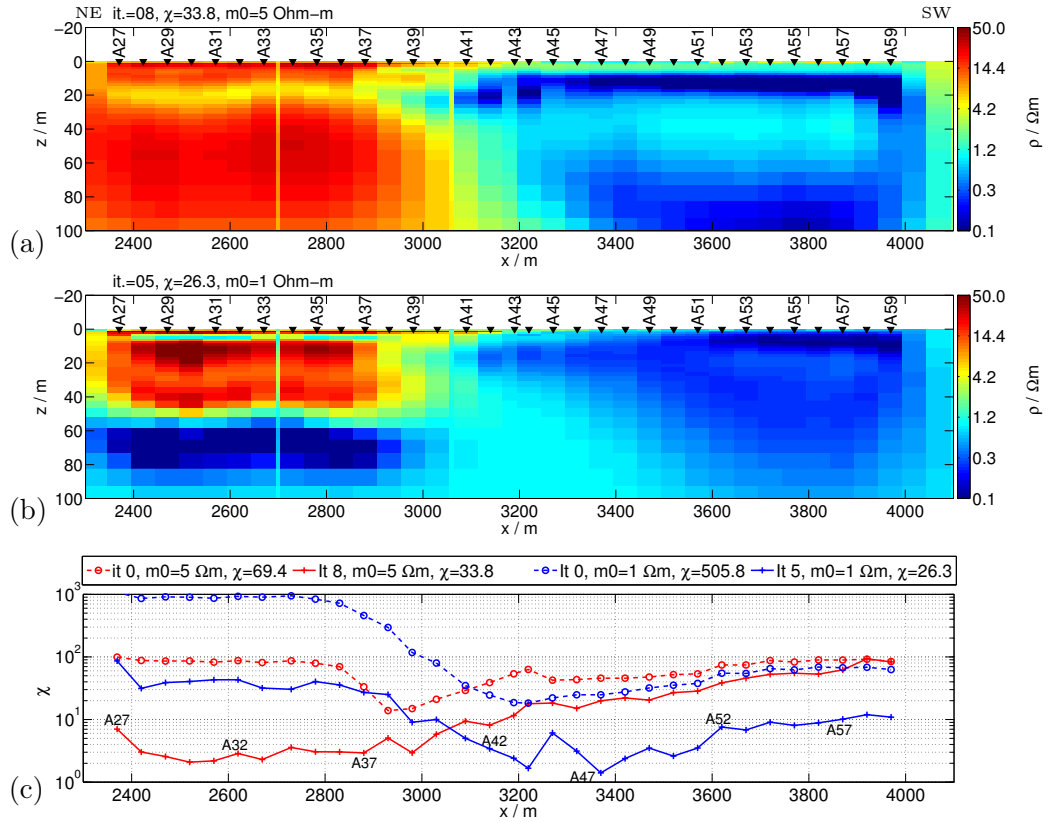

Figure 6.14: *2D inversion of the field data using an initial model resistivity of (a) 5 Ωm and (b) 1 Ωm. (c) χ plotted versus the sounding locations for the 5 Ωm initial model (red dashed line) and the corresponding final model (red solid line). The obtained χ for the 1 Ωm initial and final models are plotted in a similar manner in blue. Initial and final global χ values are given in the legend.*

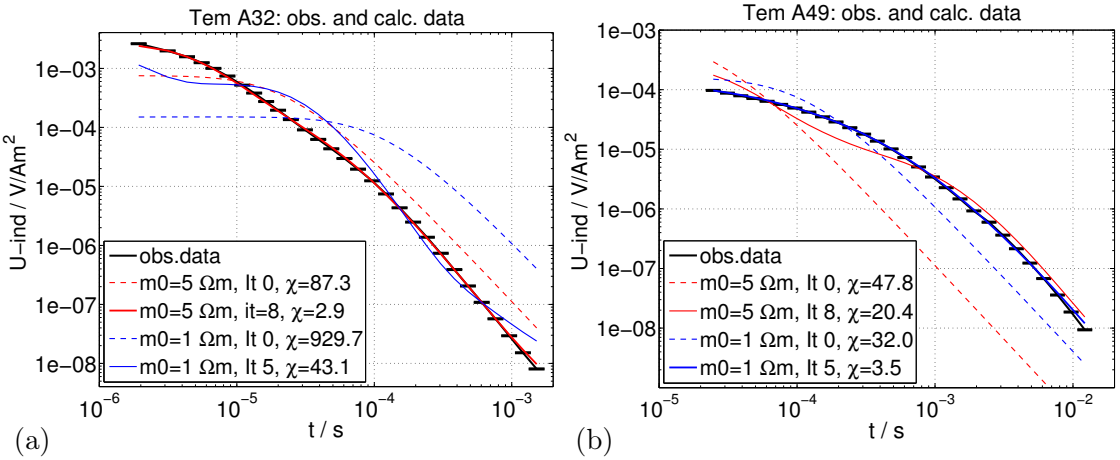

Figure 6.15: *Field data and calculated response for sounding (a) A32 and (b) A49 for both initial and final 2D models displayed in Fig. 6.14(a,b). The initial model response is denoted as a dashed red line for the 5 Ωm case and in blue for the 1 Ωm initial model. The corresponding final model response obtained with the 5 Ωm and 1 Ωm halfspace are denoted as solid red and blue lines, respectively.*

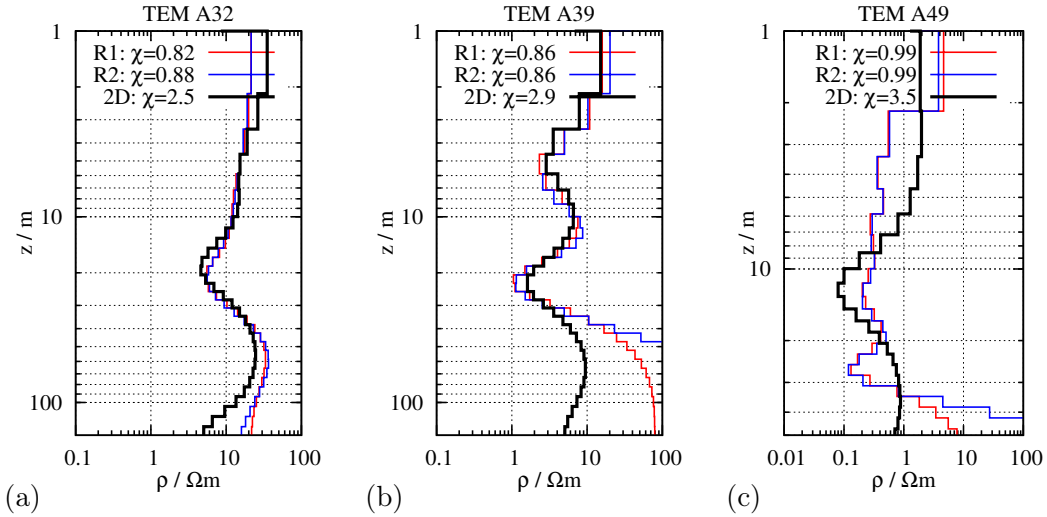

Figure 6.16: *Comparion of the 2D (black line) and the 1D inversion results (R1: red line, R2: blue line) for three soundings. Model columns are extracted at sounding (a) A32 and (b) A39 from the 2D result in Fig. 6.14(a), where the 5 Ωm initial model is used. The result displayed in (c) is extracted at sounding A49 from the 2D model in Fig. 6.14(b), where the 1 Ωm starting model is used.*

In order to fit the data southwest of sounding A40, an 1 Ωm halfspace initial model is selected. The obtained final model is displayed in Fig. 6.14(b). The subsurface structure obtained northeast of A40 has only little in common with that shown in Fig. 6.14(a). The calculated χ is plotted versus the sounding location in Fig. 6.14(c) for the initial (blue dotted line) and the final model (blue crossed line). The 1 Ωm initial model results in a χ of around 1000 northeast of A40, which can be improved at best to values around $\chi \approx 40$. Southwest of A40 the subsurface structure is meaningful and χ is significantly improved to values below $\chi \approx 10$.
A meaningful 2D model is obtained by patching the well reconstructed zones northeast of A40 of the upper model in Fig. 6.14(a) and southwest of A40 of the lower model (b) together to one single model. This theoretically results in a global fit of $\chi \approx 5$, which is not an optimal fit but satisfactory for a 2D inversion with a large number of soundings. Moreover, the result independently validates the resistivity-depth section derived from the 1D inversion results.
The field data and the calculated fit for sounding A32 and A49 are displayed in Fig. 6.15(a) and (b), respectively. The initial model response is denoted as a dashed line and the final model response is drawn solid. An initial χ of 87 is obtained for sounding A32 with the 5 Ωm starting model (red dashed line). The final model response for the 5 Ωm initial model explains the data very well with $\chi = 2.7$ (red solid line). The 1 Ωm starting model results in $\chi \approx 1000$ (blue dashed line) and the final response does not fit the data. The response curves displayed for sounding A49 exhibit a reversed behavior. The final response obtained from the 1 Ωm starting model (blue solid line) fits the data well with $\chi = 3.5$. In contrast to that, the response obtained by using a 5 Ωm initial model approaches the field data only for the last decade of time. The early time points are not fitted at all.
A comparison of the 2D inversion result the 1D inversion results is displayed for three selected soundings in Fig. 6.16. The resistivity-depth values for soundings A32 and A39 are extracted from the 2D model in Fig. 6.14(a), where the 5 Ωm starting model

is used. The agreement is remarkable for both soundings. The resistivity-depth values for sounding A49 are extracted from the model in Fig. 6.14(b). Compared to the 1D results some deviations are visible. The upper 10 m are not to be considered because the early time data is removed from the Tx-50 sounding data at A49 prior to the 2D inversion.

6.4.2 Inversion using a starting model derived from field data

A homogeneous starting model is suitable, if the lateral resistivity structure does not vary much within one model. Along profile A the resistivity varies significantly along the profile line. There are two distinct zones: the basalt zone with moderate resistivities and the high conductive mudflat zone. As discussed above, an initial model with a resistivity of $\rho = 5$ to 10 Ωm is perfectly suitable for the basalt zone, but not at all for the mudflat zone. This problem is overcome by using the minimum late time apparent resistivity $\rho_{a,lt}$ value of each sounding and constructing an initial 2D model out of that. Likewise, the early time transformation $\rho_{a,et}$ can be used to define the uppermost layer of an initial model. Another possibility is to construct the initial model from existing 1D models, which somewhat maximizes the amount of a-priori information used. The first approach is preferred, because the initial model is solely based on the field data and not on the prior application of any sophisticated 1D inversion scheme.
The derived starting model is displayed in Fig. 6.17(a). Northeast of sounding A38 the initial resistivity is 10 Ωm, which is an approximate mean value of the minimum $\rho_{a,lt}$ in that zone.
The final model is displayed in Fig. 6.17(b). The overall structure is reproduced well and comparable to that shown previously in Fig. 6.5(a) and (b). The thin resistive feature beneath sounding A39 is again reproduced. The model update is not as significant as for the previous 2D model where the 5 Ωm halfspace was used and the subsurface structure northeast of A40 is much less pronounced. The continuation of the resistor below the mudflat southwest of A38 is uncertain, because the resistivities do not change that much compared to those of the initial model.
The inversion aborts after two iterations and improves the global fit from $\chi = 15.6$ to 7.2. The obtained χ is plotted along the profile in Fig. 6.17(d) and is below $\chi = 10$ for almost all soundings. The zone northeast of A38 is not fitted as well as with the 5 Ωm starting model. Obviously the inversion aborts too early. In the transition zone, between A39 and A43, the update and the improvement of the data fit is remarkable. Since the initial model southwest of A43 explains the field data well, only a few soundings indicate a slight improvement of the data fit.
The coverage of the final model is displayed in Fig. 6.17(c) with the approximate *doi* estimate denoted as a white line. The overall structure is quite smooth and meaningful. Compared to the conductive zone, the sensitivity is increased for the deeper regions in the resistive zone. Likewise the *doi* is increased to $\delta_{doi} \approx 90$ m in that zone. Nevertheless, it is slightly over-estimated with $\delta_{doi} \approx 70$ m on the high conductive mudflat. A lateral discontinuity is visible between sounding A37 and A38 in the coverage section, where the starting and the final model exhibits the largest resistivity contrast. Such discontinuities can cause a problem, if the numerical calculation of the background fields become corrupted. As a consequence the calculated sensitivities would also become corrupted.

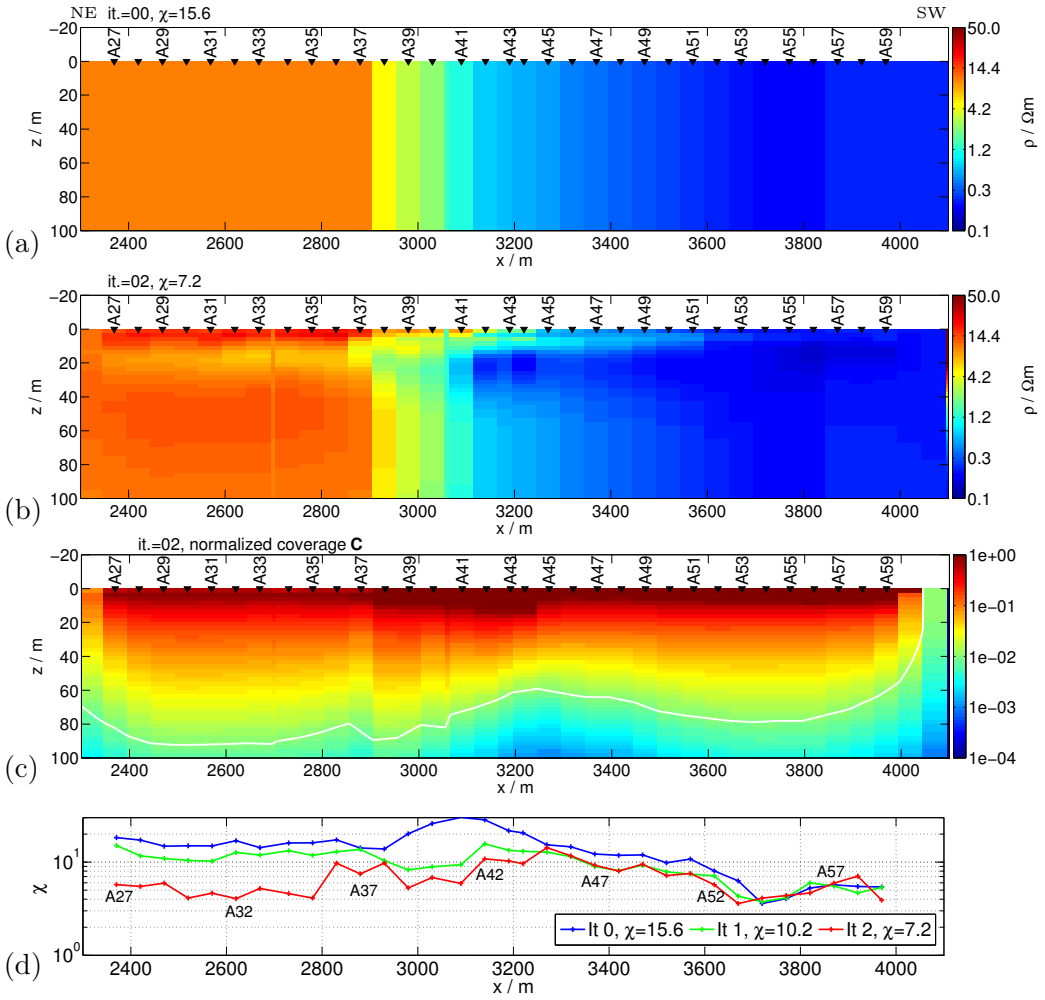

Figure 6.17: *2D inversion of the field data using late apparent resistivities derived at each sounding as initial model resistivities. The initial model is displayed in (a) and the final 2D model in (b). In (c), the coverage of the final model is shown. (d) χ plotted along the profile line for the initial model, the first and the final inverse models. The global χ is displayed in the legend.*

The data fitting for three selected soundings (A32, A41 and A49) are shown in Fig. 6.18. Particularly sounding A41 shows a remarkable update and improvement of the fit.
A logarithmic depth parameterization Δ_z is used for the inversion results where the starting model is a homogeneous halfspace. For comparison see the results discussed above in section 6.4.1. For the inversion with the $\rho_{a,lt}$ starting model, it turns out that a linear depth parameterization with $\Delta_z = 2.5$ m fits the data most uniformly. In contrast to that, a logarithmic depth parameterization provides a better update northeast of sounding A39 but almost no update for the other soundings. Particularly those on the mudflat are not updated at all. An example is shown in Fig. A.23 in the appendix. According to De Groot-Hedlin & Constable [1990] the ideal depth scale is structure dependent, even though a logarithmic depth parameterization relates best to the diffusive propagation of EM-fields. At the same time, the structure is strongly depending on the set of regularization parameters, which are automatically determined by the pareto optimization. Therefore, it is recommended to test different regularizations and model parameterizations for an successful application of the 2D inversion.

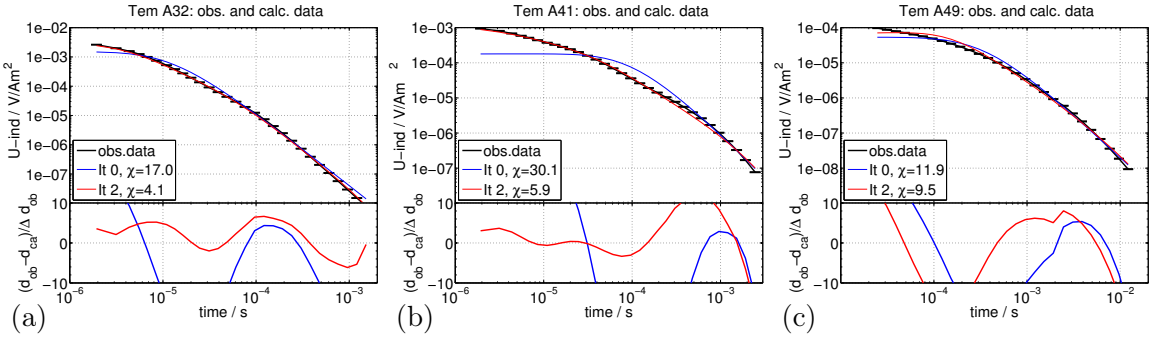

Figure 6.18: *Field data (obs.data) and calculated response for soundings A32, A41 and A49. The initial 2D model response (It 0) is denoted as a blue line and the final response (It 2) as a red line. The residuals are shown below each transient.*

6.5 Inversion of Tx-50 sounding data: fine parameterization

In order to accelerate the inversion, a coarse parameterization ($M \approx 2500$) with one model column beneath each sounding location was chosen for the previous field data examples. This parameterization is sufficient to fit the field data well. Furthermore, the results are meaningful and in good agreement with the 1D stitched models discussed in section 4.7.2.

Nevertheless, a fine parameterization may be required in cases where smaller structures are investigated and soundings are overlapping. An example is presented in Fig. 6.17 for a fine parameterization with $\Delta_x = 5$ m and $\Delta_z = 2.5$ m. This results in a total amount of $M = 392 \times 58 = 23000$ model parameters. The total amount of data-points for the 33 sounding locations is $N = 958$. Hence, the problem is clearly under-determined and the linear normal equation system requires a sufficient regularization.

As for the previous example in Fig. 6.17, the starting model is constructed from the late time apparent resistivities. The 2D model obtained after the third iteration reproduces the overall structure and is well comparable to the previously discussed 2D inversion results. Northeast of sounding A38, the conductive layer sandwiched between the two resistors is well reconstructed. The resistivities for the shallow and deeper layer range between 20 and 30 Ωm. In that zone the data-fitting is best and ranges from $\chi \approx 2$ to 3 for all soundings (see red line in Fig. 6.19(d)). The transition zone from moderate to high conductivity and the small resistive feature between A38 and A41 are both reconstructed. As discussed in the previous model in Fig. 6.17(b), the continuation of the resistive underlying layer between sounding A41 and A50 is uncertain, because these resistivities are already present in the initial model.

Coverage and *doi*

The *doi* plotted in Fig. 6.19(c) is maximal on the resistive zone and decreased between sounding A41 and A50. The *doi* is around 60 m in that zone. Further southwest of sounding A50 it is again increased to 80 m. The lateral change is indeed meaningful, because the length of the recorded transients are shorter between A41 and A50 compared to those southwest. For comparison, the maximum acquisition time is visible in the residual-section in Fig. 6.19(e). The *doi* seems over-estimated by roughly 20 m on

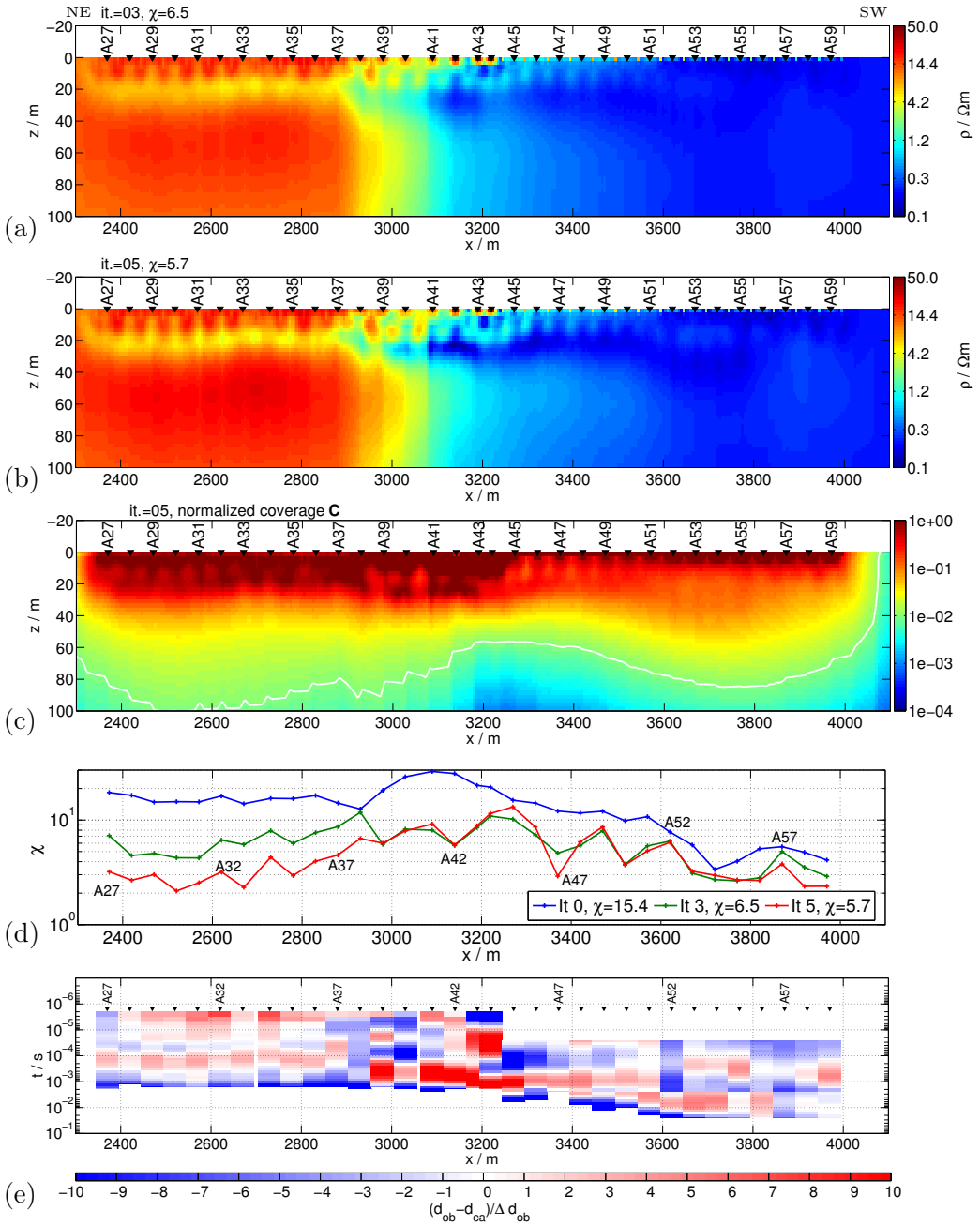

Figure 6.19: *2D inversion of the field data using a fine parameterization with* $\Delta_x = 5$ *m and* Δ_z *=2.5 m. 2D models obtained for (a) the third and (b) the final iteration. The corresponding coverage for the final 2D model is displayed in (c). The calculated* χ *for each sounding is plotted in (d) for the initial 2D model, the third iteration and the final 2D model. The global* χ *is displayed in the legend. The initial model is derived from the late time apparent resistivities similar to that shown in Fig. 6.17(a). In (d) the residuals of the final 2D model response are plotted for each time point versus the sounding location.*

the mudflat southwest of A39. For comparison see the *doi* estimate plotted for the 1D stitched results in Fig. 4.15(a,b).

A multi-grid approach involves a lot more computational effort and also uncertainties. Therefore, only one late time grid is used for the mudflat soundings southwest of A44 and the early time data with $t < 2 \cdot 10^{-5}$ s is not inverted in that zone. As a result,

the coverage on the mudflat decreases at shallow depth with $z < 20$ m. The structure of the coverage relates well to the corresponding model of the fifth iteration, especially between A37 and A43. Since the model is slightly over-structured between the receiver locations at shallow depth on the resistive zone, the coverage reflects this. In general, increased sensitivities are expected below the overlapping transmitter locations. Due to increased conductivity below the receivers, the situation is reversed.

Data fit and distribution of residuals

The inversion converges to $\chi = 6.5$ in three iterations, which corresponds to a relative misfit decrease of roughly 60% compared to the initial χ. After the fifth iteration the inversion aborts with a $\chi = 5.7$. For a 2D inversion of 33 soundings simultaneously, this is a good fitting. Furthermore, χ is quite uniformly distributed along the profile line, but the fitting is best northeast of sounding A38. To illustrate this, the residuals are plotted for each time point and sounding along the profile in Fig. 6.19(e). Large residuals are present between sounding A39 and A45, which occur mostly at later times. In that zone, the structure is quite complex, too. Northeast of A39 the residuals are much smaller. Particularly for some larger residuals, the alternation from positive to negative residuals indicate a systematic behavior. A histogram of the residuals for the model of the fifth iteration is plotted in Fig. 6.20(a). The residuals are centered around one, although there are a few outliers between -20 and -40. If 1% of the data (9 data points), which exhibit the largest residuals, are neglected, χ improves to $\chi = 4.8$. According to the QQ-plot in Fig. 6.20(b) these high residuals are not normally distributed, whereas for small deviations around ± 5 the residuals are distributed close to normal.

As an example, the calculated response for the initial model, the third and the fifth iteration for three soundings are displayed in Fig. 6.21(a-c). For soundings A32 and A41 the improvement of the fit is large. Sounding A41 is not fitted well for the last decade of time, which results in large residuals. According to the χ value, the fit for sounding A49 is only slightly improved from $\chi = 12.1$ to 8.6. In contrast to that, the final model response indicate a significant improvement of the fit, particularly for the first two decades of time.

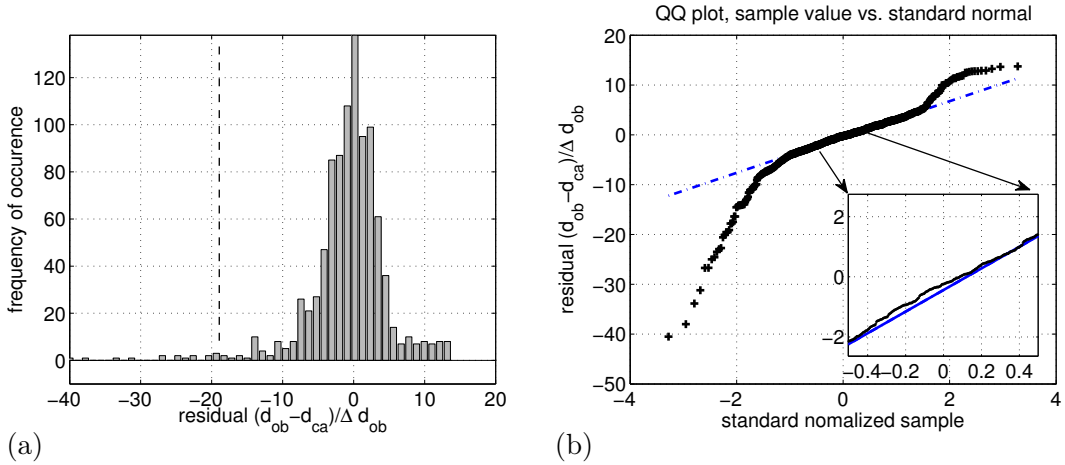

(a) (b)

Figure 6.20: *(a) Histogram of the data residuals for each time point and sounding location of the final 2D model. Left of the dashed vertical line are the 1% largest residuals. (b) QQ plot of the data residuals with magnification between* ± 0.5. *The straight line is marked dashed blue.*

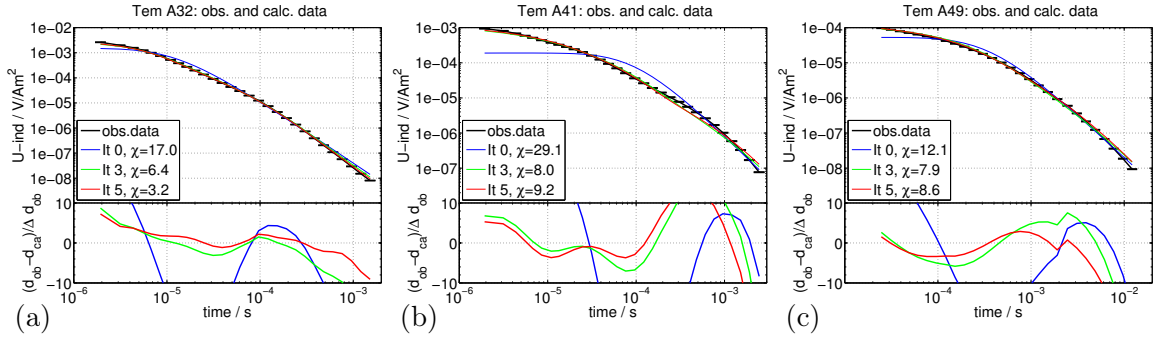

Figure 6.21: *Field data and calculated 2D response for soundings A32, A41 and A47. The initial 2D model response (It 0) is denoted a blue line and the final response (It 5) as a red line. The residuals are plotted below each sounding.*

6.5.1 Regularization parameters

The evolution of χ, the stepsize $|\Delta \boldsymbol{m}_k|$ and the regularization parameters λ_k, β and α are displayed in Fig. 6.22. The ratio of λ_x/λ_z is fixed to one and the global regularization parameter λ_k is determined automatically by the pareto optimization. The Marquardt damping β is very large compared to λ_k, particularly in the first two iterations. This usually causes a smaller stepsize of the model update $|\Delta \boldsymbol{m}_k|$. To counteract a large β and a small stepsize, the step-length α is significantly increased to a maximum of $\alpha \approx 3 \cdot 10^3$ for the first two iterations. Obviously, the inversion has a steepest descent character until the third iteration. For the iterations 3 to 5 the step length α is around one and has no considerable impact on the inversion. Another significant model update is calculated in the third iteration, where λ_k is decreased by almost 4 decades. The stepsize is maximal for the third iteration, which causes a structured model (cf. Fig. 6.19(a)). Although λ_k is increased again for the following iterations, the model remains rough. At first sight this seems unusual, but according to the global fit χ and the decreased stepsize $|\Delta \boldsymbol{m}_k|$, no large model updates are calculated after the third iteration.

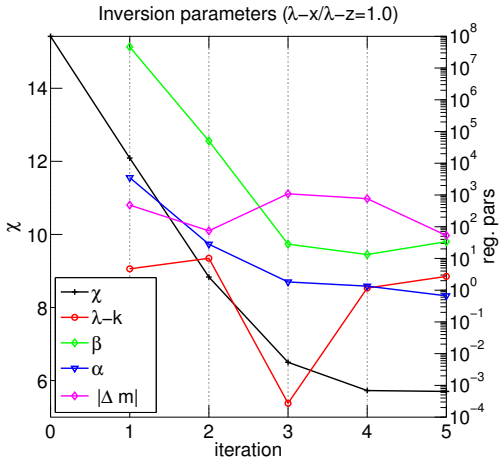

Figure 6.22: *Evolution of the global fit χ, the stepsize $|\Delta \boldsymbol{m}_k|$ and the inversion regularization parameters λ_k, β and α for each iteration.*

6.5.2 Computational requirements

For the above discussed example 33 soundings are inverted simultaneously with a total of $N = 958$ data points. The model consists of $M = 392 \times 58 = 22736$ free parameters. *SINV* is fully parallelized for the number of source-fields/transmitters and uses the Message Passing Interface (*MPI*). Since 33 soundings are inverted, it is recommended to use 33+1 computing nodes/processors (master+slave concept). For each iteration, 33 forward calculations are performed with the *SLDMem3t*. A total of MS =12000

Krylov subspace iterations is found sufficient for the numerical field calculations (see section 5.3.6 for details). The computation time takes around 20 minutes for a single forward calculation. The calculations are done on the Cologne High Performance Efficient Operating Platform for Science (*CHEOPS*) at the Regional Computing Centre Cologne (RRZK). For details on the computer architecture refer to Achter et al. [2013]. In order to compute the 3D background fields for the calculation of the Jacobian matrix another 33 forward calculations are performed. The background fields are not calculated for the complete spatial *SLDMem3t* grid (n_x, n_y and n_z), but moreover for a smaller grid frame (see section 6.1.2). For example, each forward calculation with the grid designed for the conductive mudflat results in a total of $30 \times 30 \times 25$ electric field values, computed for each component (E_x, E_y, E_z). The total required memory for one forward calculation is therefore

$$MEM = 3 \times n_x \times n_y \times n_z \times MS \times 8\,\text{Byte} = 6.04\,\text{GB}.$$

Due to memory-limitations, the required memory becomes too large if all 33 transmitters and their sensitivities are processed simultaneously. Therefore, the sensitivities are not calculated parallel. Moreover, the sensitivity calculation for one transmitter is distributed equally to all 33 processors by splitting the grid-frame. This results in $6.06\ GB/(34-1) \approx 0.18$ GB memory requirement per processor and each of the 33 parallel forward calculations. If the normal equation (6.2) is not stabilized sufficiently, the Cholesky decomposition fails. Even if it does not fail, the update may not provide a relative misfit decrease and the pareto optimization is continued. Therefore, the internal optimization involves a lot more full inversions until a proper set of regularization parameters is determined. In Fig. 6.23, the calculation time is plotted for each iteration. If an optimal set of regularization parameters is determined relatively fast, an iteration takes less than 30 hours for the example shown in Fig. 6.19. Due to the pareto optimization, each following iteration takes between 30 and 50 hours. The inversion is manually terminated after 200 hours. For comparison, each inversion step for the inversion with the coarse parameterization displayed in Fig 6.17 takes between 7 and 15 hours.

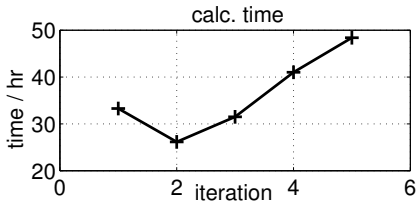

Figure 6.23: *Computation time for each iteration.*

For further details on storage requirements and implementation of the parallelization within *SINV* using *MPI* refer to Martin [2009].

6.6 Inversion of Tx-100 sounding data using a-priori information

In the previous chapters the more resistive mudflat base was discussed with respect to the late time apparent resistivity $\rho_{a,lt}$ and its first order time derivative. The 1D models and their corresponding model parameter importances were discussed and the base layer was verified by a 2D modeling study. To gain a more independent validation of the resistive mudflat base the soundings obtained between sounding A27 and A*80

are included into the 2D inversion. A total of 53 soundings recorded partly with the Tx-50 and the 100 × 100 m^2 setup along profile A are inverted together. The simultaneous inversion of both setups is challenging, because the Tx-50 data is recorded for a minimum time of approximately $t = 10^{-6}$ s, whereas the Tx-100 soundings are recorded in ZT-mode between $t = 10^{-4}$ and 10^{-1} s. Therefore, the total time range spans approximately five decades of time and the induced voltage approximately seven. As a consequence, the sensitivity is going to vary over a large amplitude range as well. Without rescaling the sensitivities, the data is not fitted at late times. Furthermore, the base of the mudflat is generally difficult to resolve with the TEM method and for some soundings it is supported only by a few late time data points (for comparison see section 4.7.4).

To ensure a sufficient model update for deeper zones, the top of the mudflat base is fixed in the 2D inversion and large blocks are included below. This approach was previously introduced in section 6.2.1 and tested for a 2D synthetic example. In Fig. 6.24(a), the initial 2D model is displayed and the top of the included blocks are marked by white lines. The top of the base is derived from the 1D stitched inversion models presented in Fig. 4.17 and the initial resistivity below is set to 0.3 Ωm. The shallower part of the initial model is derived from the late time apparent resistivities. The data misfit χ for the initial model and each sounding is displayed in Fig. 6.24(d). The initial fit is poor with a global $\chi \approx 140$ northeast of sounding A46. After the eighth iteration the global χ improves to $\chi = 5.5$, which is remarkable. The data misfit is uniformly distributed

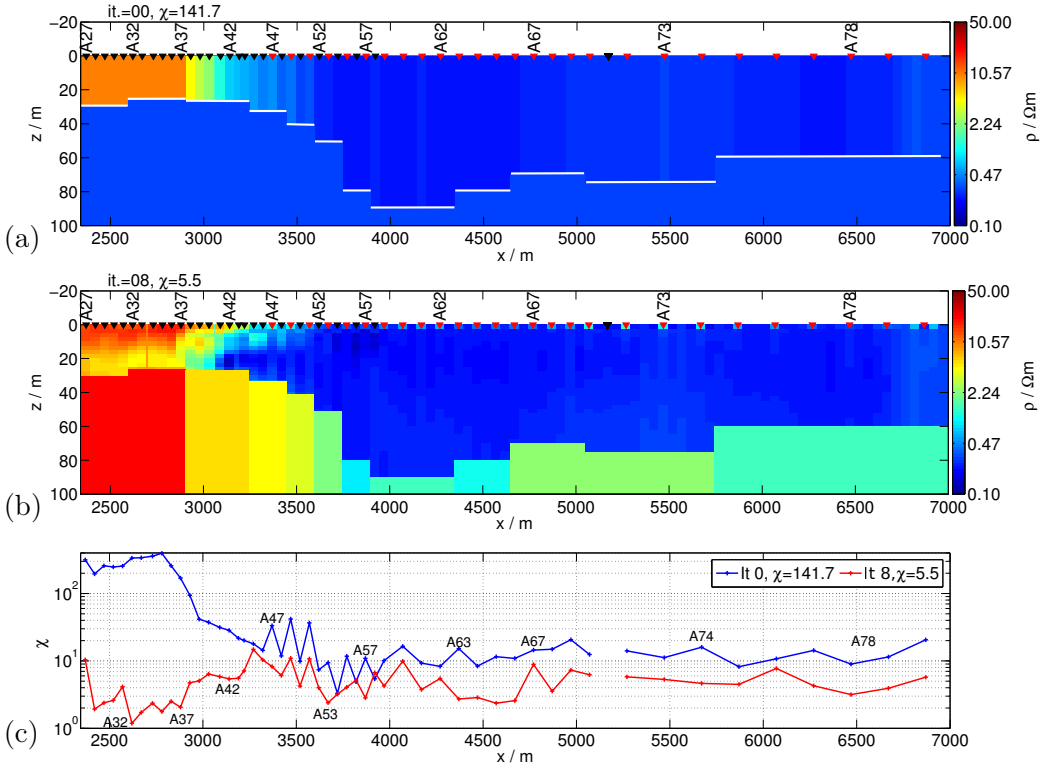

Figure 6.24: *2D inversion of Tx-50 and Tx-100 sounding data using large blocks for the basement structure with 0.3 Ωm initial resistivity. The initial model is shown in (a) and the final 2D model in (b). The calculated χ for each sounding is plotted in (c) for the initial (It 0) and the final 2D model (It 8). The global χ is displayed in the legend. The sounding locations are denoted as black and red triangles for the Tx-50 and the Tx-100 setup, respectively.*

along the profile and below $\chi = 10$ for almost all soundings. The inversion leads to a well reconstructed 2D model displayed in Fig. 6.24(b), which is in good agreement with the 1D stitched inversion results. The base is reconstructed with approximately 30 Ωm northeast of sounding A37 and decreases to around 2 Ωm on the mudflat zone. Even for the deepest part between A*57 and A*62 a model update is achieved. Since an initial base resistivity of 0.3 Ωm is used, the result is remarkable and independently verifies the resistivity increase below the mudflat. Furthermore, the reconstructed resistivity values are an approximate lower resistivity bound. In Fig. 6.25, the field data and calculated final model response is displayed for soundings A*49, A*61 and A*77. The strong late time decay for sounding A*49 corresponds to the resistor below the mudflat and is fitted well. Although the late time decay is not that prominent for sounding A*77, it is also well fitted. Sounding A*61 indicates only a poor decay for the last three data points. In that zone, the mudflat base is also deepest. Nevertheless, the model update improves the data fit also for those last data points.

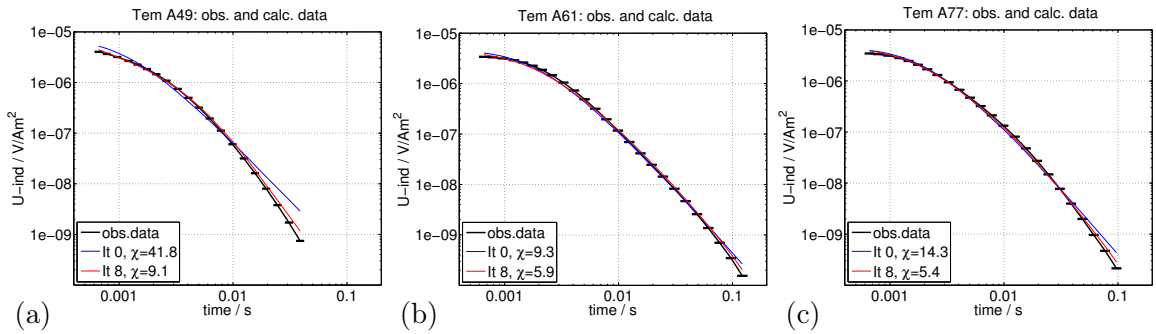

Figure 6.25: *Field data and calculated 2D response for soundings A49*, A61* and A77* obtained with the Tx-100 setup. The initial 2D model response is denoted as a blue line and the final response as a red line.*

6.7 Conclusions from the 2D inversion results

The 2D inversion algorithm *SINV* was applied to synthetic TEM data derived from two different models. On the basis of these models important aspects of the algorithm were investigated, i.e. the model parameterization, a-priori information, sensitivity, depth of investigation and particularly the pareto optimization of the regularization parameters. The first investigated model was a standard magnetotelluric model with a buried conductor and resistor. Such type of models were often used to check numerical forward and inverse algorithms, e.g. Siripunvaraporn & Egbert [2000]; Rodi & Mackie [2001]. The algorithm *SINV* performed well and reconstructed both blocks remarkably. The calculated sensitivity is meaningful and reflects better resolution of the conductor. A-priori information was incorporated by fixing the shape of the buried blocks. This approach led to an almost one-to-one image of the original model. A second synthetic model with a basin type of structure was investigated, particularly to investigate the pareto optimization. Far more control of the inversion process was achieved by fixing the ratio of the horizontal and vertical Occam regularization and introducing a global regularization. As a consequence, the 2D inversion models did not become over-structured. A pure Occam inversion was not realized, since an additional Marquardt damping term

is required to stabilize the linear equation system.
Further studies showed that very coarse parameterizations with one column below each TEM sounding produces very stable results and significantly accelerates the inversion.

To derive an independent result, which is neither based on manual forward modeling strategies nor on 1D inverse models, the 2D inversion is applied first to 33 soundings recorded along profile A. It turned out, that for an extreme lateral resistivity variation a homogeneous starting model is either suitable for the resistive or the conductive zone, but not for both at the same time. The moderate resistive zone was remarkably reconstructed using a 5 Ωm initial model. On the mudflat a 1 Ωm starting model was suitable. A comparison of the 2D model with the 1D models for three selected soundings, revealed an extremely good agreement particularly outside the mudflat. In order to fit the complete set of 33 soundings simultaneously, a starting model was derived from the late time apparent resistivity calculated from the field data. The obtained final 2D models explain the field data well and are in good agreement with the corresponding resistivity-depth section derived from the 1D results.
In the second step, the soundings recorded with the Tx-100 setup were included into the inversion, in order to independently verify the base below the high conductive mudflat. A total of 53 soundings were inverted simultaneously. To constrain the inversion and increase the sensitivity of the deeper structures, large blocks were included as mudflat base layer. Although a low initial resistivity was assigned to the blocks, the inversion reconstructed the base along the complete profile.
Conclusively, the 2D inversion results independently validate the subsurface structure along profile A. Both, the resistive basalt formation northeast of the mudflat and the resistive base of the mudflat were reconstructed. The comparability to the patched 1D results was remarkable and can be seen as a strong validation of the subsurface resistivity structure.

CHAPTER 7

Conclusions and outlook

The central part of the Azraq basin in Jordan is a unique wetland and a potential target for research within the ongoing Collaborative Research Centre 806, entitled *Our Way to Europe* (CRC-806). In the basin center, thick clay-rich sedimentary sequences are deposited forming a 10×10 km^2 mudflat. A chert-limestone formation is expected below these sediments. Outside of the mudflat a resistive buried basalt layer is present. To provide a basis for future drilling projects a 7 km and a 5 km long transects were investigated from the edge across the center of the mudflat. A total of 150 central loop transient electromagnetic (TEM) soundings were carried out along both transects. Additionally, the electrical resistivity tomography (ERT) was utilized as a complementary method to validate the TEM results. Besides providing general information about the area, the identification of the sediment thickness in contrast to the chert-limestone and to the basalt layer were the two major targets.

The TEM data was interpreted using common 1D inversion techniques in the first part of this thesis. The derived quasi 2D resistivity-depth sections are consistent and in good agreement with the geological information. Furthermore, they were correlated with lithological borehole data, which verifies the overall reliability of the models. Both profiles were analyzed in detail by model equivalence and parameter importances. The top of a resistive buried basalt layer was detected between 15 and 40 m depth in the northeastern zone of the study area. According to the geology, the basalt is expected to be interrupted at the Al Bayda fault. It was found that this resistive layer extends approximately 700 m below the high conductive mudflat zone, where a strong and abrupt decline of the resistor is present. This finding also suggests that the Al Bayda fault zone extends over 700 m. A resistivity increase below the mudflat sediments is observed along both transects which obviously corresponds to the chert-limestone layer (URC). The top of the URC ranges from approximately 30 m down to 100 m depth in the deepest zones. These two resistive formations were the target structures to resolve by the geophysical investigation. Although not the primary target, the shallow transition zone from moderate to very low resistivities was determined precisely along both transects. This is known to be a mixing zone from fresh and brackish water bearing layers to hyper saline clay sediments. Azraq is heavily exploited for freshwater and the lateral extent and thickness of the saline water body in the basin center is of topical interest for the groundwater management. Groundwater is an increasing global prob-

lem and I sincerely hope that the presented geophysical results can contribute to the groundwater management in Azraq.

Although no clear distortion effects are visible in the TEM sounding data, the subsurface resistivity varies significantly along both investigated transects. Hence, it was questionable if a 1D interpretation is adequate. To validate the quasi 2D resistivity-depth section along the north-south transect (profile A), a 2D modeling study was performed. The derived 2D model generally explained the field data well and only slightly larger residuals are present, where the lateral resistivity contrast is largest. Therefore, the 2D model validates the 1D inversion results and demonstrated that a 1D interpretation of the TEM soundings is obviously sufficient. This finding is in accordance with the general experience that the TEM sounding method can be well interpreted by layered earth models [Spies & Frischknecht, 1991; Goldman et al., 1994]. Moreover, an attempt was made to estimate the 2D effect, which the 2D final model along profile A generates. A semi-synthetic TEM-tipper was calculated from horizontal synthetic voltage data and the measured field data. This semi-synthetic TEM-tipper suggested that four to six soundings might be 2D affected. However, the benefit of this approach is limited because the 2D model was derived from vertical voltage data. For future TEM surveys additional measurements of the horizontal magnetic field components are suggested over strong lateral resistivity contrasts. They can provide a better understanding, whether the soundings are 2D/3D affected and require multi-dimensional interpretation.
The 2D models along both transects were further investigated by variation of the resistive layer below the mudflat.The 2D modeling demonstrated, that the resistor is in general required to fit the field data. Removing the layer results in a deteriorated data fit along both profiles. However, some soundings exhibit larger errors at late times and do not support the resistor as well as other soundings. If the data errors were not considered, all soundings support the resistivity increase at depth and the *RMS* significantly deteriorates. As expected for the TEM method, the overall resistivity resolution of the base is quite poor. As a consequence, it can vary roughly between 2.5 Ωm and 100 Ωm in most zones.

A drawback of the 2D modeling is, that it is always based on the prior choice of a model. In the case presented here, it was a one-to-one image of the quasi resistivity-depth sections derived from 1D models. To obtain an independent validation of the resistivity structure, a large number of soundings along the north-south transect (profile A) were interpreted using the 2D TEM inversion scheme *SINV*. The obtained final 2D model explained the field data well and was in good agreement with the resistivity-depth section derived from the 1D results. All characteristic features that are visible in the quasi 2D sections, were also reproduced by the inversion scheme. A comparison of the 2D model with the 1D models for three representative soundings, revealed a remarkable agreement for the moderate resistive zones. Conclusively, the 2D inversion provided a strong independent validation of the subsurface structure, particularly in the moderate resistive zone.
Often the soundings on the low resistive mudflat, were not reconstructed that well and the initial fit could not be improved. Due to the extremely low resistivities, the inversion of the mudflat zone requires further investigations. One approach would be to adjust the model parameterization. A promising approach was presented, to reconstruct the

deep chert-limestone layer below the mudflat. By including large blocks into the initial model parameterization, significant model updates were achieved and the deep resistive layer was well reconstructed. Although a low initial resistivity was assigned to the blocks, the inversion reconstructed the base along the complete profile.

The 2D inversion of TEM data is not state of the art yet, but the results presented in this thesis demonstrated that the present algorithm *SINV* is applicable. Besides the models derived from the field data, two synthetic examples were presented to study the capabilities of the algorithm. Both models were reconstructed remarkably well and motivate the future application of the algorithm. However, there are still possible future improvements.
The pareto optimization of the regularization parameters could be partly improved by fixing the horizontal to vertical smoothing ratio and introducing a global Occam regularization. A pure smoothness constraint Occam inversion was not realized and an additional Marquardt damping is required to stabilize the solution of the linear equation system. Currently, the pareto optimization is done by a Marquardt inversion of the regularization parameters. On the one hand the approach is innovative. On the other hand it is time-consuming and depends on the initial regularization values. Further investigations to obtain suitable starting values are required and may accelerate the pareto optimization.
At the current development stage of *SINV*, one iteration took around 20-50 hours using a fine model parameterization. Due to the long run time and to circumvent uncertainties originating from the forward solver *SLDMem3t*, a multi grid approach was avoided. Hence, the early time data was not considered for the mudflat Tx-50 soundings. At this point, the potential of *SINV* has not been fully utilized, yet. However, in the long term, Martin [2009] suggested to implement a pre-conditioned conjugate gradient based iterative solver to accelerate the inversion.
Due to convergence problems using the second order roughness constraint, only first order roughness inversions were done. Useful information about the depth of investigation and the resolution of model zones may be derived, if both roughness constraints are used.
Moreover, in this thesis the focus was on the 2D inversion of the field data obtained along the north-south transect, particularly in the transition zone and towards the mudflat. The inversion scheme can be further applied to the data which was not considered, yet.
For the future, it would be definitely interesting to apply the algorithm to other TEM field data sets. Probably very promising inversion results can be achieved, if dense (overlapping) TEM soundings are investigated using multi-component receivers over 2D or even 3D structures. A large scale 3D inversion of synthetic TEM data over a buried conductor using *SINV* was already presented by Martin [2009] and can be applied to such field data in the future. Another, promising application of the 2D inversion is the shallow coastal marine environment, where the bathymetry and coastal geometry often requires 2D treatment.

Conclusively, the results presented in this thesis are a basis for future investigations of the CRC 806 in the central Azraq basin area. The derived subsurface models provide a detailed image of the resistivity-depth distribution along both transects and agree very well with the expected geological boundaries. The buried basalt layer and the depth

to the resistive base below the mudflat are identified. If future drilling will be conducted by the CRC 806 project, the presented geophysical results provide considerably valuable subsurface information.

Bibliography

ABEM, 2010. *Terrameter SAS 4000 / SAS 1000 Instruction Manual*, ABEM Instrument AB, printed matter no. 93109 edn.

Abu Rajab, J. & El-naqa, A. R., 2013. Case History: Mapping groundwater salinization using transient electromagnetic and direct current resistivity methods in Azraq Basin, Jordan, *Geophysics*, **78**(2), 89–101.

Achter, V., Borowski, S., Nieroda, L., Packschies, L. & Winkelmann, V., 2013. *CHEOPS, Cologne High Efficient Operating Platform for Science*, Regional Computing Centre Cologne, University of Cologne.

Ahmad, K. I., 2010. *Organic chemistry of Al-Azraq basin, Jordan, an interpretation of paleoenvironment and paleoclimate using bulk organic matter*, Ph.D. thesis, Department of Geosciences, University of Missouri-Kansas City.

Ala'li, J., 1993. Exploration for Bentonite and other Minerals in Azraq Depression, Tech. rep., Natural Recources Authority, Geology Directorate, Economic Geology Division, Amman.

Archie, G. E., 1942. The electrical resistivity log as an aid in determining some reservoir characteristics, *Petroleum Transactions of AIME*, **146**(1), 54–62.

Asten, M. W., 1987. Full transmitter waveform transient electromagnetic modeling and inversion for soundings over coal measures, *Geophysics*, **52**(3), 279–288.

Auken, E. & Christensen, A. V., 2004. Layered and laterally constrained 2D inversion of resistivity data, *Geophysics*, **69**, 752–761.

Auken, E., Pellerin, L., Christensen, N. B. & Sørensen, K., 2006. A survey of current trends in near-surface electrical and electromagnetic methods, *Geophysics*, **71**(5), 249–260.

Avdeev, D. B., 2005. Three-dimensional electromagnetic modelling and inversion from theory to application, *Surveys in Geophysics*, **26**, 767–799.

Bedrosian, P. A., Burgess, M. K. & Nishikawa, T., 2013. Faulting and groundwater in a desert environment: constraining hydrogeology using time-domain electromagnetic data, *Near Surface Geophysics*, **11**(5), 545–555.

Bender, F., 1974. *Geology of Jordan. Contributions to the Regional Geology of the Earth*, vol. 7, Gebrüder Borntraeger, Berlin, Stuttgart.

Byrd, B. F., 1988. Late Pleistocene Settlement Diversity in the Azraq Basin, *Paléorient*, **14**(2), 257–264.

Börner, R.-U., 2010. Numerical Modelling in Geo-Electromagnetics: Advances and Challenges, *Surveys in Geophysics*, **31**, 225–245.

Commer, M., 2003. *Three-dimensional inversion of transient electromagnetic data: A comparative study*, Ph.D. thesis, Universität zu Köln, Institut für Geophysik und Meteorologie.

Commer, M. & Newman, G. A., 2008. New advances in three-dimensional controlled-source electromagnetic inversion, *Geophysical Journal International*, **172**(2), 513–535.

Commer, M., Helwig, S. L., Hördt, A. & Tezkan, B., 2005. Interpretation of long-offset transient electromagnetic data from Mount Merapi, Indonesia, using a three-dimensional optimization approach, *Journal of Geophysical Research*, **110**.

Constable, S. C., Parker, R. L. & Constable, C. G., 1987. Occam's inversion: a practical algorithm for generating smooth models from EM sounding data, *Geophysics*, **52**(3), 289–300.

Copeland, L., 1988. Environment, Chronology and Lower-Middle-Paleolithic Occupations of the Azraq Basin, Jordan, *Paléorient*, **14**(2), 66–75.

CRC-806, 2012. OUR WAY TO EUROPE- Culture-Environment Interaction and Human Mobility in the Late Quaternary, Online: www.sfb806.uni-koeln.de.

Danielsen, J. E., Auken, E., Jørgensen, F., Søndergaard, V. & Sørensen, K. I., 2003. The application of the transient electromagnetic method in hydrogeophysical surveys, *Journal of Applied Geophysics*, **53**(4), 181–198.

De Groot-Hedlin, C. & Constable, S., 1990. Occam's inversion to generate smooth, two-dimensional models for magnetotelluric data, *Geophysics*, **55**(12), 1613–1624.

Druskin, V. L. & Knizhnermann, L. A., 1988. A spektral semi-discrete method for the numerical solution of 3D nonstationary problems in electrical prospecting, *Physics of the Solid Earth*, **24**, 641–648.

Druskin, V. L. & Knizhnermann, L. A., 1994. Spectral approach to solving three-dimensional Maxwell's diffusion equations in the time and frequency domains, *Radio Science*, **29**(4), 937–953.

Druskin, V. L. & Knizhnermann, L. A., 1999. New spectral Lanczos decomposition method for induction modeling in arbitrary 3-D geometry, *Geophysics*, **64**(3), 701–706.

Druskin, V. L. & Knizhnermann, L. A., 2000. *User's guide for the program complex to compute 3D nonstationary electromagnetic fields in inhomogenous conductive media*.

Eiermann, M. & Ernst, O. G., 2006. A restarted Krylov subspace method for the evaluation of matrix functions, *SIAM Journal of Numerical Analysis*, **44**, 2481–2504.

El-Kaysi, K. & Talat, T., 1996. Geoelectrical survey in the Azraq mudflat area, Report, Natural Resources Authority, Geophysics and Technical Service Department, Geophysics Division, Amman.

El-Naqa, A., 2010. Final Report: Study of salt water intrusion in the Upper Aquifer in Azraq Basin, Report, IUCN-International Union for Conservation of Nature.

El-Naqa, A., Al-Momani, M., Kilani, S. & Hammouri, N., 2007. Groundwater Deterioration of Shallow Groundwater Aquifers Due to Overexploitation in Northeast Jordan, *CLEAN*, **35**(2), 156–166.

El-Waheidi, M., Merlanti, F. & Pavan, M., 1992. Geoelectrical resistivity survey of the central part of Azraq basin (Jordan) for identifying saltwater/freshwater interface, *Journal of Applied Geophysics*, **29**, 125–133.

Everett, M. E., 2011. Theoretical Developments in Electromagnetic Induction Geophysics with Selected Applications in the Near Surface, *Surveys in Geophysics*, **33**(1), 29–63.

Farquharson, C. G. & Oldenburg, D. W., 1996. Approximate sensitivities for the electromagnetic inverse problem, *Geophysical Journal International*, **126**, 235–253.

Farquharson, C. G. & Oldenburg, D. W., 2004. A comparison of automatic techniques for estimating the regularization parameter in non-linear inverse problems, *Geophysical Journal International*, **156**, 411–425.

Fitterman, D. & Anderson, W., 1987. Effect of Transmitter Turn-Off Time on Transient Soundings, *Geoexploration*, **24**, 131–146.

Fitterman, D. V. & Stewart, M. T., 1986. Transient electromagnetic sounding for groundwater, *Geophysics*, **51**(4), 995–1005.

Gaidetzka, A., Goldman, M., Helwig, S. L. & Tezkan, B., 2001. Erste Erfahrungen mit der NanoTEM- Apparatur, in *Protokoll über das 19. Kolloquium für Elektromagnetische Tiefenforschung*, pp. 68–77, Dt. Geophys. Gesellschaft.

Goldman, M. & Neubauer, F. M., 1994. Groundwater Exploration Using Integrated Geophysical Techniques, *Surveys in Geophysics*, **15**, 331–361.

Goldman, M., Tabarovskyt, L. & Rabinovich, M., 1994. On the influence of 3D structures in the interpretation of transient electromagnetic sounding data, *Geophysics*, **59**(6), 889–901.

Goldman, M., Levi, E., Tezkan, B. & Yogeshwar, P., 2011. The 2D coastal effect on marine time domain electromagnetic measurements using broadside dBz/dt of an electrical transmitter dipole, *Geophysics*, **76**(2), 101–109.

Günther, T., 2004. *Inversion Methods and Resolution Analysis for the 2D/3D Reconstruction of Resistivity Structures from DC Measurements*, Ph.D. thesis, Technische Universität Bergakademie Freiberg.

Haber, E., Oldenburg, D. W. & Shekhtman, R., 2007. Inversion of time domain three-dimensional electromagnetic data, *Geophysical Journal International*, **171**, 550–564.

Hansen, P. C. & O'Leary, D. P., 1993. The use of the l-curve in the regularization of discrete ill-posed problems, *SIAM Journal of Scientific Computing*, **14**, 1487–1503.

Hanstein, T., 1992. Iterative und parametrisierte Dekonvolution für LOTEM Daten, in *Protokoll über das 14. Kolloquium Elektromagnetische Tiefenforschung*, p. 163–172, Dt. Geophys. Gesellschaft.

Haroon, A., Goldman, M. & Tezkan, B., 2013. Marine Circular Electric Dipole (MCED): A new innovative electromagnetic technique for delineating resistive submarine targets, in *Proceedings of the 8th International Marine Electromagnetics Conference (MARELEC)*.

Helwig, S. L. & Kozhevnikov, N. O., 2003. Schwingungen in TEM Sendesignalen zu frühen Zeiten, in *Protokoll über das 20. Kolloquium für Elektromagnetische Tiefenforschung*, pp. 11–20, Dt. Geophys. Gesellschaft.

Helwig, S. L., Lange, J. & Hanstein, T., 2003. Kombination dekonvolvierter Messkurven zu einem langen Transienten, in *Protokoll über die 63. Jahrestagung der Deutschen Geophysikalischen Gesellschaft*, Dt. Geophys. Gesellschaft.

Hördt, A., 1992. *Interpretation transient elektromagnetischer Tiefensondierungen für anisotrop horizontal geschichtete und für dreidimensionale Leitfähigkeitsstrukturen*, Ph.D. thesis, Universität zu Köln, Institut für Geophysik und Meteorologie.

Hördt, A., 1998. Calculation of electromagnetic sensitivities in the time domain, *Geophysical Journal International*, **133**, 713–720.

Hördt, A. & Müller, M., 2000. Understanding LOTEM data from mountainous terrain, *Geophysics*, **65**(4), 1113–1123.

Hördt, A. & Scholl, C., 2004. The effect of local distortions on time domain electromagnetic measurements, *Geophysics*, **69**(1), 87–96.

Hördt, A., Druskint, V. L., Knizhnerman, L. A. & Strack, K.-m., 1992. Interpretation of 3-D effects in long-offset transient electromagnetic (LOTEM) soundings in the Münsterland, *Geophysics*, **57**(9), 1127–1137.

Hördt, A., Dautel, S., Tezkan, B. & Thern, H., 2000. Interpretation of long-offset transient electromagnetic data from the Odenwald area, Germany, using two-dimensional modelling, *Geophysical Journal International*, **140**(3), 577–586.

Ibrahim, K., 1996. The Regional Geologoy of Al Azraq Area, *Hashemite Kingdom of Jordan, Geological Mapping Division, Natural Resources Authority, Bulletin*, **36**.

Jackson, J. D., 1975. *Classical Electrodynamics*, John Wiley & Sons, INC., 3rd edn.

Jones, M. D. & Richter, T., 2011. Paleoclimatic and archeological implications of Pleistocene and Holocene environments in Azraq, Jordan, *Quaternary Research*, **76**(3), 363–372.

Jørgensen, F., Sandersen, P. B. & Auken, E., 2003. Imaging buried Quaternary valleys using the transient electromagnetic method, *Journal of Applied Geophysics*, **53**(4), 199–213.

Jupp, D. L. B. & Vozoff, K., 1975. Stable Iterative Methods for the Inversion of Geophysical Data, *Geophysical Journal of the Royal Astronomical Society*, **42**(3), 957–976.

Kalscheuer, T., Pedersen, L. B. & Siripunvaraporn, W., 2008. Radiomagnetotelluric two-dimensional forward and inverse modelling accounting for displacement currents, *Geophysical Journal International*, **175**(2), 486–514.

Kaudse, T., 2014. *Noble gases in groundwater of the Azraq Oasis, Jordan, and along the central Dead Sea Transform*, Ph.D. thesis, Heidelberg University.

Keller, G. V., 1987. Rock and Mineral Properties, in *Electromagnetic Methods in Applied Geophysics*, vol. 1, chap. 2, ed. Nabighian, M. N., Society of Exploration Geophysicists.

Knödel, K., Krummel, H. & Lange, G., 2005. *Handbuch zur Erkundung des Untergrundes von Deponien und Altlasten*, vol. 3: Geophysik, Springer, 2nd edn.

Koch, O., 2003. *Transient-elektromagnetische Messungen zur Erkundung einer Leitfähigkeitsanomalie am Vulkan Merapi in Indonesien*, Master's thesis, Institut für Geophysik und Meteorologie, Universität zu Köln.

Koch, O., Helwig, S., Tezkan, B. & the DESERT group, 2003. Strategien zur Erkundung einer schmalen vertikalen Leitfähigkeitsanomalie mit TEM-Methoden, in *Protokoll über das 20. Kolloquium für Elektromagnetische Tiefenforschung*, Dt. Geophys. Gesellschaft.

Koch, O., Helwig, S., Meqbel, N. & the DESERT Group, 2004. Vertical near surface conductivity anomaly detected at the Dead Sea Transform, in *Proceedings of the 17th international workshop on electromagnetic induction in the Earth, Hyderabad/India*.

Lange, J., 2003. *Joint Inversion von Central-Loop-TEM und Long-Offset-TEM Transienten am Beispiel von Messdaten aus Israel 2002*, Master's thesis, Universität zu Köln, Institut für Geophysik und Meteorologie.

Levenberg, K., 1944. A method for the solution of certain nonlinear problems in least squares, *Quarterly of Applied Mathematics*, **2**, 164–168.

Lines, L. & Treitel, S., 1984. Tutorial: A review of least-squares inversion and its application to geophysical problems, *Geophysical prospecting*, **32**, 159–186.

Marquardt, D., 1963. An algorithm for least squares estimation of non-linear parameters, *SIAM J. Sci. Stat. Comput.*, **11**, 431–441.

Martin, R., 2009. *Development and application of 2D and 3D transient electromagnetic inverse solutions based on adjoint Green functions: A feasibility study for the spatial reconstruction of conductivity distributions by means of sensitivities*, Ph.D. thesis, Universität zu Köln, Institut für Geophysik und Meteorologie.

Martin, R., Scholl, C., Helwig, S. L. & Hördt, A., 2003. Sensitivitätsberechung mit adjungierten Green'schen Funktionen für eine mehrdimensionale TEM-Inversion auf Linux-Clustern., in *Protokoll über das 20. Kolloquium für Elektromagnetische Tiefenforschung*, Dt. Geophys. Gesellschaft.

McGillivray, P., Oldenburg, D., Ellis, R. & Habashy, T., 1994. Calculation of sensitivities for the frequency-domain electromagnetic problem, *Geophysical Journal International*, **116**, 1–4.

Meju, M. A., 1994. *Geophysical Data Analysis: Understanding Inverse Problem in Theory and Practice*, Society of Exploration Geophysicists.

Menke, W., 1984. *Geophysical data analysis: discrete inverse theory*, Academic Press inc.

Meshan, O. A., 2011. Azraq oasis restoration project. Development of a Decision Support System (DSS) for Azraq Oasis, Tech. Rep. April 2009, National Center for Research and Development.

Mollidor, L., 2008. *Central-Loop-TEM auf dem Holzmaar, Eifel- Eine Machbarkeitsstudie*, Master's thesis, Institut für Geophysik und Meteorologie, Universität zu Köln.

Mudler, J., 2013. *Untersuchung des Sedimentbeckens in Azraq, Jordanien mit Radiomagnetotellurik und Gleichstromgeoelektrik*, Bachelors's thesis, Institut für Geophysik und Meteorologie, Universität zu Köln.

Nabighian, M. N., 1979. Quasi-static transient response of a conducting half-space- An approximate representation, *Geophysics*, **44**(10), 1700–1705.

Nabighian, M. N. & Macnae, J. C., 1991. Time Domain Electromagnetic Prospecting Methods, in *Electromagnetic Methods in Applied Geophysics*, vol. 2, chap. 6, ed. Nabighian, M. N., Society of Exploration Geophysicists.

Natural Resources Authority, 2006. Petroleum Exploration Opportunities in Jordan, Tech. rep., Natural Resources Authority, Petroleum Directorate, Amman.

Newman, G. A. & Commer, M., 2005. New advances in three dimensional transient electromagnetic inversion, *Geophysical Journal International*, **160**, 5–32.

Newman, G. A., Anderson, W. L. & Hohmann, G. W., 1987. Interpretation of transient electromagnetic soundings over three-dimensional structures for the central-loop configuration, *Geophysical Journal of the Royal astronimical society*, **89**, 889–914.

Oldenburg, D. W., Haber, E. & Shekhtman, R., 2013. Three dimensional inversion of multisource time domain electromagnetic data, *Geophysics*, **78**(1), 47–57.

Palacky, G. J., 1991. Resistivity characteristics of geologic targets, in *Electromagnetic Methods in Applied Geophysics*, vol. 1, chap. 3, pp. 106–121, ed. Nabighian, M. N., Society of Exploration Geophysicists.

Papen, M. V., Tezkan, B. & Israil, M., 2013. Characterization of an aquifer in Roorkee, India using the spatially constrained inversion of in-loop TEM data, *Near Surface Geophysics*, **11**, 85–94.

Pellerin, L., 2002. Applications of electrical and electromagnetic methods for environmental and geotechnical investigations, *Surveys in Geophysics*, **23**(2-3), 101–132.

Persson, L. & Pedersen, L. B., 2002. The importance of displacement currents in RMT measurements in high resistivity environments, *Journal of Applied Geophysics*, **51**(1), 11 – 20.

Petry, H., 1987. *Transient elektromagnetische Tiefensondierungen- Modellrechnungen und Inversion*, Master's thesis, Universität zu Köln, Institut für Geophysik und Meteorologie.

Raiche, A. P., 1983. Short Note Comparison of apparent resistivity functions for transient electromagnetic methods, *Geophysics*, **4**(6), 787–789.

Raiche, A. P., 1984. The Effect of Ramp Function Turn-Off on the TEM Response of Layered Earth, *Geoexploration*, **15**(1), 37–41.

Ritter, O., Ryberg, T., Weckmann, U., Hoffmann-Rothe, A., Abueladas, A. & Garfunkel, Z., 2003. Geophysical images of the Dead Sea Transform in Jordan reveal an impermeable barrier for fluid flow, *Geophysical Research Letters*, **30**(14), 1741.

Rodi, W. & Mackie, R. L., 2001. Nonlinear conjugate gradients algorithm for 2D magnetotelluric inversion, *Geophysics*, **66**(1), 174–187.

Rätz, S., 2000. *Ein dreidimensionales Finite Elemente Programm zur Simulation elektromagetischer Oberflächen und Bohrlochverfahren*, Ph.D. thesis, Universität zu Köln, Institut für Geophysik und Meteorologie.

Rödder, A., 2010. *Interpretation von SHOTEM Daten mit mehrdimensionalen Leitfähigkeitsmodellen am Beispiel der Araba Verwerfung, Jordanien*, Master's thesis, Universität zu Köln, Institut für Geophysik und Meteorologie.

Rödder, A. & Tezkan, B., 2013. A 3D resistivity model derived from the transient electromagnetic data observed on the Araba fault, Jordan, *Journal of Applied Geophysics*, **88**(0), 42 – 51.

Saad, Y., 2000. *Iterative Methods for Sparse Linear Systems*, SIAM, 2nd edn.

Scholl, C., 2001. *Die Periodizität von Sendesignalen bei Long Offset Transient Electromagnetics*, Master's thesis, Universität zu Köln, Institut für Geophysik und Meteorologie.

Scholl, C., 2004. *SINV 3D-TEM-inversion program*, Universität zu Köln, Institut für Geophysik und Meteorologie.

Scholl, C., 2005. *The influence of multidimensional structures on the interpretation of LOTEM data with one-dimensional models and the application to data from Israel*, Ph.D. thesis, Universität zu Köln, Institut für Geophysik und Meteorologie.

Scholl, C., Martin, R., Commer, M., Helwig, S. L. & Tezkan, B., 2003. 2D-Inversion von LOTEM-Daten, in *Protokoll über das 20. Kolloquium für Elektromagnetische Tiefenforschung*, Dt. Geophys. Gesellschaft.

Scholl, C., Martin, R., Koch, O., Helwig, S., Tezkan, B. & the DESERT group, 2004. 2.5d inversion of transient electromagnetic data, in *Proceedings of the 17th international workshop on electromagnetic induction in the Earth, Hyderabad/India*.

Siripunvaraporn, W. & Egbert, G., 2000. An effecient data-subspace inversion method for 2-d magnetotelluric data, *Geophysics*, **65**(3), 791–803.

Smith, J. T. & Booker, J. R., 1991. Rapid inversion of two- and three-dimensional magnetotelluric data, *Journal of Geophysical Research*, **96**(B3), 3905–3922.

Spies, B. R., 1989. Depth of investigation in electromagnetic sounding methods, *Geophysics*, **54**, 872–888.

Spies, B. R. & Eggers, D. E., 1986. The use and misuse of apparent resistivity in electromagnetic methods, *Geophysics*, **51**(7), 1462–1471.

Spies, B. R. & Frischknecht, F. C., 1991. Electromagnetic Sounding, in *Electromagnetic methods in applied geophysics*, vol. 2, chap. 5, ed. Nabighian, M. N., Society of Exploration Geophysicists.

Stanley Price, N. P. & Garrard, A. N., 1975. A Survey of Prehistoric sites in the Azraq Basin, Eastern Jordan, *Paléorient*, **3**(1), 109–126.

Steuer, A., 2008. *Joint application of ground-based transient electromagnetics and airborne electromagnetics*, Ph.D. thesis, University of Cologne, Germany.

Steuer, A., Siemon, B. & Auken, E., 2009. A comparison of helicopter-borne electromagnetics in frequency- and time-domain at the Cuxhaven valley in Northern Germany, *Journal of Applied Geophysics*, **67**(3), 194–205.

Strack, K. M., 1992. *Exploration with deep transient electromagnetics*, Methods in Geochemistry and Geophysics, Bd. 30, Elsevier, Amsterdam.

Sudha, K., Tezkan, B., Israil, M. & Rai, J., 2011. Combined electrical and electromagnetic imaging of hot fluids within fractured rock in rugged Himalayan terrain, *Journal of Applied Geophysics*, **74**(4), 205 – 214.

Telford, W. M., Geldart, L. P. & Sheriff, R. E., 1990. *Applied Geophysics*, Cambridge Univ. Press, 2nd edn.

Tezkan, B., 1999. A review of environmental applications of quasi-stationary electromagnetic techniques, *Surveys in Geophysics*, **20**, 279–308.

Tikhonov, A. N. & Arsenin, V. A., 1977. *Solution of Ill-posed Problems*, Winston & Sons, Washington.

Viezzoli, A., Christensen, A., Auken, E. & Sørensen, K., 2008. Quasi-3D modeling of airborne TEM data by spatially constrained inversion, *Geophysics*, **73**, 105–113.

Ward, S. H., 1990a. Resistivity and induced polarization methods, *Geotechnical and environmental geophysics*, **1**, 147–189.

Ward, S. H., 1990b. *Geotechnical and Environmental Geophysics: Environmental and Groundwater*, vol. I, Society of Exploration Geophysicists, Tulsa.

Ward, S. H. & Hohmann, G. W., 1991. Electromagnetic Theory for Geophysical Exploration, in *Electromagnetic methods in applied geophysics*, vol. 1, chap. 4, pp. 131–311, ed. Nabighian, M. N., Society of Exploration Geophysicists.

Weidelt, P., 1986. *Einführung in die elektromagnetische Tiefenforschung*, Lecture Technische Universät Braunschweig.

Weidelt, P., 2000. Numerical modelling of transient-electromagentic fields in three-dimensional conductors: A comparative study, in *Elektromagnetische Tiefenforschung, 18. Kolloquium*, pp. 216–231, Dt. Geophys. Gesellschaft.

Yee, K. S., 1966. Numerical solutions of initial boundary problems involving Maxwell's equations in isotropis media, *IEEE Trans. Antennas Propag.*, **14**, 302–309.

Yogeshwar, P., Tezkan, B., Israil, M. & Candansayar, M., 2012. Groundwater contamination in the Roorkee area, India: 2D joint inversion of radiomagnetotelluric and direct current resistivity data, *Journal of Applied Geophysics*, **76**, 127–135.

Yogeshwar, P., Tezkan, B. & Haroon, A., 2013. Investigation of the Azraq sedimentary basin, Jordan using integrated geoelectrical and electromagnetic techniques, *Near Surface Geophysics*, **11**, 283–291.

Zhdanov, M. S., 2009. New advances in regularized inversion of gravity and electromagnetic data, *Geophysical Prospecting*, **57**(4), 463–478.

Zhdanov, M. S. & Varentsov, I., 1997. Methods for modelling electromagnetic fields Results from COMMEMI—the international project on the comparison of modelling methods for electromagnetic induction, *Journal of Applied Geophysics*, **37**, 133–271.

Zonge, 2002. *GDP-32 II Multifunction Receiver Operation Manual*, Zonge Engineering and Research Organization.

Appendix

In the following a compilation of additional figures and tables is given. Each of them are referenced and in general further explained in the corresponding section.

A.1 TEM sounding and ERT profile locations

Table A.1: *TEM sounding locations along profile B. The sounding name, the profile meter (pr.-m.) and GPS-coordinates (lat./lon.) are given. The Tx-100 soundings are marked with an asterisk, e.g. TEM B18*. All soundings are displayed in Fig. 4.2(a).*

sounding	pr.-m.	lat.	lon.	sounding	pr.-m.	lat.	lon.
B1	0	31.867914°	36.835478°	B25*	1710	31.859859°	36.850896°
B2	50	31.867607°	36.835883°	B26	1810	31.858441°	36.853651°
B3	100	31.867338°	36.836287°	B27*	1910	31.858954°	36.852723°
B4	150	31.867022°	36.836646°	B28	2010	31.857510°	36.855442°
B5	200	31.867142°	36.837434°	B29*	2110	31.858048°	36.854551°
B6	250	31.866833°	36.837866°	B30	2210	31.856608°	36.857266°
B7	300	31.866518°	36.838258°	B31*	2310	31.857143°	36.856378°
B8	350	31.866209°	36.838632°	B32	2410	31.855710°	36.859049°
B9	400	31.864433°	36.837501°	B33*	2510	31.856237°	36.858206°
B10	450	31.863958°	36.837773°	B34	2610	31.854788°	36.860847°
B11	500	31.863580°	36.838095°	B35*	2710	31.855332°	36.860033°
B12	550	31.863262°	36.838438°	B36	2810	31.860312°	36.849982°
B13	740	31.864344°	36.842039°	B37*	2910	31.854426°	36.861860°
B14	790	31.864087°	36.842545°	B38*	3110	31.853521°	36.863688°
B15	835	31.863815°	36.842898°	B39*	3310	31.852615°	36.865515°
B16	885	31.863589°	36.843355°	B40*	3510	31.851709°	36.867342°
B17	935	31.863401°	36.843852°	B41*	3710	31.850804°	36.869169°
B18*	1030	31.862948°	36.844766°	B42*	3910	31.849898°	36.870996°
B19	1130	31.862489°	36.845692°	B43*	4110	31.848992°	36.872823°
B20*	1230	31.862043°	36.846593°	B44*	4310	31.848087°	36.874651°
B21	1340	31.861564°	36.847520°	B45*	4510	31.847181°	36.876478°
B22*	1435	31.861138°	36.848421°	B46*	4710	31.846275°	36.878305°
B23	1535	31.860642°	36.849295°	B47*	4910	31.845294°	36.880060°
B24	1610	31.859389°	36.851816°	—	—	—	—

Table A.2: *TEM sounding locations along profile A. The sounding name, the profile meter (pr.-m.) and GPS-coordinates (lat./lon.) are given. The Tx-100 soundings are marked with an asterisk, e.g. TEM A72*. If both Tx-50 and Tx-100 were recorded, the name is labeled e.g. TEM A47**. All soundings are displayed in Fig. 4.2(a).*

sounding	pr.-m.	lat.	lon.	sounding	pr.-m.	lat.	lon.
A01	10	31.890251°	36.900076°	A37	2880	31.869922°	36.881178°
A02	60	31.889952°	36.899741°	A38	2930	31.869586°	36.880955°
A03	110	31.889598°	36.899417°	A39	2980	31.869211°	36.880579°
A04	160	31.889249°	36.899082°	A40	3030	31.868867°	36.880249°
A05	210	31.888905°	36.898721°	A41	3090	31.868199°	36.880355°
A06	260	31.888539°	36.898405°	A42	3140	31.867616°	36.880427°
A07	310	31.888209°	36.898062°	A43	3190	31.867322°	36.879984°
A08	360	31.887876°	36.897715°	A44	3220	31.867377°	36.879275°
A09	650	31.885949°	36.895673°	A45	3270	31.867151°	36.878783°
A1	785	31.884911°	36.894832°	A46	3320	31.866830°	36.878354°
A2	835	31.884595°	36.894458°	A47**	3370	31.866479°	36.878018°
A3	885	31.884267°	36.894079°	A48	3420	31.866128°	36.877676°
A4	935	31.884248°	36.893309°	A49**	3470	31.865805°	36.877384°
A5	985	31.883288°	36.893027°	A50	3520	31.865428°	36.877072°
A6	1035	31.882964°	36.892764°	A51**	3570	31.865083°	36.876751°
A7	1340	31.881223°	36.890846°	A52	3620	31.864678°	36.876434°
A8	1390	31.880872°	36.890430°	A53**	3670	31.864294°	36.876174°
A9	1440	31.880570°	36.890135°	A54	3720	31.863894°	36.875919°
A10	1490	31.880253°	36.889733°	A55**	3770	31.863538°	36.875695°
A11	1540	31.879882°	36.889355°	A56	3820	31.863096°	36.875362°
A12**	1590	31.879584°	36.889016°	A57**	3870	31.862727°	36.875095°
A13	1640	31.879279°	36.888637°	A58	3920	31.862313°	36.874817°
A14	1690	31.878948°	36.888246°	A59**	3970	31.861911°	36.874523°
A15	1740	31.878614°	36.887884°	A60*	4070	31.861315°	36.873746°
A16	1790	31.878248°	36.887574°	A61**	4170	31.860563°	36.873137°
A17	1840	31.877477°	36.887900°	A62*	4270	31.859886°	36.872456°
A18	1890	31.877119°	36.887558°	A63**	4370	31.857729°	36.870540°
A19	1940	31.876744°	36.887315°	A64*	4470	31.858457°	36.871167°
A20	1990	31.876389°	36.887028°	A65**	4570	31.856217°	36.869363°
A21	2040	31.876059°	36.886700°	A66*	4670	31.857028°	36.869877°
A22	2090	31.875735°	36.886383°	A67**	4770	31.859196°	36.871793°
A23	2140	31.875368°	36.886004°	A68*	4870	31.855600°	36.868588°
A24	2190	31.875043°	36.885635°	A69**	4970	31.854871°	36.867975°
A25**	2240	31.874714°	36.885243°	A70*	5070	31.854143°	36.867343°
A26	2290	31.874368°	36.884869°	A71	5170	31.853924°	36.866421°
A27	2370	31.873618°	36.884601°	A72*	5270	31.852686°	36.866097°
A28	2420	31.873231°	36.884317°	A73*	5470	31.851229°	36.864852°
A29	2470	31.872834°	36.884005°	A74*	5670	31.849772°	36.863607°
A30	2520	31.872470°	36.883701°	A75*	5870	31.848315°	36.862361°
A31	2570	31.872093°	36.883381°	A76*	6070	31.846858°	36.861116°
A32	2620	31.871712°	36.883065°	A77*	6270	31.845401°	36.859871°
A33	2670	31.871358°	36.882711°	A78*	6470	31.843944°	36.858626°
A34	2730	31.870971°	36.882359°	A79*	6670	31.842487°	36.857381°
A35	2780	31.870610°	36.881974°	A80*	6870	31.841030°	36.856136°
A36	2830	31.870244°	36.881597°	—	—	—	—

Table A.3: *ERT profiles obtained along profile A. W-LS denotes Wenner-long/short configuration with an outer and inner electrode spacing ΔEL, e.g. 5/2.5. Third column is the total profile length. Roll-on denotes the number of Roll-on used for the ERT profile. The profile meter corresponds to profile A, where 0 m is the beginning. The coordinates are displayed for beginning and end-point of the profile. For further details on ERT configurations refer to ABEM [2010]. The ERT locations are displayed in Fig. 4.2(b)*

Profile	Configuration	ΔEL / m	length / m	#Roll-on
ERT-a1	W-LS	5/2.5	400	4
ERT-a2	W-LS	5/2.5	200	—
ERT-a3	W	2.5	150	1
ERT-a4	W-LS	10/5	600	2
ERT-a5	W-LS	10/5	1600	12

Profile	profile-meter	lat. (beg.)	lon. (beg.)	lat. (end)	lon. (end)
ERT-a1	0 – 400 m	31.890436°	36.900038°	31.887364°	36.897624°
ERT-a2	750 – 950 m	31.885109°	36.895097°	31.883835°	36.893537°
ERT-a3	990 – 1140 m	31.883609°	36.893318°	31.882534°	36.892301°
ERT-a4	1230 – 1830 m	31.881946°	36.891548°	31.877985°	36.887239°
ERT-a5	1720 – 3320 m	31.878091°	36.888497°	31.865965°	36.877574°

A.2 Survey are photographs

Pr. A: view from basalt hill towards mudflat

Pr. B: basalt close to TEM B1

Pr. A, TEM sounding on AQ-formation

Almost got stuck on the mudflat

Salt cover on mudflat

Pr. A, RMT sounding on AQ-formation

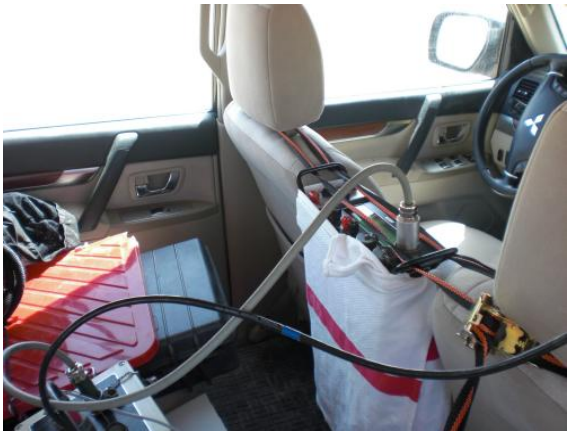

Fancy ERT installation with AC cooling

Perfect working conditions in NRA-camp

Dust vortex and TEM sounding on mudflat

TEM-3 induction coil

TEM equipment mounted on cart

Azraq wetland preserve

A.3 Additional lithological information

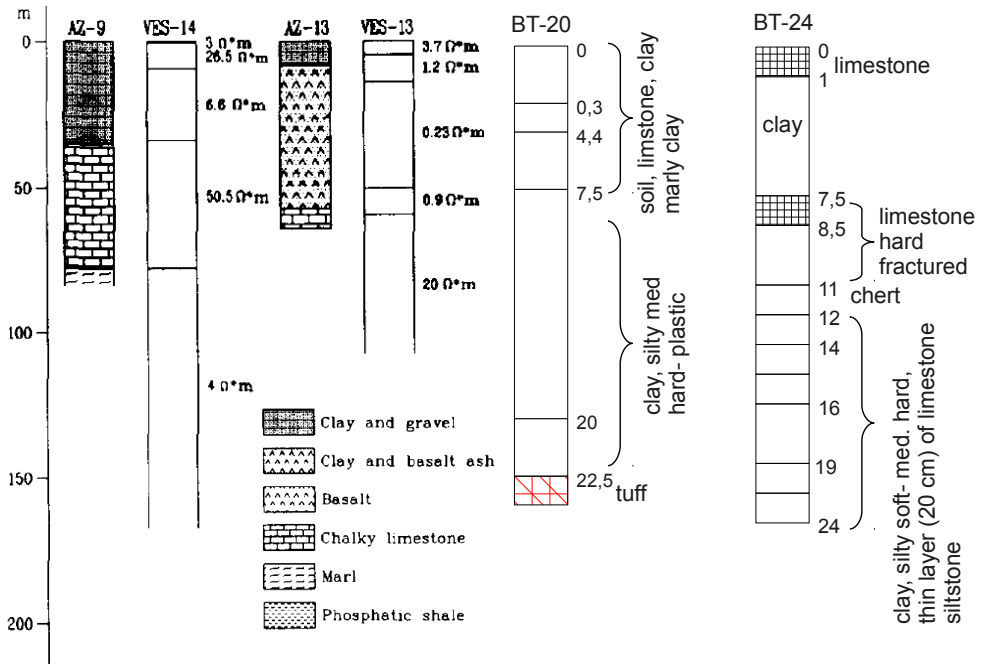

Figure A.1: *(a,b) lithological data for boreholes AZ-9 and AZ-13 compared with VES data given by [El-Waheidi et al., 1992]. Borehole lithological data for BT-20 and BT-24 after Ala'li [1993]. All locations are shown in Fig. 4.2(a), chapter 4.2.*

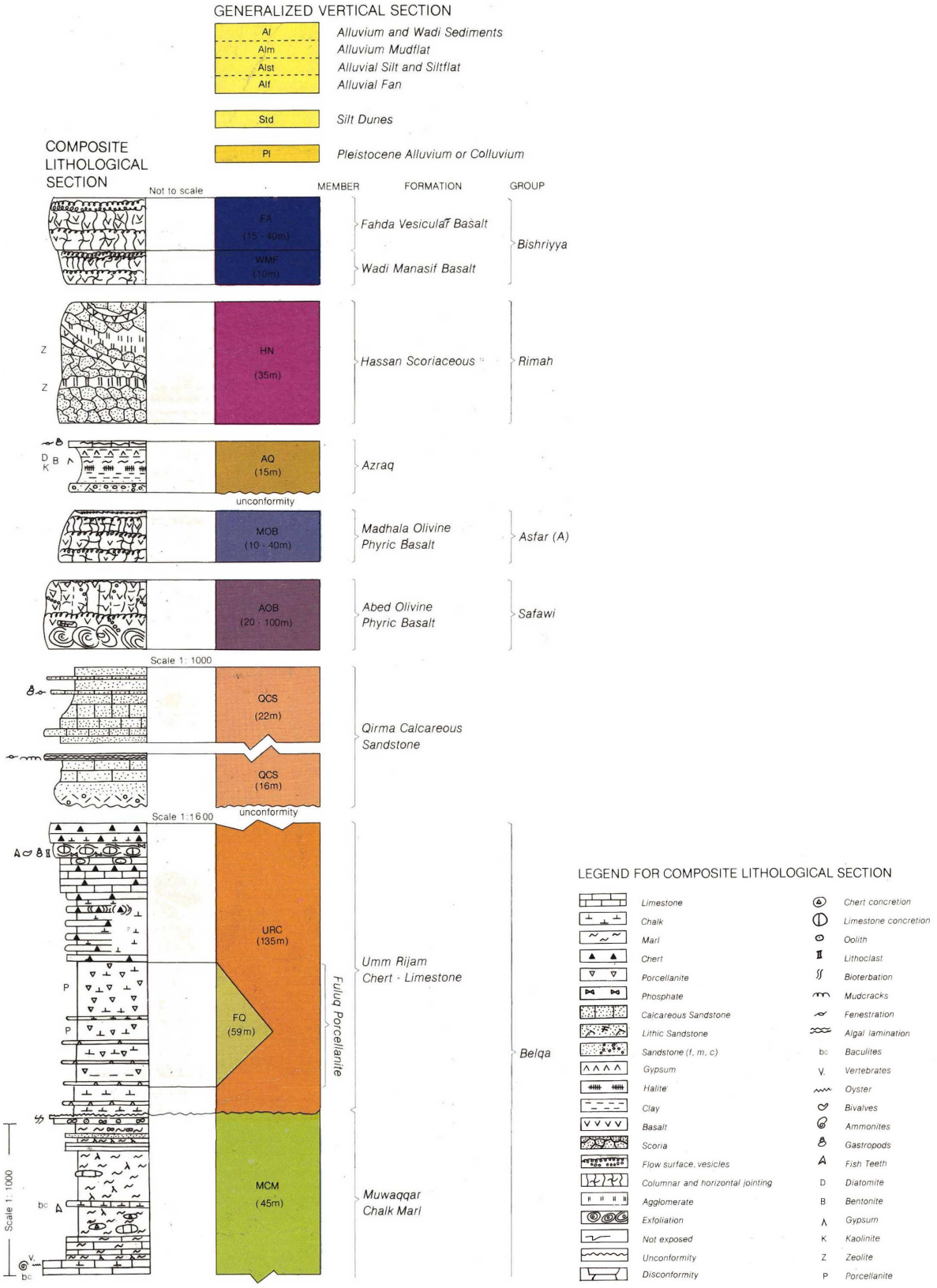

Figure A.2: *Generalized composite lithological section after Ibrahim [1996] is shown. It corresponds to the geological map and the cross-section in Fig. 4.2(a,b). Both are discussed in chapter 4.2.*

A.4 Distribution of Tx-100 sounding data and stacking error

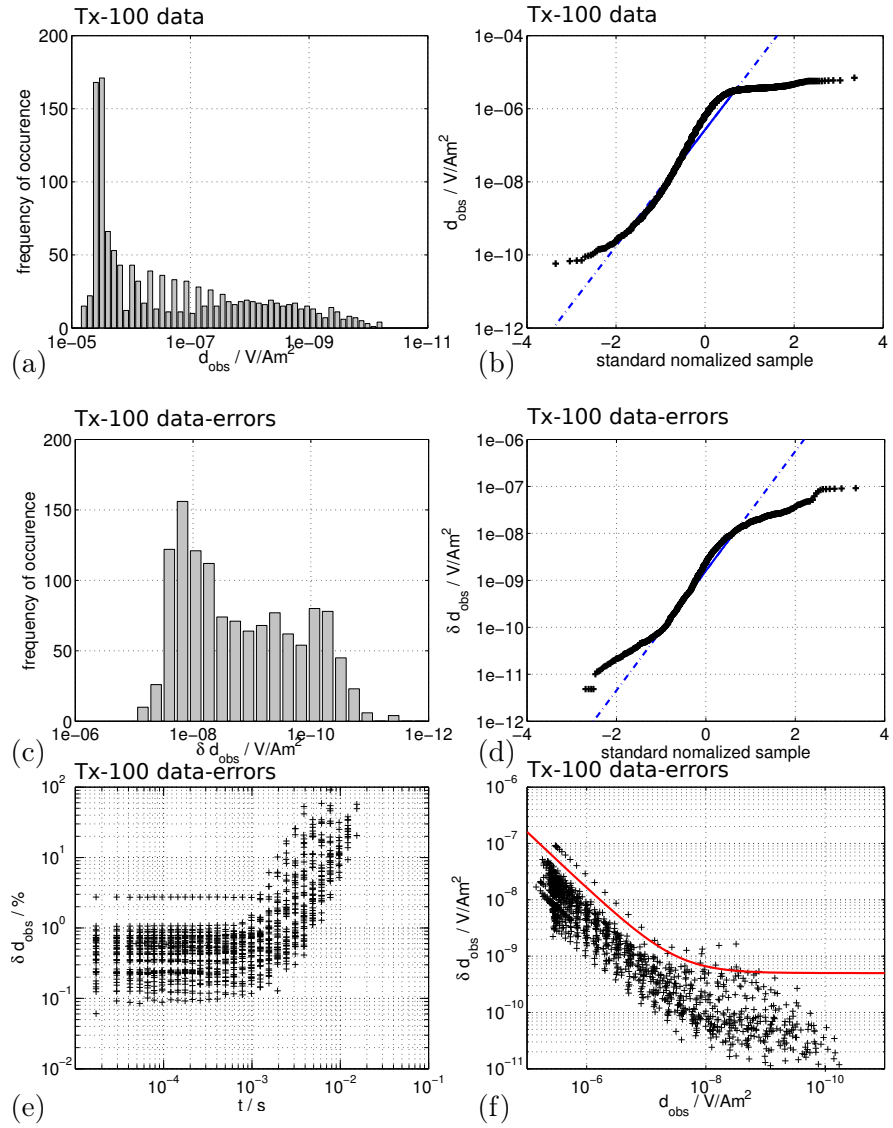

Figure A.3: *Distribution of all Tx-100 sounding data and stacking errors. (a) Histogram of all data points and corresponding (b) QQ-plot. (c) Histogram of all stacking errors and (d) corresponding QQ-plot. (e) Percentage stacking errors plotted vs. the time. (f) Absolute stacking error plotted vs. the observed data. These plots are discussed in the corresponding section 4.5.3 for the Tx-50 setup.*

A.5 Profile A: TEM field data

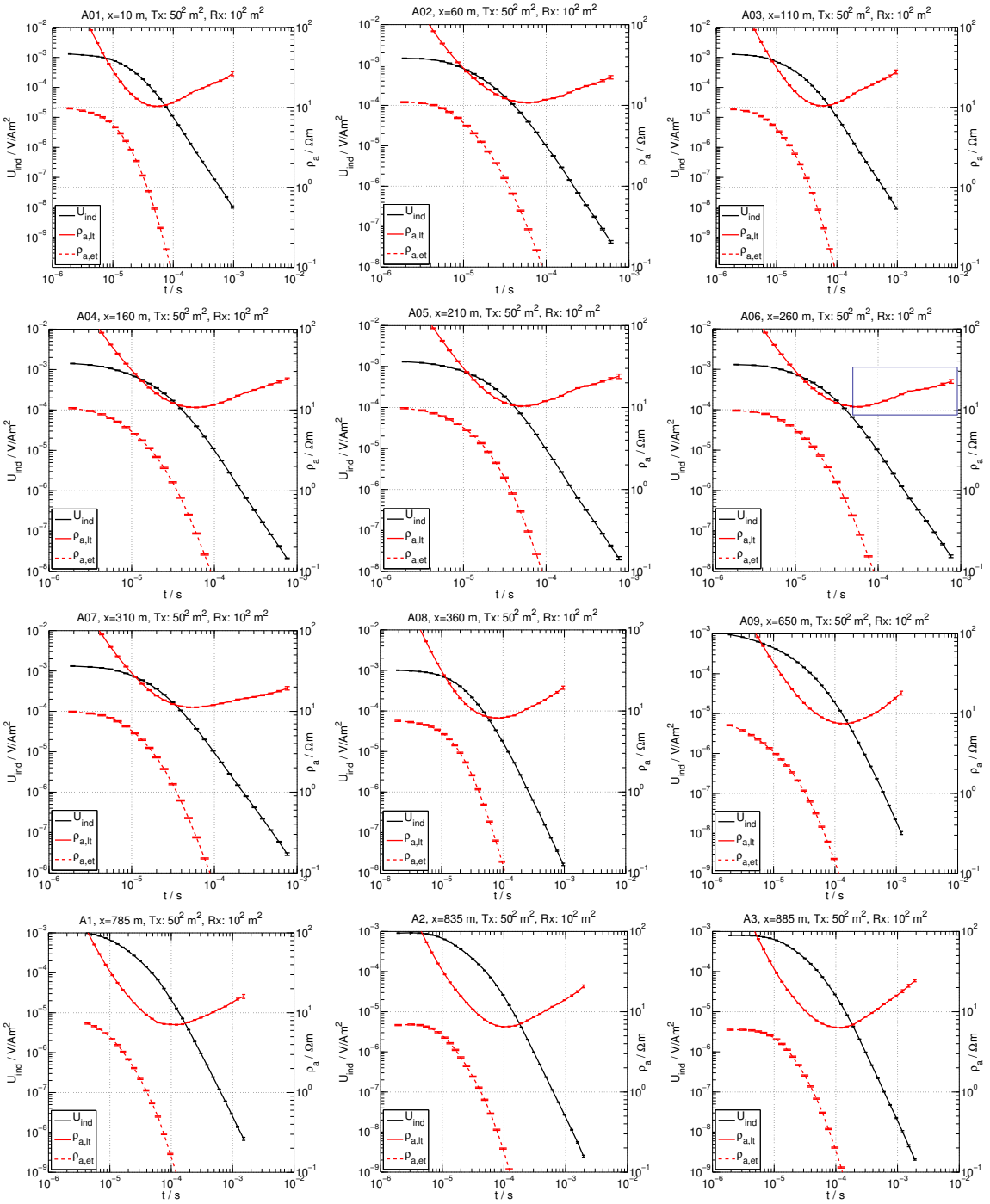

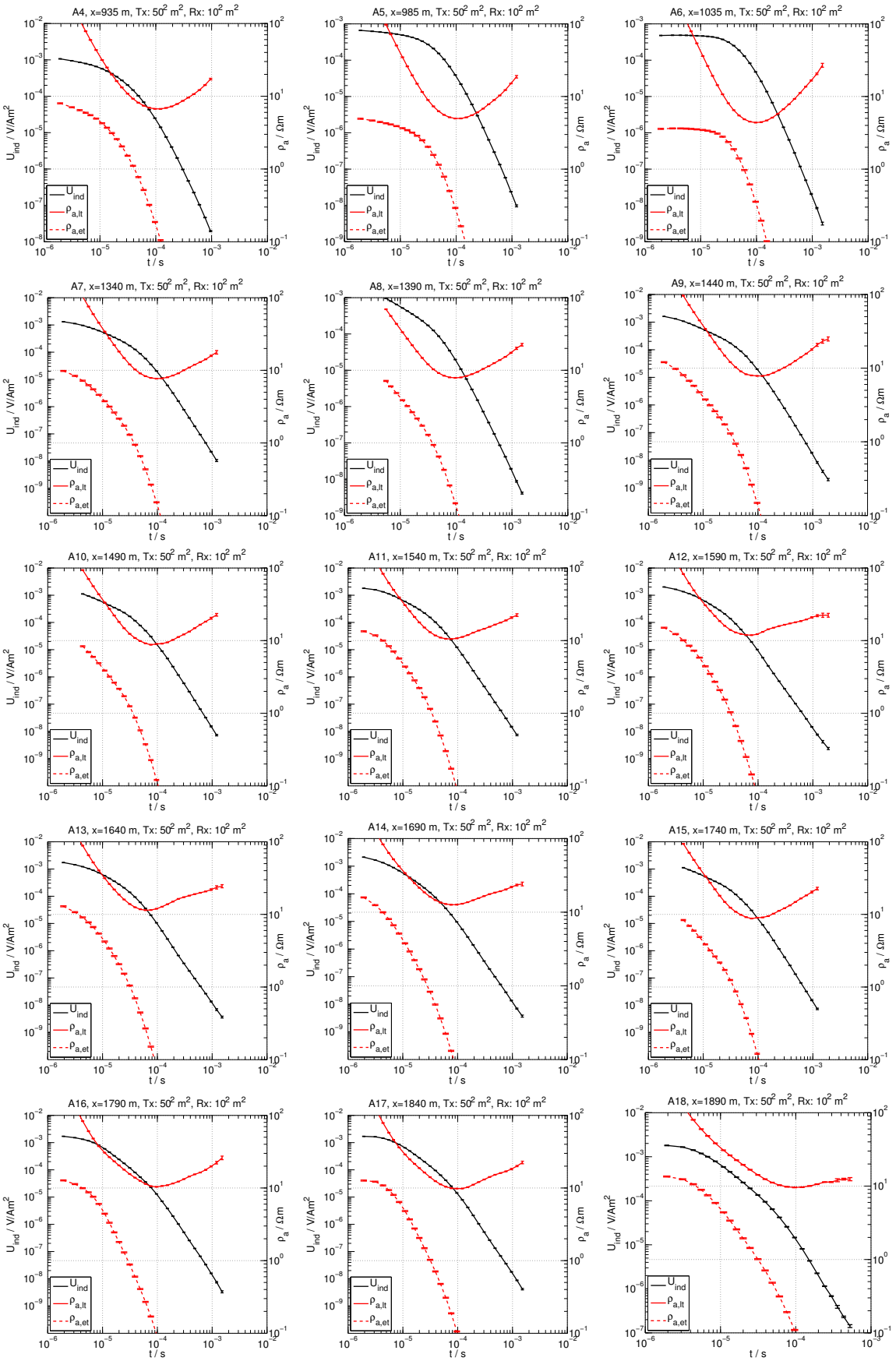
A4, x=935 m, Tx: 50² m², Rx: 10² m²
A5, x=985 m, Tx: 50² m², Rx: 10² m²
A6, x=1035 m, Tx: 50² m², Rx: 10² m²
A7, x=1340 m, Tx: 50² m², Rx: 10² m²
A8, x=1390 m, Tx: 50² m², Rx: 10² m²
A9, x=1440 m, Tx: 50² m², Rx: 10² m²
A10, x=1490 m, Tx: 50² m², Rx: 10² m²
A11, x=1540 m, Tx: 50² m², Rx: 10² m²
A12, x=1590 m, Tx: 50² m², Rx: 10² m²
A13, x=1640 m, Tx: 50² m², Rx: 10² m²
A14, x=1690 m, Tx: 50² m², Rx: 10² m²
A15, x=1740 m, Tx: 50² m², Rx: 10² m²
A16, x=1790 m, Tx: 50² m², Rx: 10² m²
A17, x=1840 m, Tx: 50² m², Rx: 10² m²
A18, x=1890 m, Tx: 50² m², Rx: 10² m²
U_ind / V/Am²
ρ_a / Ωm
t / s
U_ind
ρ_a,lt
ρ_a,et

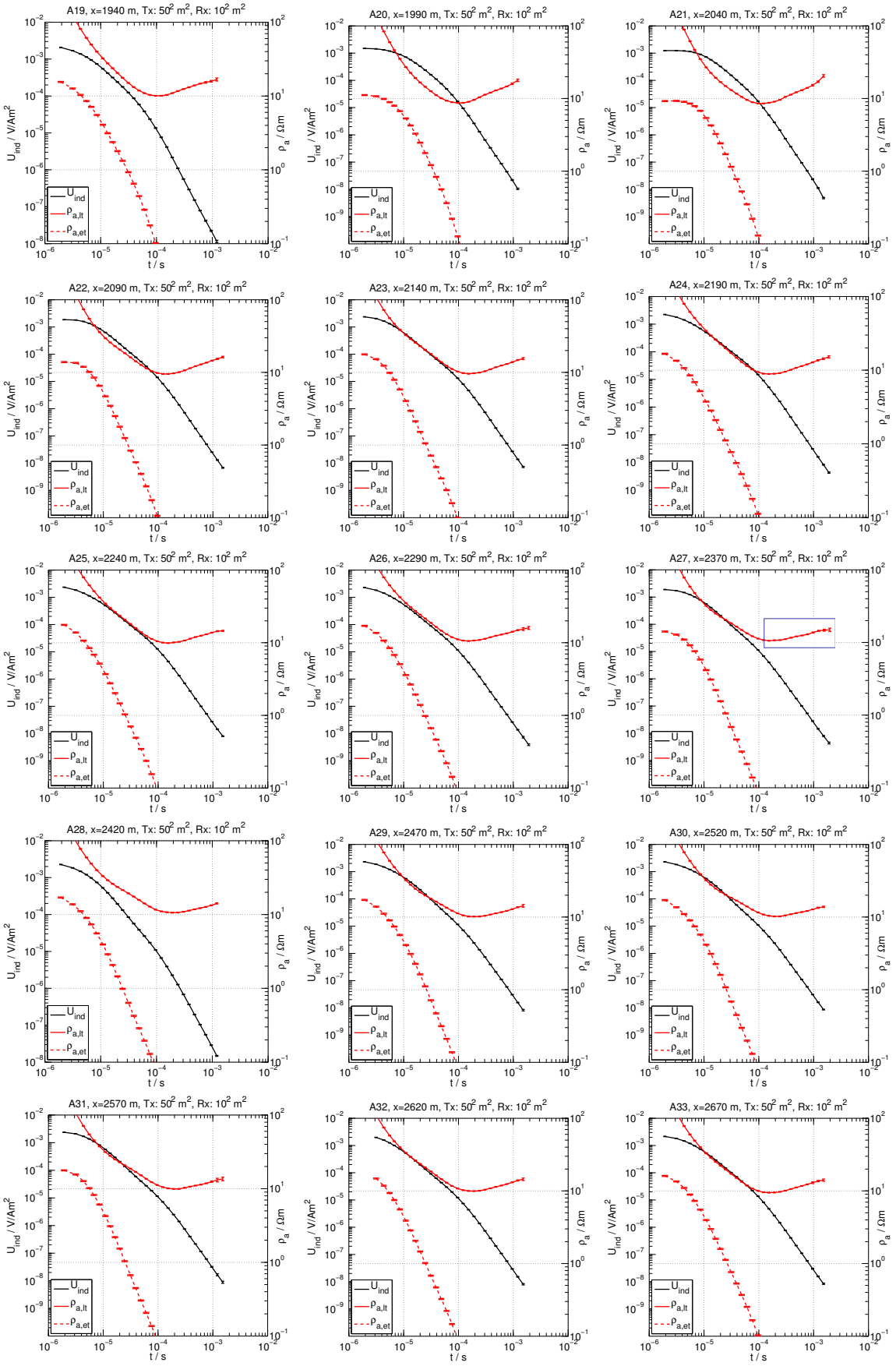
A19, x=1940 m, Tx: 50² m², Rx: 10² m²
A20, x=1990 m, Tx: 50² m², Rx: 10² m²
A21, x=2040 m, Tx: 50² m², Rx: 10² m²
A22, x=2090 m, Tx: 50² m², Rx: 10² m²
A23, x=2140 m, Tx: 50² m², Rx: 10² m²
A24, x=2190 m, Tx: 50² m², Rx: 10² m²
A25, x=2240 m, Tx: 50² m², Rx: 10² m²
A26, x=2290 m, Tx: 50² m², Rx: 10² m²
A27, x=2370 m, Tx: 50² m², Rx: 10² m²
A28, x=2420 m, Tx: 50² m², Rx: 10² m²
A29, x=2470 m, Tx: 50² m², Rx: 10² m²
A30, x=2520 m, Tx: 50² m², Rx: 10² m²
A31, x=2570 m, Tx: 50² m², Rx: 10² m²
A32, x=2620 m, Tx: 50² m², Rx: 10² m²
A33, x=2670 m, Tx: 50² m², Rx: 10² m²
U_ind / V/Am²
ρ_a / Ωm
t / s
U_ind
ρ_a,lt
ρ_a,et

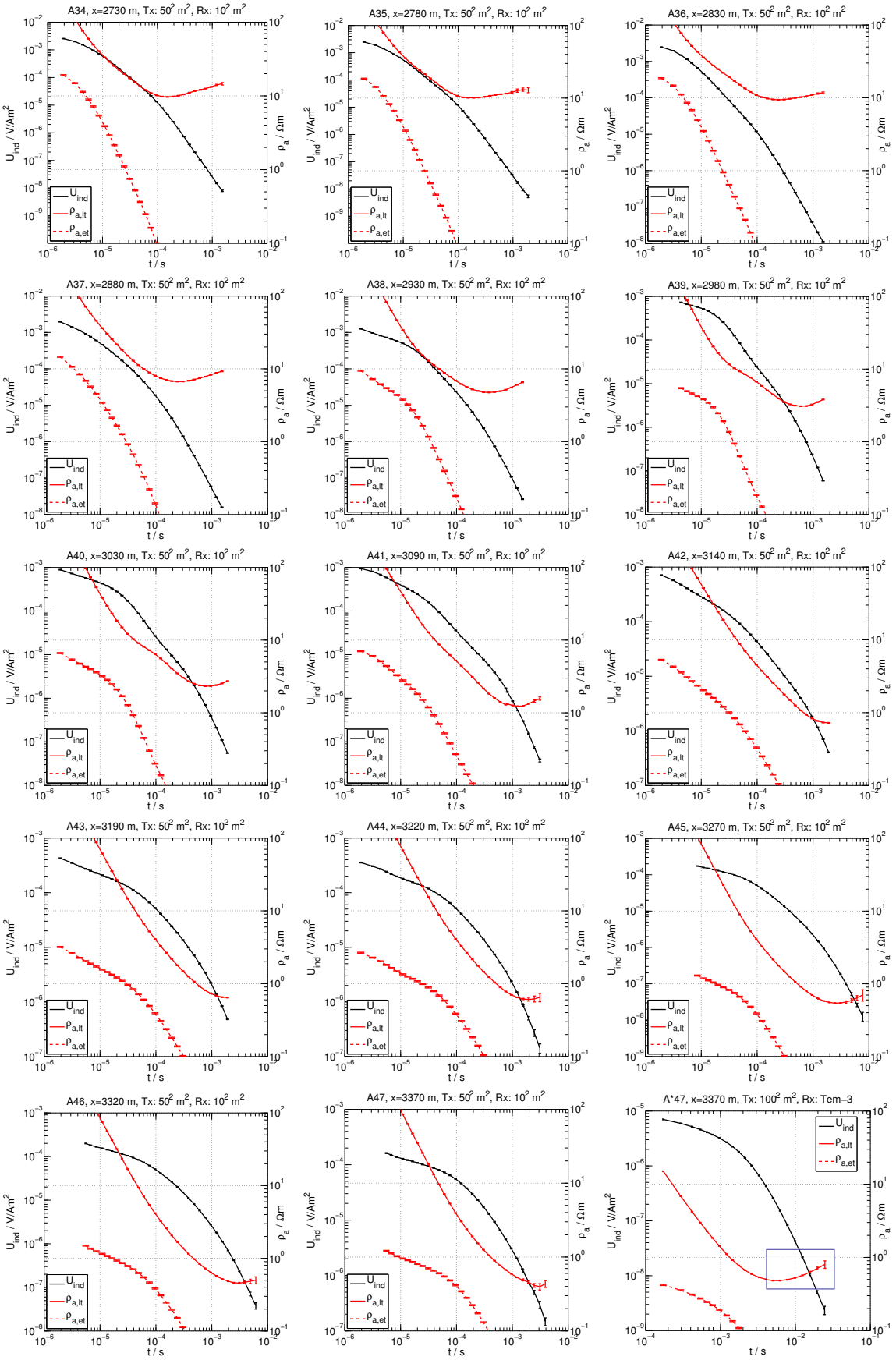
A34, x=2730 m, Tx: 50² m², Rx: 10² m²
A35, x=2780 m, Tx: 50² m², Rx: 10² m²
A36, x=2830 m, Tx: 50² m², Rx: 10² m²
A37, x=2880 m, Tx: 50² m², Rx: 10² m²
A38, x=2930 m, Tx: 50² m², Rx: 10² m²
A39, x=2980 m, Tx: 50² m², Rx: 10² m²
A40, x=3030 m, Tx: 50² m², Rx: 10² m²
A41, x=3090 m, Tx: 50² m², Rx: 10² m²
A42, x=3140 m, Tx: 50² m², Rx: 10² m²
A43, x=3190 m, Tx: 50² m², Rx: 10² m²
A44, x=3220 m, Tx: 50² m², Rx: 10² m²
A45, x=3270 m, Tx: 50² m², Rx: 10² m²
A46, x=3320 m, Tx: 50² m², Rx: 10² m²
A47, x=3370 m, Tx: 50² m², Rx: 10² m²
A*47, x=3370 m, Tx: 100² m², Rx: Tem−3
U_ind / V/Am²
ρ_a / Ωm
t / s
U_ind
ρ_a,lt
ρ_a,et

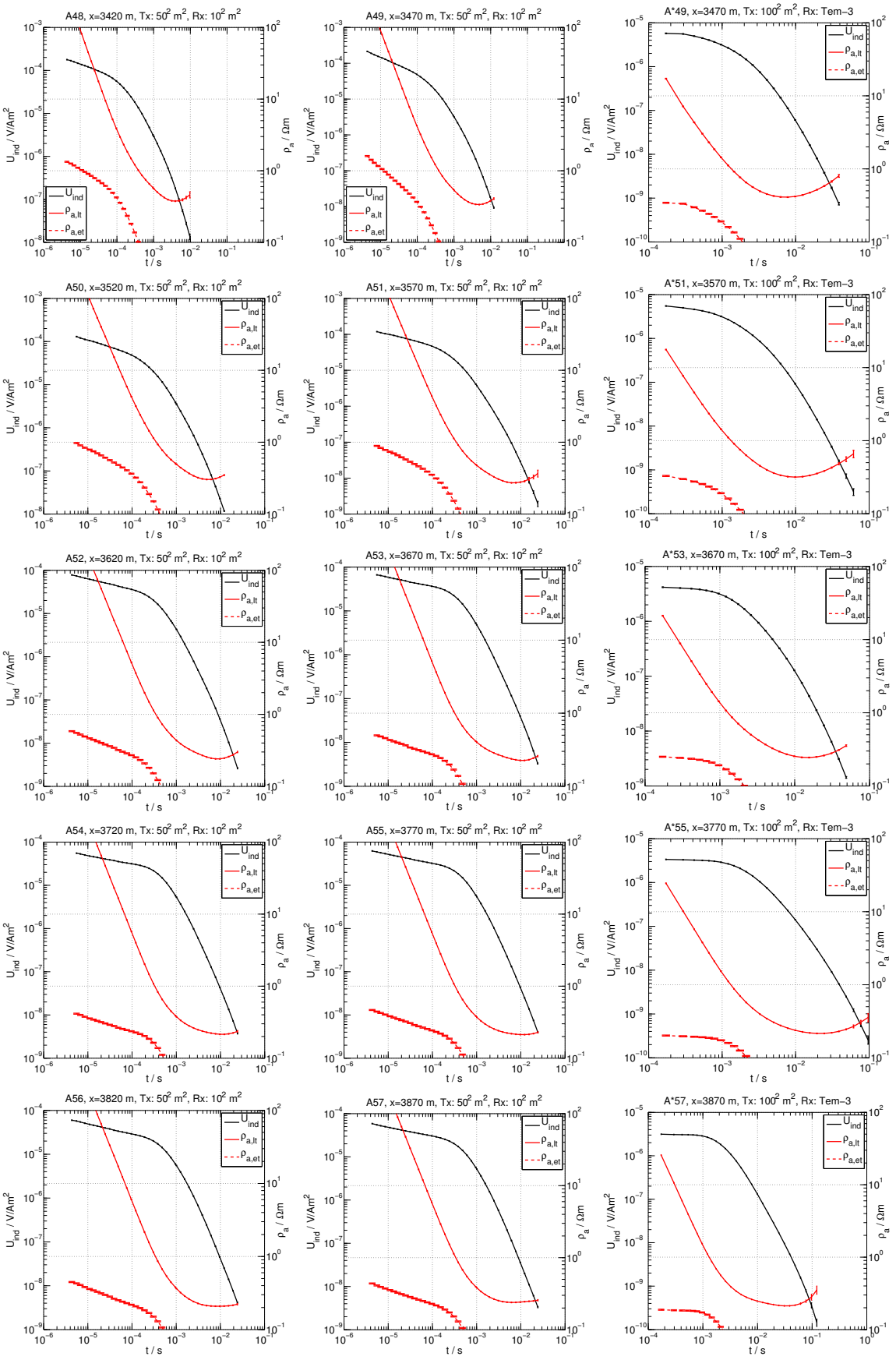
A48, x=3420 m, Tx: 50² m², Rx: 10² m²
A49, x=3470 m, Tx: 50² m², Rx: 10² m²
A*49, x=3470 m, Tx: 100² m², Rx: Tem−3
A50, x=3520 m, Tx: 50² m², Rx: 10² m²
A51, x=3570 m, Tx: 50² m², Rx: 10² m²
A*51, x=3570 m, Tx: 100² m², Rx: Tem−3
A52, x=3620 m, Tx: 50² m², Rx: 10² m²
A53, x=3670 m, Tx: 50² m², Rx: 10² m²
A*53, x=3670 m, Tx: 100² m², Rx: Tem−3
A54, x=3720 m, Tx: 50² m², Rx: 10² m²
A55, x=3770 m, Tx: 50² m², Rx: 10² m²
A*55, x=3770 m, Tx: 100² m², Rx: Tem−3
A56, x=3820 m, Tx: 50² m², Rx: 10² m²
A57, x=3870 m, Tx: 50² m², Rx: 10² m²
A*57, x=3870 m, Tx: 100² m², Rx: Tem−3
U_ind / V/Am²
ρ_a / Ωm
t / s
U_ind
ρ_a,lt
ρ_a,et

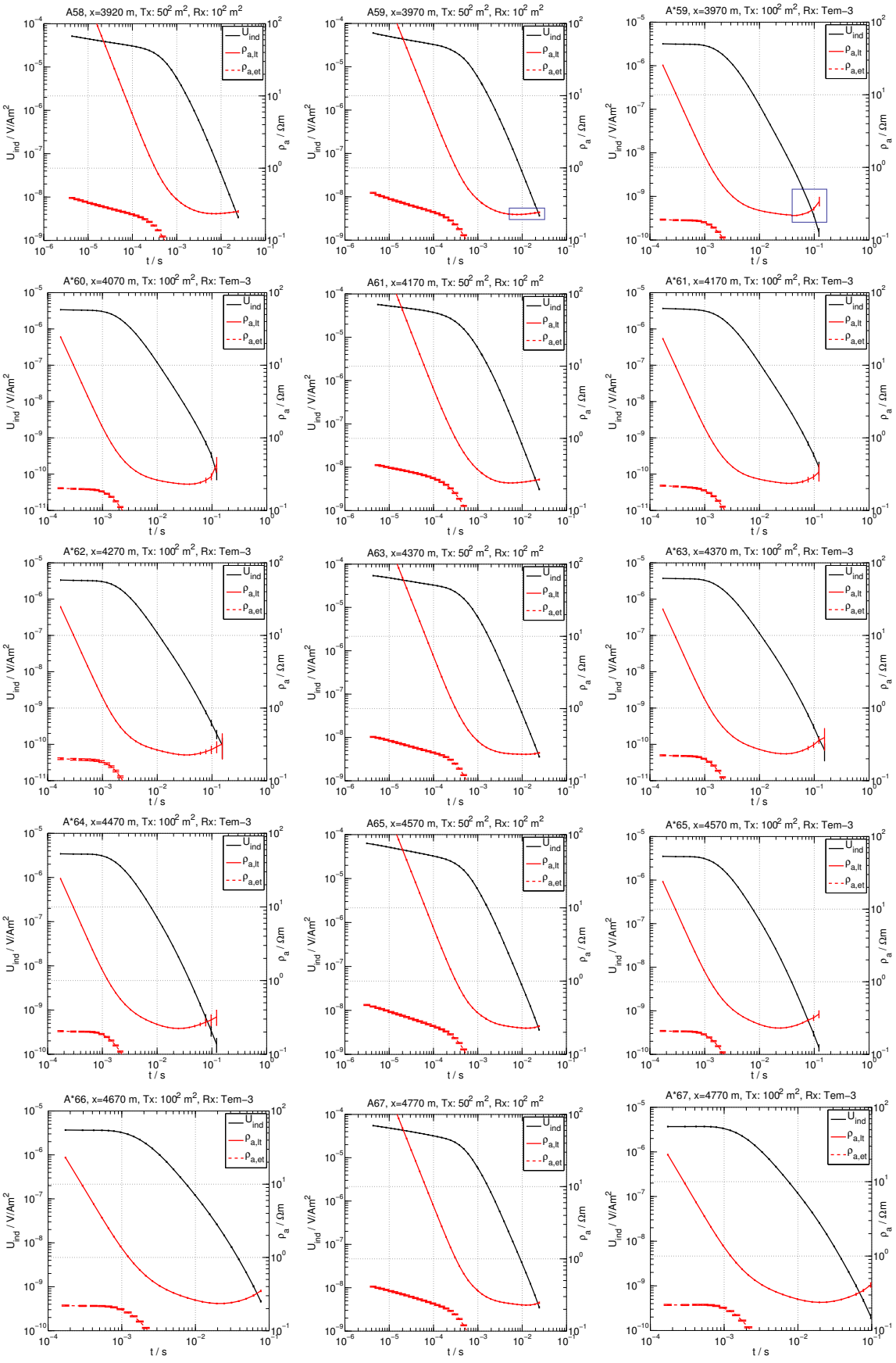
A58, x=3920 m, Tx: 50² m², Rx: 10² m²
A59, x=3970 m, Tx: 50² m², Rx: 10² m²
A*59, x=3970 m, Tx: 100² m², Rx: Tem−3
A*60, x=4070 m, Tx: 100² m², Rx: Tem−3
A61, x=4170 m, Tx: 50² m², Rx: 10² m²
A*61, x=4170 m, Tx: 100² m², Rx: Tem−3
A*62, x=4270 m, Tx: 100² m², Rx: Tem−3
A63, x=4370 m, Tx: 50² m², Rx: 10² m²
A*63, x=4370 m, Tx: 100² m², Rx: Tem−3
A*64, x=4470 m, Tx: 100² m², Rx: Tem−3
A65, x=4570 m, Tx: 50² m², Rx: 10² m²
A*65, x=4570 m, Tx: 100² m², Rx: Tem−3
A*66, x=4670 m, Tx: 100² m², Rx: Tem−3
A67, x=4770 m, Tx: 50² m², Rx: 10² m²
A*67, x=4770 m, Tx: 100² m², Rx: Tem−3
U_ind
ρ_a,lt
ρ_a,et
U_ind / V/Am²
ρ_a / Ωm
t / s

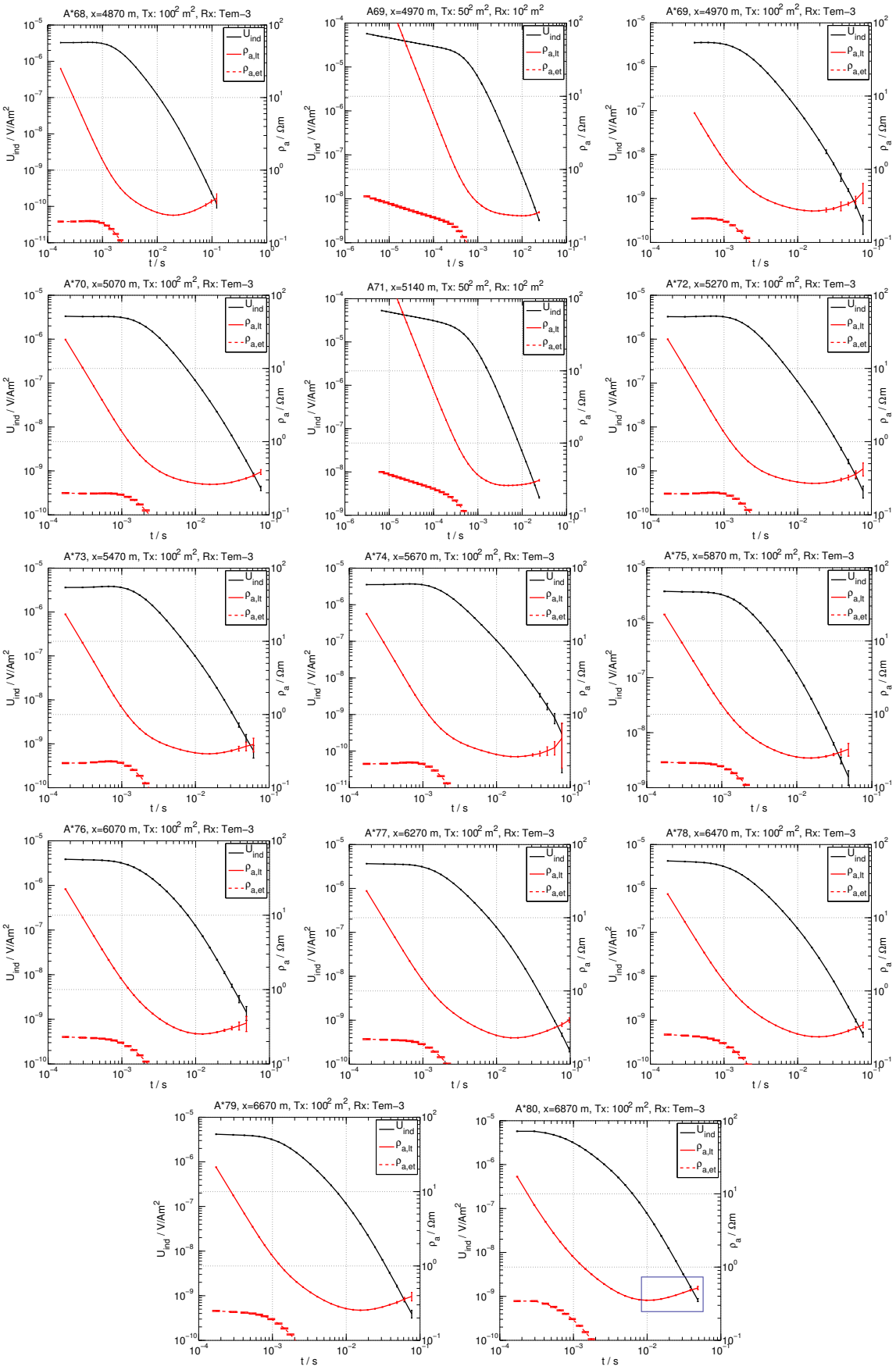
A*68, x=4870 m, Tx: 100² m², Rx: Tem–3
A69, x=4970 m, Tx: 50² m², Rx: 10² m²
A*69, x=4970 m, Tx: 100² m², Rx: Tem–3
A*70, x=5070 m, Tx: 100² m², Rx: Tem–3
A71, x=5140 m, Tx: 50² m², Rx: 10² m²
A*72, x=5270 m, Tx: 100² m², Rx: Tem–3
A*73, x=5470 m, Tx: 100² m², Rx: Tem–3
A*74, x=5670 m, Tx: 100² m², Rx: Tem–3
A*75, x=5870 m, Tx: 100² m², Rx: Tem–3
A*76, x=6070 m, Tx: 100² m², Rx: Tem–3
A*77, x=6270 m, Tx: 100² m², Rx: Tem–3
A*78, x=6470 m, Tx: 100² m², Rx: Tem–3
A*79, x=6670 m, Tx: 100² m², Rx: Tem–3
A*80, x=6870 m, Tx: 100² m², Rx: Tem–3
U_ind
ρ_a,lt
ρ_a,et
U_ind / V/Am²
ρ_a / Ωm
t / s

A.6 Profile B: TEM field data

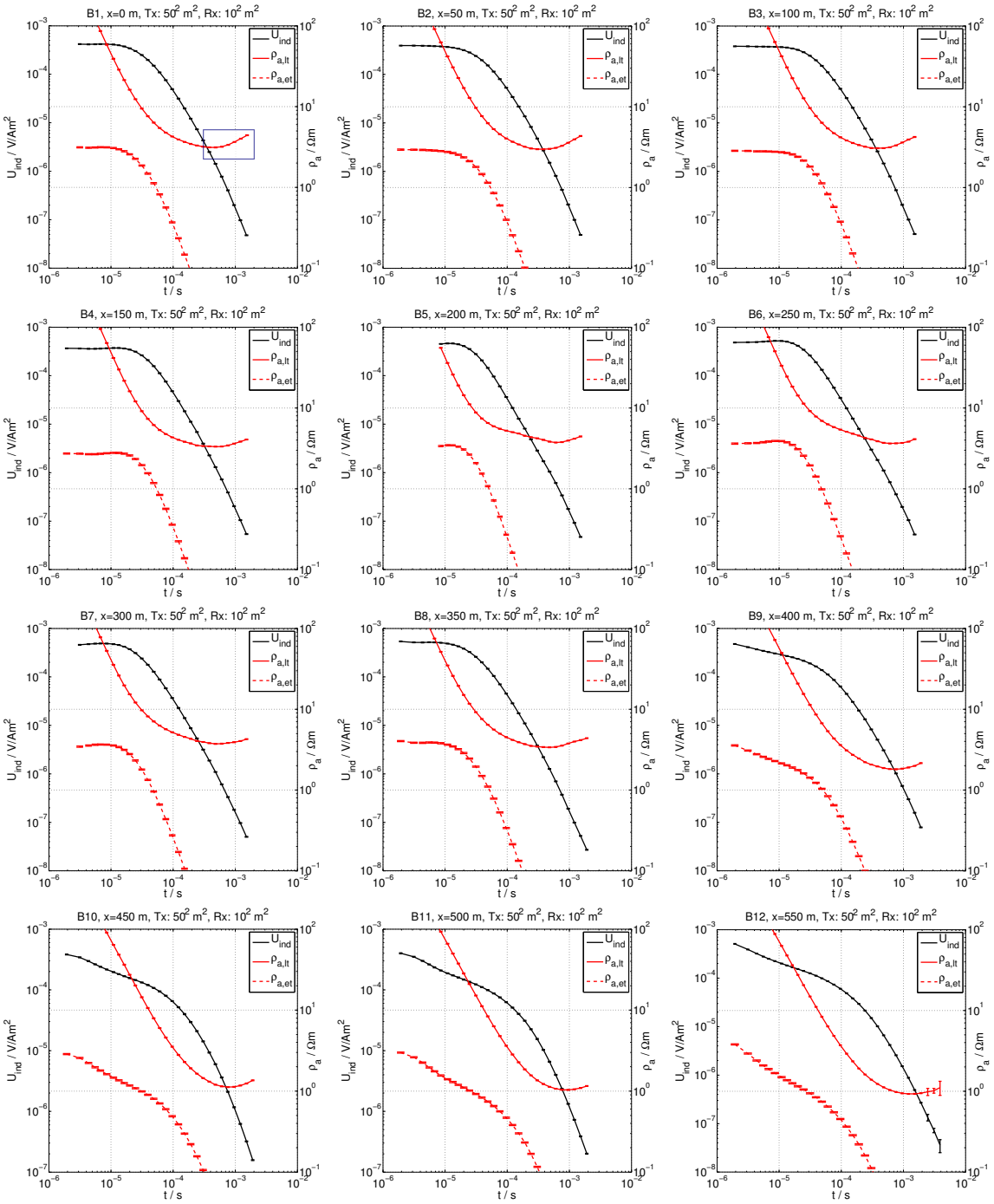

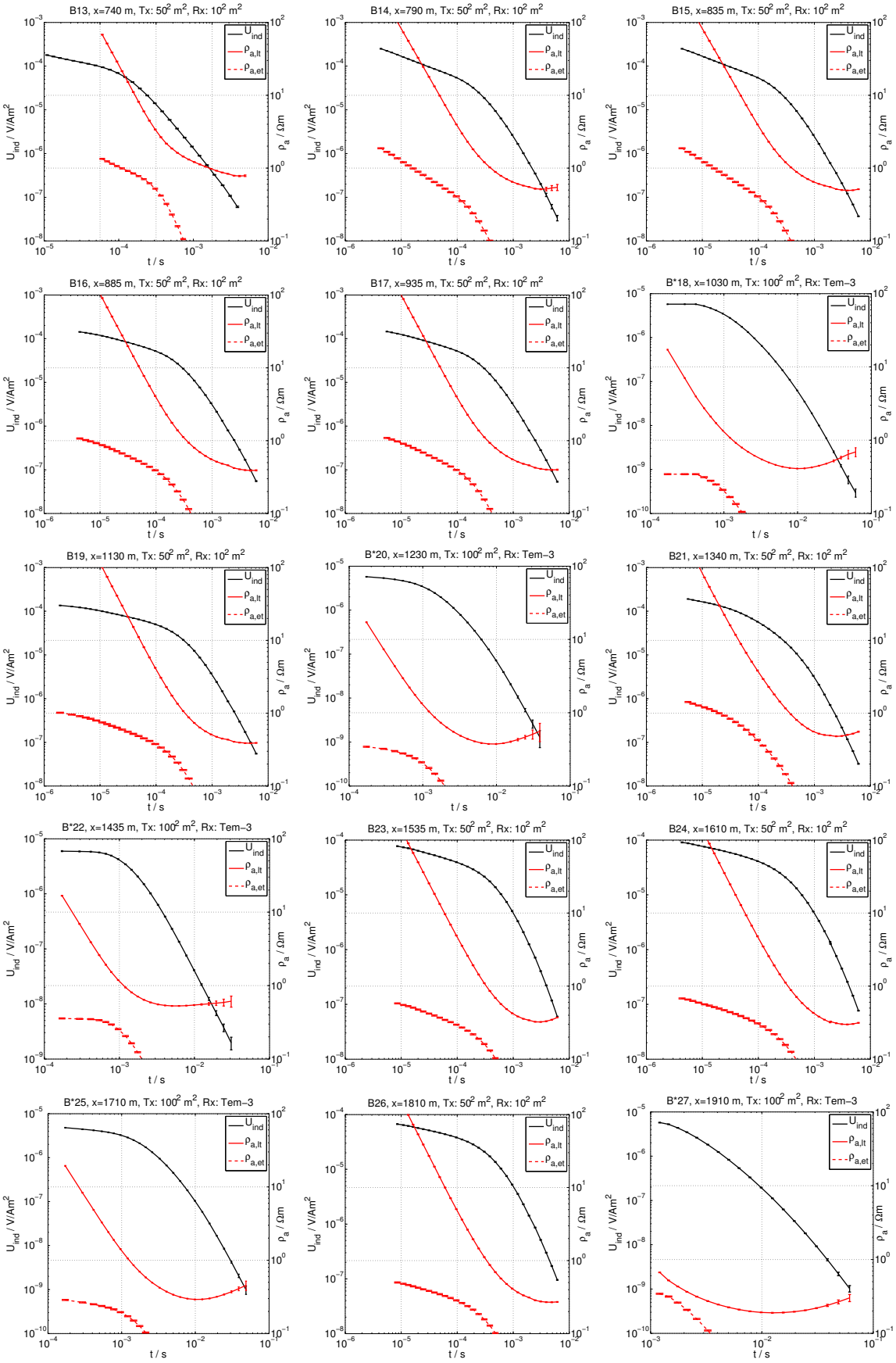
B13, x=740 m, Tx: 50² m², Rx: 10² m²
B14, x=790 m, Tx: 50² m², Rx: 10² m²
B15, x=835 m, Tx: 50² m², Rx: 10² m²
B16, x=885 m, Tx: 50² m², Rx: 10² m²
B17, x=935 m, Tx: 50² m², Rx: 10² m²
B*18, x=1030 m, Tx: 100² m², Rx: Tem−3
B19, x=1130 m, Tx: 50² m², Rx: 10² m²
B*20, x=1230 m, Tx: 100² m², Rx: Tem−3
B21, x=1340 m, Tx: 50² m², Rx: 10² m²
B*22, x=1435 m, Tx: 100² m², Rx: Tem−3
B23, x=1535 m, Tx: 50² m², Rx: 10² m²
B24, x=1610 m, Tx: 50² m², Rx: 10² m²
B*25, x=1710 m, Tx: 100² m², Rx: Tem−3
B26, x=1810 m, Tx: 50² m², Rx: 10² m²
B*27, x=1910 m, Tx: 100² m², Rx: Tem−3
U_ind
ρ_a,lt
ρ_a,et
U_ind / V/Am²
ρ_a / Ωm
t / s

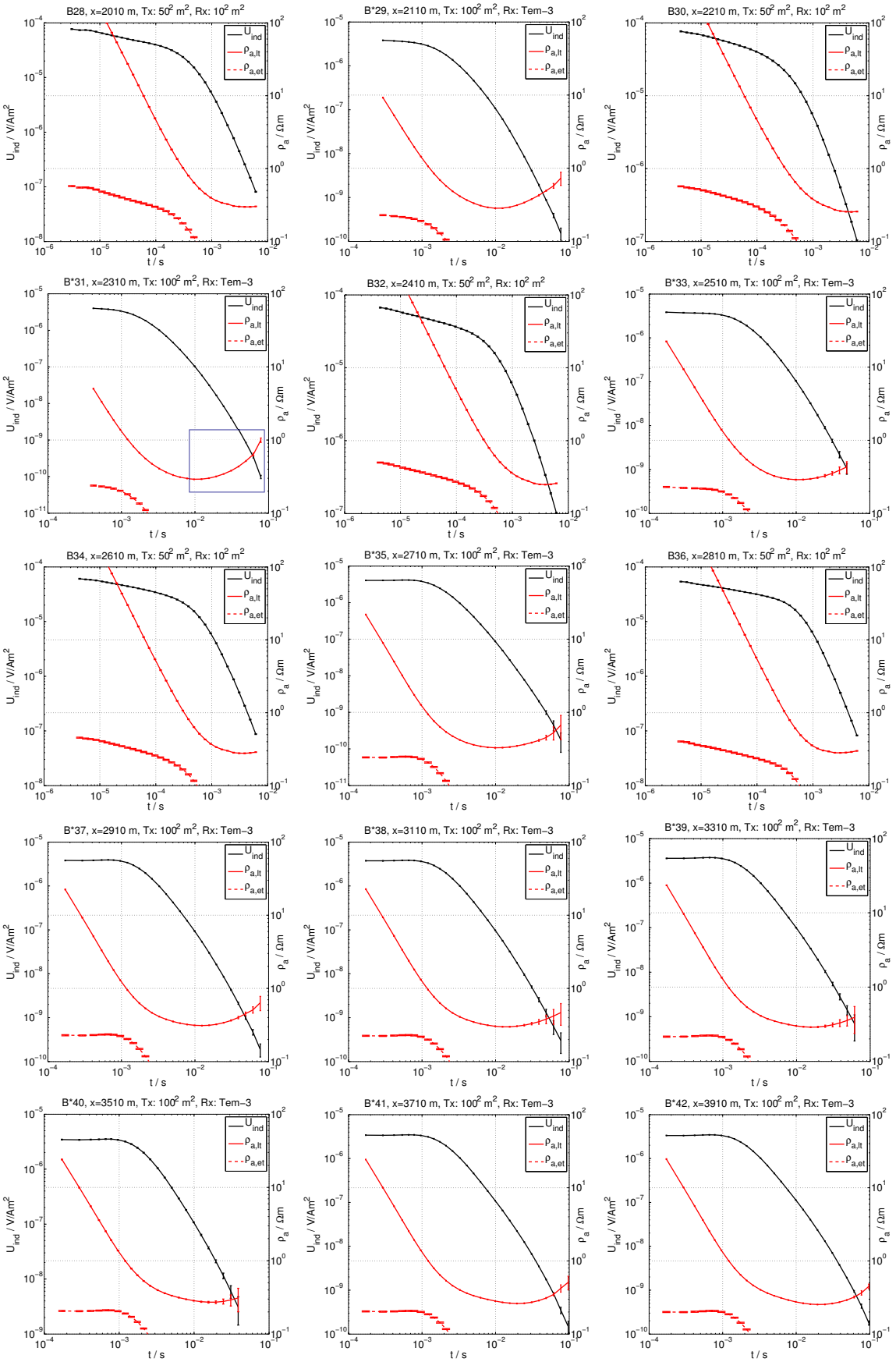
B28, x=2010 m, Tx: 50² m², Rx: 10² m²
B*29, x=2110 m, Tx: 100² m², Rx: Tem−3
B30, x=2210 m, Tx: 50² m², Rx: 10² m²
B*31, x=2310 m, Tx: 100² m², Rx: Tem−3
B32, x=2410 m, Tx: 50² m², Rx: 10² m²
B*33, x=2510 m, Tx: 100² m², Rx: Tem−3
B34, x=2610 m, Tx: 50² m², Rx: 10² m²
B*35, x=2710 m, Tx: 100² m², Rx: Tem−3
B36, x=2810 m, Tx: 50² m², Rx: 10² m²
B*37, x=2910 m, Tx: 100² m², Rx: Tem−3
B*38, x=3110 m, Tx: 100² m², Rx: Tem−3
B*39, x=3310 m, Tx: 100² m², Rx: Tem−3
B*40, x=3510 m, Tx: 100² m², Rx: Tem−3
B*41, x=3710 m, Tx: 100² m², Rx: Tem−3
B*42, x=3910 m, Tx: 100² m², Rx: Tem−3
U_ind
ρ_a,lt
ρ_a,et
U_ind / V/Am²
ρ_a / Ωm
t / s

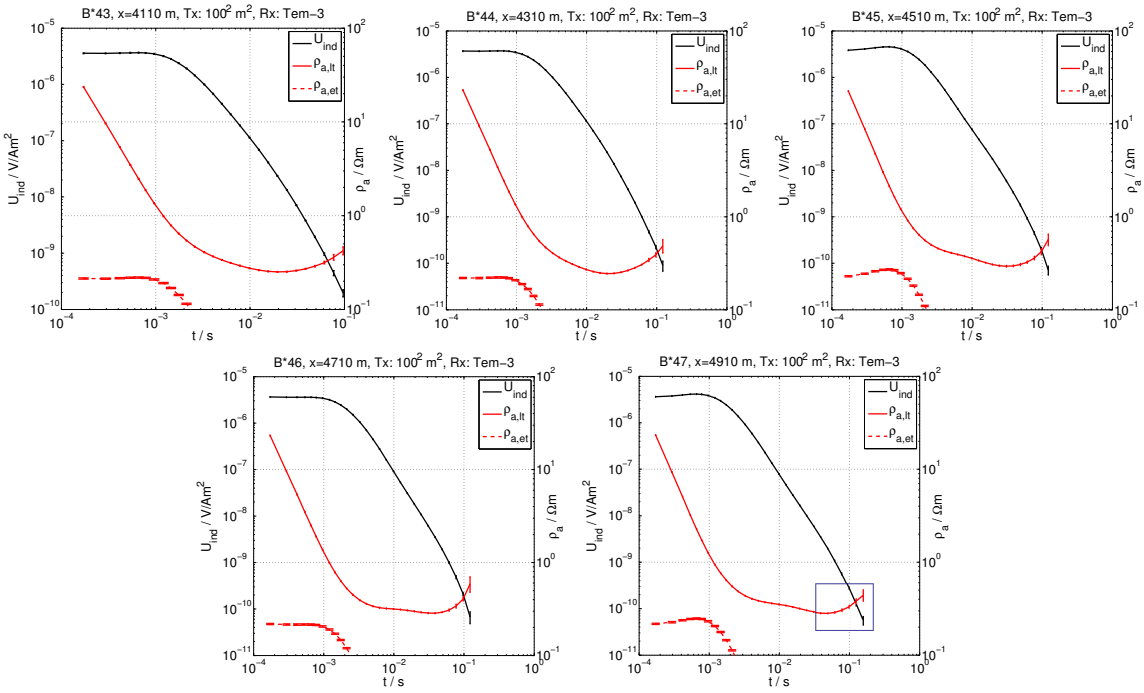
B*43, x=4110 m, Tx: 100² m², Rx: Tem−3
B*44, x=4310 m, Tx: 100² m², Rx: Tem−3
B*45, x=4510 m, Tx: 100² m², Rx: Tem−3
B*46, x=4710 m, Tx: 100² m², Rx: Tem−3
B*47, x=4910 m, Tx: 100² m², Rx: Tem−3
U_ind
ρ_a,lt
ρ_a,et
U_ind / V/Am²
ρ_a / Ωm
t / s

A.7 Profile A: 1D TEM inverse models

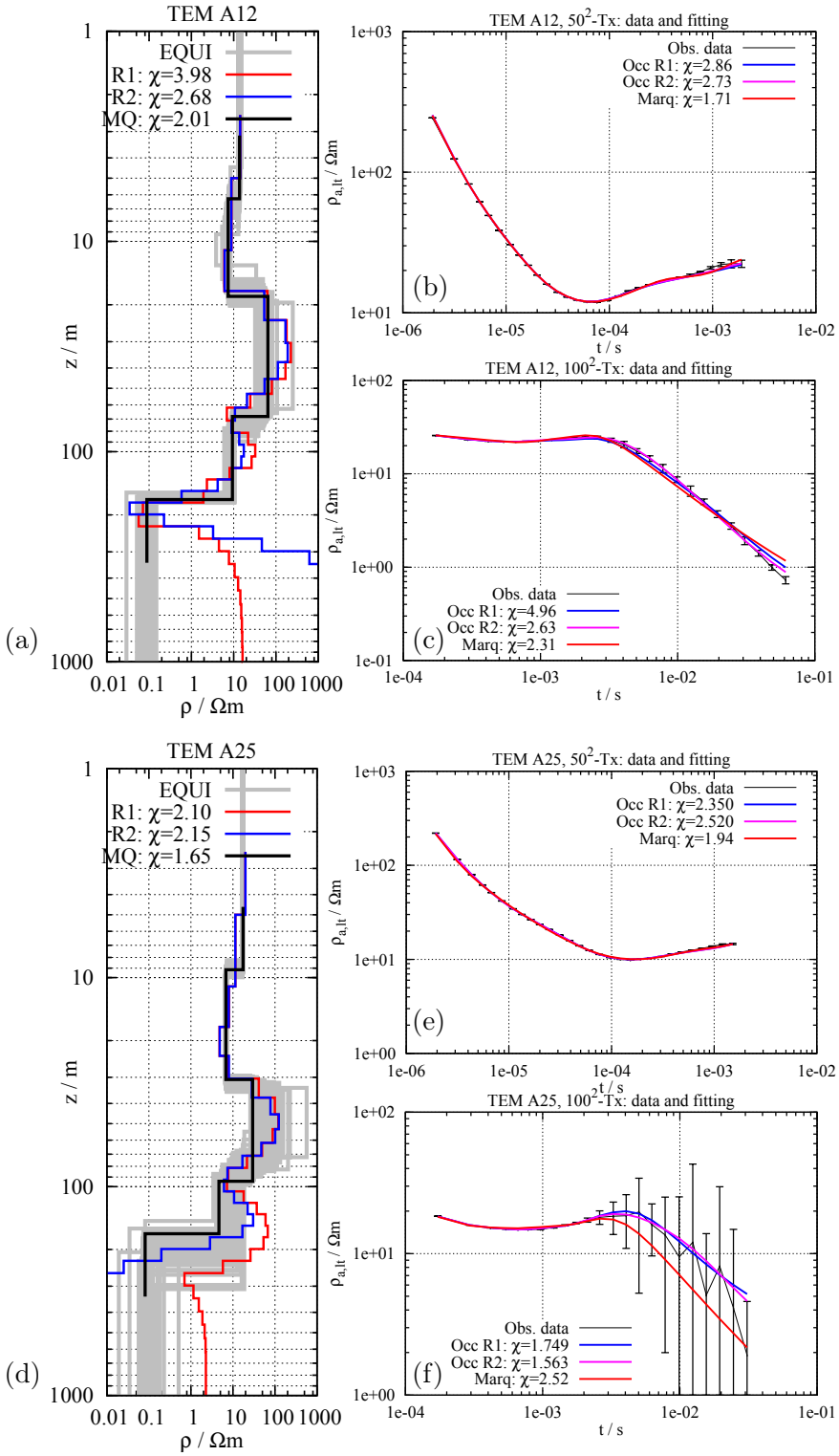

Figure A.4: *1D joint inversion result of Tx-50 and Tx-100 sounding data at (a-c) station A12 and (d-f) station A25 obtained along profile A. (a,d) Marquardt and Occam R1/R2 models. (b,e) data and fitting for the Tx-50 data and (c,f) Tx-100 data. The corresponding (overall) χ is given in each legend. Both soundings are discussed in section 4.7.2.*

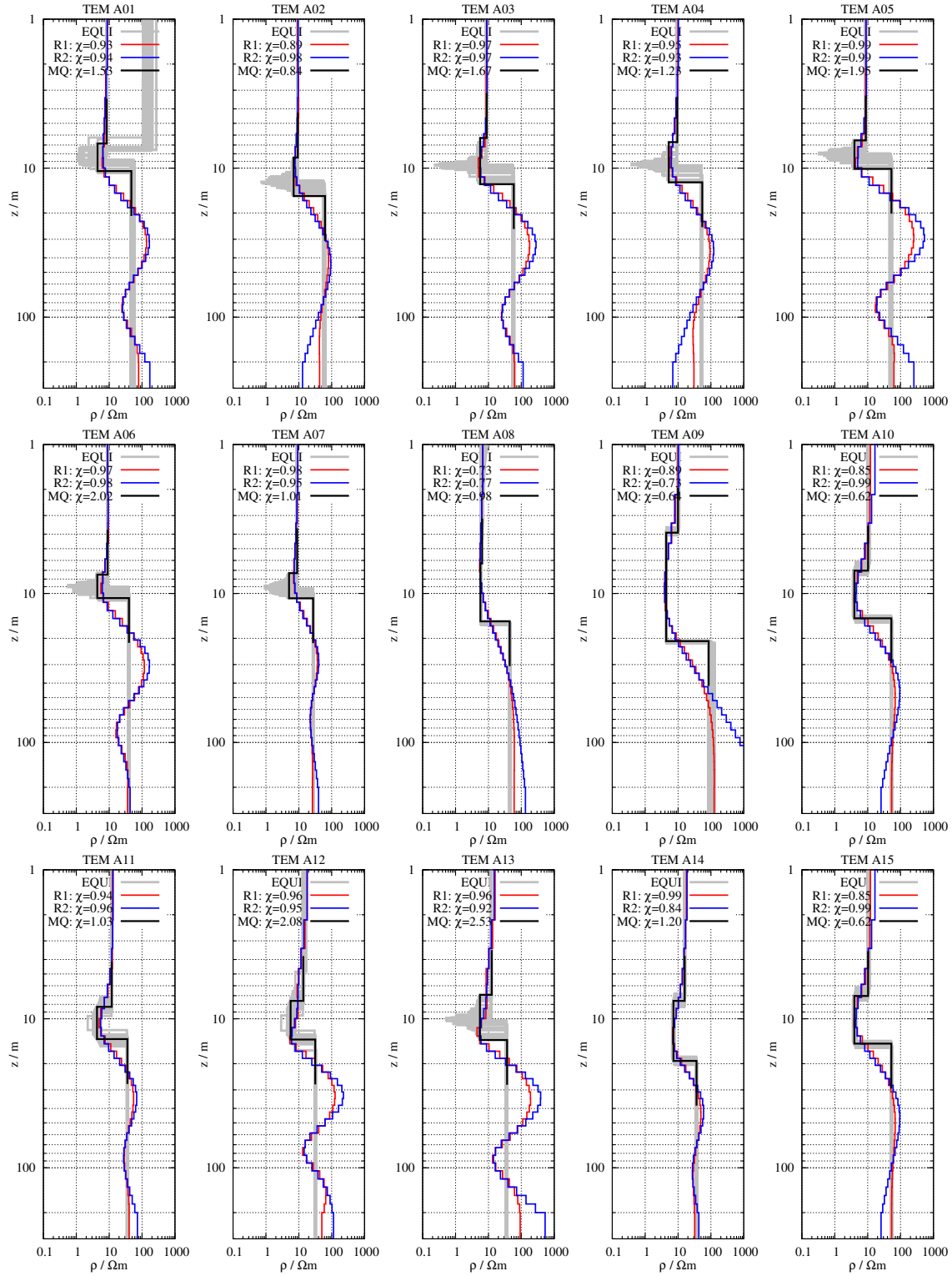

Figure A.5: *Profile A: 1D inversion results for sounding A01–A15. Tx-100 soundings are marked with an asterisk, e.g. TEM A80*.*

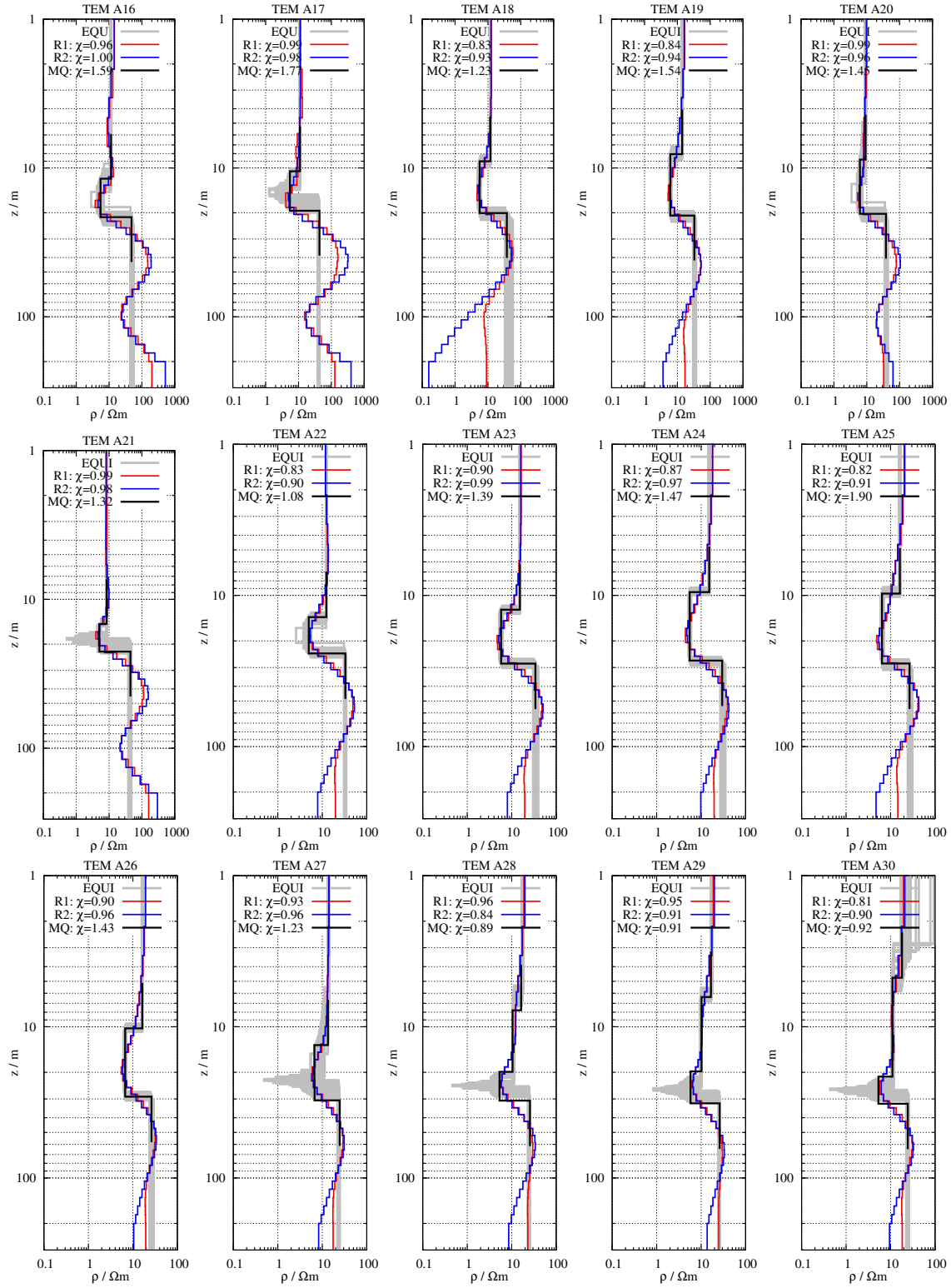

Figure A.6: *Profile A: 1D inversion results for sounding A16–A30. Tx-100 soundings are marked with an asterisk, e.g. TEM A80*.*

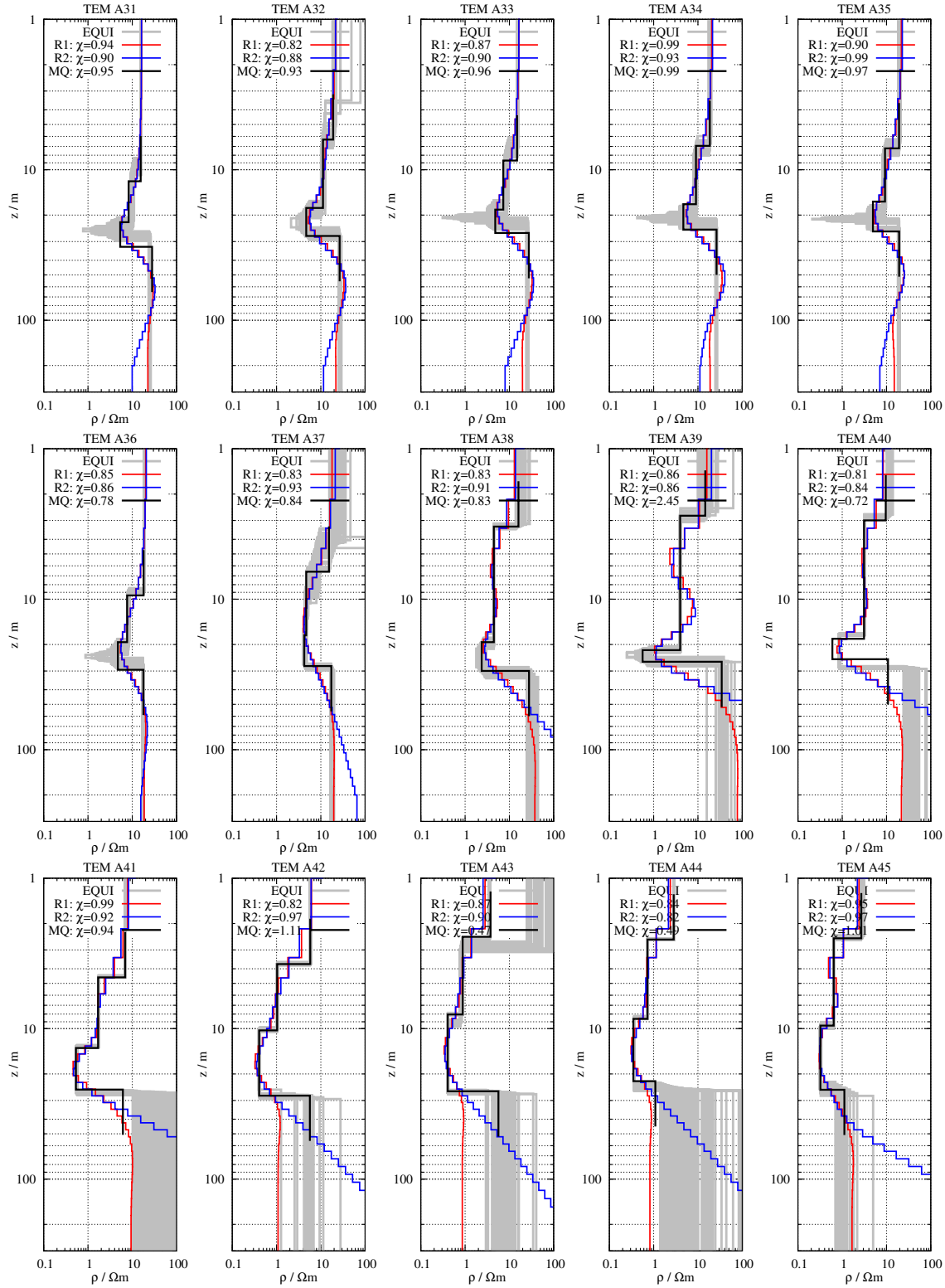

Figure A.7: *Profile A: 1D inversion results for sounding A31–A45. Tx-100 soundings are marked with an asterisk, e.g. TEM A80*.*

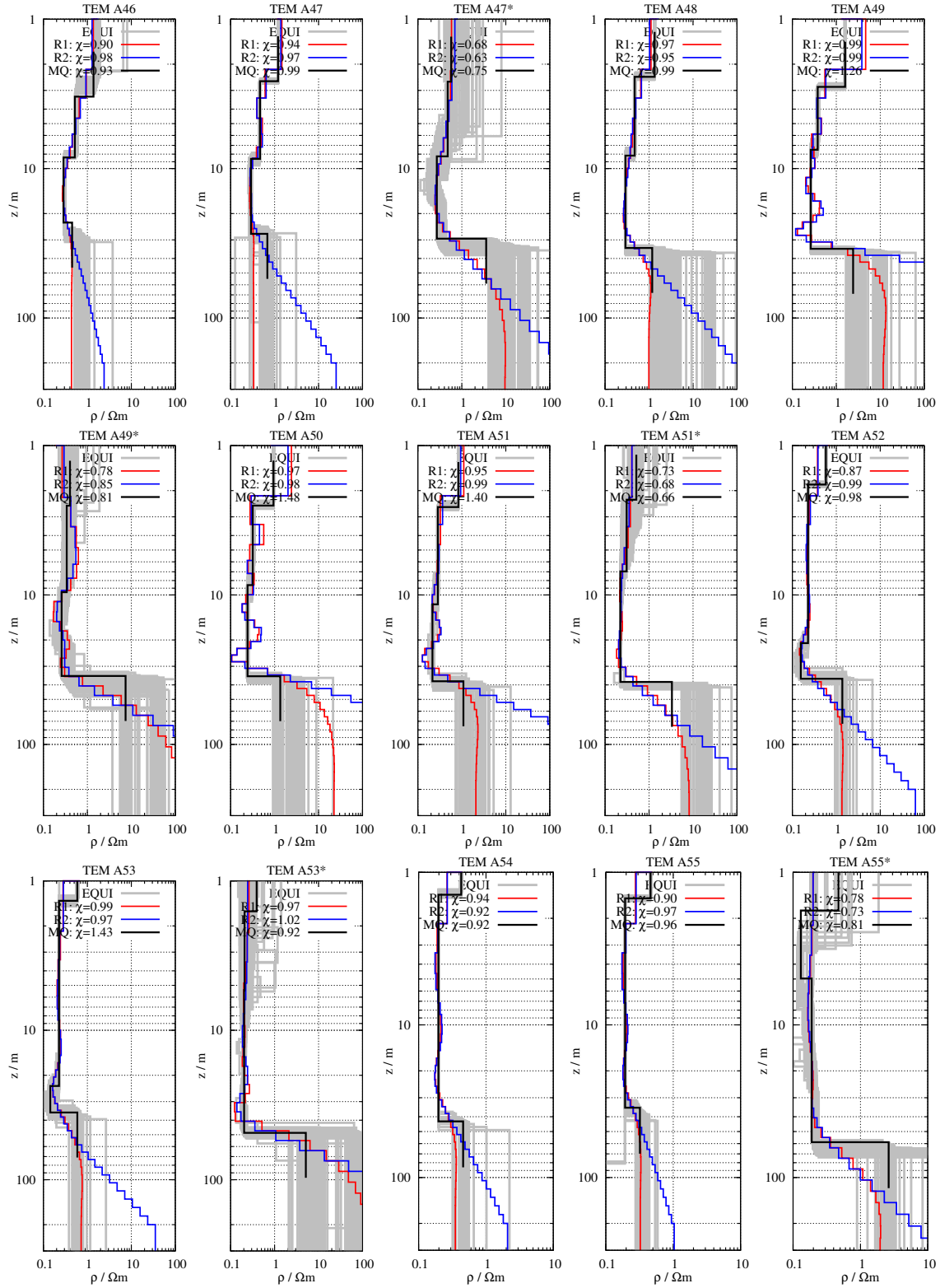

Figure A.8: *Profile A: 1D inversion results for sounding A46–A455*. Tx-100 soundings are marked with an asterisk, e.g. TEM A80*.*

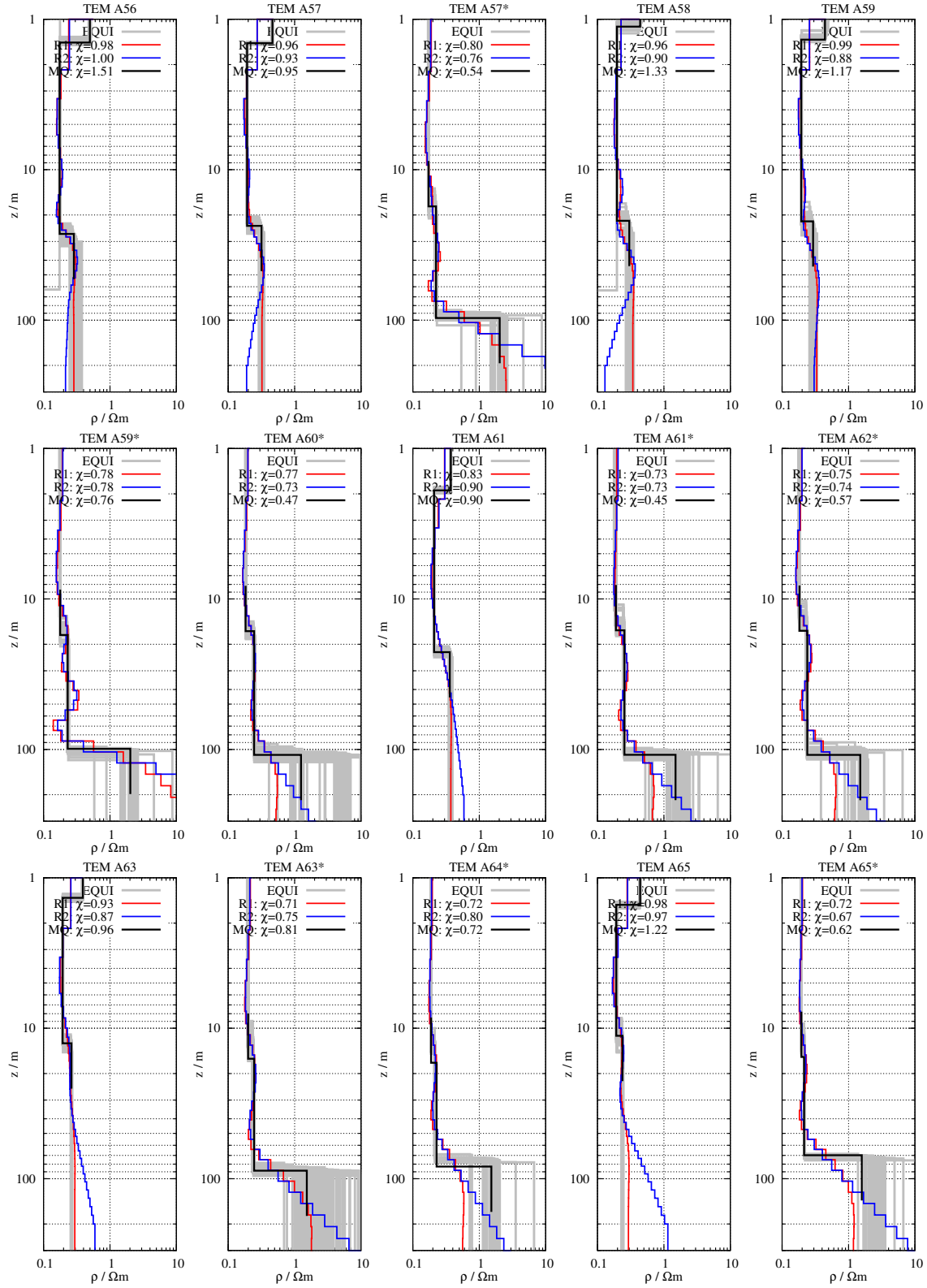

Figure A.9: *Profile A: 1D inversion results for sounding A56–A65*. Tx-100 soundings are marked with an asterisk, e.g. TEM A80*.*

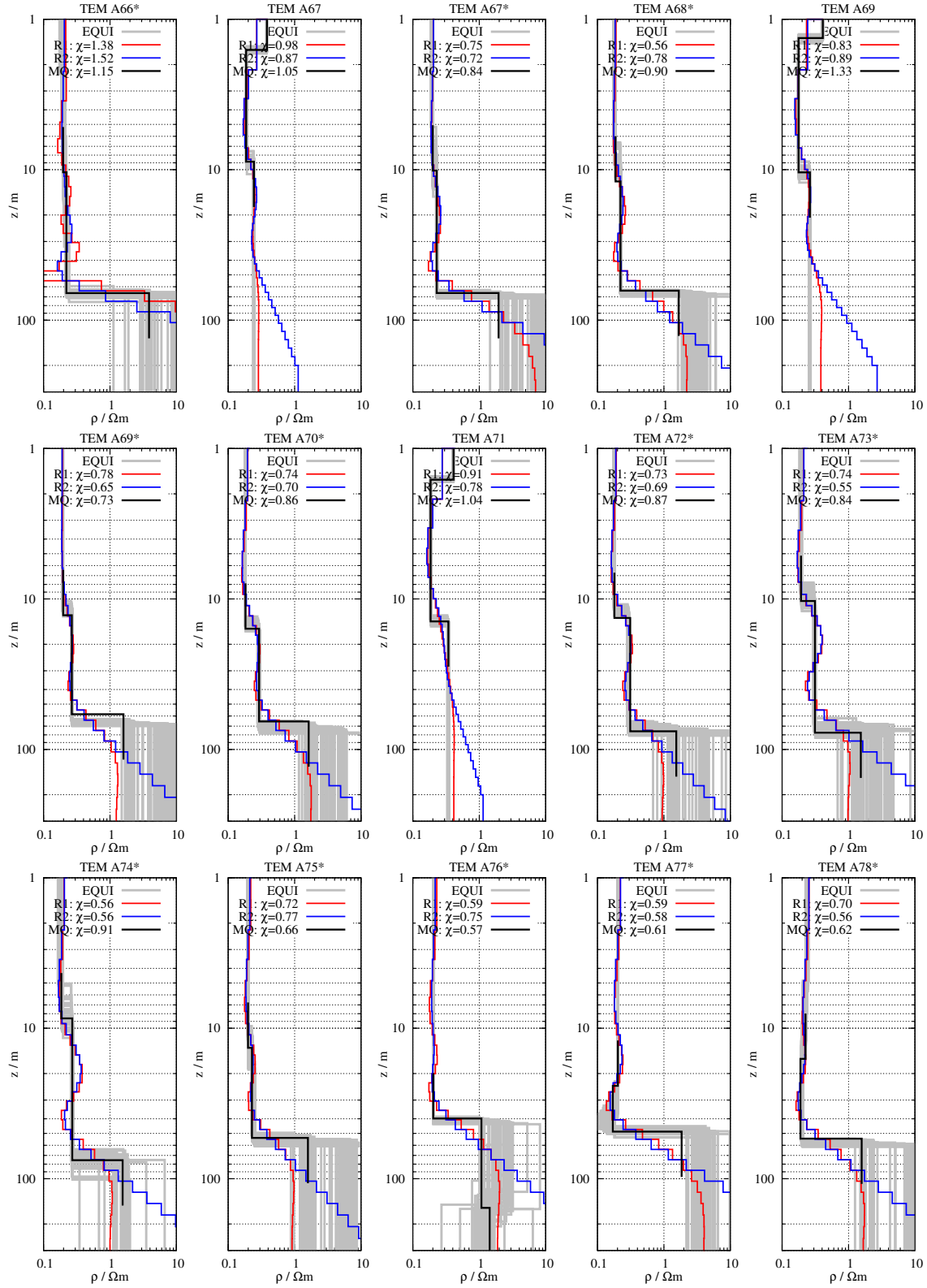

Figure A.10: *Profile A: 1D inversion results for sounding A66–A78*. Tx-100 soundings are marked with an asterisk, e.g. TEM A80*.*

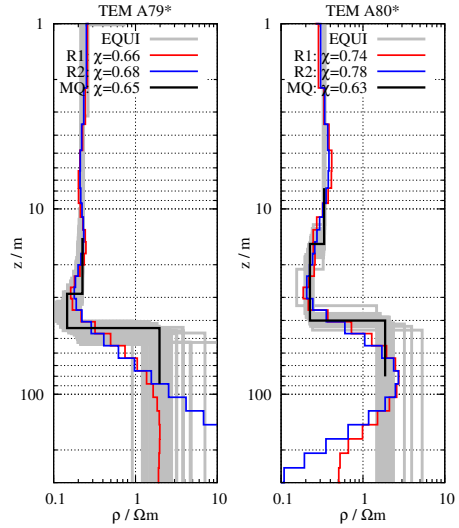

Figure A.11: *Profile A: 1D inversion results for sounding A79–A80*. Tx-100 soundings are marked with an asterisk, e.g. TEM A80*.*

A.8 Profile B: 1D TEM inverse models

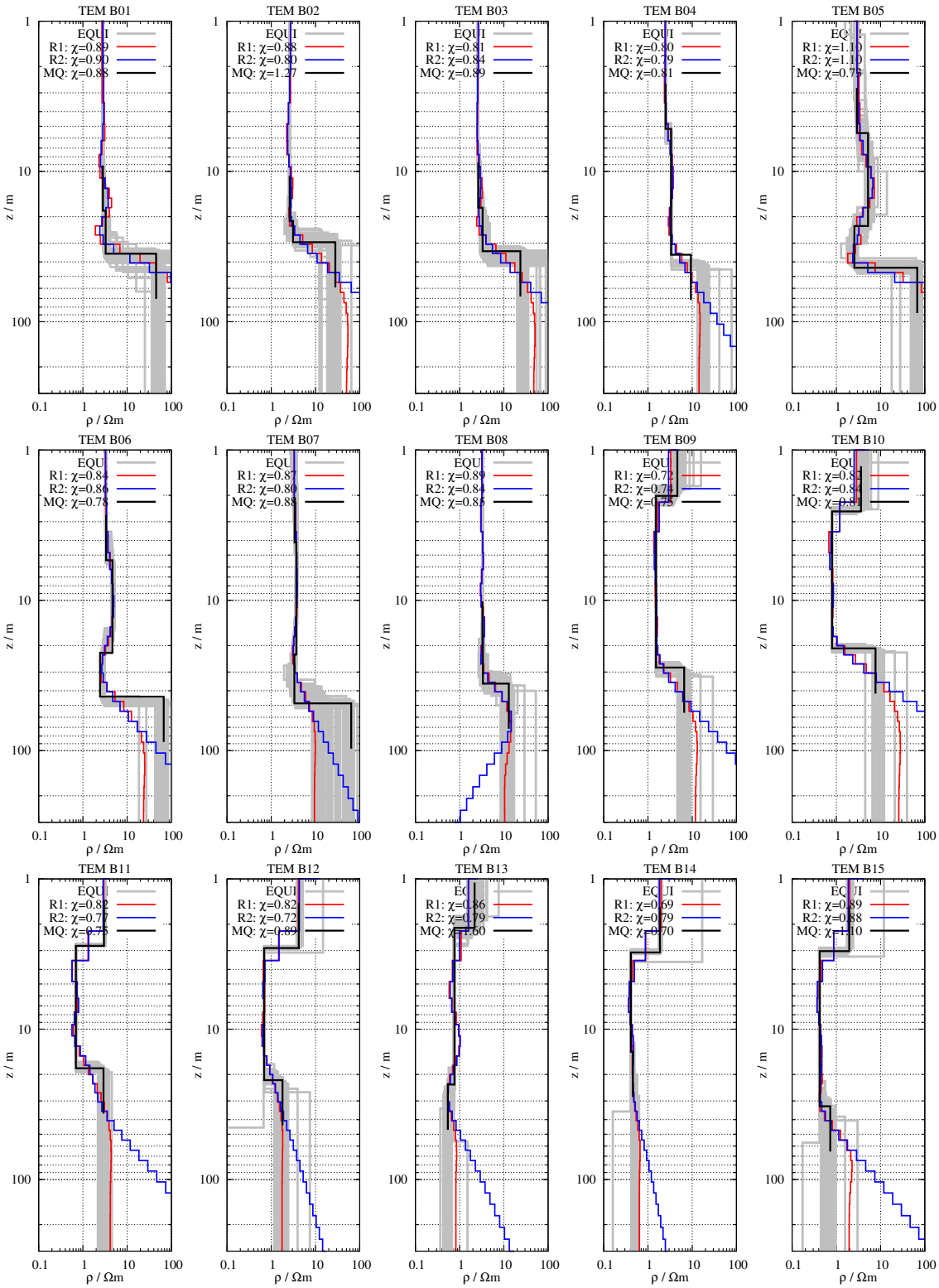

Figure A.12: *Profile B: 1D inversion results for sounding B01–B15. Tx-100 soundings are marked with an asterisk, e.g. TEM B18*.*

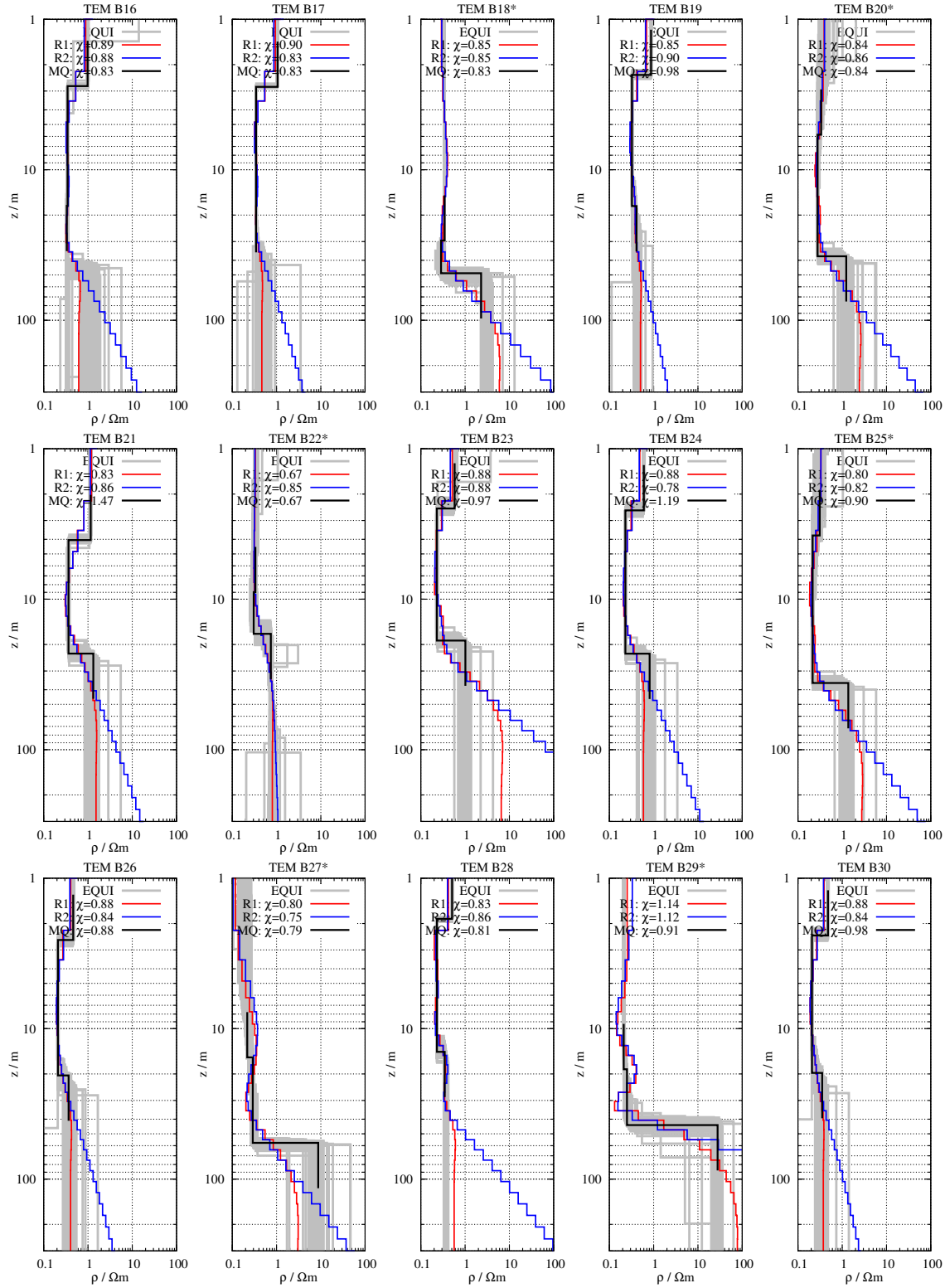

Figure A.13: *Profile B: 1D inversion results for sounding B16–B30. Tx-100 soundings are marked with an asterisk, e.g. TEM B18*.*

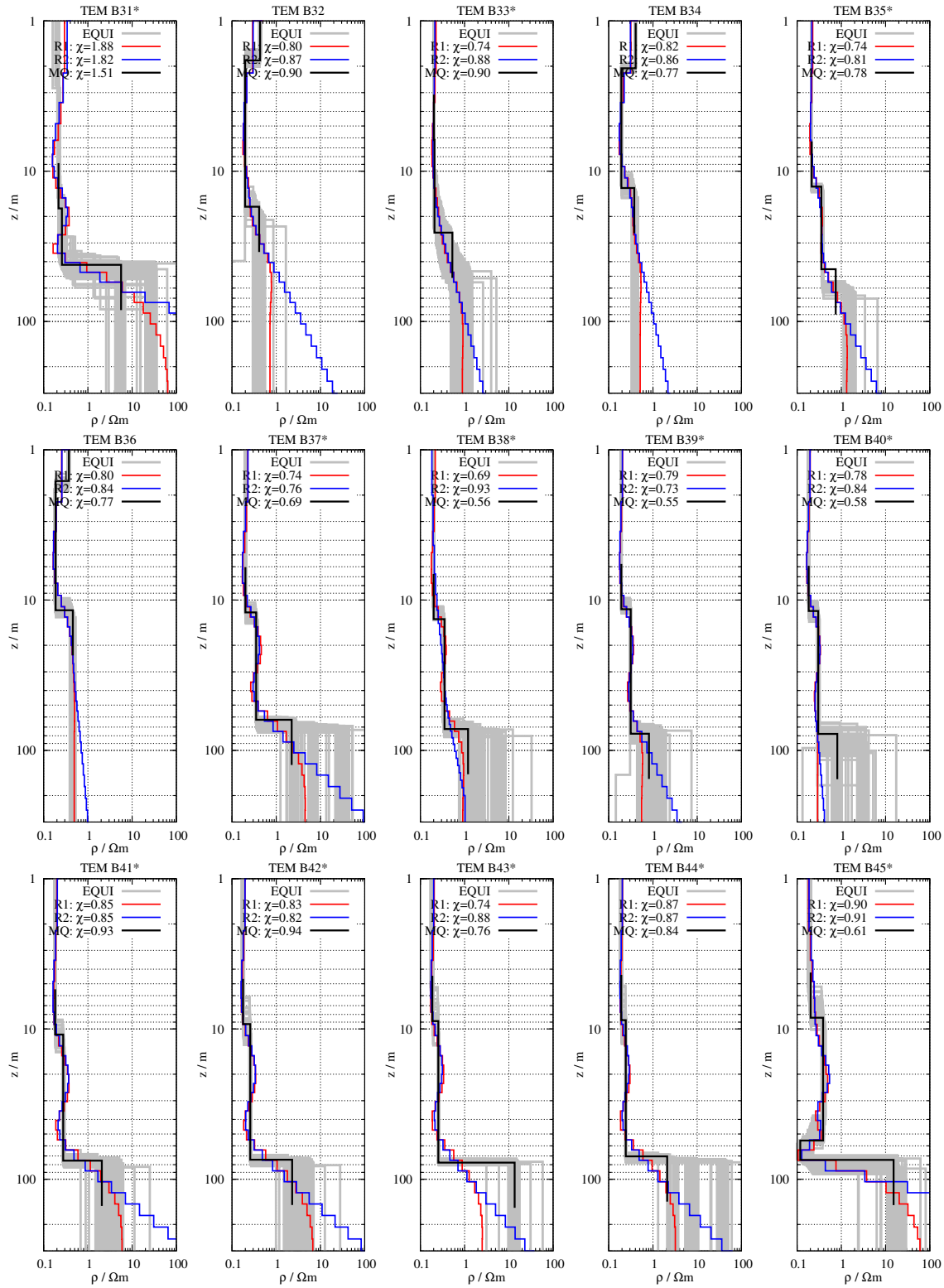

Figure A.14: *Profile B: 1D inversion results for sounding B31*–B45*. Tx-100 soundings are marked with an asterisk, e.g. TEM B31*.*

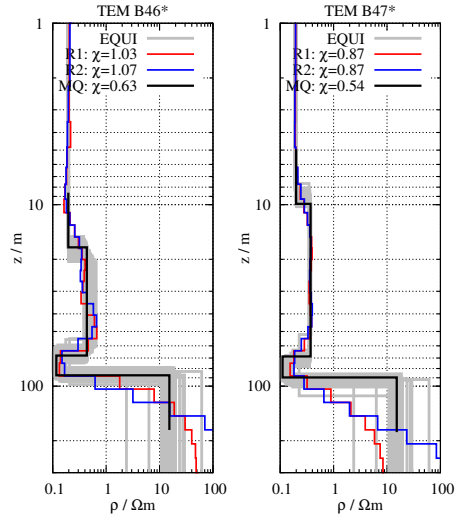

Figure A.15: *Profile B: 1D inversion results for sounding B46*–B47*. Tx-100 soundings are marked with an asterisk, e.g. TEM B47*.*

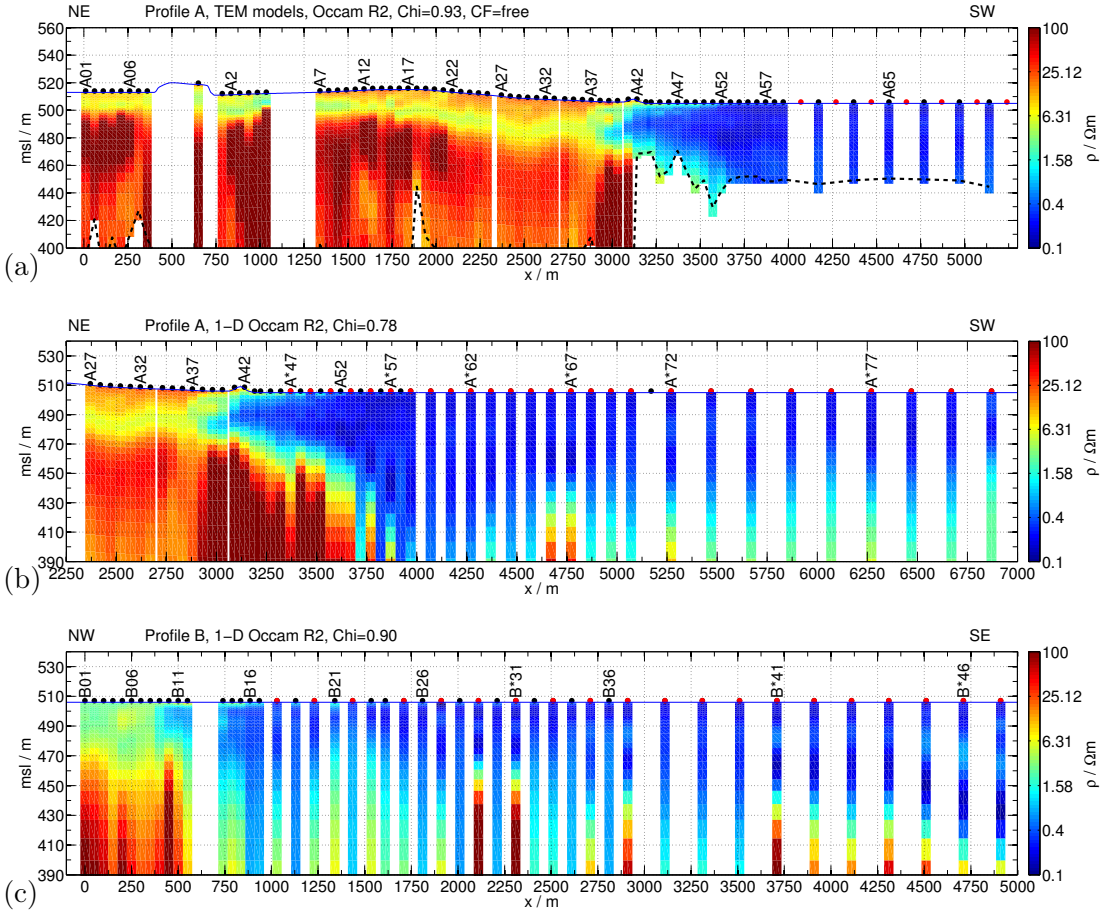

Figure A.16: *Quasi 2D resistivity-depth sections for Occam R2 results. (a) Profile A obtained from 1D inversion of Tx-50 sounding data between A01 and A72. (b) Profile A obtained from 1D inversion of Tx-50 and Tx-100 sounding data between A27 and A*80. (c) Profile B obtained from 1D inversion of Tx-50 and Tx-100 sounding data. The resistivity-depth sections are discussed in section 4.7.*

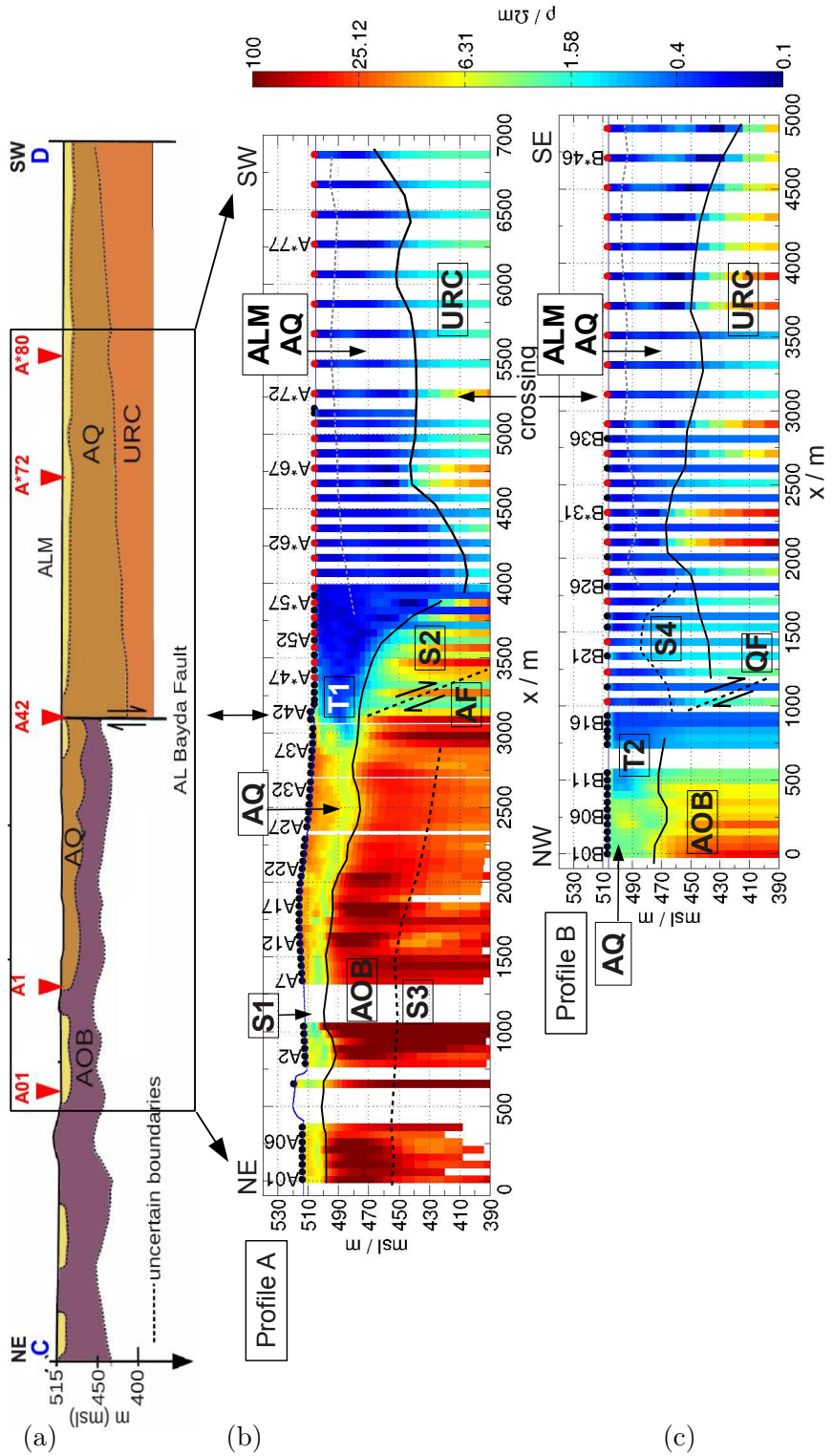

(a) (b) (c)

Figure A.17: *(a) Geological cross-section modified after Ibrahim [1996], which is representative for profile A. Quasi 2D resistivity-depth sections for (b) profile A and (c) profile B derived from 1D Occam models. Further explanation is given in chapter 4.8.*

A.9 2D ERT inversion results and data

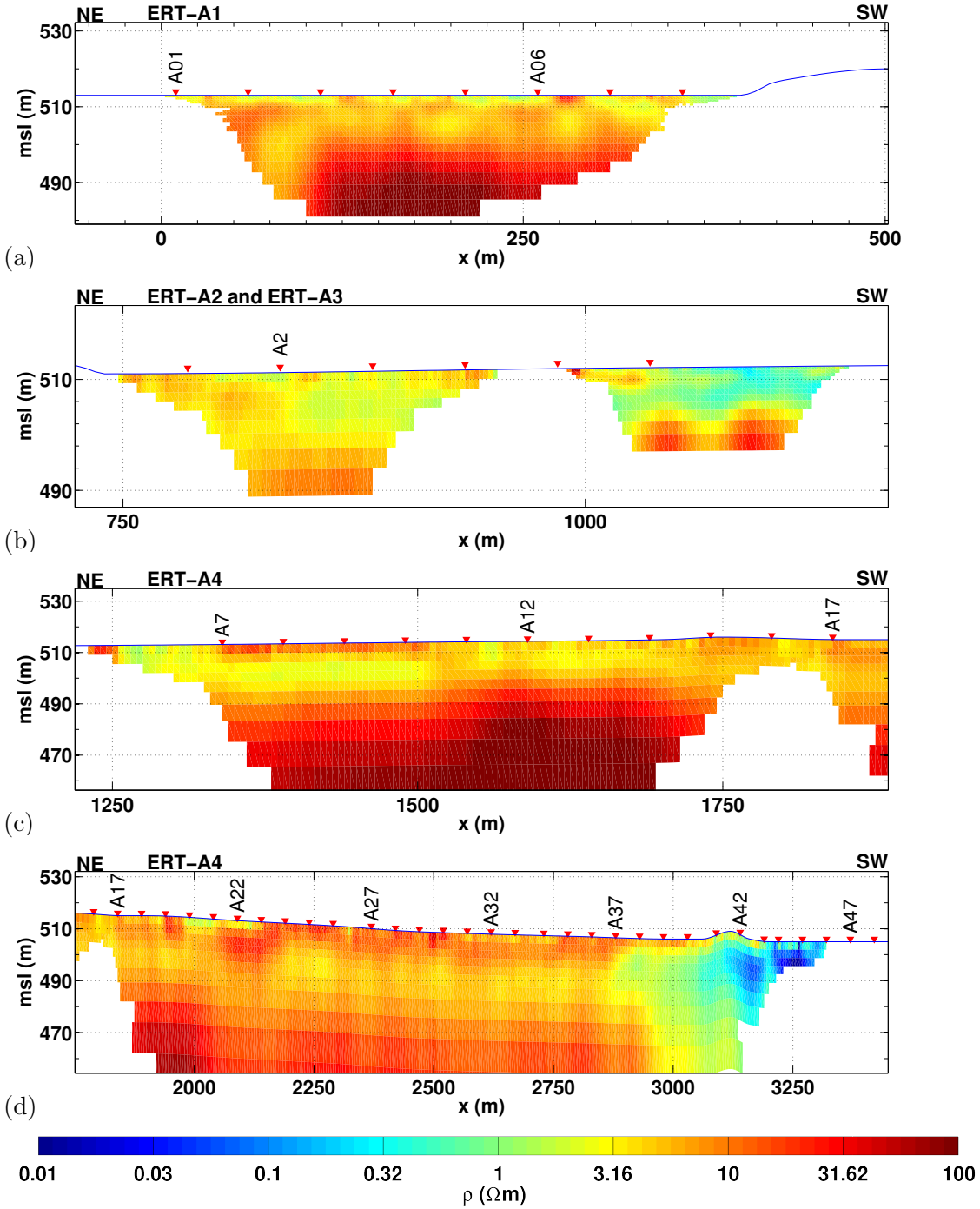

Figure A.18: *2D inversion results of the ERT data along profile A. The Profile name is given above each model. The x-scale is the profile meter. For comparison the TEM sounding locations are marked in each section.*

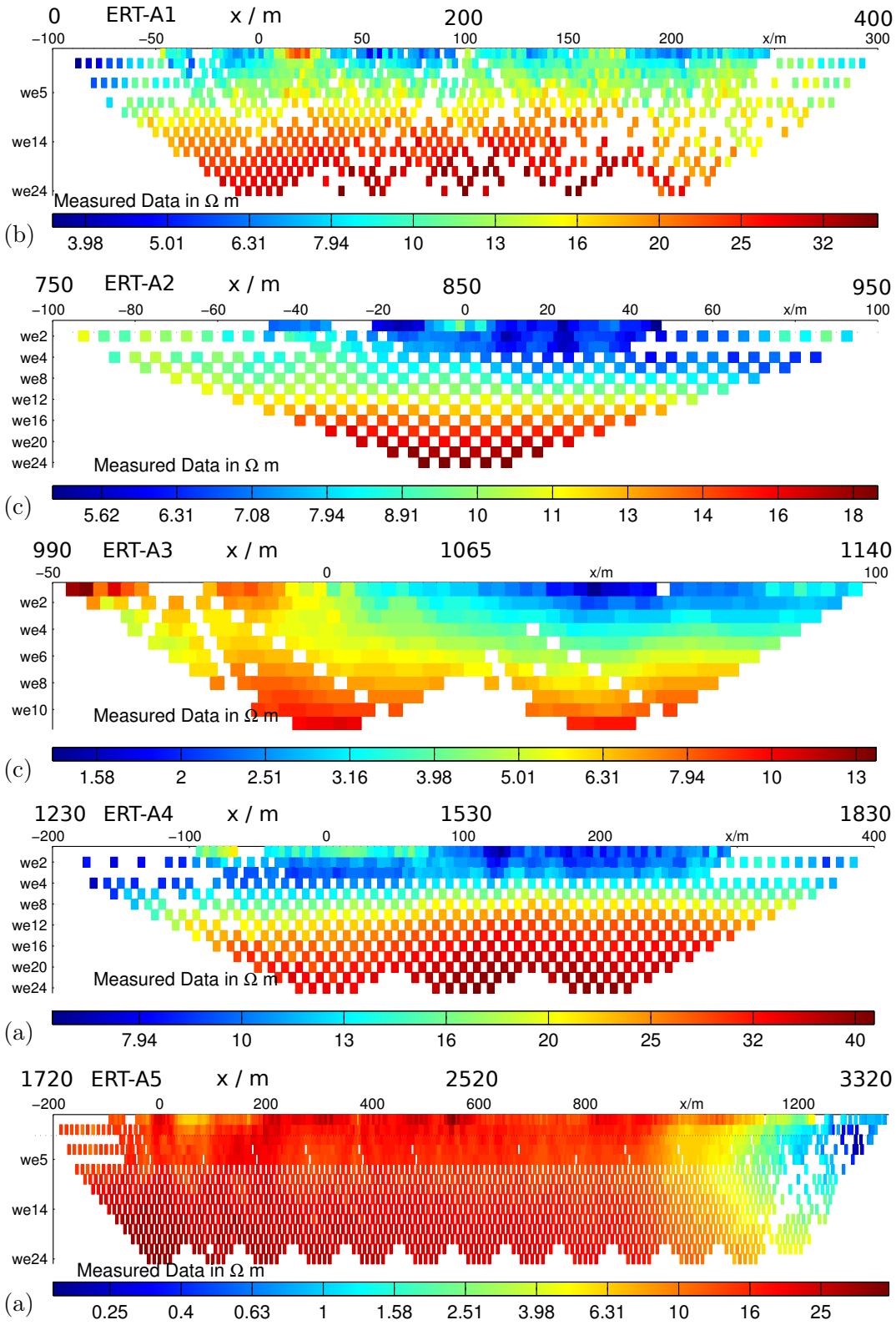

Figure A.19: *ERT field data pseudosections along profile A. The profile name is given above each section. The upper x-scale is always the profile meter and corresponds to the inversion results in Fig. A.18; the lower scale is the distance to the center electrode (of the first Roll-along).*

A.10 Additional 2D forward and inverse modeling results

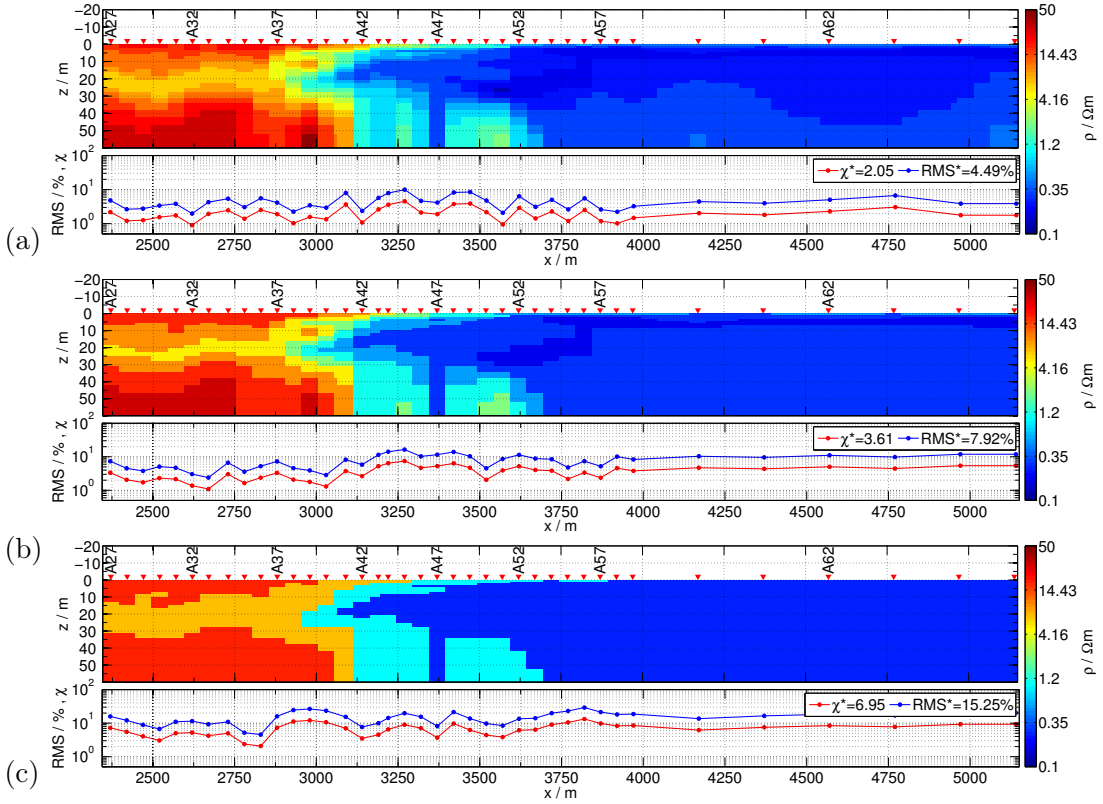

Figure A.20: *2D models derived by spatial interpolation of 1D Occam models onto a 2D grid for a lateral discretization of $\Delta_x = 50$ m. The resistivities are joined into (a) 20, (b) 10 and (c) 5 logarithmically equidistant bands. The corresponding RMS and χ are displayed below each 2D model.*

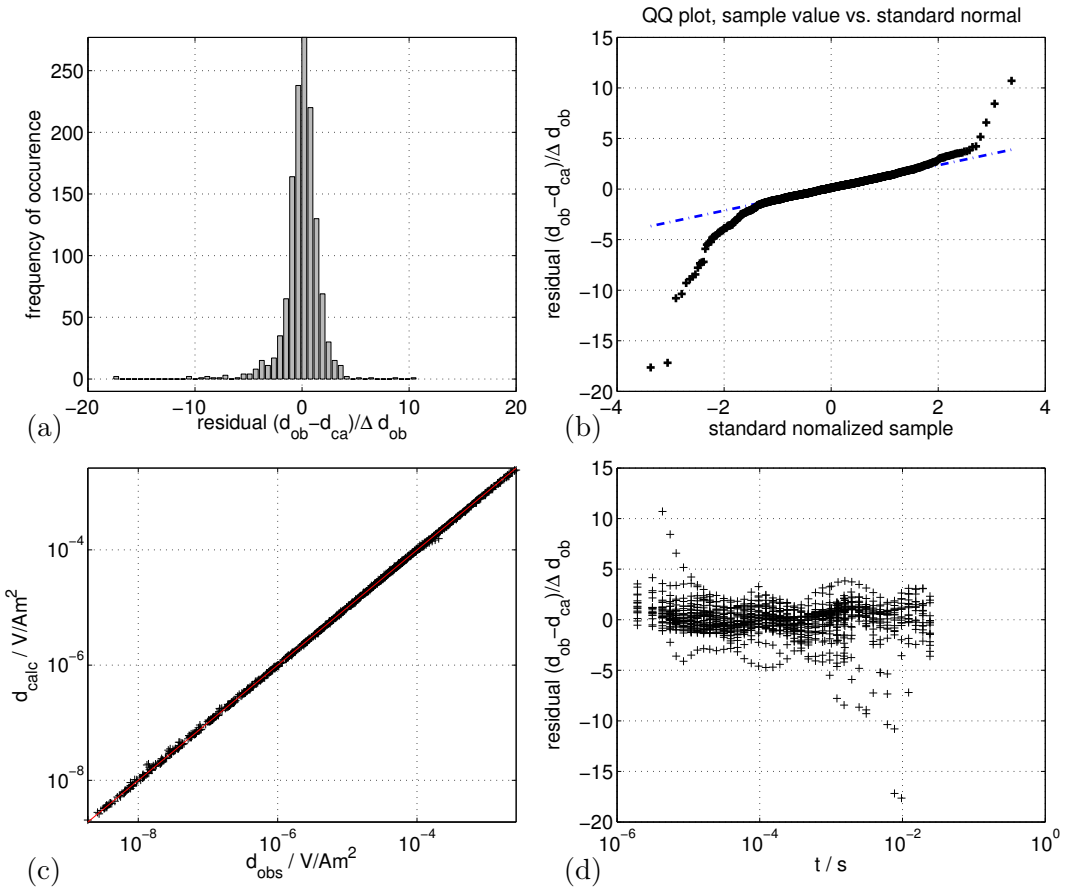

Figure A.21: *(a) Histogram of the data residuals for each time point and sounding location of the the best-fit 2D Occam model discussed in section 5.5.2. (b) QQ plot of the data residuals. The straight line with slope one is marked dashed blue. (c) Calculated data d_{calc} plotted versus the field data d_{obs}. (d) Residuals plotted versus the transient time.*

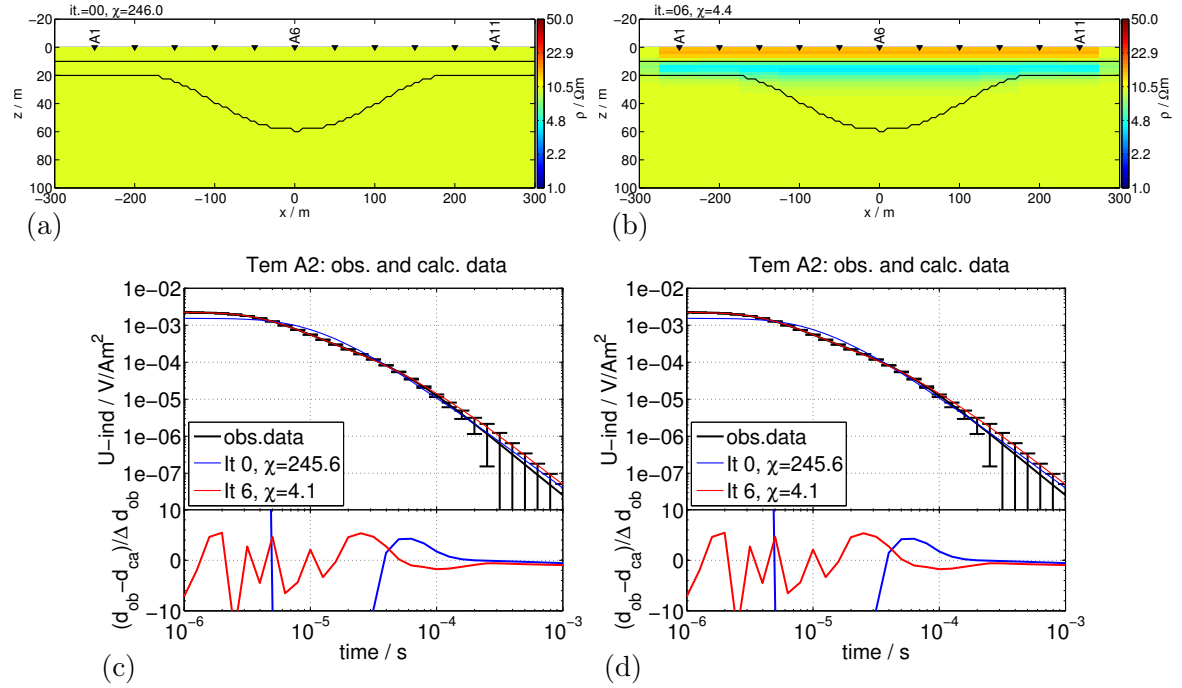

Figure A.22: *2D inversion results for the basin structure using large errors at late times. The down-weighting of late time data is discussed in section 6.1.3. (a) Homogeneous starting model with 10 Ωm. (b) Final inverse model after the 6th iteration. The global χ is given above the model. Synthetic data (obs.data) and model response for soundings (a) A2 and (b) A5. The response for the starting model (It 0), the final iteration (It 6) are plotted. The corresponding residuals are displayed below the response.*

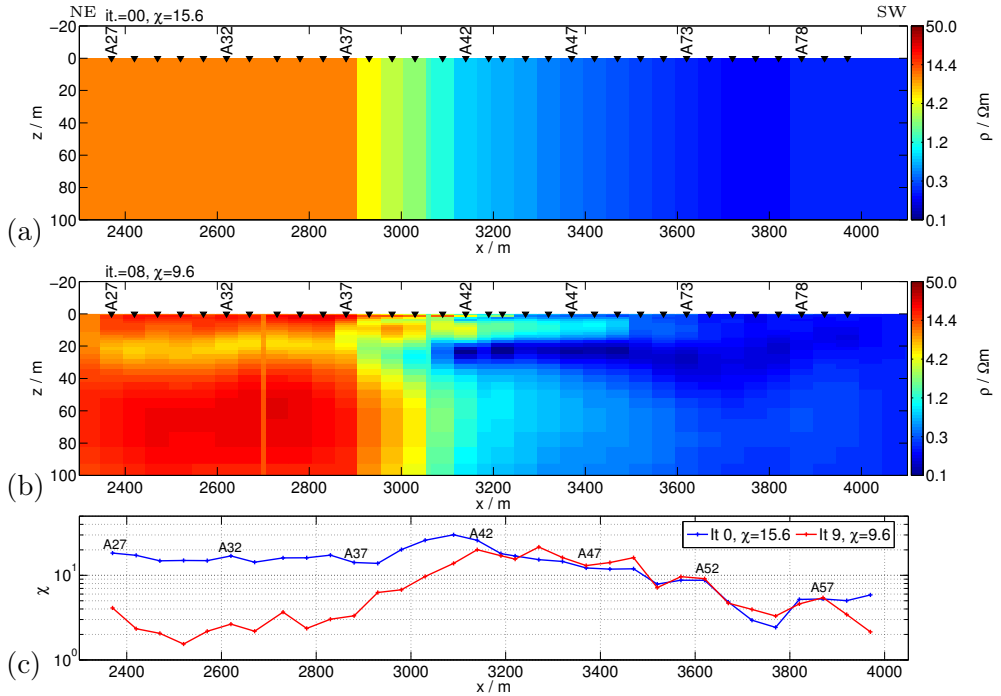

Figure A.23: *2D inversion of Tx-50 data using $\rho_{a,lt}$ values as starting model. A logarithmic depth parameterization is used for comparison with the result discussed in section 6.4.2.(a) Initial model (It 0); (b) final 2D model after 8 iterations (It 8). In (c) χ plotted along the profile line for (a) and (b). The global χ is displayed in the legend.*

Acknowledgments

At this point I would like to express my gratitude.

Prof. Dr. Bülent Tezkan is the supervisor of this thesis. He advised, supported me throughout the past years and made this work possible. I am tremendously thankful for all the opportunities he has provided- I participated in interesting projects and had great experiences.

Prof. Dr. Andreas Junge appraised this thesis and gave me good suggestions during the last Schmucker-Weidelt colloquium.

Dr. Roland Martin supported me since I started as a student helper eight years back. I have learned so much from him and all the discussions about electromagnetics were a pleasure. He has contributed tremendously to my research and he made all kinds of modifications to the algorithm *SINV*. His encouragement and friendship was a great support over the past years.

I am tremendously thankful to all the Jordan colleagues, who supported me in the organization and made these two surveys possible. The Natural Resources Authority in Amman provided the basis for the field work in Azraq. My gratitude especially to Dr. K. Abu-Ayyash who has arranged really everything for us; to Dr. T. Yasjeen, who supported us with all the organization and custom organization prior to the first survey; to Dr. A. Sawarieh, who rescued the second survey, which was almost canceled. My very heartfelt thankfulness goes to Tasin Thalat, who helped me with everything throughout both field campaigns. He provided me with numerous additional information and reports about Azraq. The field work with Tasin, Jamal, Nirdal, Dr. Hussain, Ali, Mohammed, Jan W., Jan M. and Amir was great. I will never forget the great hospitality and friendliness.

Dr. Roland Martin and Dr. Carsten Scholl who developed the (current) 2D TDEM inversion algorithm *SINV*. Dr. Thomas Günther for providing his DC2DINVRES inversion algorithm. V. Druskin and L. Knizhnerman for *SLDMem3t*.

Rainer Bergers for all his support in technical issues. Thanks to Michael Lohmar for his great work with the TEM cart and of course also thanks to Andreas Busse.

Dr. Stefan Kröpelin has done really everything to rescue the originally planned field survey in the Western Sahara. Prof. Dr. Jürgen Richter decisively motivated me to shift the geophysical survey to Jordan. The organizational support by Dr. Werner Schuck within the SFB 806 was great.

Dr. Sudha for many helpful discussions and sharing so many years together in the office.

I want to thank all my colleagues at the IGM. Particularly Mitch for all the discussions and creative breaks over the last years; Klaus for all the project-experiences we had together; Amir for re-writing many plot-scripts and discussions; Jan for his motivation for sports in the final phase; A thanks goes also to Hannah, Juliane, Mitch, Amir, Jan, Olliver, Fab and Sarah in the final phase of writing this thesis.
My gratitude to all the people from both working groups at the IGM-Cologne for the good atmosphere

Thank to the RRZK and the possibility to use CHEOPS. The support was very good and always friendly.

The German Research Foundation (DFG) has funded this work within the frame of the Collaborative Research Center SFB-806/1.

★ Finally, my deep gratitude to Judith for being with me all the time, her encouragement and patience in tough times. All my very close friends are part of my life and were part of this work in different ways. My family was with me all the time...

Erklärung

Ich versichere, dass ich die von mir vorgelegte Dissertation selbständig angefertigt, die benutzten Quellen und Hilfsmittel vollständig angegeben und die Stellen der Arbeit -einschließlich Tabellen, Karten und Abbildungen-, die anderen Werken im Wortlaut oder dem Sinn nach entnommen sind, in jedem Einzelfall als Entlehnung kenntlich gemacht habe; dass diese Dissertation noch keiner anderen Fakultät oder Universität zur Prüfung vorgelegen hat; dass sie -abgesehen von unten angegebenen Teilpublikationen -noch nicht veröffentlicht worden ist sowie, dass ich eine solche Veröffentlichung vor Abschluss des Promotionsverfahrens nicht vornehmen werde. Die Bestimmungen dieser Promotionsordnung sind mir bekannt. Die von mir vorgelegte Dissertation ist von Prof. Dr. Bülent Tezkan betreut worden.

Köln, Mai 2014

Teilpublikationen

Yogeshwar, P., Tezkan, B. & Haroon, A., 2011. *Investigation of the Azraq Basin in the Eastern Desert of Jordan using Integrated Geoelectrical Techniques*, 24. Schmucker-Weidelt Kolloquium für Elektromagnetische Tiefenforschung, Neustadt.

Yogeshwar, P., Tezkan, B. & Haroon, A., 2012. *Investigation of the Azraq Basin, Jordan using Integrated Geoelectrical Techniques: 2D Modeling of Transient Electromagnetic Data*, 21st Electromagnetic Induction Workshop, Darwin, Australia.

Yogeshwar, P., Tezkan, B. & Haroon, A., 2013. *Investigation of the Azraq Sedimantary Basin, Jordan using Integrated Geoelectrical and Electromagnetic Techniques*, Near Surface Geophysics, 11, 381-389.